Development of a velocity and anisotropy tomography from first-arrival traveltimes : applications to field and laboratory seismic or electromagnetic data in carbonates

Marco Antonio Salcedo Arciniega

To cite this version:

Marco Antonio Salcedo Arciniega. Development of a velocity and anisotropy tomography from first-arrival traveltimes : applications to field and laboratory seismic or electromagnetic data in carbonates. Earth Sciences. Université Grenoble Alpes [2020-..], 2021. English. NNT : 2021GRALU036 . tel-03609417

HAL Id: tel-03609417
https://theses.hal.science/tel-03609417v1

Submitted on 15 Mar 2022

Université
Grenoble Alpes

THÈSE

Pour obtenir le grade de

DOCTEUR DE L’UNIVERSITÉ GRENOBLE ALPES

Spécialité : Sciences de la Terre et de l'Univers et de l'Environnement

Arrêté ministériel : 25 mai 2016

Présentée par

Marco Antonio SALCEDO ARCINIEGA

Thèse dirigée par **Stéphane GARAMBOIS**,Enseignant chercheur, Université Grenoble Alpes
et codirigée par **DANIEL BRITO**,Professeur, Université de Pau et des Pays de l'Adour

préparée au sein du **Laboratoire Institut des Sciences de la Terre**
dans **l'École Doctorale Sciences de la Terre de lEnvironnement et des Planètes**

Développement d'une méthode de tomographie de vitesse et d'anisotropie à partir des temps de parcours des ondes : applications à des données sismiques ou électromagnétiques aux échelles du terrain et du laboratoire dans les carbonates

Development of a velocity and anisotropy tomography from first-arrival traveltimes: applications to field and laboratory seismic or electromagnetic data in carbonates

Thèse soutenue publiquement le **13 décembre 2021**,
devant le jury composé de :

Monsieur Stéphane GARAMBOIS
PROFESSEUR DES UNIVERSITES, Université Grenoble Alpes, Directeur de thèse
Monsieur Daniel BRITO
PROFESSEUR DES UNIVERSITES, Université de Pau et des Pays de l'Adour, Co-directeur de thèse
Monsieur Frédéric NGUYEN
PROFESSEUR, Université de Liège, Rapporteur
Madame Albane SAINTENOY
MAITRE DE CONFERENCE HDR, Université Paris-Saclay, Rapporteure
Monsieur Diego AROSIO
PROFESSEUR ASSOCIE, Università degli Studi di Modena e Reggio Emilia, Examinateur
Monsieur Michel DIETRICH
DIRECTEUR DE RECHERCHE, CNRS délégation Alpes, Président

Acknowledgement

There are many people that have been part of this PhD and I want to apologize in advance for forgetting anyone.

First and foremost I want to thank my supervisor Stéphane Garambois who put his academic confidence in me after some online interviews and email exchanges when I was still in Brazil due to my master studies. During these four years Stéphane always showed complete availability for the development of my work, which I really appreciate as well as his guidance and support. I would like to thank my co-supervisor Daniel Brito who had a crucial involvement the last two years of my work, first during my stay in Pau where thanks to him I had a satisfactory research environment, I learned how to perform an experimental acquisition and several things behind this experimental world, while after he had an important role during the data processing giving new ideas and constructive comments.

I would like to thank Jean Virieux for his guidance during the first two years of my PhD, he developed the isotropic version of our tomography code which was my starting point for different computational updates, I thank his availability and the tasks he used to give me which contributed a lot for the improvement of my scientific skills. Special thanks to Philippe Le Bouteiller who developed the forward part of our code during his PhD, he was always kind and patient to explain me all the details behind his code, and I also thank the theoretical discussions we had.

I would like to thank all the members of my jury, I appreciate their time to read my manuscript and the questions they did during my PhD defense. Another important jury is regarding my thesis committee, so I would like to thank Franck Plunian and Emmanuel Chaljub for their monitoring after each year in order to ensure a proper PhD work as well as their helpful advices.

I thank all the members of SEISCOPE consortium, which is led by Romain Brossier and Ludovic Métivier, thank you very much for giving us the opportunity to present this research in different meetings, and several suggestions and discussions that helped to improve my work.

I would like to thank Weiguang He (previous SEISCOPE post-doc researcher, now at Armaco Beijing) for providing helpful comments on parametrization analysis which were crucial during the initial part of this work. I thank Yubing Li (previous SEISCOPE post-doc researcher, now at Armaco Beijing) who developed the Bessel filter code we are using, and for his collaboration and comments during the building of our first journal publication. Special thanks to Hugo Sanchez (previous SEISCOPE PhD studend, now permanent researcher at ISTerre), first of all for his friendship and then for scientific discussions regarding inversion theory, his large knowledge and computational skills were quite important at the beginning of my PhD.

Thanks to Federico Sanjuan (Université de Pau & Pays Adour)for his supervision and guiding during the laboratory experiments and Chengyi Shen (Université de Pau & Pays Adour) for sharing his experimental expertise during the acquisition of the laboratory data.

I would like to thank Edwin Fagua (post-doc researcher at Universidade Federal do Rio Grande do Norte, Brazil) who I met during my master studies in Brazil. We always kept in touch during my PhD for several discussions regarding inverse problems, but the most important is certainly his friendship which I appreciate very much.

This work was partially funded by the ALBION Project conducted between Total and several french universities. I would like to thank the LSBB Underground Research Laboratory, Avignon University and CNRS, Rustrel, France (https://lsbb.cnrs.fr) for allowing us to use the facility to acquire the borehole GPR measurements. Special thanks to Charles Danquigny, Gérard Massonnat and Jean-Paul Rolando from Total for making the ALBION Project possible as well as Guy Sénéchal and Dominique Rousset from the Université de Pau & Pays Adour for the GPR borehole acquisition and discussions.

This PhD work was financially supported by the National Secretary of Higher Education, Science, Technology and Innovation (Senescyt, Ecuador) on behalf of the Ecuadorian people and it is gratefully acknowledged.

I would like to thank Polita Wunsche who I met during the Visa Pour L'Emploi PhD course as my coach, she was always monitoring the development of my PhD and giving my several advices for the life after the studies, it was very comfortable to talk with her.

Deeply thanks to my family, my parents were always present during my stay in France, it was not easy for them my absence in Ecuador but they always made a lot of effort to make me feel comfortable in spite of the distance. I would like to thank Rafaela Tirado, someone can guess how important she is that I write her name just next to my parents, we have shared many things the last three years, and I have no words to describe how grateful I am to her.

Finally, I would really like to mention all the people that made this happen, but I am afraid to forget someone, and I will probably need several pages to write a complete, ordered and detailed list. To all of you, to whose who contributed to a greater or lesser extent to achieve this goal, from near or from far away, thank you very much.

Grenoble, March 13, 2022

Abstract

A novel traveltime tomography approach has been developed to invert both velocity and anisotropy restricted to 2D geometry. The fundamental equation whose solution gives us the first-arrival traveltimes between a source and a receiver is the Eikonal equation, which becomes more complex when anisotropy is considered. In order to solve the Eikonal, an Eulerian formulation based on element-discretization discontinuous Galerkin method is adopted. The use of a direct solver allows us to obtain the total solution of the Eikonal, this includes diffraction events that may occur in the presence of large-velocity contrasts, while the widely used ray solution does not include these events. For the inverse part, an iterative local gradient-based optimization is chosen, where a least-square misfit function between picked and synthetic traveltimes need to be minimized. Contrary to other tomography approaches that usually compute the expensive sensitivity matrix, we avoid this computation by using the adjoint-state method. The adjoint formulation allows us to obtain the gradient efficiently by solving a transport equation that propagates the residuals from receivers to each source location, thus describing the sensitivity of the data to the model. We have developed a workflow that includes model regularization and data-weight matrix. Anisotropy is obtained under the elliptical assumption, thus two parameters are inverted simultaneously with an optimal parametrization that includes vertical and horizontal velocities, this choice being driven by a sensitivity analysis and synthetic examples. The code was used for active seismic and electromagnetic data acquired in carbonates both at the field and laboratory scale with different acquisition configurations. A first example concerns crosshole GPR acquisitions performed at the field scale within the Laboratoire Souterrain à Bas Bruit (LSBB) facilities, where the presence of a deep gallery makes the inversion challenging. In this weak anisotropy environment, the results are confronted to full wave inversion results and to geological data. At the laboratory scale, a multi-physics acquisition including seismic and GPR data was tested on a cubic rock sample. It underlines some issues related to the size of the sources/receivers compared to the dimension of the sample, which must be tackled before considering any inversion. Then, the datasets are inverted and velocity/anisotropy images are obtained and discussed in terms of heterogeneity and potential localized fractures.

Résumé

Une nouvelle approche de tomographie des temps de parcours des ondes a été développée pour inverser à la fois la vitesse et l'anisotropie, ceci dans une géométrie 2D. L'équation fondamentale dont la solution nous donne les temps de parcours de première arrivée entre une source et un récepteur est l'équation d'Eikonal, qui devient plus complexe lorsque l'anisotropie est considérée. Afin de résoudre cette équation, une formulation eulérienne basée sur la méthode de discrétisation par éléments dite de Galerkin-discontinus est adoptée. L'utilisation d'un solveur direct nous permet d'obtenir la solution totale de l'Eikonal, ce qui inclut les événements de diffraction qui peuvent se produire en présence de contrastes de vitesse importants, alors que la solution classique de rayon n'inclut pas ces événements. Pour la partie inverse, une optimisation locale itérative basée sur le gradient est choisie, où une fonction par moindres carrés, qui compare les temps de parcours mesurés et synthétiques, doit être minimisée. Contrairement à d'autres approches de tomographie qui calculent généralement la coûteuse matrice de sensibilité, nous évitons ce calcul en utilisant la méthode de l'état adjoint. La formulation adjointe nous permet d'obtenir efficacement le gradient en résolvant une équation de transport qui propage les résidus des récepteurs à chaque emplacement de la source, décrivant ainsi la sensibilité des données au modèle. Nous avons développé un algorithme qui inclut la régularisation du modèle et une matrice de pondération des données. L'anisotropie est obtenue sous l'hypothèse elliptique : seuls deux paramètres sont inversés simultanément avec une paramétrisation optimale qui inclut les vitesses verticale et horizontale, ce choix étant conduit par une analyse de sensibilité et des exemples synthétiques. Le code a été utilisé pour des données sismiques et électromagnétiques actives acquises dans les carbonates à la fois sur le terrain et à l'échelle du laboratoire avec différentes configurations d'acquisition. Un premier exemple concerne des acquisitions GPR entre forages réalisées à l'échelle du terrain au sein des installations du Laboratoire Souterrain à Bas Bruit (LSBB), où la présence d'une galerie profonde rend l'inversion difficile. Dans cet environnement à faible anisotropie, les résultats sont confrontés aux résultats de l'inversion des champs d'ondes complets et aux données géologiques. A l'échelle du laboratoire, une acquisition multi-physique incluant des données sismiques et GPR a été testée sur un échantillon de roche cubique. Cela met en évidence certains problèmes liés à la taille des sources/récepteurs par rapport à la dimension de l'échantillon, qui doivent être corrigés avant de considérer toute inversion. Dans un second temps, les jeux de donnée sont inversés et des images de vitesse/anisotropie sont obtenues et discutées en termes d'hétérogénéité et de fractures localisées potentielles.

Contents

General introduction

Basic concepts of Geophysics

The knowledge of the structure, properties and composition of the Earth's interior is essential for the understanding of different phenomena occurring at different scales and for several goals, ranging from the entire Earth to localized exploration activity. Although drilling is possible, it remains expensive, intrusive, generally not very representative of the heterogeneities or even impossible when the depths are too great. Consequently, indirect and non-invasive methods have been designed thanks to scientific achievements and technological advancement, these methods belong to a broad and interdisciplinary science denoted as Geophysics[1], which literally means the knowledge of the earth and it is based on mathematics, physics, geology and astronomy. The characterization of subsurface structures that are inaccessible to our eyes is defined as geophysical imaging.

Geophysics has different branches or usually denoted as geophysical methods, seismology is referred as the study of Earth's free oscillations or vibration to understand the source mechanism and to reconstruct the interior structure (Shearer, 2009). Localization of earthquake epicentres was the first application of seismology: in the early first century Zhang Heng used a seismoscope to detect an earthquake which is considered the first success in history. The energy expands from the epicentre through the medium in the form of seismic waves (mechanical waves), and the fact that the earthquake is a natural source, makes seismology to be usually defined as passive seismic. Currently, the seismic vibrations are recorded by seismometers which are denoted as geophones if they are located in land or hydrophone if they are located in the marine environment, in both cases the recorded seismic vibrations are named seismograms which are the measures of ground motion such as the velocity, acceleration or particle displacement. However, seismology is more than earthquakes detection. Oldham (1906) built the first seismological model of the earth in 1906 and noticed that some phases of the shear wave (S-wave) are missing on the seismographs coming from stations far from the epicenter, while the compressional waves (P-waves) phases were still present in the recordings. This was a warning for scientists about potential discontinuities related to the presence of fluid that could justify the missing of S-waves (Oldham, 1906). Mohorovicic (1909) noticed a discontinuity at shallow depth that was later interpreted as the boundary between the crust and the mantle. A few years after, Gutenberg (1914) could identify the existence of a core (core-mantle boundary), while Lehmann (1936) divided the core into inner and outer parts. The understanding of each layer composition from the crust to the inner core is crucial for the explanation of various phenomena, for instance the Earth's magnetic field caused by the convection at the liquid metallic outer core, or the plate tectonics due to the mantle convection, being the responsible of orogeny, subduction zones and most of the earthquakes and volcanoes.

---

[1] The word Geophysics has the prefixes *geo* and *physics* that come from the ancient Greek indicating earth and knowledge of nature, respectively.

Exploration geophysics is an applied branch of geophysics, where geophysical methods are used to satisfy the society needs for natural resources. When the applications are located at very shallow depths, this is referred as near surface geophysics covering many different socio-economical needs. Contrary to seismology, exploration geophysics used to employ artificial or controlled source, which arise the definition of active seismic, although noise-based methods are developing very fastly nowadays . Mallet in 1884 performed the first controlled-source experiment to characterize the subsurface. Regarding environmental geosciences and geoengineering, there are many fields where geophysical methods are important such as archaeology (Hesse, 1999; Gaffney, 2008), hydrogeophysics (Rubin and Hubbard, 2006; Vereecken et al., 2006), geomorphology (Jongmans and Garambois, 2007; Kneisel et al., 2008), and civil engineering (McCann and Forde, 2001; Metje et al., 2007). These fields can be tackled with different physical phenomena, where the chosen one depends on the properties of the studied medium, the targets (sensitivity, size) and the penetration depth. Besides seismic method, other techniques can be used to characterize the properties of the subsurface such as gravity to detect density anomalies; methods that are sensitive to electrical properties of the medium: induced or spontaneous polarization and electrical resistivity tomography (ERT); or sensitive to electromagnetic properties: from electromagnetic induction methods (EMI) to ground-penetrating radar (GPR), magnetometry, radiometry.

In this context, this thesis is part of the development of a method for imaging the arrival times of waves propagating in a given medium, whether they are seismic or electromagnetic. The development consists mainly in introducing complexity in the models to get closer to reality by taking into account the anisotropy of materials.

Principles of active seismic measurement

Active seismic methods can be applied at all scales, ranging from several kilometers in the field to laboratory experiments in samples with dimensions in centimeters. Although they are widely used for hydrocarbon exploration such as oil and gas, they can be used for exploration of other natural resources like nuclear fuel and minerals or other purposes in hydrology or natural hazard. A seismic experiment includes a controlled source, in land acquisitions (on-shore), the source can be a dynamic blast or seismic vibrators that are usually integrated in a truck, in marine acquisitions (off-shore) the source is an airgun, while at laboratory scale, piezoelectric devices are usually used as a source (PZT), although modern acquisitions include the use of a laser (Shen et al., 2021). The source is triggered by the user at a specific position and excitation time, the seismic wave propagates through the medium interacting with different formations (subsurface heterogeneities) and creating different types of events, such as reflection, refraction, scattering, transmission or diving waves. An array of seismic receivers is deployed over the region of interest. In land, the receivers are located on the surface, or at depth within a vertical well (if it is available) in vertical seismic profiling (VSP). In marine the receivers (hydrophones) can be located near the sea surface and tied to the source (towed-streamer acquisition) or stationary on the sea bed in ocean bottom seismic (OBS). At laboratory scale, PZT are usually chosen for the recording, but a laser can be used such as a Laser Doppler Vibrometer (LDV). The seismic application presented in this thesis is under laboratory conditions, however, our approach does not have limitations in a domain of thousands of kilometers.

Principles of GPR measurement

Ground-penetrating radar is a non-invasive subsurface prospecting technique based on the propagation of electromagnetic waves. The source is an antenna which is emitting an electromagnetic signal into the ground and creating different events like in seismic. A receiver antenna is located in the zone of interest where the electromagnetic signals arrive after the propagation. In most of the geophysical applications, the central frequency of the emitted signal is usually about 10-500MHz in the field (meter scale) or 0.9-3GHz in laboratory conditions (centimeter scale), consequently the imaging of structures can be achieved at different scales, from hundred of meters to centimeters, depending mainly on the electrical resistivity of the formations. Signals will be strongly attenuated in low-resistive media such as clays while they can be weakly attenuated in high-resistive media such as air, ice and carbonates for example. The central frequency is also linked to the dimensions of the antennas, increasing when antenna size decreases. Size of the antennas is substantially important when the studied domain is very small, for instance, in crosshole[2] GPR data if the separation between Tx/Rx is less than $10\,m$ (Irving and Knight, 2005) for 100 MHz antennas.

One of the main applications of GPR is on-ground acquisitions where reflection or scattering events are analyzed, thus two types of surveys are usually performed depending of the Tx/Rx facilities to move: i) if Tx/Rx are separated by a fixed distance, then the entire instrument is moved along the acquisition profile, this is denoted as common-offset measurements; and ii) in case we have the freedom to vary the distances between Tx/Rx, this is defined as multi-offset measurements.

The applications presented in this thesis are performed within a transmission framework, where Tx and Rx face each other and/or with a particular angle. Crosshole acquisition is one of these configurations widely used in GPR but is can also be used though walls, pillars or sample blocks. In transmission, two common measurements are performed: i) Locate Tx/Rx always facing each other while we vary the depth, this is known as zero-offset profile (ZOP), which is useful when the user wants to quickly localize anomalies in a stratified environment; and ii) Tx is fixed and Rx is moved at different positions of the opposite face, or Rx is fixed and Tx moves, these measurements are denoted as multi-offset profile (MOP) with different angles.

Basic concepts of tomography

Whether it is seismic or GPR data, the receivers record a large amount of information related to the medium where the waves propagated. Such information can be classified in two groups: i) kinematic information which is related to the traveltime of the different events propagating from the source to the receiver; and ii) amplitude information of the recorded events. The former is a function of the trajectory and propagation velocity of the wave, the latter is affected by different factors such as reflection/transmission coefficients at the interfaces, geometrical spreading and intrinsic attenuation.

The developments in this thesis are devoted to the kinematic information contained in each recorded trace, the first onset of the first-arrival events that we call the ‘observations’ (data). A vector gathering all the observations (data space) is denoted as **d**. In order to simulate the observations, we perform a forward modeling, where we presume to know the structures of the earth. For that, we propose a model

---

[2] A crosshole acquisition or crosswell experiment is one in which the receivers are located along a vertical well and the sources are located along another vertical well offset from the receiver well.

where the physics of wave propagation is used to predict the observations, formally

$$\mathbf{d} = \mathbf{G}\mathbf{m}, \tag{1}$$

where $\mathbf{m}$ is a model vector (often denoted as model space) where each element is a pixel containing the model parameters of interest, i.e., $\mathbf{m}$ is the discrete description of the continuum model, which in the context of traveltimes, is velocity or its inverse value known as slowness. Figure 1 shows an example of a discretized medium where each cell/pixel has a constant slowness value, and the propagation of one diving wave is given by a dashed path. This path is defined as a 'ray' whose detailed review about the physics and mathematics behind this term is given in the next chapter. The simulated traveltimes obtained from the forward problem are usually denoted as synthetics which ideally are very close to the observations, and $\mathbf{G}$ is the forward problem operator that connects the physical medium to the simulated observations. Therefore, under some model simplification and theoretical constraints, one may propose different models to predict the observations. This can be seen as a trial-error-process certainly extensive due to the exhaustive search through the model space.

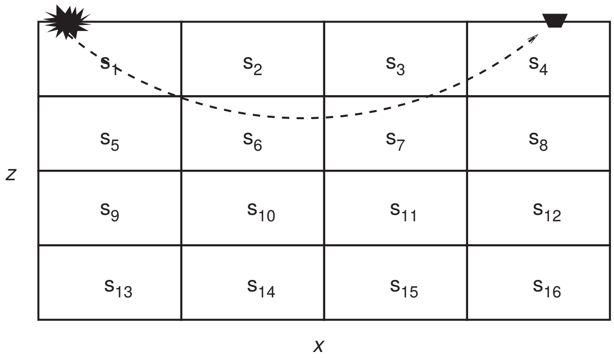

Figure 1: Example of a discretized domain, where each cell/pixel has a constant slowness value. Source is denoted as a star and receiver as a bucket. Surface acquisition with 1 diving wave whose propagation path through the subsurface is given by a dashed line. Figure modified from Schuster (2017).

In contrast, inversion or tomography[3] is the procedure for reconstructing earth properties (model) from observed values (Aki et al., 1977; Nolet, 1987). The term inversion is quite general, while tomography is usually associated to the process of finding a model with smooth variations (Van Avendonk et al., 1998; Zelt and Barton, 1998). Based on our observations, this type of inversion is defined as first-arrival traveltime tomography (FATT). For the sake of brevity, we use only the word traveltimes instead of first-arrival traveltimes in what follows. In the simple case where the data linearly depend on the sought parameters through the operator $\mathbf{G}$, one can compute $\mathbf{m} = \mathbf{G}^{-i}\mathbf{d}$, where the superscript $-i$ is associated to some type of inverse (pseudoinverse, regularized inverse, etc.). However, FATT is a nonlinear problem where $\mathbf{G}$ implicitly depends on $\mathbf{m}$, thus the exact inverse of $\mathbf{G}$ does not exist, due to the ill-posedness of the problem, i.e., many models $\mathbf{m}$ may yield the same predictions in the data space (model non-uniqueness), and/or data inaccuracy (garbage in, garbage out). Due to the nonlinear nature of FATT, the common strategy is to linearize the problem around an accurate initial guess close to the actual model. Synthetic traveltimes are computed from the initial guess and then compared to the observations in order to measure the discrepancies, defined as the misfit function. Consequently, the inverse problem to solve can be expressed as

$$\delta\mathbf{d} = \mathbf{G}\delta\mathbf{m}, \tag{2}$$

---

[3] The word tomography comes from the Greek *tomos* which means slice, part or section.

where $\delta\mathbf{d}$ is the traveltime residual vector, $\mathbf{G}$ is computed in the initial guess, $\delta\mathbf{m}$ is the model perturbation we are looking for and given by the chosen inversion technique. Such perturbation is added to the initial guess to create a more accurate model where synthetics are recomputed, and the problem proceeds in an iterative manner until converge, i.e., reduction of the misfit. The different techniques for both forward and inverse problems are largely addressed in the next chapter.

Basics of velocity anisotropy

The velocity structure is a signature of the properties of the medium, and heterogeneity (sometimes called inhomogeneity) refers to variation of velocity as a function of the spatial location. On the contrary, anisotropy refers to variation of velocity along different directions at a fixed location, or in other words, the propagation velocities depend on the angle of incidence (Cholet and Richard, 1954; Hagedoorn, 1954). For instance, McCollum and Snell (1932) identified that velocities along the vertical bedding planes of Lorraine Shale (Quebec) were 40% higher than the velocities accross the bedding. Similarly, Helbig (1956) noted that velocities along the foliation of Devonian schists located in iron mines were about 20% higher than velocities across the foliation. The information of anisotropy may help to improve the imaging of faults and to detect dominant orientations of fractures (Matonti et al., 2017).

Whether a material is heterogeneous or anisotropic is often a matter of scale, the presence of anisotropy implies the existence of a certain structure on the scale of the propagated wavelength (Tsvankin, 2001). In other words, anisotropy, similar to heterogeneity, is scale-dependent. This property is explained from the two mechanisms that cause anisotropy: i) intrinsic anisotropy due to mineralogical structure, which exists at all scales (Musgrave, 1970); for instance if crystals forming a rock are aligned in a preferred orientation, the macroscopic wave velocity will depend on the direction of the wave propagation relatively to the crystal orientation, another intrinsic example is the orientation of cracks that constitute heterogeneities at a low scale but exhibit anisotropic behavior at large scale (Dey-Barsukov et al., 2000; Schijns et al., 2012); ii) extrinsic anisotropy, also called apparent anisotropy, which refers to the effects induced on the wave propagation due to small heterogeneities; for instance, alternating layers of stiff and soft material can be heterogeneous at the small scale, while it can be seen as homogeneous anisotropic at large wave scale (Backus, 1962; Helbig, 1994). In practice, it is not straightforward to decipher how much of the observed anisotropy is due to intrinsic or extrinsic components (Fichtner et al., 2013), but at least in large scale acquisitions, where the wavelength is much greater than the grain size of the minerals in the upper crust, we may suspect that most of the anisotropy is extrinsic. On the contrary, at the laboratory scale, which is one of the applications in this thesis, the information of the wavelength along with the size of the domain and the tomographic results need to be evaluated to conclude about the anisotropic type. In general, the correct description at large scale of any heterogeneous material which is not randomly heterogeneous in an isotropic way should include anisotropy (Capdeville and Marigo, 2007).

The processing of anisotropy requires detecting its presence, evaluating its effect in the data, and probably the most crucial, to design an adapted model to mimic the anisotropy pattern. In this thesis, we represent anisotropy with the layer-induced transverse isotropy (TI) model, which although is the most simple model with a single symmetry axis, is still widely used in many anisotropic studies. Depending of the orientation of the symmetry axis, three variants are possible and shown in figure 2a. The vertical transverse isotropy (VTI), often called the layer-cake model, is the most common model to represent the Earth. The horizontal transverse isotropy (HTI) is useful to represent rocks with nearly vertical fractures. Finally, the more realistic being the tilted transverse isotropy (TTI) which can be used to represent rocks with dipping beds, for instance the flanks of salt domes.

The effect of anisotropy on the wave propagation is illustrated in figure 2b, where a source is located at the center and two snapshots are shown. In an isotropic medium with a homogeneous velocity, the wavefront is perfectly spherical (green in figure 2b). In a homogeneous VTI model using the same velocity of the isotropic case for the vertical direction but imposing 10% of velocity increase along the horizontal direction, the wavefront is no longer spherical and is elongated along the horizontal direction. This simple example shows that the traveltime recorded in the horizontal direction will be shorter than the vertical one, so that we can investigate anisotropy from the kinematics of waves. In an isotropic model, the output of the tomography is simply a velocity model with the corresponding heterogeneities, while, considering anisotropy implies that there is more than one velocity at each local point. The model space now gathers the different velocities, i.e., the tomography problem becomes multiparameter. The next chapter discuss the mathematical background to simulate anisotropy and the strategy to implement it in the tomography workflow.

One of the main reasons to ignore anisotropy is in general due to the short offset data available that makes hard to detect it (Helbig and Thomsen, 2005). This can be observed in the wavefront example of figure 2b: if the acquisition was only performed along the vertical direction, it will not be possible to reconstruct the velocity in the horizontal one. This is related with the term illumination, which is the number and angular variations of source/receiver paths traversing a given location. The effects of illumination in the anisotropy reconstruction are largely addressed in the course of this manuscript. On the contrary, if a medium is highly anisotropic, failure to account for it in the tomography reconstruction may result in serious imaging errors. In this direction, we present in chapter 3 a seismic example obtained in a fractured block with a high degree of anisotropy, which illustrates the importance of including anisotropy in the inversion workflow.

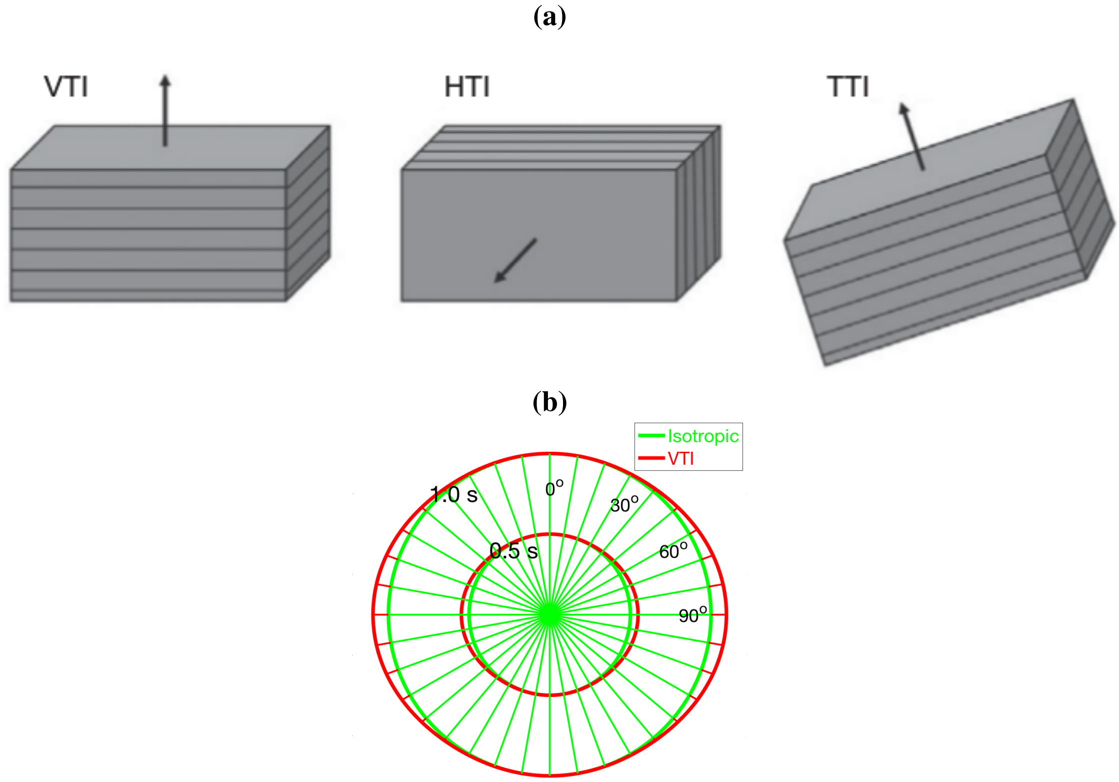

Figure 2: (a) Three types of transverse isotropy (TI) models: left, vertical transverse isotropy (VTI); middle, horizontal transverse isotropy (HTI); right, tilted transverse isotropy (TTI). Figure modified from Zhou (2014). (b) Snapshots of two wavefronts whose source is located at the center. In green the wave propagates in a homogeneous isotropic medium, while in red the medium is homogeneous VTI with 10% of anisotropy in the horizontal direction. Figure courtesy of Weiguang He.

Carbonate formations

This work has benefited from a more general collaborative research project on the study of carbonates, the ALBION 2 project. This project aims to better understand the hydrological flows within these formations at different scales. Indeed, about half of the world's hydrocarbon reserves are found in carbonate formations, i.e., in calcareous or dolomitic rocks; in the Middle East for instance, about 90% of the gas and 80% of the oil are found in carbonate formations. However, carbonates are characterized by their significant heterogeneity mainly caused by: i) their brittle deformation behavior that gives rise to naturally fractures and faulted rocks more than other types of rocks (Nelson, 2001); ii) biological processes; iii) diagenetic transformations; and iv) chemical instability of Calcium-carbonate mineral (Dolomite, Calcite, Aragonite, Aragonite) (Anselmetti et al., 1997). These factors have a strong impact on the petrophysical, mechanical and anisotropic properties of carbonates, making their understanding and geological or permeabilities properties interpretation a challenge in terms of hydrocarbon extraction, water resource management, geothermal power extraction, greenhouse gas sequestration or hazard studies.

Carbonate heterogeneities appear at different scales. At the microscale, heterogeneities are due to the variety in calcite crystal composition and type (aragonite, sparite, micrite), the porosity amount and pore type, and the potential presence of microcracks and stylolites. At the reservoir kilometer scale, the heterogeneities may come from the sedimentary architecture, the fracture networks and the hectometer faults. These features have been mainly studied through seismic reflection profiles allowing sedimentary layers picking and structural modeling. These heterogeneity properties are known to impact on the relationship between the rock solid skeleton density and wave velocities, or in other words, they increase or decrease the velocity of waves traversing the rock, which certainly depends also on the propagation direction (anisotropy).

The scales investigated in this study are limited from a multi-decameter study performed with GPR in a crosshole configuration, followed by a laboratory experiment at the decimeter scale (10 to 100 centimeters), where both seismic and GPR data were acquired on the same sample, potentially paving the way for a multi-physics investigation.

Objectives and outline of the thesis

The objectives of this research can be separated into two complementary parts. In the first part, a methodological development has been carried out to propose a new anisotropic tomography workflow. From an existing Galerkin-discontinuous Eikonal solver already taking into account anisotropy, we designed a consistent mathematical and physical connection with the multiparameter inverse part of the tomography through an adjoint approach. In order to test and validate the workflow as well as to evaluate different parametrizations of the anisotropic problems, we designed synthetic tests considering different acquisition configurations.

In the second part, the workflow previously proposed has been applied to several types of data, seismic and electromagnetic, acquired at different scales within carbonate formations in order to image their heterogeneities and anisotropy properties. This part required on the one hand to complete the workflow with terms of regularization and selection of data for a GPR acquisition configuration between drillings, but also to acquire data according to an experimental protocol in the laboratory with both seismic and electromagnetic approaches. The analysis of these data has sometimes required the development of a method of semi-automatic pointing, particularly for radar data, but also procedures for correcting the position of sources and/or receivers that have proved too extensive at the scales and wavelengths considered. This led to multi-physical images of heterogeneities and anisotropy of blocks in 2D, which are then discussed. These different approaches are detailed in the manuscript within four independent chapters before concluding and proposing perspectives.

- Chapter 1 introduces the concepts of forward and inverse problems. In the former, the high-frequency approximation is introduced, the fundamental Eikonal equation is derived for both seismic and electromagnetic physics, with a detailed review of the existing methods to solve this equation. This is followed by the presentation of our method highlighting its advantages. In the latter, we define the conventional workflow and then we introduce an alternative mathematical formulation that allows us to efficiently compute the gradient of the misfit function. The chapter ends with a sensitivity analysis of two parametrizations to give some preliminary insights about the sensitivity of each of them.

- Chapter 2 concerns the processing of existing crosshole GPR data, starting with a specific sensitivity analysis dedicated to the field acquisition configuration and complemented by an analysis of the tomography reconstruction through a synthetic realistic model obtained from a previous

Full Waveform Inversion (FWI) of the data. The final tomography workflow is then tested on real crosshole GPR data acquired at the field scale, where a deep gallery is present. The results obtained from this challenging dataset in a weak anisotropic environment are discussed in terms of carbonate properties which are linked to the available geological information.

- In chapter 3, we present the experimental laboratory seismic acquisitions performed on a block of carbonates data and the manually picked traveltime distribution. We show that the extension of the seismic source at this scale requires corrections of positions and lengths of the rays, which are also addressed thanks to a synthetic approach considering a discretization of the source. We also introduce a simple data-driven methodology for the choice of the suitable anisotropic model. Then, isotropic and anisotropic tomographies are obtained and discussed for this block presenting moderate anisotropy. The same approach is then proposed on already existing data acquired on a larger block presenting higher anisotropy, which well illustrates the imaging and interpretation artifacts generated when anisotropy in not considered in the inversion process.

- Chapter 4 focus on the corresponding laboratory experiment performed with Ground Penetrating radar antennas on the same block initially used in the seismic analysis of chapter 3. This block experiment was complemented with air acquisitions designed to better evaluate the antenna properties. For all these experiments, a semi-automatic picking method based on cross-correlation is developed and discussed. The picking analysis shown even more complex traveltime patterns than in the seismic case, which also require source and receiver corrections and might be sensitive to the presence of the large air velocity surrounding the block. The proposed empirical corrections appear to be dependent whether there is no antenna coupling (air) or air-rock coupling (carbonate). As in seismic, isotropic and anisotropic tomographies are performed on the corrected traveltimes, with limited success as the block appears rather homogeneous and isotropic.

Chapter 1

First-arrival traveltime tomography: an anisotropic formulation

Contents

Introduction

In this chapter, we present the mathematical and physical concepts behind first-arrival traveltime tomography (FATT) (Nolet, 1987). In order to describe the propagation of mechanical waves, we introduce in section 1.1.1 the theory of linear elastodynamic equation which can be formulated in a general inhomogeneous, anisotropic and elastic medium (Červený, 2001; Chapman, 2004). Since we are also working with electromagnetic (EM) waves, an introduction to Maxwell's equations is given in section 1.1.2, which describe the effect of the electromagnetic field on material objects (Kline and Kay, 1965; Born and Wolf, 1970). In order to formulate FATT, we approximate the wave propagation systems by the high-frequency approximation[1] (Bleistein, 1984), this allows us to mathematically derive two fundamental partial differential equation (PDE) from which the Eikonal equation (Bruns, 1895) is the cornerstone of this thesis, first under the isotropic assumption and then considering that velocity of waves varies with respect to the observational angle, i.e., anisotropy (Winterstein, 1990; Helbig and Thomsen, 2005) (section 1.1.3).

---

[1] According to (Bleistein, 1984) this means that the characteristic wavelength of the velocity fluctuations must be more than three times longer than the source wavelength.

Physical description of the Eikonal PDE is addressed, followed by a complete review of the methods to obtain its solution (section 1.1.4) being defined as the forward problem part of tomography. The classical method is to obtain a system of ordinary differential equations (ODEs) and solve it in terms of characteristics (Courant and Hilbert, 1966). We adopt a Hamiltonian formalism (Goldstein, 1980) to obtain the system of ODEs denoted as symplectic integrators in classical mechanics. Rays are defined as the characteristic curves of the Eikonal equation, thus the system (often called ray tracing system) is used to determine the ray trajectory and the traveltime along it, we therefore present the different techniques involving ray tracing (Rawlinson et al., 2007) for both isotropy and anisotropy. However, Eikonal equation can be directly solved without invoking ray tracing, the work of Vidale (1988, 1990) was the pioneer, where a grid discretization is applied to the medium and the Eikonal is solved by finite-difference (FD), we therefore give all the works that address the solution of the Eikonal, most of them in a FD context (Gómez et al., 2019). Anisotropic methods that have been successfully extended to invert anisotropy are discussed. In this study, the Eikonal is solved through the novel approach of Le Bouteiller et al. (2018), which remains within the Hamiltonian formalism to express the Eikonal in a pseudo-time-dependent form, the system is solved locally by an element-based discontinuous Galerkin approach (DG), while for the global solution the fast-sweeping method has been implemented (FSM-DG) (Le Bouteiller et al., 2019). We justify our motivation to choose FSM-DG method, the advantages compared to the conventional FD and all the ingredients that have been added in order to make the method efficient and highly accurate.

After solving the Eikonal equation, traveltimes at receiver locations are extracted, the solution is denoted as synthetic traveltimes which need to be compared to the observations, the mathematical comparison is evaluated by a misfit function having a least-square form in our study (section 1.2), consequently, in FATT we basically look for the optimum model that decrease the value of the misfit function. We rely on local descent optimization where we introduce the concept of linearization, however, since FATT is non-linear by nature the procedure becomes iterative until a certain criteria given by the user is attained. Different references to solve the optimization are given along with applications in seismic/EM. In conventional tomography, we need to iterate to find the update model either by reconstruction techniques (Gordon et al., 1970; Gilbert, 1972) or by conjugate-gradient methods (LSQR (Paige and Saunders, 1982) or CGLS (Scales, 1987)), then the Eikonal equation needs to be solved in the new model by using the forward solver, the procedure is repeated leading to a two loops approach. We propose to reduce the complexity of the problem by a gradient-based approach where the updated model is directly obtained after providing the gradient of the misfit function (see Schuster (2017), chapter 5). The formal definition of the gradient requires the computation of the sensitivity matrix which in the framework of rays it contains the portions of ray lengths traversing through the discretized model cells, however, this matrix can be quite expensive to storage, thus we rely on the adjoint-state method (section 1.2.1) which offers a framework to compute the gradient free of any explicit sensitivity matrix building (Sei and Symes, 1994). When anisotropy is considered, the adjoint-based gradient allows us to define the sensitivity of each parameter which depends on the chosen parametrization (Gholami et al., 2013a; Tavakoli F. et al., 2019). Thus we explore the sensitivity of two parametrizations in section 1.2.2 by using a full-illumination experiment in order to cover all the possible angles between source-receiver couples. Our preliminary conclusions for each parametrization are validated in chapter 2 by realistic synthetic examples followed by real applications and geological descriptions of the anisotropy. In general, this study is dedicated to the inversion when considering anisotropic models: an original contribution compared to more standard tomography based on ray tracing strategies.

1.1 High-frequency wave modeling: Theory

1.1.1 Elastodynamic equations

In this section we give an overview of the equations that describe seismic wave propagation, we refer the reader to Červený (2001) and Chapman (2004) for more details about the derivations and wave propagation.

Based on continuum mechanics we can describe a medium with effective elastic parameters and with the Hooke's law which states a linear relationship between the stress and strain. Thus, in an anisotropic, inhomogeneous and perfectly elastic medium with no attenuation, the linear elastodynamic equation can be expressed as

$$\rho u_{i,tt} = (c_{ijkl} u_{k,l})_{,j} + f_i \tag{1.1}$$

where $\boldsymbol{f}(\boldsymbol{x}, t)$ denotes the source field, $c_{ijkl}(\boldsymbol{x})$ being the elastic tensor, $\rho(\boldsymbol{x})$ the density, and $\boldsymbol{u}(\boldsymbol{x}, t)$ the displacement field. Note that we rely on the Einstein convention for summation over indices i, j, k, l that take value in $\{1, 2, 3\}$, and a comma between subscripts to indicate space and time partial derivatives. Based on the second Newton's law, this equation relates the spatial variation of the stress with the time variation of the displacement field.

The components $c_{ijkl}(\boldsymbol{x})$ of the elastic tensor are also called elastic moduli, or stiffness tensor which has in general 81 components, however, these components satisfy some symmetry relations, thus reducing the number of independent components from 81 to 21, which also represents the general triclinic symmetry system of anisotropy, we refer the reader to Helbig (1994) for a review of the basic symmetries of the elastic tensor. We discuss about the chosen symmetry system for our applications afterward. We begin the analysis assuming an isotropic solid, where the components of the elastic tensor can be expressed in terms of two independent elastic moduli λ and μ, which are also known as Lamé parameter. Moreover, considering plane waves as the solutions of elastodynamic equation, we can obtain two wave modes being i) Compressional P-waves with velocity $V_P = \sqrt{\frac{\lambda+2\mu}{\rho}}$, where the displacement vector is in the same direction of the wave propagation, and ii) Shear S-waves with velocity $V_S = \sqrt{\frac{\mu}{\rho}}$, which has the displacement vector in the plane perpendicular to the propagation direction.

The elastodynamic equation remains valid even in a fluid medium where S-waves do not propagate, if we work with pressure $P(\boldsymbol{x}, t)$ instead of displacement, and ρ assumed constant, the scalar wave equation away from the source zone reads

$$\frac{1}{v^2} P_{,tt} - P_{,ii} = 0, \tag{1.2}$$

where $v(\boldsymbol{x})$ is called the acoustic velocity. It is possible to obtain an analytical or semi-analytical solution of this partial differential wave equations (PDE) under specific considerations, for instance, wave propagation in isotropic homogeneous or laterally homogeneous media (Aki and Richards, 1980). Conversely, in arbitrary heterogeneous media, numerical methods must be employed to approximate the partial derivatives in time and space of the acoustic wave equation, we refer the reader to Virieux et al. (2011) for a complete review of the methods used to solve this PDE in the context of continuum mechanics, while Virieux et al. (2012) presents some applications in exploration geophysics and earthquake seismology.

Since all the entire signal is simulated, the solution of the wave equations demands high computational resources due to the high oscillation of the wavefields. Moreover, in the presence of smooth variations of velocity, we can expect a smooth behaviour of the waves compared to the wave oscillation frequency. Based on this hypothesis, we can solve the acoustic wave equation under the high-frequency approximation which gives us another fundamental equation whose solution is the wave traveltime at one particular position (e.g., receiver geophone in seismic or receiver antenna in electromagnetism).

We can adopt a general solution under the form of the ray ansatz

$$P(\boldsymbol{x},\omega) = A_0(\boldsymbol{x})\mathrm{e}^{\mathrm{i}\omega T(\boldsymbol{x})}, \tag{1.3}$$

where A_0 is the amplitude of the seismic wave and $T(\boldsymbol{x})$ is the time at the position $\boldsymbol{x}$. Wavefronts are defined by the same traveltime, which means that particles on the same wavefront have the same phase, i.e., $T(\boldsymbol{x}) = const.$. These two terms being assumed smooth and independent of the frequency. This approximation is often called the zero-order approximation of the ray method.When introducing this solution in equation (1.2), it is possible to develop separately the derivatives and after somve vectorial calculus we obtain

$$\omega^2 A_0\left[(\nabla T)^2 - \frac{1}{v^2}\right] + \mathrm{i}\omega\left[2\nabla A_0 \cdot \nabla T + A_0\nabla^2 T\right] + \nabla^2 A_0 = 0. \tag{1.4}$$

Since we are interested in the high-frequency solution, the most important terms will be the first (with ω^2) and the second term (with ω^1), leading to the Eikonal equation,

$$\|\nabla T\|^2 = \frac{1}{v^2}, \tag{1.5}$$

and the transport equation,

$$2\nabla A_0 \cdot \nabla T + A_0\nabla^2 T = 0. \tag{1.6}$$

The traveltime gradient is called the slowness vector that we denote by $\boldsymbol{p}$. These two equations are fundamental in ray theory, the Eikonal equation gives us the traveltime (kinematic information) while the solution of the transport equation gives us the amplitude (dynamic information). Let us underline that the third term neglected in equation (1.4) might be combined with the second term to construct a frequency-dependent transport equation. Similarly, the use of the third term along with the first term (Eikonal) builds the frequency-dependent Eikonal, also called hypereikonal (Biondi, 1992; Zhu and Chun, 1994). Although some studies rely on the finite-frequency approximation to perform what is called wave-equation tomography (Luo and Schuster, 1991; Woodward, 1992), we focus our study on the high-frequency framework which has been used in several applications (Nolet, 1987; Zelt and Smith, 1992; Iyer and Hirahara, 1993).

In an isotropic medium with smooth velocity heterogeneities imagine a wavefront moving with time T, curves orthogonal to the wavefronts, i.e., parallel to the slowness vector can be defined, these curves carry the energy flux and we call them rays with $\boldsymbol{p}$ pointing the direction. We can give an interpretation of equations (1.5) and (1.6), the traveltime between two points depends on the ray geometry, i.e., the local direction of propagation which is the unknown information, however, since we know locally the velocity $c(\boldsymbol{x})$, the Eikonal equation must be verified. Regarding the transport equation, it is an advection equation for the energy which flows along the ray tube between two points and honoring the energy conservation, the observed variation of energy being associated with geometrical spreading, namely how rays converge or diverge, and also to the variation of the velocity in the medium.

It is worth noting that we did the analysis on the acoustic wave equation because in this study we focus on P-waves, however, high-frequency approximation can be also applied in the elastic wave equation which leads to the same Eikonal equation for each mode, thus in case the traveltimes of S-waves are available, equation (1.5) is valid and the velocity used to compute synthetics will be the velocity of S-waves.

1.1.2 Maxwell's equations

We introduce the basic properties of the electromagnetic field which is formed when electric charges produce an state of excitation in space. This field is represented by two vectors, $\boldsymbol{E}(\boldsymbol{x}, t)$ and $\boldsymbol{B}(\boldsymbol{x}, t)$, called the electric vector and the magnetic induction, respectively. Moreover, to understand the effect of electromagnetic field on the material, we need to introduce other group of vectors, the electric current density $\boldsymbol{J}(\boldsymbol{x}, t)$, the electric displacement $\boldsymbol{D}(\boldsymbol{x}, t)$, and the magnetic vector $\boldsymbol{H}(\boldsymbol{x}, t)$. Thus, we use the Maxwell's equations to relate the space and time derivatives of the the five vectors as

$$\nabla \times \boldsymbol{H} - \frac{1}{c}\boldsymbol{D}_{,t} = \frac{4\pi}{c}\boldsymbol{J}, \qquad \text{Faraday's Law,} \tag{1.7}$$

$$\nabla \times \boldsymbol{E} + \frac{1}{c}\boldsymbol{B}_{,t} = 0, \qquad \text{Ampère's Law,} \tag{1.8}$$

$$\nabla \cdot \boldsymbol{D} = 4\pi\rho, \qquad \text{Gauss' Law,} \tag{1.9}$$

$$\nabla \cdot \boldsymbol{B} = 0, \qquad \text{Gauss' Law of Magnetism,} \tag{1.10}$$

where $\rho(\boldsymbol{x}, t)$ is the electric charge density and $c(\boldsymbol{x})$ is the velocity of light in the vacuum which in our study, since we have applications at different scales, it will take two possible units, either $300\, m/\mu s$ or $30\, cm/ns$, for the sake of clarity, we omit the coordinate dependency of the mentioned variables. Faraday's law states that a time-varying magnetic flux $\boldsymbol{B}$ generates an electric field $\boldsymbol{E}$ which rotates around $\boldsymbol{B}$. Moreover, Ampère's Law indicates that a current $\boldsymbol{J}$ or a time-varying electric flux $\boldsymbol{D}$ generates a rotating magnetic field $\boldsymbol{H}$. The last two equations constitute the Gauss' Law which states that an electric charge density ρ is the source of an electric flux $\boldsymbol{D}$ while a magnetic flux source $\boldsymbol{B}$ does not exist. It must be noted that Maxwell's equations are not linearly independent, we may apply some vector identities on the equations (1.7) and (1.8) to obtain the Gauss' law equations (1.9) and (1.10), thus we put spetial attention on the first two laws in what follows.

In order to obtain a unique determination of the electromagnetic fields from a given distribution of currents and charges, these equations needs some relations that describe the behaviour of the physical properties of the medium under the influence of the field. These relations are known as the constitute relations which have a relatively simple form under certain considerations, such as the field being time-harmonic, the bodies are at rest or in slow motion relative to each other, and assuming an isotropic medium, thus these relations are

$$\boldsymbol{J} = \sigma(\boldsymbol{x}, t)\boldsymbol{E}, \tag{1.11}$$

$$\boldsymbol{D} = \varepsilon(\boldsymbol{x}, t)\boldsymbol{E}, \tag{1.12}$$

$$\boldsymbol{B} = \mu(\boldsymbol{x}, t)\boldsymbol{H}, \tag{1.13}$$

where σ is the electrical conductivity, ε is known as the dielectric permittivity and μ is called the magnetic permeability, these electromagnetic properties being frequency dependent, they behave differently over various frequency ranges acting in the medium (Powers, 1997). In addition, these three quantities have real and imaginary part where the latter is associated with energy losses or energy dissipation occurring during the transient response of the medium to the applied electromagnetic field, the imaginary part of permittivity, conductivity and permeability correspond to energy loss from polarization lag, from faradic diffusion and from magnetization, respectively. However, in this work we are not considering losses in our formulation, and conductivity of the material is assumed low as it is for many geologic materials, therefore equation (1.11) may be neglected. Regarding permittivity and permeability in equation (1.12) and (1.13), they are usually referred as a relative values since the value of the medium is divided by the value of vacuum, and this is the convention we adopt in our derivations, we should underline that in general, relative permeability is considered 1 for most sedimentary materials (non-magnetic medium), however we retain this variable in mathematical formulations.

The electromagnetic field is characterized by very rapid oscillations, namely high frequencies or in other words, very small wavelengths compared to the size structures in the medium. Consequently, high-frequency approximation might be applied in Maxwell's equations, the reader is referred to Born and Wolf (1970) for major details in the derivation. In a non-conducting isotropic medium we may consider a general time-harmonic field

$$\boldsymbol{E}(\boldsymbol{x},t) = \boldsymbol{E_0}(\boldsymbol{x})\mathrm{e}^{-\mathrm{i}\omega t}, \tag{1.14}$$

$$\boldsymbol{H}(\boldsymbol{x},t) = \boldsymbol{H_0}(\boldsymbol{x})\mathrm{e}^{-\mathrm{i}\omega t}, \tag{1.15}$$

where $\boldsymbol{E_0}$ and $\boldsymbol{H_0}$ are complex vector functions of positions, however, if equations (1.14)-(1.15) are taken as linear operations, the real part of these expressions are understood to represent the fields. Considering the absence of current and charges ($\rho = \boldsymbol{J} = 0$), and replacing $\boldsymbol{E_0}$ and $\boldsymbol{H_0}$ as the fields that satisfy Maxwell's equations in a time-free form, equations (1.7)-(1.10) are expressed as

$$\nabla \times \boldsymbol{H_0} + \mathrm{i}k_0\varepsilon\boldsymbol{E_0} = 0, \tag{1.16}$$

$$\nabla \times \boldsymbol{E_0} - \mathrm{i}k_0\mu\boldsymbol{H_0} = 0, \tag{1.17}$$

$$\nabla \cdot \varepsilon\boldsymbol{E_0} = 0, \tag{1.18}$$

$$\nabla \cdot \mu\boldsymbol{H_0} = 0. \tag{1.19}$$

Note that constitute relations (1.12) and (1.13) have been used and $k_0 = \omega/c = 2\pi/\lambda_0$, where λ_0 is the vacuum wavelength.

If we consider a distance far away from the dipole ($\boldsymbol{x} \gg \lambda_0$) also known as the far-field region of the antenna, and assuming plane waves as the solution, we can propose more general types of field in the form

$$\boldsymbol{E_0} = e(\boldsymbol{x})\mathrm{e}^{\mathrm{i}\omega\mathcal{L}(\boldsymbol{x})}, \quad \boldsymbol{H_0} = h(\boldsymbol{x})\mathrm{e}^{\mathrm{i}\omega\mathcal{L}(\boldsymbol{x})}, \tag{1.20}$$

where $\mathcal{L}(\boldsymbol{x})$ is a real scalar function of position, $e(\boldsymbol{x})$ and $h(\boldsymbol{x})$ being vector functions of positions. The fields in (1.20) are used as trial solutions of the Maxwell's equations to obtain a set of relations between e, h and $\mathcal{L}$, thus we need to apply some vector identities as $\nabla \times \boldsymbol{H_0}$, $\nabla \cdot \mu\boldsymbol{H_0}$ and the same for $\boldsymbol{E_0}$ and $\varepsilon\boldsymbol{E_0}$, we see that equations (1.16)-(1.19) become

$$\nabla\mathcal{L} \times h + \varepsilon e = -\frac{1}{\mathrm{i}k_0}\nabla \times h, \tag{1.21}$$

$$\nabla\mathcal{L} \times e - \mu h = -\frac{1}{\mathrm{i}k_0}\nabla \times e, \tag{1.22}$$

$$e \cdot \nabla\mathcal{L} = -\frac{1}{\mathrm{i}k_0}(e \cdot \nabla \log \varepsilon + \nabla \cdot e), \tag{1.23}$$

$$h \cdot \nabla\mathcal{L} = -\frac{1}{\mathrm{i}k_0}(h \cdot \nabla \log \mu + \nabla \cdot h). \tag{1.24}$$

$$\tag{1.25}$$

In a high-frequency regime where the wavelength of the signal λ_0 is very small, or in other words, the value of k_0 is very large, the right-hand side of the equations may be neglected, consequently they reduce to

$$\nabla\mathcal{L} \times h + \varepsilon e = 0, \tag{1.26}$$

$$\nabla\mathcal{L} \times e - \mu h = 0, \tag{1.27}$$

$$e \cdot \nabla\mathcal{L} = 0, \tag{1.28}$$

$$h \cdot \nabla\mathcal{L} = 0. \tag{1.29}$$

It must be noted that equations (1.26) and (1.27) can be obtained applying a scalar multiplication of $\nabla\mathcal{L}$ on equations (1.28) and (1.29), consequently our attention is focused on equations (1.26)-(1.27) which can be seen as a set of six simultaneous linear scalar equations for the cartesian components of e and h, the solutions for these equations are non-trivial only if the vanishing of the associated determinant is satisfied. This can be obtained taking h from equation (1.27) and its expression being inserted in equation (1.27) which yields

$$\frac{1}{\mu}\left[(e \cdot \nabla\mathcal{L})\nabla\mathcal{L} - e(\nabla\mathcal{L})^2)\right] + \varepsilon e = 0. \tag{1.30}$$

We can eliminate the first term based on equation (1.28), therefore this equation reduces to

$$(\nabla\mathcal{L})^2 = n^2(\boldsymbol{x}), \tag{1.31}$$

also known as the Eikonal equation where $n = \sqrt{\varepsilon\mu}$ is called the refractive index, and $\mathcal{L}(\boldsymbol{x}) = const$ denotes the wavefront moving with a time $\mathcal{L}(\boldsymbol{x})$ as in seismic. Since we are considering a simple kind of waves, i.e., plane waves as the solution of the fields, it can be demonstrated that electromagnetic waves travel with a velocity given by $v = c/\sqrt{\varepsilon\mu}$, consequently, the right-hand side of the Eikonal equation (1.31) is also equal to $(c/v)^2$ which is the definition of the dielectric permittivity, often called dielectric constant when a non-magnetic medium is considered ($\mu = 1$), such a constant being 81 in water and 1 in air, thus one can see the sensitivity of the dielectric constant to water content. However, there are other factors that also influence the dielectric constant of a material, for instance, the temperature, its composition (matrix mineralogy) and porosity (Knight and Endres, 1990; Knight and Dvorkin, 1992; Martinez and Byrnes, 2001). Moreover, an important property of electromagnetic propagation at distances far away from the dipole is referred to transversality, i.e., electric and magnetic fields are in phase and perpendicular to each other, these fields lie in planes normal to the direction of propagation given by $\nabla\mathcal{L}(\boldsymbol{x})$ (Eikonal equation (1.31)), we see in next section that transversality is modified when electrical anisotropy is considered. We may thus conclude that in an isotropic medium, the same fundamental equation is obtained regardless of the physics (EM or seismic), i.e., the gradient of the traveltime field at any time and position is equal to the inverse of the local velocity.

1.1.3 Eikonal equation for anisotropy

The general case We have been working only in terms of velocity since the medium is assumed isotropic, or in other words, at one medium position, we have the same velocity regardless the direction. However, in an anisotropic media, other concepts neeed to be introduced, thus we recall the elastic moduli from elastodynamic equation which can be expressed in a more compact form using the Voigt notation

$$\boldsymbol{C} = \begin{bmatrix} C_{11} & C_{12} & C_{13} & C_{14} & C_{15} & C_{16} \\ & C_{22} & C_{23} & C_{24} & C_{25} & C_{26} \\ & & C_{33} & C_{34} & C_{35} & C_{36} \\ & & & C_{44} & C_{45} & C_{46} \\ & & & & C_{55} & C_{56} \\ & & & & & C_{66} \end{bmatrix}. \tag{1.32}$$

As explained before, we have 21 elastic parameters which constitute the most general triclinic symmetry, while the parameters below the diagonal are not shown because the matrix is symmetric. Similar to the isotropic case, we want to derive the Eikonal equation, therefore we introduce the ansatz solution in the elastodynamic system (1.1), three terms are obtained and we focus on the first one that yields a general Eikonal equation given by

$$(\Gamma_{ik} - \delta_{ik})A_k = 0, \tag{1.33}$$

where δ_{ik} is the kronecker delta function, $\boldsymbol{A}$ denotes the displacement vector and Γ is called the Christoffel matrix defined as

$$\Gamma = \frac{c_{ijkl}}{\rho} T_{,j} T_{,l} = \frac{c_{ijkl}}{\rho} p_j p_l. \tag{1.34}$$

Here, $p_j = T_{,j}$ and $p_l = T, l$ are the slowness vector components such that $\boldsymbol{p} = \nabla T$, note that all the elements of the Christoffel matrix are function of the spatial coodinates. Moreover, one important difference compared to the acoustic case, is that now the amplitude coming from the ansatz is a vector function since we consider the displacement field in the elastodynamic system. To get nontrivial solution, the following system must be satisfied:

$$\det(\Gamma_{ik} - G\delta_{ik}) = 0, \tag{1.35}$$

where G are the eigenvalues of the Christoffel matrix also called the roots of the characteristic equation. Equation (1.35) represents a cubic algebraic equation with three eigenvalues that we denote as G_m and the corresponding eigenvector $g^m(m = 1, 2, 3$, no summation over $m)$, each of them describes one of the three body waves P, S_1 and S_2 that propagate in general anisotropic medium, the eigenvalues are associated with the traveltime information while the eigenvectors give the wave polarization. Note that equation (1.35) is satisfied only if one of the three eigenvalues equals unity, therefore we obtain the first order non-linear partial differential Eikonal equation

$$G_m(p_i) = 1, \quad m = 1 \text{ or } 2 \text{ or } 3. \tag{1.36}$$

Since we are considering plane waves as the solution, we can define the unit vector normal to the wavefront given by

$$N_i = \frac{p_i}{\sqrt{p_k p_k}} = \frac{\boldsymbol{p}}{\|\boldsymbol{p}\|}, \quad \text{such that} \quad p_i = \frac{N_i}{C^{(m)}}, \tag{1.37}$$

where C^m denotes the phase velocity, thus we can express equation (1.34) in terms of the N_i, and according to Eikonal equation (1.36), we obtain

$$C^{(m)} = \sqrt{G_m(N_i)}. \tag{1.38}$$

Consequently, the phase velocity of any propagation mode in anisotropic medium depends on the direction of propagation of the wavefront N_i. The reason we introduced the phase velocity is because there is another fundamental parameter in anisotropic medium known as the group velocity vector which carries the energy flux and it is parallel to the rays, here denoted $\vec{\mathcal{U}}$ and being different from the phase velocity vector $\vec{C}$, both in direction and in magnitude. In other words, the energy of waves does not propagate perpendicular to the wavefront. We should recall that for Eikonal equation in isotropic medium we only defined v as the acoustic velocity, the reason is that for this particular assumption, the phase velocity and group velocity equal in both direction and magnitude. We use a Hamiltonian formalism to obtain a formal expression for the group velocity vector in section 1.1.4.

The vertical case Transverse isotropy (TI) is the most common anisotropy system used in exploration geophysics and seismology since it is caused by shales and fine layering. TI solids are invariant with respect to any rotation around the axis, therefore we can consider the vertical axis as the rotational symmetry to definte a vertically transversely isotropic (VTI) which reduces the number of significant elastic moduli to five parameters, thus

$$\boldsymbol{C}_{VTI} = \begin{bmatrix} C_{11} & C_{11}-2C_{66} & C_{13} & 0 & 0 & 0 \\ C_{12}-2C_{66} & C_{11} & C_{13} & 0 & 0 & 0 \\ C_{13} & C_{13} & C_{33} & 0 & 0 & 0 \\ 0 & 0 & 0 & C_{44} & 0 & 0 \\ 0 & 0 & 0 & 0 & C_{44} & 0 \\ 0 & 0 & 0 & 0 & 0 & C_{66} \end{bmatrix}. \tag{1.39}$$

We can follow equation (1.34) to write the elements of the Christoffel matrix in a 3D VTI elastic medium as

$$\begin{aligned} \Gamma_{11} &= (C_{11}p_1^2 + C_{66}p_2^2 + C_{55}p_3^2)/\rho, \\ \Gamma_{22} &= (C_{66}p_1^2 + C_{11}p_2^2 + C_{55}p_3^2)/\rho, \\ \Gamma_{33} &= (C_{55}(p_1^2 + p_2^2) + C_{33}p_3^2)/\rho, \\ \Gamma_{12} &= (C_{11} + C_{66})p_1p_2/\rho \\ \Gamma_{13} &= (C_{13} + C_{55})p_1p_3/\rho \\ \Gamma_{13} &= (C_{13} + C_{55})p_2p_3/\rho. \end{aligned} \tag{1.40}$$

In this study, our applications are performed considering a 2D propagation in the (xOz)-plane, moreover, since we know that the compressional velocity is always higher than the shear velocity and the data we use for imaging purposes are the first arrivals, we can rely on the the acoustic approximation, thus $p_2 = 0$ and $C_{44} = C_{66} = 0$ because they represent the S-wave propagations, and Christoffel matrix reduces to

$$\Gamma_{ik} = \begin{bmatrix} \frac{C_{11}}{\rho}p_1^2 & 0 & \frac{C_{13}}{\rho}p_1p_3 \\ 0 & 0 & 0 \\ \frac{C_{13}}{\rho}p_1p_3 & 0 & \frac{C_{33}}{\rho}p_3^2 \end{bmatrix}. \tag{1.41}$$

We follow the same condition of equation (1.35) which was used to obtain the general Eikonal equation (1.36), and the Eikonal equation in a 2D VTI media yields

$$\frac{C_{11}}{\rho}p_1^2 + \frac{C_{11}}{\rho}p_3^2 - p_1^2p_2^2\frac{C_{33}C_{11} - C_{13}^2}{\rho^2} = 1, \tag{1.42}$$

where C_{11} and C_{33} describe the anisotropy properties in the vertical and horizontal propagation, respectively.

The obtained Eikonal may be expressed in a more compact form using the parameters introduced by Thomsen (1986) who defined the vertical P-wave velocity V_v being parallel to the symmetry axis and two dimensionless anisotropic parameters, ϵ and δ. The mathematical formulation of these parameters being

$$V_P = V_v = \sqrt{\frac{C_{33}}{\rho}}, \quad \epsilon = \frac{C_{11} - C_{33}}{2C_{33}}, \quad \delta = \frac{C_{13}^2 - C_{33}^2}{2C_{33}^2}. \tag{1.43}$$

Note that ϵ is mostly related with horizontal propagation paths since the dominant term is C_{11}, while δ having a dominant term in C_{13}, control the near-vertical anisotropy. Considering the Thomsen parametrization and defining $p_1 = T_{,x}$ and $p_1 = T_{,z}$, the Eikonal equation reads

$$V_v^2(1+2\epsilon)T_{,x}^2 + V_v^2 T_{,z}^2 - 2V_v^4(\epsilon-\delta)T_{,x}^2 T_{,z}^2 - 1 = 0. \tag{1.44}$$

It must be noted that if we set $\epsilon = \delta = 0$, we retrieve the isotropic Eikonal equation, $\epsilon = \delta \neq 0$ leads to the elliptical Eikonal equation whose physics can be explained as a dilatation applied to the isotropic case along the axis orthogonal to the rotation-symmetry axis, see Grechka (2009) for some particularities about this case. We should also define the equations that relate the different velocities with the Thomsen parameters, the horizontal velocity $V_h = V_v\sqrt{1+2\epsilon}$ often called perpendicular velocity, the normal move-out velocity $V_n = V_v\sqrt{1+2\delta}$ which according to Thomsen (1986), it relates the near-vertical anisotropic response. Moreover, a more rigorous study on V_n was conducted by Alkhalifah and Tsvankin (1995) who introduced the anellipticity parameter η to relate V_h to V_n:

$$V_h = V_n\sqrt{1+2\eta}, \quad \text{and} \quad \eta = \frac{\epsilon-\delta}{1+2\delta}, \tag{1.45}$$

where η is also dimensionless. Therefore, Eikonal VTI (1.44) might be modified considering other parametrizations. The extension of the Eikonal to a propagation in 2D TTI medium is quite simple since the TTI case can be seen as a VTI formulation with a tilted symmetry axis. This angle being defined as $\theta(\boldsymbol{x})$ is called the tilt angle which modifies the traveltime derivatives of equation (1.44) to

$$\hat{T}_{,x} = T_{,x}\cos\theta - T_{,z}\sin\theta, \quad \hat{T}_{,z} = T_{,x}\sin\theta - T_{,z}\cos\theta, \tag{1.46}$$

while the other terms remain the same, and thus the 2D Eikonal TTI is obtained. We define in our numerical implementations, the value of $\theta = 0°$ to obtain the VTI case and θ increases for a clockwise rotation, therefore we can retrieve the HTI formulation imposing $\theta = 90°$ which is also interesting to describe rocks with nearly vertical fractures.

We have obtained the Eikonal equation from the elastodynamic equation, however, we will present some application using first-arrival information from GPR antennas, i.e., the physic is totally different compared to mechanical propagation. Carcione and Cavallini (1995) and Ikelle (2012) showed that particularly in 2D propagation the acoustic velocity-stress system and the Maxwell's equations share mathematical analogies, thus the same code can be use regardless of the physics. However, we do not need these equivalences since we approximated the systems through the high-frequency regime, but it is crucial to understand who describes the anisotropy in electromagnetic fields in order to make the link with the anisotropic Eikonal. Thus, we assume that the medium is magnetically isotropic but electrical anisotropic, in other words, the electrical excitation depend on the direction of the electric field. Mathematically, this is explained using the constitute relation $\boldsymbol{D} = \varepsilon\boldsymbol{E}$, which in isotropic medium this equation implies that the vector $\boldsymbol{D}$ coincides in the direction of the vector $\boldsymbol{E}$, these fields being perpendicular to the direction of propagation, however, when anisotropy is considered, ε becomes a tensor and the constitute relation writes $\boldsymbol{D}_k = \varepsilon_{kl}\boldsymbol{E}_l$, i.e., $\boldsymbol{D}$ and $\boldsymbol{E}$ will have different directions (see figure 1.1). The concepts introduced in seismic regarding slowness vector and group velocity vector are also valid in electromagnetism, the former being perpendicular to $\boldsymbol{D}$ and thus also perpendicular to the wavefront, while the latter carrying the energy flux being perpendicular to $\boldsymbol{E}$, in other words, the energy is not propagated in the direction of the wave normal, moreover, due to transversality and the magnetic isotropy, $\boldsymbol{H} \parallel \boldsymbol{B}$ remains orthogonal to mentioned vectors. Similar to seismic, when 2D is considered, one principal axis must be defined, therefore, dielectric constants and thus also electromagnetic velocities are defined with reference to this axis such that $\varepsilon_z \neq \varepsilon_x$, consequently, the Eikonal

TTI formulation may be also applied to describe anisotropic propagation of electromagnetic waves, V_v being the velocity along the symmetry axis while the Thomsen parameters being perceived only as a quantification of the anisotropy of electromagnetic velocity in the electromagnetic case.

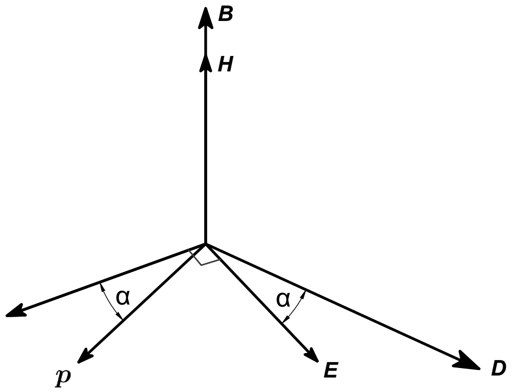

Figure 1.1: Relative direction of the field vectors, the slowness vector $\boldsymbol{p}$ normal to the wavefront and the group velocity vector $\mathcal{U}$ carrying the energy in anisotropic medium. In the isotropic case, $\boldsymbol{D} \parallel \boldsymbol{E}$. Figure modified from Born and Wolf (1970).

1.1.4 Numerical solution of the Eikonal equation

The Eikonal equation is a non-linear partial differential equation of the first order whose solutions in usually obtained in terms of characteristics, also known as Lagrangian formulation. In ray theory, we define rays as the characteristics of the Eikonal equation which are described by a system of ordinary differential equation (ODEs), often called the ray tracing system. Subsequently, traveltime along the rays can be calculated by quadratures once the characteristic is known. The reader is referred to Kline and Kay (1965), Courant and Hilbert (1966) and Bleistein (1984) for a detailed derivation of the characteristic system. We adopt the Hamiltonian formalism of classical mechanics to express the Eikonal equation as $\mathcal{H}(x_i, p_i) = 0$, thus the ODEs system reads

$$\frac{dx_i}{du} = \frac{d\mathcal{H}}{dp_i}, \quad \frac{dp_i}{du} = -\frac{d\mathcal{H}}{dx_i}, \quad \frac{dT}{du} = p_k \frac{d\mathcal{H}}{dp_k}. \tag{1.47}$$

This system consists of seven equation in a 3D medium connecting the position $x_i(u)$, the slowness vector $p_i(u)$, and the traveltime $T(u)$. The variable u along the characteristic cannot be chosen arbitrarily, it depends on the specific form of the Hamiltonian $\mathcal{H}$, for instance, considering the isotropic Eikonal equation (1.5) where p_i are the components of the slowness vector such that $p_i p_i = 1/v^2$, the Hamiltonian can be written as

$$\mathcal{H}(x_i, p_i) = \frac{1}{2}(v^2 p_k p_k - 1) = 0, \tag{1.48}$$

we can see that the derivative of the time with respect to u given by the ray tracing system (1.47) becomes the unit, consequently, the variable u along the ray equals the traveltime, while the other two derivatives complement the ray tracing system. Other important formulation is related to the energy flux carried by the group velocity vector, following Červený (2001), it is given by

$$\vec{\mathcal{U}} = \frac{\dfrac{d\mathcal{H}}{dp_i}}{p_k \dfrac{d\mathcal{H}}{dp_k}}. \tag{1.49}$$

Note that for the Hamiltonian form in (1.48), the denominator becomes the unit, and $\vec{\mathcal{U}} = \dfrac{d\mathcal{H}}{dp_i}$. We underline the importance of the group velocity vector because we look for the solution of the Eikonal in media with anisotropy, i.e., the ray vector and the wavefront normal differ, thus considering the Hamiltonian Eikonal VTI (1.44), it reads

$$\vec{\mathcal{U}} = \frac{1}{V_v^2(1+2\epsilon)T_{,x}^2 + V_v^2 T_{,z}^2 - 2V_v^4(\epsilon-\delta)T_{,x}^2 T_{,z}^2} \begin{pmatrix} V_v^2(1+2\epsilon)T_{,x} - 2V_v^4(\epsilon-\delta)T_{,x}T_{,z}^2 \\ V_v^2 T_{,z} - 2V_v^4(\epsilon-\delta)T_{,x}^2 T_{,z} \end{pmatrix}. \tag{1.50}$$

We see in section 1.2.1 that the group velocity vector plays an important role in the inversion of anisotropic parameters as well.

There are mainly two categories to solve the ray tracing system (1.47): 1) Initial-value raty tracing and 2) boundary-value ray tracing. In the former, the direction of the ray is known at some points of the ray, this is used as an initial condition in order to solve the ray system. In the latter, the direction of the ray is unknown, but the ray must satisfy some conditions, for instance, the ray must connect two points. Each category is subdivided in other ray tracing methods, we mention some of them in what follows, the reader is referred to Červený (2001),Rawlinson et al. (2007) and Virieux and Lambaré (2015) for a complete review on ray tracing. It is worth mentioning that all the ray tracing techniques have been successfully applied to compute traveltimes in both seismic and electromagnetism.

As part of the initial-value ray tracing approach we have: 1) Numerical solution of ray-tracing equations with some initial conditions and supplemented by Snell's law at points where the ray contacts structural interfaces. 2) Analytical solution of the ray tracing system, this is only possible in isotropic models with constant gradient velocities. 3) Semi-analytical solutions where the model is subdivided into layers and analytical solution is computed inside these layers, other option is to divide the velocity model into cells, in which the ray is also computed analytically. Regarding the boundary-value ray tracing different strategies exist: 1) The shooting method where the source is located and an initial trajectory of the ray is defined given by the take-off angle, thus have an initial position and initial slowness vector, then the trajectory is updated iteratively by changing the initial take-off angle such that the final ray connects the source and the receiver, we should underline that this connection is not guaranteed, i.e., the ray does not reach the receiver. 2) Bending method, here the source and receiver are connected by a ray somehow arbitrary and probably non-physical, subsequently, the ray is iteratively bent by a perturbation method until it satisfies some physics such as the Fermat principle of minimum traveltime. To our knowledge, in practice, the bending method is the most used for tomographic purposes and several attempts have been presented in order to find the most physically consistent ray, we can mention: 1) The minimization of traveltime where a straight path is divided in two segments, the midpoint of them is located and displaced according to the local velocity gradient, then the first two segments are subdivided and the procedure is repeated, at the end the ray is divided in several segments and we stop when a stable minimum time is attained, this method was implemented in a widely used GPR/Seismic tomographic software called 3DTOM from Jackson and Tweeton (1996) where the technique was improved in order to handle abrupt changes of velocity. 2) Methods based on perturbation theory where first-order perturbation equations for traveltimes are derived, it can be divided in two approaches, the first and commonly used in seismology, is based on Fermat's principle (Aki and Richards, 1980; Nolet, 1987), here the ray-path bending is ignored since that corresponds to second-order perturbation, Vasco et al. (1998) successfully used this method in active seismic acquisition to invert velocity whose local variations in each cell included anisotropic constants; the second method works directly on the Eikonal equation to derive the first-order perturbation of the ray tracing system in the vecinity of a reference unperturbed ray, this method being particularly simple when the Eikonal is expressed in Hamiltonian form (Farra and Madariaga, 1987; Virieux et al., 1988; Farra et al., 1989; Farra, 1992). Perturbation theory has been investigated in general anisotropic medium in order to derive first-order quantitative relationship between traveltimes perturbation and the elastic moduli perturbation in the medium (Cerveny et al., 1982; Červeny et al., 1982; Hanyga, 1982), Farra (1989) applies perturbation within the elliptical case, Jech and Pšenčík (1989) give an extension to overcome the singularity problem of the shear waves modes, and Gajewski and Pšenčík (1990) solved the exact dinamic ray tracing system for inhomogeneous anisotropic media to obtain vertical seismic profiles in 3D laterally varying structures. These works opened the option to invert anisotropy parameters, Chapman and Pratt (1992) and Pratt and Chapman (1992) took the mathematical formulations of Jech and Pšenčík (1989) to design a multiparameter anisotropic tomography code, while Vasco et al. (1997) used the same work to solve the system of equations 1.26-1.27 we obtained from Maxwell's equations in which they added group velocity vector in the formulation, velocity was inverted accounting for anisotropy in the traveltime computation and showed that anisotropy can be included progressively for a better fitting of the data. It is worth mentioning that these anisotropic studies based on perturbation theory relied on the big assumption of weak anisotropy, Zhou and Greenhalgh (2005) get rid of this limitation by modifying the traveltime perturbation equation, the new equation has some derivatives computed by analytical expressions which allowed to consider any level of anisotropy, the methodology was used by Zhou and Greenhalgh (2008a) to invert anisotropy in a multiparameter framework. As we see, once the ray is computed, the traveltime is obtained along the ray, however, for tomographic purposes, it is the traveltime the important factor, therefore, it might be convenient to obtain directly the traveltime without invoking ray tracing, moreover, although ray tracing is widely used in tomography, it suffers some drawbacks: 1) the traveltime is not necessarily available at the receiver location, and interpolation considering the nearest rays is needed to attain the station. 2) High levels of heterogeneities lead to non-uniform sampling of the medium, this implies that traveltime interpolation is not possible in some regions of the model, in addition, the presence of low-velocity zones introduce the the concept of shadow zones, i.e., parts where the rays do not exist. 3) When triplication occurs in the wavefield, it is not possible to guarantee that the computed traveltime corresponds to the first-arrival. 4) Large-velocity contrasts and obstacles produce diffraction phenomenon, we should underline that ray tracing is the singular solution of the Eikonal equation and although diffraction is part of the Eikonal, the ray solution does not account for this phenomenon, Keller (1962) introduced geometrical theory of diffraction (GTD) by adding this effect with extra terms in the ansatz, however, this requires geometrical information of the boundaries or obstacles, for instance, a cylinder generates creeping rays that follow the surface and are then emitted behind the obstacle while the tip of a wedge leads to infinite set of diffracted rays in all directions, therefore, it is not practical to implement this kind of theory in tomography where the information inside the medium is not always available.

In order to have a better sampling of the medium, we might reconstruct a wavefront and make it evolve step by step. In these methods an initial wavefront is computed assuming homogeneous model close to the source, short element of rays are traced in the initial wavefront and the normal plane of these rays is used to construct the new wavefront, since ray tracing is part of the modeling, these methods are denoted as semi-Lagrangian and they are quite useful to compute multivalued traveltimes and amplitudes (Qin and Schuster, 1993; Vinje et al., 1993, 1996a,b). In this approach, the user has control on the sampling of the medium, i.e., one might reduce or increase the ray density by interpolation, which can be done by paraxial ray equations in order to define a criterion for the ray density (Lambaré et al., 1996; Lucio et al., 1996). However, the entire sampling of the medium might be computational intensive, besides of the exchange between ray tracing and interpolation for a proper sampling, while inclusion of anisotropy in these methods would demand a high complexity, therefore it is convenient to consider an option where the rays are not computed.

Other interesting approach to trace rays is based on theory of graphs, initially proposed by Dijkstra (1959), here the medium is discretized on grid point and all the possible paths between source receiver are computed being a node-to-node formulation, following Fermat's minimum-time principle, the first-arrival is the minimum time over all the possible paths connecting source and receiver, the hole procedure is called network shortest-path ray tracing and a very detailed review is given by Moser (1991) and Moser et al. (1992), while Nolet and Moser (1993) shows some applications. Recently, Meléndez et al. (2019) implemented anisotropy in this method to build a multiparameter inversion code. The fact that all the nodes are connected may be rather time consuming, and it is very important to estimate the maximum error in computing the first-arrival as highlighted by Klimeš and Kvaskička (1994).

However, the Eikonal equation can be directly solved and the solution being obtained at any position of the model: this property is quite attractive for traveltime tomography by avoiding the challenging two-points ray tracing problem. The Eikonal equation belongs to the general class of Hamilton-Jacobi equations and its nature of non-linear makes the finding of a solution not straightforward, however, inside the Hamilton-Jacobi framework, a general solution which satisfy the equation almost everywhere has been studied by Lions (1982), while Crandall and Lions (1983) introduced the mathematical concept of viscosity solution, i.e., there is a unique solution among all the numerous generalized solutions. This viscosity concept has a physical meaning regarding the Eikonal equation, it denotes the shortest path, or in other words, the first-arrival, which can result from any type of event, transmitted, head waves, obstacles, etc., thus we have a substantial difference with the solution of ODEs in ray tracing, when the Eikonal PDE is numerically solved we are able to obtain the complete physics behind. To do so, grid-based solvers have been initially proposed by Vidale (1988, 1990), the Eikonal equation was solved by finite-difference (FD) and the physics behind the computation relies on the Huygens principle which states that the new wavefront is the envelope of spheres drawn from an initial wavefront with local velocity. After those studies, several attempts have been presented in order to improve the technique, we mention some of them, Podvin and Lecomte (1991) introduced a new FD operator in order to handle large-velocity contrasts. Hole and Zelt (1995) identified one inconsistency in the treatment of head waves, one operator for these events was introduced by considering a reverse propagations to better sample the low-velocity zones. The first attempts to use FD method in anisotropic medium were given by Lecomte (1993), Qin and Schuster (1993) and Eaton (1993), these studies showed high computational cost, problems of source initialization, and the existence of a stable solution was not guaranteed, consequently, the necessity of increasing the accuracy and efficiency for anisotropy was declared. An important property of these methods is the definition of a global strategy to propagate the solution on the grid points, this depends on the ordering of the grid points and the number of updates we do in each point, the cited methods are basically single-pass, namely each point will be updated only once, while the reverse propagation proposed Hole and Zelt (1995) can be seen as a multi-pass option since the time computation is refined, however, this reverse propagation requires the supervision of the user. Two main methods have been developed in the field of applied mathematics to propagate the solutions relying on the ordering of the nodes, the first denoted as the fast marching method (FMM) being single-pass combines de Dijkstra's-like algorithm with upwind FD, where the main idea relies on tracking the wavefront and make it evolve in the direction of its normal, FMM was initially proposed by Tsitsiklis (1995) within a Hamilton-Jacobi formulation, although the popular references for this method are referred to Sethian (1996, 1999) in a level-set context. The second approach is a multi-pass algorithm called fast-sweeping method (FSM) (Tsai et al., 2003; Kao et al., 2004; Zhao, 2005) that combines Gauss-Seidel iterations with alternating sweeping ordering to solve the Eikonal equation, this iterative process is known to converge in a finite number of sweeps, although this number is problem-dependent. A comparison between the two methods based on the numerical efficiency is given by Gremaud and Kuster (2006) where they identify FMM as a faster method depending of the problem and considering realistic grid sizes. Other methods have been derived taking FMM and FSM as a starting point, and being extended to other discretizations and formulations, the reader is refereed to Gómez et al. (2019) for a detailed review of nine isotropic grid-based fast methods. Moreover, special treatment must be applied at the source point where the traveltime is zero and the gradient is not defined, the absence of a special treatment leads to large errors due to the singularity close to the source. The first approach was given by Pica (1997) who introduced an analytical variable called celerity which is an average velocity weighted by the straight-line distance from the source, this was combined with FSM by Zhang et al. (2005) to show a good accuracy on traveltime computation. However, the most popular methods to handle the singularity are attributed to Fomel et al. (2009) who introduced the word factorization and Luo and Qian (2011), which consists in apply a reference solution that can be multiplicative or additive factorization, respectively, while Luo and Qian (2012) compared both factorization considering anisotropy, after these works, it is quite common to see Eikonal solver codes that have factorization as a mandatory ingredient. In the presence of anisotropy, the Eikonal equation becomes more complex due to the presence of quadratic equations and adequate numerical strategies needs to be implemented. We mention a few recent works, regarding FMM, Mirebeau and Portegies (2019) proposed new approaches leading to a high efficiency, but in practice, most of the methods solving the anisotropic Eikonal rely on FSM and we can mention: the first extensions restricted to the elliptical case (Tsai et al., 2003; Qian et al., 2007), for the TTI case, Waheed et al. (2015a) avoid the computational cost of directly solving the quartic equations by representing anellipticity as a perturbation of the elliptical case, and Waheed et al. (2015b); Waheed and Alkhalifah (2017) introduce a fixed-point iteration technique which solves the elliptical equation iteratively while an anelliptic term is updated. Most of the solvers are implemented withing a finite-difference formalism, while in our study, we take advantage of the novel approach of Le Bouteiller et al. (2018) which uses discontinuous Galerkin (DG) finite-element discretization, following a general Hamiltonian formalism, isotropic and anisotropic TTI Eikonal can be expressed in a pseudo-time-dependent formulation by

$$\partial_\xi u(\mathbf{x},\xi) + \mathcal{H}(\mathbf{x},\nabla_\mathbf{x} u(\mathbf{x},\xi)) = 0, \tag{1.51}$$

where ξ is the pseudotime evolution parameter, $u(\mathbf{x},\xi)$ is the unknown function of time and space, and $\mathcal{H}(\mathbf{x},\nabla_\mathbf{x} u(\mathbf{x},\xi))$ is the Hamiltonian. Since we are looking for traveltime computation, the stationary state of equation (1.51) is needed along with the Hamiltonian such that the static Eikonal equation is verified as $\mathcal{H} = 0$. Once the the stationary state is reached, we may write $\lim_{\xi\to\infty} u(\mathbf{x},\xi) \equiv T(\mathbf{x})$, where $T(\mathbf{x})$ is the traveltime field at any local position of the velocity model which for our tomographic purposes, it is the traveltime extracted at the receiver locations.

Our forward engine use a Runge-Kutta discontinuous Galerkin (RK-DG) scheme to solve equation (1.51). A direct solution with RK-DG was initially tried by Cheng and Shu (2007) leading to some problems of entropy within the cells, thus Cheng and Wang (2014) addressed this problem and this work is formally the state-of-the-art of our forward engine. Let us mention some improvements, advantages and particularities of our solver:

- The additive source factorization of Luo and Qian (2012) was added in Le Bouteiller et al. (2018) which allowed an increase in the convergence order of traveltimes and spatial derivatives computation in TTI.

- Special treatment at the edges of the elements was implemented in the original scheme of Cheng and Wang (2014) to guarantee suitable radiative boundary conditions.

- The FSM was implemented in the DG formulation (FSM-DG) by Le Bouteiller et al. (2019), where it was shown that for a given level of error, FSM-DG is much faster than FSM-FD, i.e., increase of efficiency.

- Although we do not work in our study with complex topographies, Le Bouteiller et al. (2019) showed experiments in which a vertically-deformed mesh could handle topography in a natural way due to the finite-element formulation. Thus, this is an important property that we can exploit in the future in terms of imaging.

- The solution inside each element is described by a P^1 polynomial approximation based on 3 basis functions with 3 degrees of freedom, this allows the solution to reach an optimal second-order convergence being validated by synthetic tests where the exact solution is known, validation being made for both the first arrivals and the traveltime derivatives (Le Bouteiller et al., 2018). The total number of degrees of freedom in our computations is obtained by $\#\mathrm{ndof} = Nx \times Nz \times 3$, where Nx and Nz are the number of elements in each dimension. Compared to the conventional FD approach which computes the solution on grid points and then it needs to be interpolated to obtain it at other positions, the DG approach allows us to access directly to the solution at any point inside each element and no interpolation is required.

- The fact of having a direct solver allows us to obtain all the physics behind the Eikonal equation, sampling of shadow zone, diffractions coming from obstacles, head waves, etc. We see on chapter 2 the performance of our solver in the presence of a large-velocity contrast. This substantial advantage being out of the ray solution. In addition, our solver does not follow any low-degree anisotropy approximation as we can see in ray-based solvers, thus large values of anisotropy are not a limitation.

1.2 Least-Squares optimization

In first-arrival traveltime tomography (FATT) we look for the optimal model (velocity/anisotropy) of the earth which minimizes the data misfit, also known as the objective function. We consider a least-squares misfit function as a sum over source-receiver couples N_{sr} given by

$$\mathcal{C}(\mathbf{m}) = \frac{1}{2} \sum_{sr} (T_{syn}(\mathbf{m}) - T_{obs})^2, \tag{1.52}$$

where T_{obs} are the picked first-arrival times on recorded traces at receivers r for a known source position s, and $T_{syn}(\mathbf{m})$ are the synthetic traveltimes in the current model. It must be noted that $T_{syn}(\mathbf{m})$ is non-linear, a physical interpretation can be achieved by ray tracing where large-velocity changes lead to changes in the raypaths, this dependency on $\mathbf{m}$ defines FATT as a non-linear optimization problem.

In this study we formulate the inverse problem as a local optimization, we start from an initial guess and the optimum model is found iteratively downhill along the objective function and we stop at the first minimum encountered. The minimum of the misfit function $\mathcal{C}(\mathbf{m})$ is searched in the vecinity of an initial guess $\mathbf{m}_0$, we assume that the true model is given by the initial guess plus one small perturbation as $\mathbf{m} = \mathbf{m}_0 + \Delta\mathbf{m}$. Thus, a second-order Taylor expansion of the misfit function reads

$$\mathcal{C}(\mathbf{m}_0 + \boldsymbol{\Delta}\mathbf{m}) = \mathcal{C}(\mathbf{m}_0) + \Delta\mathbf{m}^t\nabla\mathcal{C}(\mathbf{m}_0) + \frac{1}{2}\Delta\mathbf{m}^t\nabla^2\mathcal{C}(\mathbf{m}_0)\Delta\mathbf{m}^t + \mathcal{O}(\mathbf{m}^3). \tag{1.53}$$

Taking the derivative with respect to the model parameters yields

$$\nabla\mathcal{C}(\mathbf{m}) = \nabla\mathcal{C}(\mathbf{m}_0) + \nabla^2\mathcal{C}(\mathbf{m}_0)\Delta\mathbf{m}. \tag{1.54}$$

The minimum of the misfit function in the vicinity of the point $\mathbf{m}_0$ is obtained when the first derivative of the misfit function is zero, which allows us to obtain the perturbation model by solving the linear system

$$\nabla^2\mathcal{C}(\mathbf{m}_0)\Delta\mathbf{m} = -\nabla\mathcal{C}(\mathbf{m}_0). \tag{1.55}$$

This expression tells us that the perturbation model is searched in the opposite direction given by the gradient of the misfit function at the point $\mathbf{m}_0$, while the second derivative denotes the Hessian and it defines the curvature of the misfit function at the point $\mathbf{m}_0$. Considering the definition of the misfit function (1.52) and taken $\mathbf{m} = \mathbf{m}_0$, the expression for the gradient reads

$$\nabla\mathcal{C}(\mathbf{m}) = -\frac{\partial T_{syn}(\mathbf{m})}{\partial\mathbf{m}}(T_{obs} - T_{syn}(\mathbf{m})) = -\mathbf{G}^t\boldsymbol{\Delta}\mathbf{d}, \tag{1.56}$$

where $\mathbf{G}$ denotes the Fréchet derivative matrix which determine the sensitivity of the calculated data to the model parameters, while $\boldsymbol{\Delta}\mathbf{d}$ is the traveltime residual vector. The procedure is repeated to obtain the Hessian which can be approximated as $\nabla^2\mathcal{C}(\mathbf{m}) \approx \mathbf{G}^t\mathbf{G}$.

The formulation presented is known as the linearization of the inverse problem, however, the same can be done for the forward modeling, we again assume $\mathbf{m} = \mathbf{m}_0 + \Delta\mathbf{m}$, thus by first-order Taylor series around the reference model $\mathbf{m}_0$ we obtain

$$T_{obs} = T_{syn}(\mathbf{m}_0) + \frac{\partial T_{syn}(\mathbf{m}_0)}{\partial\mathbf{m}}\Delta\mathbf{m} + \mathcal{O}(\mathbf{m}^2), \tag{1.57}$$

We can ignore the $\mathcal{O}(\mathbf{m})$ term and rewrite this expression in a compact form as

$$T_{obs} - T_{syn}(\mathbf{m}_0) = \boldsymbol{\Delta}\mathbf{d} = \mathbf{G}\boldsymbol{\Delta}\mathbf{m}. \tag{1.58}$$

This expression linearly links the model parameter perturbation to the data perturbation, Aldridge (1994) derive the same system by linearization of the Eikonal equation. The system can be written more compactly as

$$\mathbf{G}^t\mathbf{G}\Delta\mathbf{m} = \mathbf{G}^t\boldsymbol{\Delta}\mathbf{d}, \tag{1.59}$$

which represents the normal equations. Note that system (1.59) and (1.55) are equivalent, the former known as the Gauss-Newton approximation of the latter because the full Hessian $\nabla^2\mathcal{C}(\mathbf{m})$ is not considered, it was approximated to $\mathbf{G}^t\mathbf{G}$.

In the classical ray-based tomography, the elements of $\mathbf{G}$ are the portions of ray lengths traversing through the model cells, figure 1.2 shows a model discretized in 4 cells, 7 straight rays are traced with the corresponding traveltime, and each ray segment is an element of the matrix $\mathbf{G}$. Then, the system (1.58) needs to be inverted to obtain $\boldsymbol{\Delta}\mathbf{m}$, this can be don by row-action methods like algebraic reconstruction technique (ART) (Gordon et al., 1970), see McMechan (1983) for a pedagogical presentation of this method. There is an improved version being the simultaneous iterative reconstruction technique (SIRT) (Gilbert, 1972), which currently is widely used, see Cai et al. (1996); Fullagar et al. (2000); Tronicke et al. (2001); Becht et al. (2004) for some GPR applications, and Trampert and Lévêque (1990) for a detailed analysis of the method. Other method being quite efficient for solving large and sparse least squares problem are the conjugate-gradient methods, LSQR (Paige and Saunders, 1982) or CGLS (Scales, 1987), both being mathematically equivalent, they works on system (1.59) by computing a set of basis vectors that are mutually conjugate with respect to $\mathbf{G}^t\mathbf{G}$, these basis vectors allow the computation of the model perturbation where only matrix-vector and vector-vector products are required, this methodology has been used in seismology (Latorre et al., 2004), GPR (Dafflon et al., 2011), and geophysical exploration (Zelt and Barton, 1998). Both SIRT and conjugate-gradient estimate the model perturbation iteratively, this is referred as the inner loop, then this perturbation is added is to the initial model and ray tracing needs to be performed in the new model, this is denoted as the outer loop, the procedure is repeated until the minimum of the misfit function reaches some given criteria. It must be noted that in a linear problem, the outer loop does not exist and the convergence is obtained in one iteration, since tomography is non-linear by nature, we need to iterate in order to take into account the non zero error term $\mathcal{O}(\mathbf{m})$ neglected in the Taylor expansion (equations (1.53) and (1.57)). Moreover, we need to recall that a direct Eikonal solver is involved in our formulation, thus one strategy to build $\mathbf{G}$ relies on computing rays a posteriori, i.e., from receivers to sources following the negative traveltime gradient previously computed in the forward modeling (see Podvin and Lecomte (1991)), consequently, one can still take advantage of an accurate traveltime computation.

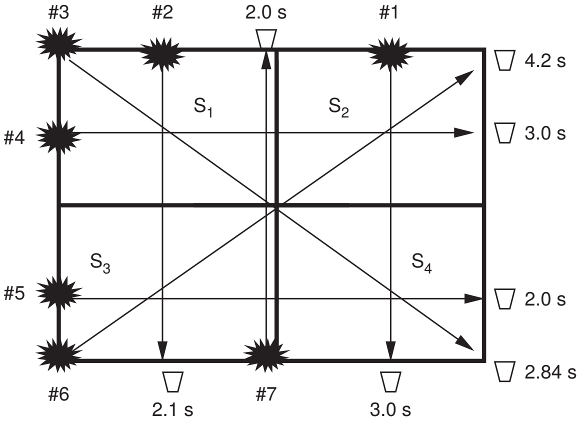

Figure 1.2: Discretized domain in 4 slowness cells, 7 straight rays are traced between sources (stars) and receivers (buckets) where the traveltime is added. The ray segments inside the cells are the element of matrix $\mathbf{G}$ which has as dimensions the number of traveltimes by the number of discretized model parameters. Figure modified from Schuster (2017).

We remain in the Newton framework, where a local descent algorithm is adopted, often called gradient optimization method. The iterative local descent optimization writes

$$\mathbf{m}_{k+1} = \mathbf{m}_k + \alpha_k \mathbf{\Delta m}_k, \tag{1.60}$$

where α is a positive scalar, th so-called step-length and the model update or the descent direction $\mathbf{\Delta m}$ given by equation (1.55). The first ingredient α requires a 1D optimization problem:

$$\min_{\alpha>0} = \mathcal{C}(\mathbf{m}_k + \alpha_k \mathbf{\Delta m}_k) \tag{1.61}$$

The step-length by exact line-search has an analytical expression where the Hessian is required being quite expensive to compute, consequently an inexact line-search is usually preferred by satisfying the Wolfe conditions: the sufficient and the curvature conditions (Nocedal and Wright, 2006). Regarding the descent direction, in system (1.55) the Hessian can be approximated by the identity matrix which leads to the steepest-descent method whose efficiency might be very slow, an improvement can be obtained by considering the descent direction at the previous iteration, this formulation is denoted as the non-linear conjugate-gradient, both methods having a linear convergence. However, any of the mentioned methods takes into account the Hessian which is substantially important when the problem is ill-conditioned, this is particularly true when multiparameter inversion is performed, unfortunately the explicit computation is expensive. Our strategy is to approximate the Hessian by the quasi-Newton l-BFGS-B method, where the initial letter l comes from limited memory, the next four letters are abbreviations of the authors and the last letter B indicates that bounded constraints are allowed if needed. In terms of practical implementation, the Hessian is not built, l-BFGS-B approximates the product $(\nabla^2\mathcal{C})^{-1}\nabla\mathcal{C}$ from system (1.55) by a two-loop recursive algorithm and by taking into account l previous gradients and models (Nocedal and Wright, 2006), $l = 15$ in our computations. At the first iteration, there is not previous gradient, consequently the method reduces to the steepest-descent, the next iteration relies on the non-linear conjugate-gradient while the remaining iterations consider the l previous information. We must underline that a gradient-based method allows us to suppress the inner loop, once the gradient is supplied, the search direction in system (1.60) is directly obtained, thus reducing the complexity. The l-BFGS-B code we use can be found in Métivier and Brossier (2016) where major details for the step-length computation are given, moreover, they validate by synthetic examples that l-BFGS-B consumes less computational time and it has a faster convergence than steepest-descent and non-linear conjugate gradient.

1.2.1 Gradient computation with the adjoint-state method

The remaining ingredient to perform the inversion is the gradient, one option is to compute the matrix $\mathbf{G}$ by a posteriori ray tracing and multiply it by the residuals, however the dimensions of this matrix are the number of traveltimes by the number of discretized model parameters, thus being quite expensive to storage in the presence of large datasets. The mathematical theory allowing to compute the gradient of the misfit without forming the matrix of Fréchet derivatives is the adjoint-state method within a Lagrangian formalism and being implemented by Sei and Symes (1994) in the framework of FATT, the reader is referred to (Plessix, 2006) for a detailed review on the method. We build the Lagrangian misfit function by augmenting the misfit function $\mathcal{C}(\mathbf{m})$ with equality constraints as

$$\mathcal{L}(\mathbf{m}, t, \lambda) = \frac{1}{2}\sum_{sr}(t_{syn}(\mathbf{m}) - T_{obs})^2 - \frac{1}{2}\sum_{s=1}^{N_s}\langle\lambda_s(\mathbf{x})|\mathcal{H}(\mathbf{x}, \nabla t(\mathbf{x}))\rangle_\Omega \tag{1.62}$$

where the second term is the constraint defined on the targeted subsurface domain Ω, and being the scalar product $\langle\cdot,\cdot\rangle$ between the Lagrangian multiplier (also called adjoint-state variable) $\lambda_s(\mathbf{x})$, and the Eikonal Hamiltonian, note that $\lambda_s(\mathbf{x})$ is defined for each source until the total number of sources N_s is reached. The adjoint-state variable can be viewed as a penalty term to ensure that at the optimum, the state variable $t(\mathbf{x})$ is the solution of the state Equation, namely the Eikonal Hamiltonian, and thus equal to $T(\mathbf{x})$.

According to Karush-Kuhn-Tucker (KKT) conditions (also known as first order optimality conditions) the gradient of the Lagrangian with respect to t, λ_s and $\mathbf{m}$ should be zero at optimum. The optimization to satisfy these three conditions is similar to system (1.60) including the three variables in the search direction, this is called as the full space method, however, in presence of large-scale problem this is not practical, thus we rely on a reduced space method which is based on a block elimination of the constraints, and consequently leads to an unconstrained optimization problem. The first constraint:

$$\nabla_\lambda \mathcal{L} = \mathcal{H}(\mathbf{x}, \nabla t(\mathbf{x})) = 0, \tag{1.63}$$

requires the Eikonal equation and results in the state variable. Moreover, with the second constraint $\nabla_t \mathcal{L} = 0$ we obtain

$$\nabla_t \mathcal{L} = \sum_{sr} (t_{syn}(\mathbf{m}) - T_{obs}) - \sum_{s=1}^{N_s} \Big(\big(\nabla \cdot (\lambda_s(\mathbf{x}) \nabla t(\mathbf{x}))\big)_\Omega - \big(\lambda_s(\mathbf{x}) \nabla t(\mathbf{x}) \cdot \mathbf{n}\big)_\Gamma \Big), \tag{1.64}$$

where the second term is obtained by integration by parts (Leung and Qian, 2006; Taillandier et al., 2009). Here, Γ denotes the boundaries of Ω and $\mathbf{n}$ is the unit vector normal to surface. Without loss of generality, we will impose Dirichlet boundary conditions for the adjoint variable, so that $\lambda_s(\mathbf{x}) \nabla t(\mathbf{x}) \cdot \mathbf{n} = 0$ over Γ: this will be a non-restrictive hypothesis as long as all sources and receivers are inside the numerical domain. Finally, zeroing equation (1.64), the adjoint-state transport equation satisfied by $\lambda_s(\mathbf{x})$ at the optimum yields

$$\big(\nabla \cdot (\lambda_s(\mathbf{x}) \nabla T(\mathbf{x}))\big)_\Omega = - \sum_{sr} (T_{syn}(\mathbf{m}) - T_{obs}). \tag{1.65}$$

Note that we implement the traveltime residuals as source terms at the receiver positions in the right-hand side of the adjoint equation rather than as a boundary condition like Leung and Qian (2006); Taillandier et al. (2009), consequently we avoid problems of initialization at the boundaries of the domain. Our implementation assuming shots and receivers inside the domain Ω was mathematically proposed by Sei and Symes (1994), implemented by Bretaudeau et al. (2013, 2014) where synthetic examples are shown, and suggested by Waheed et al. (2016) to incorporate crosshole acquisitions into the computation of the adjoint-state variable. It is worth mentioning that adjoint-state equation (1.65) has been derived within an isotropic framework whose physical interpretation is provided by Taillandier et al. (2009): traveltime residuals are the energy initialized at the receivers, they are back-propagated along a ray tube honoring the conservation of energy, where the direction of propagation is governed by the slowness vector ∇T until the source position is reached. However, in anisotropy, the direction of the energy flux is given by the group velocity vector $\vec{\mathcal{U}}$ whose expression was previously defined in equation (1.50), the mathematical derivation we showed to obtain equation (1.64) can be also applied to derive the anisotropic adjoint-state equation with the only difference of the group velocity vector replacing the slowness vector. For the solution of the adjoint-state equation (1.65), due to its linearity, the expensive DG formulation can be avoided, Le Bouteiller (2018) proposed a finite-volume (FV) solver which can be seen as a lower-order formulation of DG using piecewise constant approximation, FV is complemented by the FSM for the global scheme (FSM-FV), thus the same scheme used for the Eikonal computation (FSM-DG). Moreover, FSM for the solution of adjoint-state equation has been also used byLeung and Qian (2006) and Taillandier et al. (2009) within the FD framework.

After verifying the Eikonal and adjoint-state equations, the third condition $\nabla_{\mathbf{m}} \mathcal{L} = 0$ defines the gradient of the misfit function, in other words, $\mathcal{L}(\mathbf{m}, t, \lambda) = \mathcal{C}(\mathbf{m})$. The desired gradient reads

$$\nabla_{p(\mathbf{x})} \mathcal{C} = -\frac{1}{2} \sum_{s=1}^{N_s} \lambda_s(\mathbf{x}) \frac{\partial \mathcal{H}(\mathbf{x}, \nabla T(\mathbf{x}))}{\partial p(\mathbf{x})} \tag{1.66}$$

where $p(\mathbf{x})$ denotes either v for the isotropic case or V_v, ϵ and δ for the VTI case. The second term is known as the weighting factors of the adjoint field being simply the derivative of the forward operator with respect to the model parameters and controls how the gradients with respect to different parameter classes differ. For the isotropic case, the gradient of the misfit function with respect to the velocity v is easily derived from the Eikonal equation, it yields

$$\nabla_{v(\mathbf{x})}\mathcal{C} = -\sum_{s=1}^{N_s} \frac{\lambda(\mathbf{x})}{v^3(\mathbf{x})}. \tag{1.67}$$

Same expression is also shown by Leung and Qian (2006) and Taillandier et al. (2009), although other works prefer to invert slowness leading to a slightly different expression (Sei and Symes, 1994; Bretaudeau et al., 2013, 2014; Tong, 2021). For the anisotropic case, we might consider to invert the four parameters of the complete TTI Hamiltonian, however, the fourth parameter being the tilted angle can be obtained either by *a priori* information or by a data-driven optimization as we propose in chapter 3, we therefore propose to reduce the model space to three parameters by continuing with the VTI Eikonal (equation (1.44)), from which the Hamiltonian derivatives can be straightforwardly inferred as

$$\frac{\partial\mathcal{H}(\mathbf{x},\nabla T)}{\partial V_v(\mathbf{x})} = 2V_v(1+2\epsilon)T_{,x}^2 + 2V_vT_{,z}^2 - 8V_v^3(\epsilon-\delta)T_{,x}^2T_{,z}^2, \tag{1.68}$$

$$\frac{\partial\mathcal{H}(\mathbf{x},\nabla T)}{\partial \epsilon(\mathbf{x})} = 2V_v^2T_{,x}^2 - 2V_v^4T_{,x}^2T_{,z}^2, \tag{1.69}$$

$$\frac{\partial\mathcal{H}(\mathbf{x},\nabla T)}{\partial \delta(\mathbf{x})} = 2V_v^4T_{,x}^2T_{,z}^2. \tag{1.70}$$

Same derivatives are shown by Tavakoli F. et al. (2019) in the framework of slope tomography, note that for the sake of brevity we omit the coordinate dependency of the parameters on the right-hand side of the Hamiltonian derivatives. After these derivations, let us underline the advantages and particularities of the adjoint-state method:

- We can see from equation (1.66) that the gradient of the misfit function is the weighted summation of the adjoint field $\lambda(\mathbf{x})$, the derivatives of the Hamiltonian being the weights.

- The weights either for isotropy (equation (1.67)) or anisotropy (equations (1.68)-(1.70)) built the spatially-dependent coefficients that contribute to the sensitivity kernel of the subsurface parameters update along the receiver to source propagation paths.

- The gradient calculation is matrix-free because the sensitivity matrix is not constructed, the complexity being reduced to the number of model parameters, namely the size of the adjoint field, moreover, even in the presence of several receivers, the problem is reduced to the number of sources, i.e., in each iteration, we only need to solve the Eikonal and the adjoint-state equations for each source in order to obtain the traveltime at the receivers and the back propagation of the residuals, respectively, while in the matrix formulation we need to trace a ray for each source-receiver couple.

- The Hamiltonian derivatives which define the anisotropy contribution of each parameter in equations (1.68)-(1.70) are simply analytical expressions while in ray-based tomography, it requires *ab initio* parameter selection as needed for numerical evaluation of Fréchet derivative, see Brantut (2018) and Meléndez et al. (2019) for some details regarding the implementation of the anisotropy in the ray-based approach.

- Other parametrizations for the anisotropic Eikonal can be proposed (Waheed et al., 2016; Tavakoli F. et al., 2019) leading to different Hamiltonian derivatives, however, the adjoint field is independent of the parametrization, it does need to be modified if the user wants to try other parametrization.

We need to discuss the Hamiltonian derivatives in equations (1.68)-(1.70), they control the amplitude variations of the gradient of each parameter, $\nabla_{V_v}\mathcal{C}$, $\nabla_{\epsilon}\mathcal{C}$ and $\nabla_{\delta}\mathcal{C}$ along the spatial domain spanned by the adjoint-state variable. For weights associated with $\nabla_{V_v}\mathcal{C}$ in equation (1.68) the first two terms are dominant, which means horizontal and vertical spatial derivatives of traveltime, therefore, $\nabla_{V_v}\mathcal{C}$ is basically sensitive to vertical and horizontal propagation paths with a slight increase in the horizontal pattern due to the term $(1 + 2\epsilon)$, which is not present in the vertical one. The second derivative, equation (1.69) has a higher amplitude only in the horizontal spatial derivative, leading $\nabla_{\epsilon}\mathcal{C}$ to be sensitive to horizontal paths. Finally, equation (1.70) has only one term which is multiplying the product of vertical and horizontal spatial derivatives, making $\nabla_{\delta}\mathcal{C}$ mostly sensitive to oblique propagation.

Regarding the parameter discretization, we now explain how is distributed between the forward and the inverse problems:

1. Each parameter has a node discretization which is the same for the inversion grid.
2. In the forward problem, the user chooses the number of elements to discretize each model parameter, consequently the model grid is projected on elements in order to solve the Eikonal equation.
3. In the inverse problem, the same elements discretization chosen in step 2 is used to compute the adjoint field and the Hamiltonian derivatives, consequently the gradient also has a FV formulation, the main feature in the gradient is that we have only one value at the center of each element while in the forward problem we have the traveltime at any position of the element due to the DG formulation.
4. The gradient is projected on the inversion grid defined in step 1, and it enters to the optimization. The update model from the inversion tool is added to the reference one and it is then projected on the element discretization, namely we come back to step 2, and the procedure is repeated until the desired convergence is achieved.

The fact of moving from nodes to elements discretization allows the user to choose a finer element discretization for the forward problem and a coarse node discretization for the inverse problem. We should recall that FATT relies on the high-frequency approximation, namely we are looking for the low-wavenumber information which can be justified by a coarse discretization of the inversion grid.

1.2.2 Sensitivity kernel of different parametrizations

One parametrization has been presented, namely (V_v, ϵ, δ), and followed by an explanation based on the dominant terms. In this section we present the gradient for each parameter and propose another parametrization which might be more convenient.

A circular experiment is designed in order to guarantee a complete illumination, the scale we adopt is centimeters since we use the same scale in chapter 3 and 4 for a real dataset acquired from laboratory measurements. Figure 1.3 shows the acquisition of the esperiment, in a 2D domain of $33 \times 33\,cm$, we locate 40 sources equally spaced and denoted with red asterisks, the receiver are located along all the perimeter of the circle being denoted as blue triangles and associated with each source, a solid black line is traced between each source-receiver couple and the lines are decimated in order to have a better illustration of the acquisition. Regarding the discretization, we use square elements in each dimension with edges of $0.538\,mm$ while for the grid discretization we have $0.5\,mm$ separation between nodes in both dimensions.

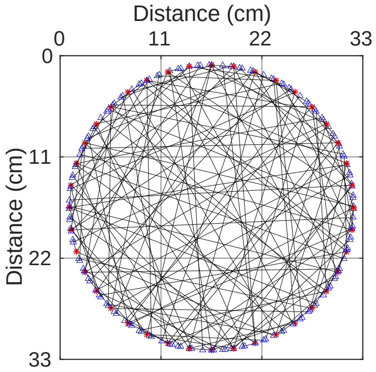

(a)

Figure 1.3: Circular full-illumination experiment at the lab scale, 44 sources are equally separated and denoted by red asterisks, while receiver are located along all the perimeter of the circle being denoted by blue triangles and associated with each source. A solid line is drawn for each source-receiver couple, however, the lines are decimated to improve the illustration of the acquisition.

We run a forward computation using the models of figure 1.4a-c for V_v, ϵ and δ, respectively, in order to obtain the observed traveltimes. Each parameter has a small Gaussian anomaly of $2\,cm$ radius and the values used represent a maximum anisotropy of 28.8% located at the center of the anomaly. We now compute the sensitivity of each parameter given by the gradient of the misfit function, as an initial model to compute our synthetic traveltimes we use the background value of each parameter, namely $V_v = 0.27\,cm/\mu s$, $\epsilon = 0.03$, and $\delta = 0.01$, where the difference between observed and synthetic times denotes the residuals used to initialize the adjoint field. The first gradient of each parameter is shown in figure 1.5a-c, therefore these are the gradients before entering the optimization, as a first feature, note the adjoint signature in each source which comes from numerical computations, the same signature is also illustrated by other adjoint-based workflows (Taillandier et al., 2009; Waheed et al., 2016; Tavakoli F. et al., 2019) and can be attenuated by using a filter, however, here we consider suitable to show the raw gradient. The gradient of $\nabla_{V_v}\mathcal{C}$ (figure 1.5a) shows information basically in all the directions, with a slight increase in the horizontal pattern, the second gradient $\nabla_{\epsilon}\mathcal{C}$ (figure 1.5b) shows a sensitivity well defined for horizontal paths, while the vertical paths do not show information, we emphasize that the adjoint field is present in all the domain for each source-receiver couple, however, the Hamiltonian derivative for this parameter (equation (1.69)) does not contribute in the vertical direction. The last gradient $\nabla_{\epsilon}\mathcal{C}$ (figure 1.5c) shows the main amplitudes in oblique propagation paths. The main difficulty with this parametrization arises between $\nabla_{V_v}\mathcal{C}$ and $\nabla_{\epsilon}\mathcal{C}$ since they share the horizontal paths, this will produce a leakage between parameters when the inversion is performed, in other words, one parameter will contaminate the update of the other and vice versa.

Another parameterization might be proposed in order to evaluate the leakage, we can modify the VTI Hamiltonian of equation (1.44) and express it in terms of the three velocities (V_v, V_h, V_n), this can be done by considering the expressions of $V_h = V_v\sqrt{1+2\epsilon}$ and $V_n = V_v\sqrt{1+2\delta}$, thus the new

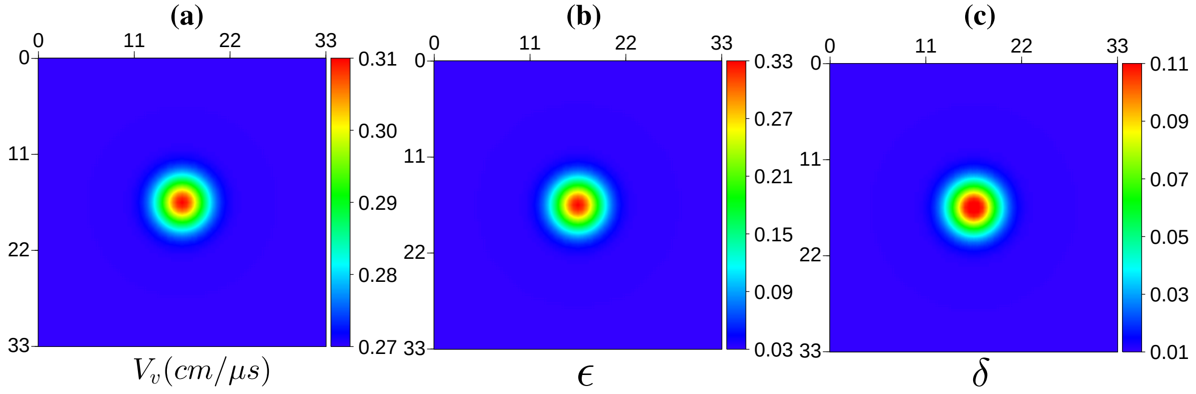

Figure 1.4: True models used to compute observed traveltimes with our forward engine, each parameter has a Gaussian anomaly with $2\,cm$ of radius. a) V_v $(cm/\mu s)$, b) ϵ, and c) δ. At the center of the anomaly we reach a maximum anisotropy of 28.8%.

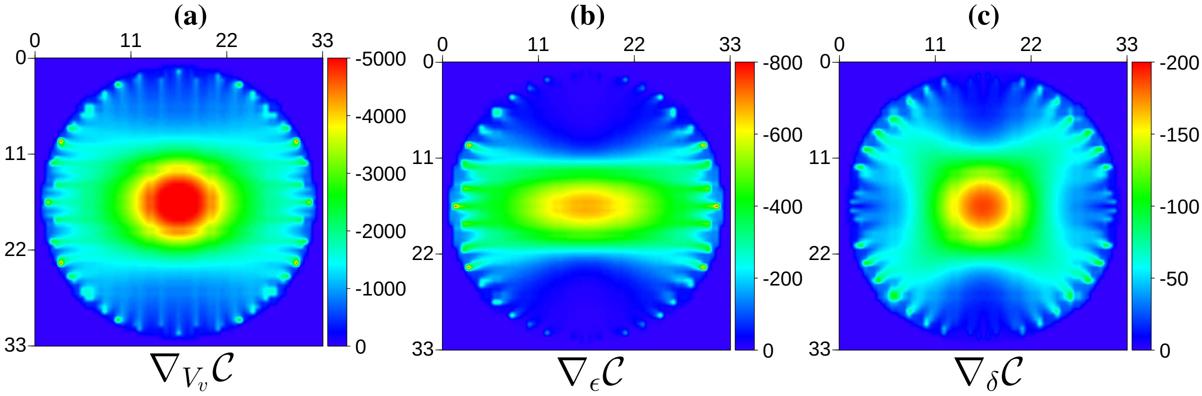

Figure 1.5: Misfit function gradient of each parameter under the parametrization (V_v, ϵ, δ), they are computed using the adjoint field and the Hamiltonian derivatives of equations (1.68)-(1.70). a) $\nabla_{V_v}\mathcal{C}$, b) $\nabla_{\epsilon}\mathcal{C}$, and c) $\nabla_{\delta}\mathcal{C}$.

Hamiltonian writes

$$\mathcal{H}_{\text{VTI}}(\mathbf{x}, \nabla T) = V_h^2 T_{,x}^2 + V_v^2 T_{,z}^2 - V_v^2(V_h^2 - V_n^2)T_{,x}^2 T_{,z}^2 - 1. \tag{1.71}$$

Then, the analytical expressions for the derivatives are given by

$$\frac{\partial \mathcal{H}(\mathbf{x}, \nabla T)}{\partial V_v(\mathbf{x})} = 2V_v T_{,z}^2 - 2V_v(V_h^2 - V_n^2)T_{,x}^2 T_{,z}^2, \tag{1.72}$$

$$\frac{\partial \mathcal{H}(\mathbf{x}, \nabla T)}{\partial V_h(\mathbf{x})} = 2V_h T_{,x}^2 - 2V_h V_v^2 T_{,x}^2 T_{,z}^2, \tag{1.73}$$

$$\frac{\partial \mathcal{H}(\mathbf{x}, \nabla T)}{\partial V_n(\mathbf{x})} = 2V_n V_v^2 T_{,x}^2 T_{,z}^2. \tag{1.74}$$

Since the forward modeling is independent from the inverse problem, we can continue using the observations we obtained from the true models (figure 1.4a-c), and use the Hamiltonian of equation (1.71) for the estimation of the gradients, the optimization will give us an update model with the three different velocities, we then need to compute ϵ and δ before entering the forward computation which is simple due to the mathematical relations between the Thomsen parameters and the velocities, this being required at each iteration of the optimization. As explained before, we use the same adjoint field but considering the new weights from the derivatives (equation (1.72)-(1.74)). The first gradient $\nabla_{V_v}\mathcal{C}$ in figure 1.6a shows a strong difference with the same gradient of the first parametrization in figure 1.5a, even if we are referring to the same parameter. With this parametrization, $\nabla_{V_v}\mathcal{C}$ is mostly defined for the vertical paths with a slight contribution on the oblique direction as we see in equation (1.72), the two other gradients $\nabla_{V_h}\mathcal{C}$ and $\nabla_{V_n}\mathcal{C}$ are shown in figures 1.6b-c, respectively, one may see the main sensitivity in the horizontal for the former and the oblique pattern for the latter, we basically arrive to the same conclusions of the the previous parametrization (figure 1.5b-c). However, this parametrization clearly shows a better decoupling between gradients which certainly suppress the cross-talk during the optimization.

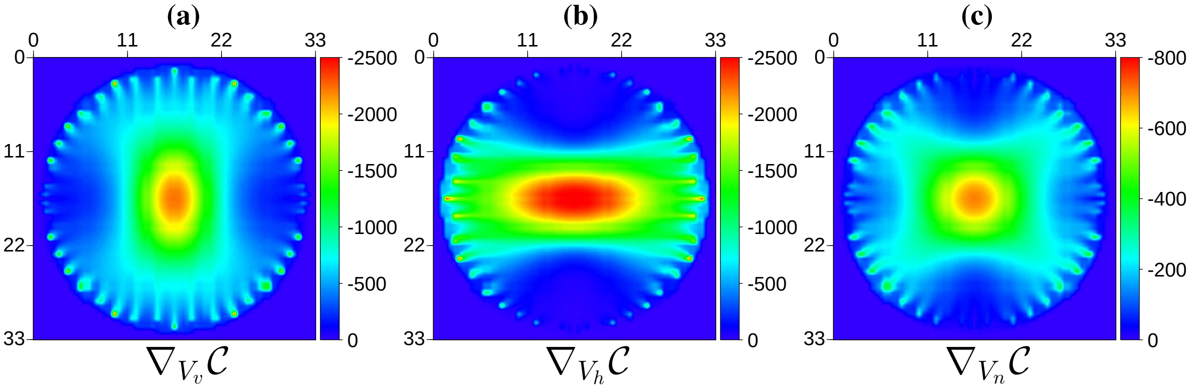

Figure 1.6: Misfit function gradient of each parameter under the parametrization (V_v, V_h, V_n), they are computed using the adjoint field and the Hamiltonian derivatives of equations (1.72)-(1.74). a) $\nabla_{V_v}\mathcal{C}$, b) $\nabla_{V_h}\mathcal{C}$, and c) $\nabla_{V_n}\mathcal{C}$.

The other point to discuss is about the amplitudes of the gradients in each parametrization, in the firs using (V_v, ϵ, δ) we may see a major difference between the gradients of the Thomsen parameters and the one of vertical velocity, for instance, $\nabla_{V_v}\mathcal{C}$ is 6.25 times higher than $\nabla_{\epsilon}\mathcal{C}$ (figure 1.5a-b), this is certainly due to the different orders of magnitude of the different parameter classes, note that we are working with one parameters with velocity units and the other two dimensionless, this can be overcome by using a scaling factor for the Thomsen parameters in order to have the same order of the vertical velocity as suggested by Tavakoli F. et al. (2019) or by normalization of the three parameters followed by a suitable scaling factor, this second option is the adopted in our study whose details are shown in the next chapter. Both cases will produce a better balance between gradients to avoid the differences we see in the first parametrization. However, the finding of a suitable scaling factor is problem-dependent, the user has to perform several inversions evaluating different scaling values until a stable update is obtained, namely we avoid strong updates in one parameter compared to the others due to the no balance of gradients. This scaling factor analysis certainly makes the use of this parametrization less robust in terms of computational efficiency. Conversely, in the second parametrization with (V_v, V_h, V_n), scaling is not needed since the three parameters share the same units, this being consistent with the amplitudes of the gradients in figure 1.6a-c, where strong differences are not present.

Although the second parametrization shows a better decoupling, the inclusion of three parameters increases the ill-posedness of the inversion being quite challenging to retrieve the three parameters simultaneously. When looking at the gradients of the second parametrization (figure 1.6a-c), we may see that vertical and horizontal velocities have the best decouple while the normal velocity still shares some information with the other two velocities, this is also true in the first parametrization, the third parameter δ shares some angles with the other two parameters, we therefore propose to evaluate third parameter in both parametrization, namely δ and V_n, a forward problem is performed in homogeneous $V_v = 0.27\, cm/\mu s$ and $\epsilon = 0.03$, while for the case of δ we use the model with the anomaly (figure 1.4c), in order to compute the observations. We then compute the gradient of the misfit function using the true model for V_v and ϵ, and homogeneous $\delta = 0.01$, consequently we can visualize the effect of the third parameter on the other two. Figure 1.7a-b shows the gradient of vertical velocity and ϵ, which we previously saw that both parameters are mostly sensitive to horizontal paths, however, in both gradients there is no sensitivity in that direction because the model we use is equal to the true model, instead, we clearly see the imprint of the parameter δ producing a oblique pattern, the same conclusion is deduced in the second parametrization (Figure 1.8a-b), the vertical velocity and horizontal gradient do not show information in the vertical and horizontal direction, respectively, while the effect of the third parameter is present. In order to avoid this effect, we might consider to fix the third parameter based on some *a priori* information or approximate the medium with an elliptical case where $V_h = V_n$ or $\epsilon = \delta$, we therefore reduce the model space to have two parameters. Elliptical approximation is valid since the kinematics of waves is mainly governed by two parameters (Alkhalifah and Tsvankin, 1995), this is consistent with our sensitivity analysis (figures 1.5a-c and 1.6a-c), note that the third parameter in both parametrization, either δ or V_n, both have the less contribution in the gradient, consequently, the inversion will be mainly driven by the other two parameters, we show in chapter 3 some average velocity versus angle analysis to validate the small effect of the parameter δ on the data, which indeed was validated by Jiang and Zhou (2011) after computing traveltime derivative with respect to δ and showing that it is the weakest parameter on the data, similarlyCheng et al. (2014) illustrated the effect on the data after applying some perturbation in each parameter and concluding that δ does not change dramatically the kinematics of waves, and Meléndez et al. (2019) shows that although δ is the weakest parameter, it cannot be neglected and at least one homogeneous value should be used. Moreover, Michelena et al. (1993) suggests that inversion of anisotropy within the elliptical framework can be a useful intermediate step before the full characterization of anisotropy. Therefore, we may invert under the elliptical assumption to obtain the two parameters and use them as fixed parameters in a single-parameter inversion of the third parameter, namely a hierarchical approach as proposed by Waheed et al. (2016), however, we do not explore the inversion of the third parameter and it remains as a perspective of our study which relies on the elliptical case in what follows.

It is worth mentioning that this sensitivity analysis has been done within a transmission framework, our conclusions being consistent with other works that show the sensitivity analysis of transmission pattern in FWI (Gholami et al., 2013a,b; Alkhalifah and Plessix, 2014; He and Plessix, 2017). However, in a surface to surface acquisition our preference of the second parametrization will certainly fail because it is not possible to retrieve the vertical velocity, we can only retrieve the horizontal velocity with wide-angle data and the normal velocity with intermediate-angle data Alkhalifah (2000); Tsvankin (2001); Plessix and Cao (2011), one may consider to obtain a smooth model of vertical velocity from isotropic inversion and invert for the other two parameters while the vertical velocity remains fixed. As part of our study, all the synthetic and real experiments are performed in crosshole environment (chapter 2) and full illumination at laboratory (chapters 3 and 4), thus we can continue with the validation of our preliminary results for each parametrization. In the next chapter we design a workflow for the multiparameter inversion of anisotropy, first we evaluate each parametrization by realistic synthetic inversion where the solution is known, and the preferred being applied in real data, the better results are expected with the parametrization where the Thomsen parameters are not considered.

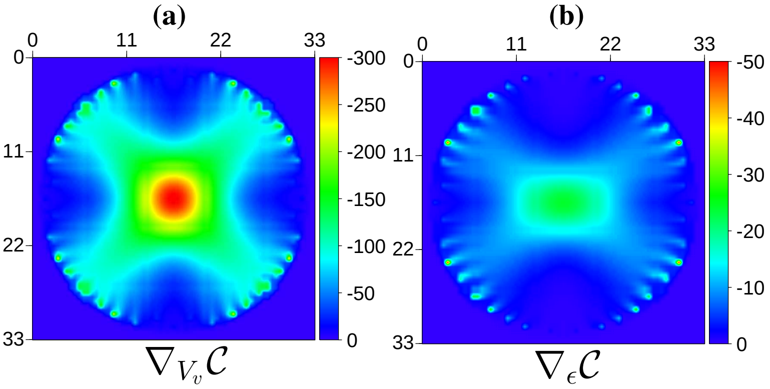

Figure 1.7: Parametrization (V_v, ϵ, δ). Effect of the parameter δ on the gradient of the other two parameters. Observations are computed considering the anomaly only present in δ and homogeneous for V_v and ϵ, while for the synthetics all the parameters are homogeneous. a) $\nabla_{V_v}\mathcal{C}$ and b) $\nabla_{\epsilon}\mathcal{C}$.

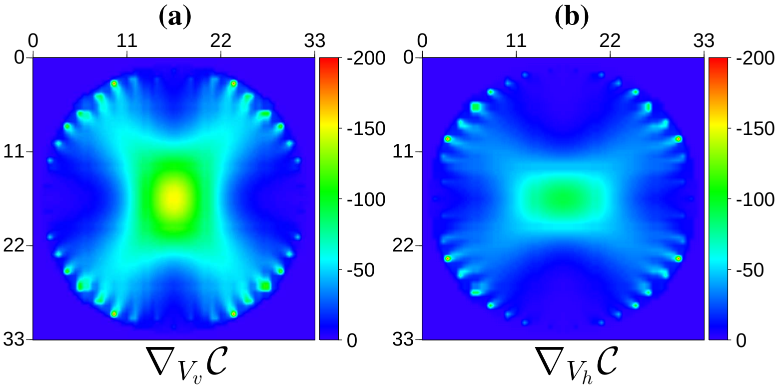

Figure 1.8: Parametrization (V_v, V_h, V_n). Effect of the parameter V_n on the gradient of the other two parameters. Observations are computed considering the anomaly only present in δ and homogeneous for V_v and ϵ, while for the synthetics all the parameters are homogeneous. a) $\nabla_{V_v}\mathcal{C}$ and b) $\nabla_{V_h}\mathcal{C}$.

1.3 Conclusion

In this chapter we have presented the elastodynamic and the Maxwell system of equations that allow us to describe the propagation of mechanical and electromagnetic waves, respectively, the physics behind each system was discussed. In both physics, the high-frequency approximation can be applied, i.e., the heterogeneities in the medium are bigger than the characteristic wavelength of the signal. Under this assumption, the Eikonal equation being the main ingredient of our tomography approach was derived, from seismic we rely on the acoustic case while in electromagnetism, it can be obtained from Maxwell's equations. Eikonal equation is a nonlinear, partial differential equation of the first order whose solution gives us the first-arrival traveltime of the waves at one local position. The same fundamental Equation was obtained for the anisotropic case under the VTI assumption in 2D for the moment, different parameters arise which control the velocities depending of the direction of propagation. Since the anisotropic Eikonal equation was obtained from the elastodynamic system, we justified the use of the same equation to describe the anisotropy of electromagnetic waves. We proceed to give a detail review of the different methods to solve the Eikonal equation in both isotropy and anisotropy, we formulate the Eikonal equation under a Hamiltonian formalism to obtain the characteristic system of ordinary differential equations (ODEs) to solve. The main and still widely used method to solve the system being ray tracing where a ray connecting source-receiver is designed and the time is computed along the ray, our review discuss all the variations of the ray tracing technique with some extensions that were applied in tomography. Other method to solve the Eikonal relies on the Eulerian formalism which consider the Huygens' principle to compute the wavefronts, thus we do not trace rays. Although most of the methods are grid-based with the use of finite-difference to solve the Eikonal, we adopt another formulation being discontinuous Galerkin finite-element discretization under a Hamiltonian formalism to express the Eikonal in a pseudo-time-dependent form, the advantages and particularities of our method are discussed.

The inversion part is presented where a local optimization framework is adopted, we rely on least-square formulation to design the misfit function. The mathematical and physical assumptions are given to linearize the problem, and obtain the Newton system of equations to solve. Several studies still rely on reconstruction techniques or conjugate-gradient, both methods need to iterate to obtain the update model and then we need to solve the Eikonal equation on the new model also iteratively, therefore two loops are required. We propose to reduce the complexity following a gradient-based approach where only the gradient is needed, the updated model is directly obtained avoiding the iterations, then we compute the Eikonal on the new model reducing the problem to a single-loop. Since it is the main ingredient of our approach is the computation of the gradient, the formal definition implies to build the sensitivity matrix which can be very expensive to storage since the dimensions of the matrix are number of model discretized parameters and the number of source-receiver couples. In order to avoid this matrix, we rely on the adjoint-state method to formulate the inversion under a Lagrangian formulation with constraints, after satisfying the constraints, the gradient of the misfit function is given by the adjoint field weighted by an analytical expression depending of the Hamiltonian, the complexity of the problem being reduced to the number of discretized model parameters, advantages and justifications of the adjoint-state method are given. When anisotropy is considered, each parameter has a specific analytical expression which controls its contribution on the gradient, we proposed two parametrizations along with a full-illumination experiment to illustrate the different sensitivities, the first parametrization considering the Thomsen parameters shows that vertical velocity and ϵ have the same sensitiviy, namely they both are sensitive to the same propagation paths, this will produce a leakage between the parameters during the optimization, conversely, the second parametrization which considers velocities and avoids the Thomsen parameters shows a better decouple between parameters. In the next chapter, we validate the results of each parametrization with realistic synthetic examples where the solution is known, the preferred parametrization being applied in real data followed by an efficient workflow to handle the multiparameter inversion.

Chapter 2

Matrix-free crosshole elliptical-anisotropy tomography: parametrization analysis and ground-penetrating radar applications in carbonates

Contents

In this chapter, the multiparameter code introduced in chapter 1 to invert velocity and anisotropy from first-arrival times is applied synthetic and real crosshole ground penetrating radar (GPR) data at the field scale in carbonate formations. Most of the material presented in this chapter is extracted from the publication Salcedo et al. (2020) and some preliminary results were presented in Salcedo et al. (2019), therefore this chapter follows a paper style.

Abstract A novel traveltime tomographic approach is applied to anisotropic media, limited to 2D geometry for the moment. A general anisotropic Eikonal solver based on a discontinuous Galerkin method is combined with an efficient adjoint formulation for multiparameter least-squares inversion. This new approach is tested considering synthetic crosshole Ground Penetrating Radar data in a configuration inspired from a real experiment acquired in layered carbonate media disturbed by the presence of a

deep gallery, which induces a localized high-electromagnetic contrast. This made it possible to define a well-adapted general workflow in this context. We notably show that under the elliptical anisotropic assumption, the parametrization based on vertical and horizontal velocities provides less biased results than those obtained by considering the vertical velocity and the relevant Thomsen parameter ϵ. The initial vertical and horizontal velocity models are identical and built from an isotropic inversion. The presence of the high-contrast gallery generates a weak diffraction pattern, which is taken into account in our tomography approach. It also creates potential artefacts due to the model discretization, which are mitigated by a model regularization term within the definition of the misfit function. This general workflow is then applied to the real experiment dataset. The vertical and horizontal velocity images provide similar structures as those previously obtained by isotropic full waveform inversion, complemented by an image of a rather weak elliptical anisotropy.

Introduction

A wide range of geophysical methods are available for the characterization of near-surface formations. They differ by their sensitivity, resolution, and penetration depths. Whether in seismic or electromagnetism, first-arrival traveltime tomography (FATT) can be performed from surface/surface acquisitions or between boreholes to recover the spatial distribution of velocities of waves from picked traveltimes between sources and receivers. As for many geophysical inverse problems, FATT methodology can be divided into two parts: *(i)* the forward modeling, which aims at computing synthetic traveltimes between sources and receivers in a given medium and *(ii)* the inversion, during which the misfit between synthetic and measured traveltimes should decrease from an initial smoothed velocity model to a more accurate one. We should underline that since the applications presented in this chapter come from GPR data, most of the references are also focused on GPR tomography, however, as we explained in chapter 1, our approach is free to be used in both physics EM and seismic, the reader is referred to chapter 3 for seismic applications at laboratory scale.

The synthetic traveltimes depend nonlinearly on the subsurface parameters, yielding a nonlinear optimization problem. Global optimization algorithms have been used for GPR tomography (Gloaguen et al., 2005; Giroux et al., 2007; Hunziker et al., 2017). They rely on a guided-random sampling of the model space to find the global minimum of the objective function. However, although several GPR studies adopt row-action methods such as simultaneous iterative reconstruction technique (SIRT) (Gilbert, 1972; Dines and Lytle, 1979) to invert crosshole first arrivals (Fullagar et al., 2000; Tronicke et al., 2001; Becht et al., 2004), in this study, we rely on local descent algorithms which have been also proposed for GPR tomography (Irving et al., 2007; Dafflon et al., 2011) as they take fewer iterations and need less expensive computations to converge. The problem is linearized around some background model and the minimum is found following the descent direction (gradient) of the objective function in an iterative manner. Fréchet derivatives, often estimated by combining an Eikonal solver with posterior ray tracings for different source-receiver pairs (Hanafy and Al Hagrey, 2005), are used in conjugate-gradient iteratives techniques such as the efficient least-squares QR factorization (LSQR) (Paige and Saunders, 1982) or CGLS (Scales, 1987). Conversely, when Eikonal approach is combined with the adjoint formulation, the gradient is directly estimated with a reduced complexity only related to the model dimension (Sei and Symes, 1994; Leung and Qian, 2006). Such a formulation is denoted matrix-free because we avoid the computation of Fréchet derivatives or sensitivity matrix which has a complexity as the product of the number of data by the number of parameters. Once the gradient is derived, optimization methods like the quasi-Newton l-BFGS method, which estimates the Hessian from previous gradient and model computations (Nocedal, 1980), can be used as long as the linearized optimization is valid. Besides, the Hessian favours consistent descent search when multiparameter reconstruction is require (Operto et al., 2013; Tavakoli F. et al., 2019).

Whether for seismic or electromagnetic waves, their propagation exhibits significant directional-dependent features, which may sometimes require taking into account the anisotropic nature of formations crossed by waves involved in the phase picking. For FATT, the perturbation technique of Jech and Pšenčík (1989) which assumes weak velocity anisotropy and initially applied in seismic by Chapman and Pratt (1992) and Pratt and Chapman (1992), was extended to GPR tomography by Vasco et al. (1997) who showed that the ray approach ignoring anisotropic effects may induce strong bias in velocity estimation when anisotropic effects exist while including them with decent smoothing and damping parameters in the inversion does not harm the inversion procedure when only isotropic effects exist. Recently, Waheed et al. (2016) and Tavakoli F. et al. (2019) have introduced efficient finite-difference schemes for computing both time and adjoint fields for vertical transverse isotropic (VTI) and tilted transverse isotropic (TTI) media, respectively. For Ground Penetrating Radar (GPR) data, Giroux and Gloaguen (2012) used ray-tracing in geostatistical tomography considering elliptical anisotropic media.

We propose to pursue these investigations on FATT in 2D anisotropic media by taking benefit of the recent work of Le Bouteiller et al. (2019) who have developed a highly efficient and very accurate traveltime computation approach in anisotropic media based on the fast-sweeping method and a discontinuous Galerkin-based (DG) Eikonal solver. This level of accuracy can be crucial when high contrasts are at stake. Moreover, Le Bouteiller (2018) has developed the related DG solver for the associated adjoint partial differential equation (PDE) needed to build the gradient of the traveltime misfit, opening the road to anisotropic traveltime tomography for large-contrast media. The challenge of multiparameter inversion for anisotropic models lies in the possible trade-off between parameters, the leakage depending on acquisition and model properties. In this first investigation, we restrict our analysis to an elliptical vertical transverse isotropic (EVTI) model.

The evaluation of capabilities and limits of our novel FATT approach is illustrated through synthetic anisotropic models inspired by a real GPR crosshole data set, which will be the real example being investigated in this work. The real example model has the originality to be crossed at depth by an underground gallery, which induces strong electromagnetic contrasts, generating weak diffraction events. This constitutes a challenge in terms of velocity reconstruction. The crosshole configuration leads to a specific illumination reduced to transmission-like angles. Our synthetic approach enables to study the effects generated by such illumination on anisotropic reconstruction. We also compared the efficiency and accuracy of two parametrization sets: *(i)* the vertical velocity V_v and the (equivalent) Thomsen parameter ϵ (equal to the other Thomsen parameter δ) (Thomsen, 1986) and *(ii)* the vertical velocity V_v and the horizontal velocity V_h. The same data exhibit different sensitivity kernels depending on these two parameter sets as it has been shown in FWI (Gholami et al., 2013a,b; Alkhalifah and Plessix, 2014; He and Plessix, 2017) and recently in slope tomography (Tavakoli F. et al., 2019), consequently each parametrization leads to different model reconstruction.

The nonuniqueness of the ill-posed problem can be mitigated by adding a regularization term in the misfit design. Tikhonov and Arsenin (1977) have proposed a regularization strategy to find a smooth solution able to explain the data. A stabilizing functional is added to the original misfit function to guide the solution to be close to some prior estimates of the model. We follow this approach to construct a prior model and a model weighting diagonal matrix since the location of the gallery and its dimensions are known. The results obtained on the synthetic data allowed us to identify the optimal approach for the processing of the real data, for this acquisition configuration and this environment. In particular, we could assess the effect of including anisotropy in our model reconstruction when compared with an isotropic formulation.

In this chapter, after considering methodological ingredients for modeling traveltimes and for estimating the misfit gradient through adjoint formulation, we present a synthetic analysis considering a realistic anisotropic model, which helps us to design a specific workflow introducing data weighting and model regularization. This workflow was then applied to a real crosshole dataset acquired in a carbonate environment.

2.1 Methodology

Most of the methodology shown in this section was introduced in chapter 1. To avoid redundancy, only the main equations are presented again except those that have not been addressed previously.

First-arrival traveltime tomography aims to reconstruct a velocity model $\mathbf{m}$ of the subsurface that minimizes the difference between observed t_{obs} and synthetic t_{syn} traveltimes for all available source-receivers couples N_{sr}. This non-linear problem can be written in a least-squares sense, with the misfit function $\mathcal{C}$ defined as

$$\mathcal{C}(\mathbf{m}) = \frac{1}{2}\sum_{sr}(t_{syn}(\mathbf{m}) - t_{obs})^2, \tag{2.1}$$

where the synthetic traveltimes $t_{syn}(\mathbf{m})$ non-linearly depend on the model $\mathbf{m}$ discretized by nodal parameters m_j reaching a total number N_m. Starting from an initial velocity model, the inversion proceeds iteratively by solving the Eikonal equation and by model parameter updating.

2.1.1 Computation of synthetic traveltimes based on Eikonal solver

The Eikonal equation is a non-linear PDE belonging to the general class of Hamilton-Jacobi equations. The first-arrival traveltime is provided by the viscosity solution for which existence and uniqueness have been established by Crandall and Lions (1983). This solution includes diffraction effects (Podvin and Lecomte, 1991) while ray-tracing solution does not (Cerveny, 1985). Accurate and efficient schemes have been recently designed for solving this non-linear PDE for anisotropic models (Cheng and Wang, 2014; Le Bouteiller et al., 2018) based on a discontinuous Galerkin method, which are more accurate and flexible than finite-difference schemes (Waheed et al., 2015b; Waheed and Alkhalifah, 2017). We consider, for both isotropic and anisotropic media, a general Hamiltonian formalism introducing a pseudo-time-dependent Hamilton-Jacobi evolution equation given by

$$\partial_\xi u(\mathbf{x}, \xi) + \mathcal{H}(\mathbf{x}, \nabla_\mathbf{x} u(\mathbf{x}, \xi)) = 0, \tag{2.2}$$

where the pseudo-time variable is denoted by the symbol ξ, the unknown field depending on space and pseudo-time by $u(\mathbf{x}, \xi)$ and where the Hamiltonian (Eikonal) is denoted by $\mathcal{H}(\mathbf{x}, \nabla_x u(\mathbf{x}, \xi))$. The stationary state of equation (2.2) provides the traveltime through $\lim_{\xi \to \infty} u(\mathbf{x}, \xi) = t_{syn}(\mathbf{x})$. Although Le Bouteiller et al. (2019) considered tilted orthorhombic anisotropy for traveltime computations, we remain in a 2D framework where the VTI Hamiltonian (chapter 1, equation 1.44) can be reduced by applying the elliptical approximation, thus the elliptical Eikonal $\mathcal{H}$ yields

$$\mathcal{H}_{\text{EVTI}}(\mathbf{x}, \nabla T) = A(\mathbf{x})T_{,x}^2 + B(\mathbf{x})T_{,z}^2 - 1, \tag{2.3}$$

where spatially dependent quantities A and B are defined by

$$\begin{cases} A(\mathbf{x}) = V_v^2(1 + 2\epsilon) = V_h^2, \\ B(\mathbf{x}) = V_v^2. \end{cases} \tag{2.4}$$

The Thomsen parameter ϵ proposed by Thomsen (1986) is identical to the Thomsen parameter δ in such elliptical anisotropy. The coefficients $A(\mathbf{x})$ and $B(\mathbf{x})$ describe the spatial variations of model properties with the chosen parametrization, and for the sake of brevity we omit the coordinate dependency of the anisotropic parameters on the right-hand side of equation 2.4.

2.1.2 Model update based on adjoint solver

Minimizing the misfit function can be performed using a linearized formulation and we focus our study on the Newton-based local optimization scheme which updates in an iterative manner the model $\mathbf{m}$ at iteration k:

$$\mathbf{m}_{k+1} = \mathbf{m}_k + \alpha_k \boldsymbol{\Delta}\mathbf{m}_k, \tag{2.5}$$

where the step length is denoted by the symbol α_k and the model update by $\boldsymbol{\Delta}\mathbf{m}$. The descent direction is obtained by solving the Newton system

$$H(\mathbf{m})\boldsymbol{\Delta}\mathbf{m} = -\boldsymbol{\gamma}(\mathbf{m}), \tag{2.6}$$

where the Hessian $H(\mathbf{m})$ of the misfit function is approximatively derived from the gradient of the misfit function $\boldsymbol{\gamma}(\mathbf{m}) = \boldsymbol{\nabla}\mathcal{C}$ estimated by the adjoint approach (Plessix, 2006). For a given parameter $p(\mathbf{x})$ of the model, the gradient is given by the expression

$$\nabla_{p(\mathbf{x})}\mathcal{C} = -\frac{1}{2}\sum_{s=1}^{N_s} \boldsymbol{\lambda}_s(\mathbf{x}) \frac{\partial \mathcal{H}(\mathbf{x}, \nabla T(\mathbf{x}))}{\partial p(\mathbf{x})}, \tag{2.7}$$

where the symbol $p(\mathbf{x})$ denotes either V_v or ϵ parameters for the first set of model parameters or V_v and V_h parameters for the second set. Only the number of sources N_s is now involved in the gradient estimation because the adjoint field $\boldsymbol{\lambda}_s$ integrates all receivers related to a given active source. The adjoint field is independent of the chosen parameter set and honors the linear transport equation

$$\boldsymbol{\nabla} \cdot (\boldsymbol{\lambda}_s(\mathbf{x})\boldsymbol{\mathcal{U}}) = -\sum_r (t_{syn}(\mathbf{m}) - t_{obs}), \tag{2.8}$$

where the group (ray) velocity $\boldsymbol{\mathcal{U}}$ is defined by

$$\boldsymbol{\mathcal{U}} = \frac{\partial \mathcal{H}}{\partial(\nabla T)}(\mathbf{x}) / \Big(\nabla T(\mathbf{x}) \cdot \frac{\partial \mathcal{H}}{\partial(\nabla T)}(\mathbf{x})\Big). \tag{2.9}$$

Let us remark that a rather simple finite-volume (FV) approach (equivalent to DG scheme with constant piece-wise interpolation) allows us to solve this linear transport equation (Le Bouteiller, 2018). Here the reduced gradient calculation is matrix-free meaning that the explicit building of the sensitivity matrix is not needed, reducing the complexity to the model dimension. It should be noted that, in such gradient estimation, the parameter p is only involved in the derivation of the analytical expression of the Eikonal equation (2.3), while the parameter selection impacts directly the discrete computation of the Fréchet derivatives through ray tracing. We should underline that although we do not trace rays to compute the traveltimes (forward problem), we will frequently use the word rays to explain different features of tomography such as acquisition, illumination and resolution. This is not a conflict since the group velocity vector who carries the energy flux of rays is part of the tomography workflow (equation (2.9)).

For the optimization, the quasi-Newton l-BFGS method (Nocedal, 1980) is implemented in a reverse-communication strategy using the SEISCOPE optimization toolbox (Métivier and Brossier, 2016). We choose to keep 15 previous models and gradients in our different numerical illustrations to approximate the inverse of the Hessian operator. Such a operator mitigates the potential leakage between parameter types and compensates for differences in the dimensions of the various parameters. However, normalization is often performed in order to avoid ambiguity coming from the units of the different parameter classes. In our case, normalization is applied for each parameter type by

$$p'(\mathbf{x}) = \frac{p - p_{min}}{p_{max} - p_{min}} \qquad 0 < p' < 1 \tag{2.10}$$

$$\frac{\partial \mathcal{H}(\mathbf{x}, \nabla T(\mathbf{x}))}{\partial p'(\mathbf{x})} = \frac{\partial \mathcal{H}(\mathbf{x}, \nabla T(\mathbf{x}))}{\partial p(\mathbf{x})}(p_{max} - p_{min}), \tag{2.11}$$

where p_{max} and p_{min} are the expected possible extreme values, and p' the new quantities that belong to the interval $[0, 1]$, regardless of the parameter type. The second expression being the Hamiltonian derivative obtained by chain rule. In order to speed up the convergence to the minimum, preconditioning is applied through a diagonal operator P, leading to the preconditioned Newton system

$$P(\mathbf{m})H(\mathbf{m})\boldsymbol{\Delta}\mathbf{m} = -P(\mathbf{m})\boldsymbol{\gamma}(\mathbf{m}). \tag{2.12}$$

This new operator $P(\mathbf{m})$ is simply the identity for each parameter type multiplied by a scaling factor for each parameter type, i.e. two values in our case involving only two parameter classes. This preconditioning accelerates the convergence but does not influence the final solution which is based on normalized quantities. One could iterate more without preconditioning and the same solution would come out. However, the absence of this operator will lead to a unstable inversion, namely, major update in one parameter than in the other due to the no balance between gradients, such a balance is needed to control the relative contribution of each parameter class. After obtaining the model update with the two normalized parameters, we can easily come back to the parameter p with equation (2.10) in order to perform the forward modeling on the correct parameter quantities. It is worth noting that this procedure is only required for the parametrization (V_v, ϵ), while it can be avoided in the second parametrization (V_v, V_h) since both belong to the same class.

Wavenumber content of the model reconstruction is implicitly controlled by the grid sampling, where the FV gradient needs to be projected. Consequently, as for any tomographic problem, one has to also control the expected spatial resolution depending on the data, the acquisition geometry, and the prior geological information by smoothing the raw data gradient before optimization. The concept behind smoothing, is to penalize the differences between neighboring points of the gradient, which as illustrated by Fomel and Claerbout (2003), it can provide faster convergence at early iterations by focusing on the low-wavenumbers of the expected model, something desired to respect the physics of FATT. Therefore, in our study, we convert the raw gradient into a smooth gradient with a Bessel filter designed with pre-defined vertical and horizontal coherent lengths (Hale, 2007; Wellington et al., 2017). For efficiency, Bessel smoothing is implemented by solving a related PDE (Trinh et al., 2017) rather than using an explicit convolution, for instance with a Gaussian function. The tail of Bessel function does not decrease too fast, while it provides flexibility for structure-oriented smoothing and is more efficient when 3D implementation is envisaged.

2.2 Evaluation of the tomographic approach using synthetic crosshole data

2.2.1 Sensitivity kernels

Similar than in section 1.2.2 where we illustrate the parameter sensitivity using a small Gaussian perturbation, we evaluate the relative sensitivity of the two discussed possible parametrizations by considering sensitivity kernels in a homogeneous anisotropic model case. They have been simultaneously drawn for three different receiver positions and for a single source. The model consists in a vertical velocity V_v of $80\,m/\mu s$ and a value of ϵ of 0.02. The crosshole acquisition configuration has been chosen to reproduce the synthetic and real data cases discussed hereafter: the two $52\,m$ deep boreholes are separated by $18\,m$ horizontally. Figure 2.1a shows three different raw adjoint fields computed for three source-receiver configurations representative of various illumination angles. These fields are independent of the parametrization choice as they are directly computed from the transport equation (2.8). Figure 2.1b shows the sensitivity kernel when the problem is restricted to an isotropic parametrization. Here, the gradient contribution is relatively identical in all directions as expected due to the nature of isotropic medium. Figure 2.2 shows sensitivity kernels for the two proposed anisotropic parametrizations : V_v (a) - ϵ (b) and V_v (c) - V_h (d). They only differ within the term of the derivative of the Hamiltonian. Looking at equation (2.4), one may notice that for parametrization (V_v,ϵ), the V_v parameter appears in both A and B coefficients. Consequently, for this parametrization set, the sensitivity kernel of V_v is dominant in both vertical and horizontal directions with a slightly major contribution on the horizontal direction due to the term $(1 + 2\epsilon)$ of A and not present on B, this sensitivity is somehow similar to the isotropic case (figure 2.1b). In contrast, the sensitivity of ϵ is mostly dominant along the horizontal paths, leading to a strong leakage between the two parameters when propagation is sub-horizontal, which is the dominant propagation when crosshole configuration is involved. Figures 2.2c-d show the different sensitivity kernels obtained considering the other parameter set (V_v, V_h). Here, the vertical velocity information is mainly controlled by vertical dominant propagation, while the anisotropic information is dominated from sub-horizontal propagation. There is almost no leakage between the two parameters, suggesting that this parameter set would be the most adapted to our crosshole acquisition configuration with dominant sub-horizontal propagation.

2.2.2 Synthetic analysis considering a realistic anisotropic model

In this section we propose to explore the performance of the code in the crosshole configuration using two synthetic models, and to present two important tools that have been added in our tomography workflow when real data are concerned. A pedagogical simple synthetic model consists in an EVTI model whose parameters are shown in figure 2.3a-d as the true models of (a) V_v, (b) ϵ, (c) V_h has been computed using the equation (2.4), while (d) is the percentage of anisotropy expressed as $R = [(V_h/V_v) - 1] \times 100$. The background value of ϵ being 0, we have the same V_v and V_h velocities as background, $80\,m/\mu\,s$. The target higher-velocity dip layer has a value of $100\,m/\mu s$ for V_v, 0.06 for ϵ and $105\,m/\mu s$ for V_h. Note that the vertical symmetry we have decided is somehow unrealistic since the anisotropy model should be tilted with the symmetry axis being normal to the high-velocity layer, however, as our first example, we remain on the vertical symmetry. The acquisition is designed considering the same number of sources and receiver as in our real dataset presented afterwards: 44 sources separated by 1 m are located inside a $52\,m$ deep well between elevations $528\,m$ and $571\,m$, while 200 receivers separated every $0.25\,m$ are located from $527\,m$ to $576.75\,m$, and the separation between bore-

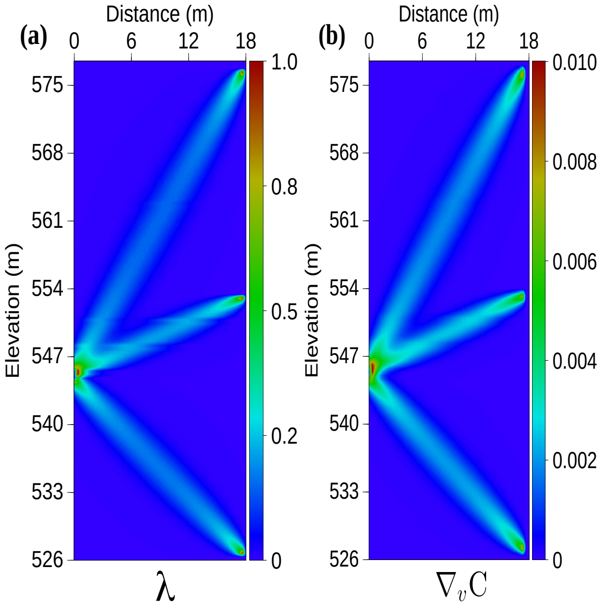

Figure 2.1: (a) Three different adjoint fields with different illumination samplings, and (b) related velocity gradient $\nabla_v \mathcal{C}$ under the isotropic assumption.

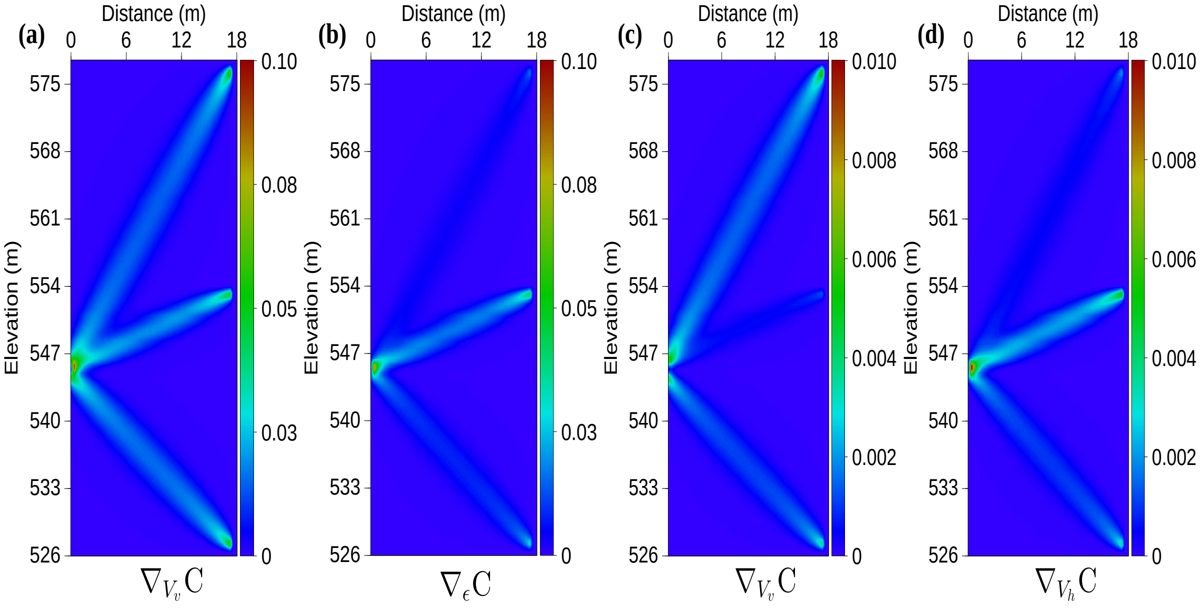

Figure 2.2: (a)-(b) Gradients $\nabla_{V_v}\mathcal{C}$ and $\nabla_\epsilon \mathcal{C}$ under the parametrization (V_v, ϵ). (c)-(d) Gradients $\nabla_{V_v}\mathcal{C}$ and $\nabla_{V_h}\mathcal{C}$ under the parametrization (V_v, V_h) which highlight a better decoupling between vertical and horizontal propagation paths.

holes is $18\,m$. We compute 6741 synthetic traveltimes by using a fine square DG discretization of 150 horizontal elements and 415 vertical elements with a uniform element edges of $dx = dz = 0.125\,m$.

Our second synthetic model is more realistic since it has been constructed considering isotropic full-waveform-inversion results obtained from the same real crosshole GPR data as those used hereafter (Pinard et al., 2016). We consequently designed a target model for vertical velocity V_v (figure 2.4a)

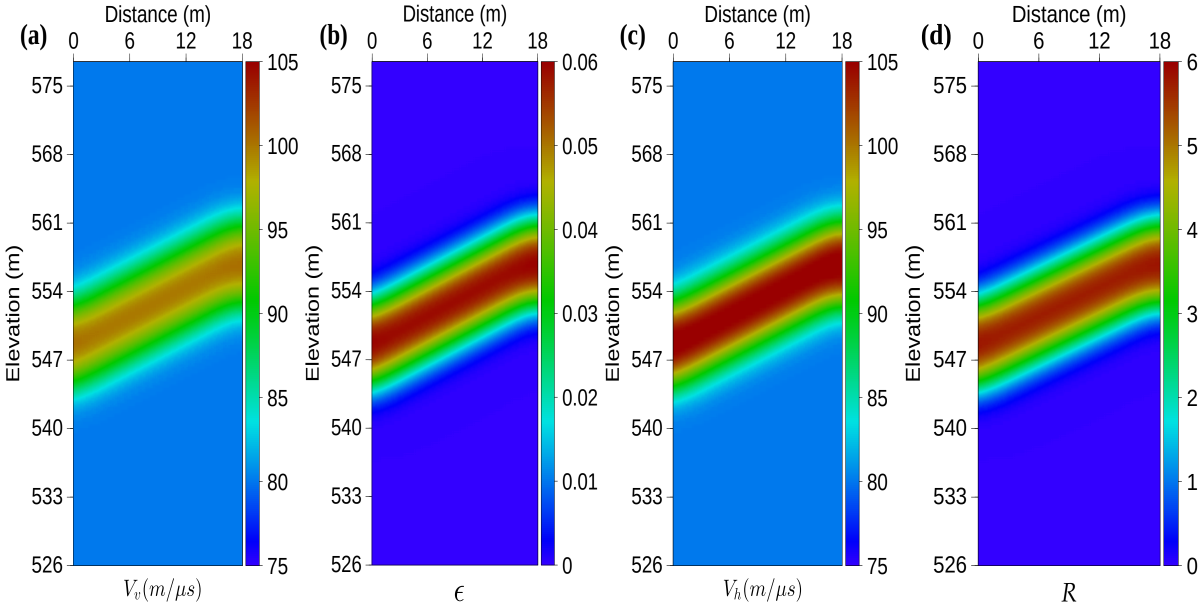

Figure 2.3: Synthetic model one for (a) V_v, (b) ϵ, and (c) V_h computed from V_v and ϵ using equation (2.4). (d) Percentage of anisotropy R based on the vertical and horizontal velocities.

and propose an EVTI model for the ϵ anisotropic parameter (figure 2.4b). The horizontal velocity V_h (figure. 2.4c) has been deduced using equation (2.4). We also show in figure 2.4d, the percentage of anisotropy R. Our second model can be decoupled into 3 different blocks: 1) over the first 30 meters (above $554\,m$ of elevation), a rather low-velocity compartment is characterized by a stratification slightly dipping to the right, with a small anisotropy; 2) from $538\,m$ to $554\,m$ of elevation, a larger velocity block marked by a more important anisotropy reaching $5\,\%$ in places and also by the presence of a localized 2-m wide gallery, the center of which being located at $544\,m$ of elevation and characterized by a very large isotropic velocity; 3) below $538\,m$ of elevation, a lower velocity compartment representing saturated layers, with almost no anisotropy. The source-receiver configuration is the same used than the one used in the first model, while the discretization for the computation of the observations is also equal to our first experiment. We should underline that the two synthetic models (figures 2.3-2.4) exhibit mainly low-wavenumber content and consequently are suitable for traveltime tomography

2.2.3 Data-weighting matrix

In tomography, the inverted traveltimes may contain errors coming from noise, instrument errors and picking uncertainties. Because least-squares optimization is sensitive to these outliers, a data-weighting matrix W_d is designed, giving the following data misfit function

$$\mathcal{C}(\mathbf{m}) = \frac{1}{2}\sum_{sr}({W_d}^{sr}(t_{syn}(\mathbf{m}) - t_{obs}))^2. \tag{2.13}$$

Such weight matrix is designed following the approach of Berryman (1989), which consists of assigning a smaller weight to longer wave-propagation paths. Advocated justifications are: *(i)* the smaller the offset between source-receiver is, the more certain the observation should be, since the signal-to-noise ratio is expected to be larger and *(ii)* shorter propagation paths are more likely to correspond

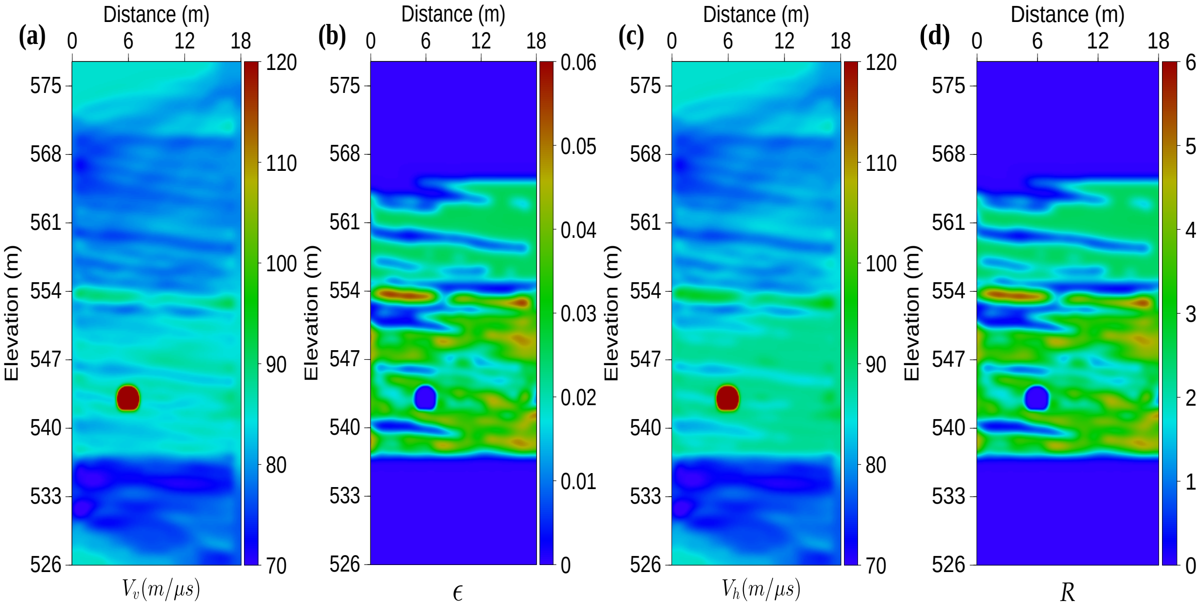

Figure 2.4: Synthetic realistic model two for (a) V_v, (b) ϵ with the presence of a localized high-velocity isotropic anomaly. (c) V_h computed from V_v and ϵ using equation (2.4). (d) Percentage of anisotropy R based on the vertical and horizontal velocities.

to real paths that remain completely in the image plane when two-dimensional reconstruction is concerned. The data weighting is defined in terms of the offset between source-receiver as

$$W_d = \begin{cases} 1, & \text{for } d \leq d_a, \\ 1 - (d - d_a)/(d_b - d_a), & \text{for } d_a < d < d_b, \\ 0, & \text{for } d \geq d_b \end{cases} \tag{2.14}$$

where the distance between source-receiver pair is denoted by the symbol d. The choice of parametric values d_a and d_b is user-dependent (figure 2.5). It can be empirically based on try and error tests performed to derive a balance between what is geological realistic while keeping the range of illumination angle broad enough.

2.2.4 Prior model information

To overcome non-uniqueness of solutions of this ill-posed inverse problem, a regularization term is often incorporated in the original misfit function. Following Tikhonov and Arsenin (1977), the regularized misfit function may be defined as

$$\mathcal{C}(\mathbf{m}) = \frac{1}{2}\sum_{sr}({W_d}^{sr}(t_{syn}(\mathbf{m}) - t_{obs}))^2 + \frac{1}{2}\eta\sum_{j}({W_m}^{j}(\mathbf{m}_j - \mathbf{m}_j^p))^2, \tag{2.15}$$

where the second term, the prior model norm, estimates residuals between the current model at a given iteration and a prior model $\mathbf{m}^p$ considered at the same iteration. The classical Tikhonov term based on requiring a smooth spatial model gradient (roughening operator) can be replaced by the Bessel smoothing with no mathematical conflicts since both are equivalent (Fomel and Claerbout, 2003). The

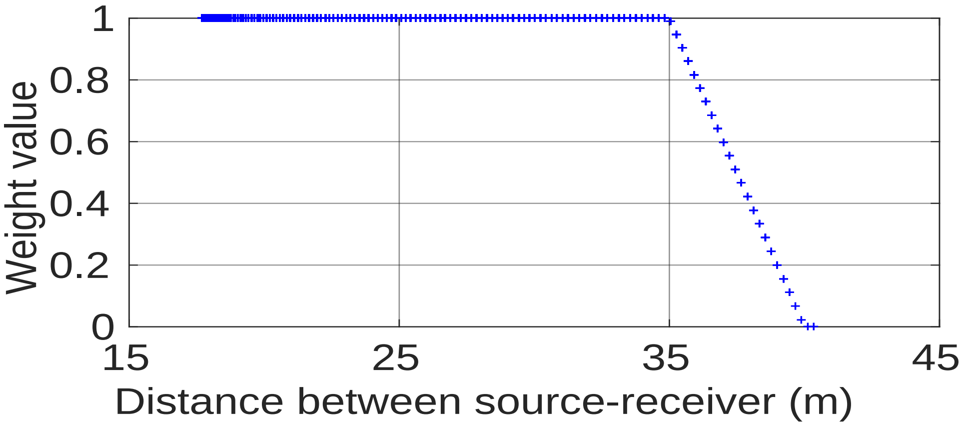

Figure 2.5: Weight data values as a function of the source-receiver distance (m). The weights for offsets higher than $35\,m$ are linearly decreased.

hyperparameter η is a small positive scalar damping parameter: large values of η increasing the need of satisfying this constrain rather than satisfying the data misfit. The choice of η is based on the ratio between the model term and the data term as stated by Asnaashari et al. (2013). We adjust η so that this ratio is lower than one, guaranteeing a larger contribution of data. The matrix W_m is a weighting operator applying on the model space. The hyperparameter scales also the model weighting matrix which can be chosen in the range of $[0, 1]$. Following Asnaashari et al. (2013), we select a diagonal W_m matrix, which is the inverse of the prior model uncertainty estimation. We should recall that in our realistic synthetic model and the real experiment a gallery is present, since the location and dimensions of the gallery are known, we could construct a prior model, depicted in figure 2.6a, where the velocity in the gallery is gently smoothed and a maximum value of 277 m/μs is reached. The use of an abrupt and high homogeneous value in the gallery would have introduced artefacts in the area surrounding the gallery due to the resolution limitations of tomography. Moreover, the model contribution should be important inside the gallery leading to the highest weighting value $W_m = 1$ (figure 2.6b). Around the gallery, a rapid decrease accounts for the absence of information about the material used for its construction until a value $W_m = 0$ everywhere else is reached, leading to a reconstruction mainly driven by the data contribution. Similar to the prior velocity model, W_m is smoothed on the gallery location. Such ingredients allow us to drive the optimization towards the expected gallery in the model space. Besides, before starting the optimization, a scaling factor is multiplied by the total misfit (equation (2.15)) and consequently by the gradient as well, the parameter β being defined as

$$\beta = \frac{|\mathbf{m}^0|}{|\gamma^0|} = \frac{\sqrt{\sum_j \left(\mathbf{m}_j^0\right)^2}}{\sqrt{\sum_j \left(\gamma_j^0\right)^2}}, \tag{2.16}$$

where $\mathbf{m}^0$ and γ^0 are the initial model and the gradient computed in such a model, respectively. Therefore, the misfit and the gradient become

$$\mathcal{C}' = \beta\mathcal{C} \quad \text{and} \quad \nabla\mathcal{C}' = \beta\nabla\mathcal{C}. \tag{2.17}$$

The role of this scaling parameter is to handle the units of the updated model $\mathbf{\Delta m}$. For instance, at the first iteration $k = 1$, there are no previous gradients, and the steepest descent method is used to compute the model increment given by $\mathbf{\Delta m} = -\nabla\mathcal{C}$. The introduction of β will guarantee the correct units of the updated model. Note that we have done the normalization by the expected possible extreme values in parametrization (V_v, ϵ), and we have used β in the parametrization (V_v, V_h).

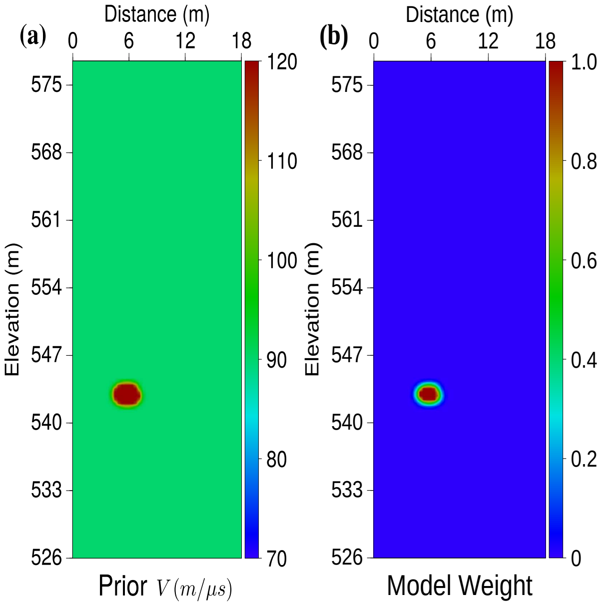

Figure 2.6: (a) Prior model based on the location and diameter of the gallery, defined with a velocity of $300\,m/\mu s$. (b) Weight model values used for the regularized inversion: prior model contribution is applied only on the gallery.

2.2.5 Inversion results on the synthetic dataset

In the following, unless otherwise stated, we use the same discretization for the forward modeling and the inversion grid, namely #DG elements=$(Nx - 1)(Nz - 1)$ where Nx and Nz are the number of nodes in each direction of the inversion grid, while we always use the same grid spacing in both direction $dx = dz$. For the two tested different parametrization and the two synthetic models, the same discretization was used with 52 horizontal nodes and 139 vertical nodes and a grid spacing of $0.375\,m$ in both directions. This sampling will provide a fair discretization of the target model while suppressing partially the inverse crime (Wirgin, 2004; Kaipio and Somersalo, 2007), since the discretization used to simulate the recorded data (section 2.2.2) is not the same used for the computation of the predicted data in the inversion process. In the gradient of each iteration, correlation lengths of the smoothing operator are slightly increased at source locations in order to remove the signature coming from the adjoint field (section 1.2.2). Conversely, the lengths are gently decreased in the rest of the domain to favour the fitting of the data. In our workflow, we propose to use our isotropic code to design a suitable initial model for the anisotropic inversion, although there is no noise or picking uncertainty in our simulated data, which can be tackled with the data-weighting matrix approach.

It is worth mentioning that in crosshole experiments there is always a cross-shaped pattern in the results caused by the acquisition configuration, however, the data matrix can be used in the isotropic part to partially suppress this pattern and design an appropriate initial model for anisotropy. A similar strategy is suggested by Becht et al. (2004) in GPR crosshole isotropic tomography by using different data subsets according to the transmitter-receiver angle in order to design a suitable initial model for the final inversion. We start the analysis with the high-velocity layer model (figure 2.3), and found that 4 iterations were sufficient to design an initial model. Figure 2.7a shows the model when the data-weighting matrix is avoided, characterized by the strong cross-shaped pattern as well as certain smearing on the borehole location. After different trials looking for a good compromise between the geological representation of structures and attenuation of artefacts, the values $d_a = 25\,m$ and $d_b = 30\,m$ are chosen as suitable parameters. Figure 2.7b shows the corresponding result where the target structures has a higher velocity, due to the suppression of the large paths which are sensitive to the target V_v (figure 2.3a), while the near-horizontal paths are sensitive to the target ϵ (figure 2.3b). Although the model of figure 2.7b seems to be a fair model which shows the main target, we found better results using a smoothed version (figure 2.7c), as over-fitted results coming from the incorrect isotropic assumption are avoided. Such a strategy has been proposed for anisotropic FWI as well (Operto et al., 2009; Gholami et al., 2013a; Hadden et al., 2019). We should underline that the initial model of figure 2.7c will be used for V_v and imposing $\epsilon = 0$ as the initial model in parametrization (V_v, ϵ), and it will be used for V_v and the same for V_h in parametrization (V_v, V_h). Moreover, since the resolution of V_v is mainly driven by large offsets in (V_v, V_h), we do not consider the data weights in any of the two parametrization in order to have a fair comparison between them. We performed 15 iterations with the anisotropic code enough to evaluate the efficiency of both parametrization.

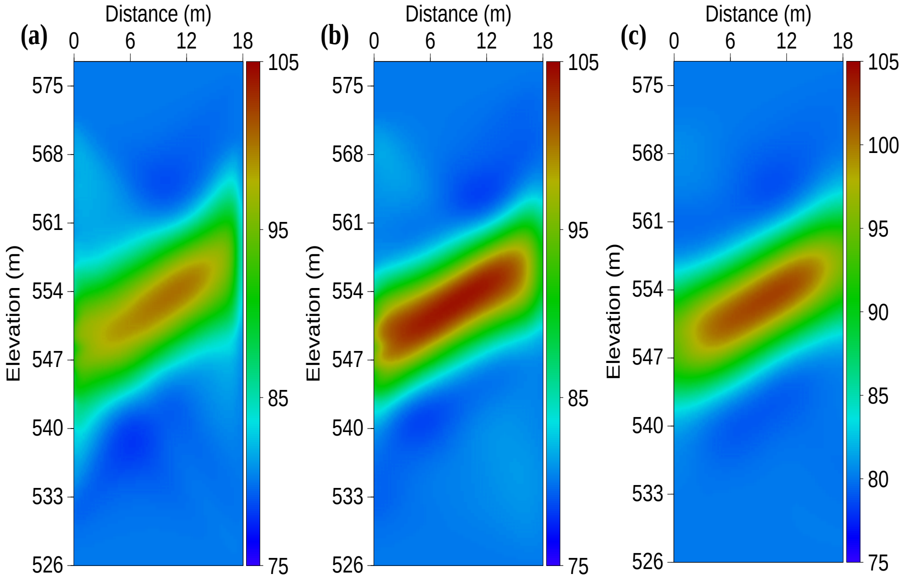

Figure 2.7: Isotropic inversion ($\epsilon = \delta = 0$) of an anisotropic dataset created from the target model of figure 2.3, 4 iterations are performed. (a) Velocity if we do not use the data-weighting matrix. (b) We find $d_a = 25\,m$ and $d_b = 30\,m$ as suitable parameters of the data matrix. (b) Smoothed version of (a) and being used as an initial model for the anisotropic inversion of both parametrizations.

For the first parametrization (V_v, ϵ), after testing different combinations of scaling factors in order to reach a balance between gradients, figure 2.8a shows the result for V_v. One can see that the shape of the high-velocity layer is thicker and the velocity slightly over estimated than the true model (figure 2.3a), because the influence of the second parameter ϵ is inducing this increment (leakage). Such an increment, similar to the one observed in the isotropic result (figure 2.7b), can be understood recalling the sensitivity kernel analysis presented in figures 2.1b and 2.2a where we show that the isotropic approach and V_v exhibit very similar sensitivity patterns. Hence, one can expect to have similar results considering an isotropic inversion using an anisotropic dataset and the obtained V_v with this parametrization. At the same time, the anisotropy ϵ (figure 2.8b) cannot reach the high true values in the high-velocity layer, again because of this leakage. The poor reconstruction of ϵ does not allow us to reach the correct values of percentage (figure 2.8d), we see mostly values around 3-4% while the true value is about 6% (figure 2.3d), in addition, we obtain an RMS$= 1.49 \times 10^{-4}\,\mu s$ at the end of this inversion.

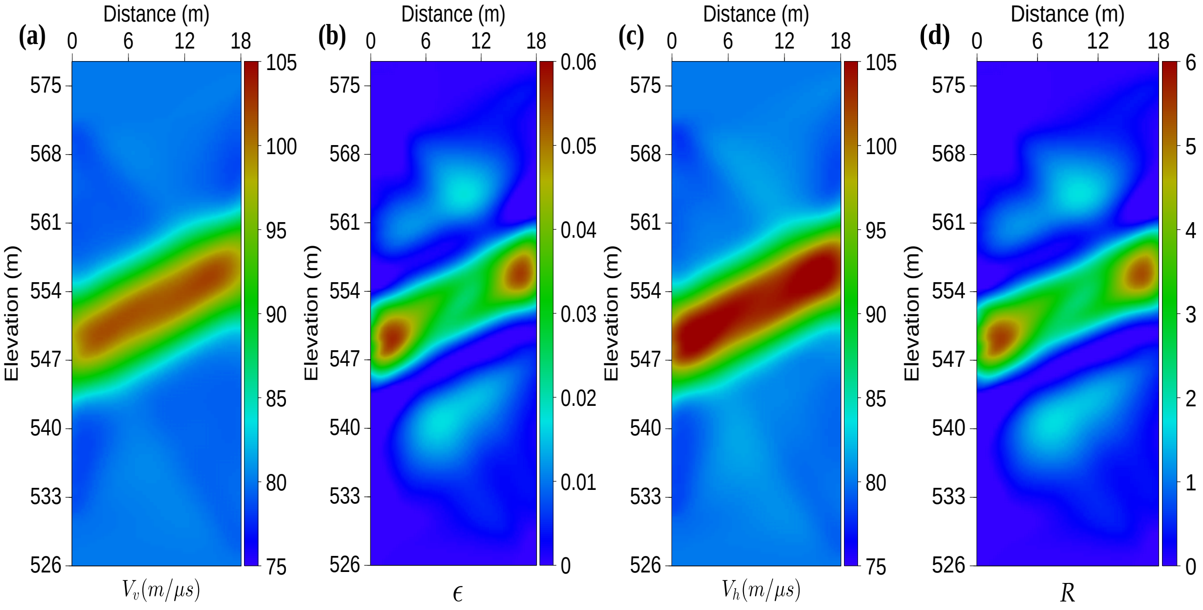

Figure 2.8: Inversion results of synthetic model one with parametrization (V_v, ϵ). (a) V_v and (b) ϵ inverted models, (c) Deduced V_h model using equation (2.4), and (d) Percentage of anisotropy R based on the vertical and horizontal velocities.

Regarding the second parametrization (V_v, V_h), when looking at figure 2.9a which shows the inverted V_v, one can see similarities between figure 2.8a and figure 2.9a. However, in the high-velocity layer, V_v reach values around 100 m/μs and the thick is closer to the true model (figure 2.3a). Figure 2.9c shows the inverted V_h, which reach the higher values of 105 m/μs and the shape close to the true model (figure 2.3b). Using these two velocity models, we compute ϵ in figure 2.9b, where the cross-shaped pattern is certainly coming from the inverted V_v. We should recall that in tomography horizontal rays best resolve the velocity variations perpendicular to the ray direction (Fawcett and Clayton, 1984), for this reason, horizontal-like layers are well resolved by crosshole traveltime tomography, a mathematical foundation of this idea is given by the projection-slice theorem (Bracewell, 1990): tilted rays reconstruct layers tilted at the same angle. Since V_v has the sensitivity on near-vertical propagation paths, the rays going from the transmitter around $561 - 568\,m$ elevation to the receivers at the bottom are perpendicular to the high-velocity layer, namely the rays are parallel to the variation of velocity producing the artefacts, while the signature of the rays from the transmitters at the bottom to the receivers at the top is less pronounced since the structure is tilted about the same direction of the rays, note that this cross-pattern is also present with the first parametrization (V_v, ϵ), in both cases, one may consider to use the data-weighting matrix to attenuate this pattern, at the expense of reducing even more the resolution of V_v mainly in the second parametrization (V_v, V_h), therefore we do not consider this as a good strategy. Another artefact being present in both parametrizations is the lower estimation of values in ϵ particularly around the target (figure 2.8 and 2.9). This is also coming from the acquisition because all the information is focused on the high-velocity layer which causes resolution gaps, i.e., less coverage above and below the target zone. However, the lower estimated values of ϵ reach a minimum value of -0.01 which is close to the true value being 0 outside the target (figure 2.3b). In spite of the acquisition limitations, the deduced ϵ in figure 2.9b exhibits the correct values for the target model (figure 2.3b), due to the nice decoupling between the parameters V_v and V_h during the optimization, and consequently the percentage of anisotropy (figure 2.9d) reaches the correct values around 6%, with an RMS= $1.28 \times 10^{-4}\,\mu s$. This synthetic analysis demonstrates that the correct values of anisotropy are reached with the second parametrization (V_v, V_h). This simple example illustrates well the statement derived from the sensitivity kernel analysis (figure 2.2).

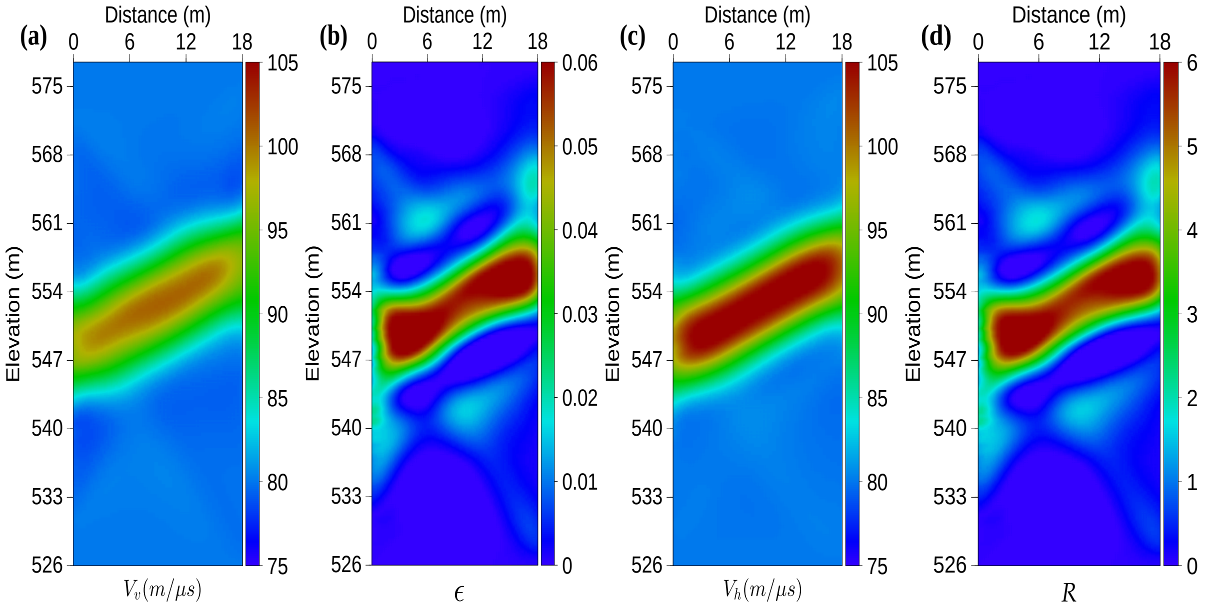

Figure 2.9: Inversion results of synthetic model one with parametrization (V_v, V_h). (a) V_v, (b) ϵ model deduced from (c) the inverted V_h by using equation (2.4), and (d) Percentage of anisotropy R based on the vertical and horizontal velocities.

The second realistic synthetic model where a gallery is included (figure 2.4), it is tackled with the strategy of designing a suitable initial model by using the isotropic code. The parameters for the data-weighting matrix are estimated as $d_a = 35\,m$ and $d_b = 40\,m$. Subsequently, we assess the efficiency of the regularization, by performing 10 iterations. Figure 2.10a shows the velocity distribution obtained without any prior model. Although the smooth results are quite consistent with the expected synthetic model, the large velocity gallery spreads laterally which is expected due to the acquisition that mostly accounts for horizontal paths, the maximum value in the gallery being 123 m/μs, far from the true value. Figure 2.10b clearly shows that the velocity model is better recovered when regularization is added, the shape of the gallery being better recovered with a velocity of 277 m/μs, however, the presence of cross pattern nearby the gallery will imprint incorrect values in the final anisotropy model. After evaluating different initial models, we found that after 5 iterations of the isotropic inversion, the result is largely smooth (figure 2.10c), it removes most of the artefacts near the gallery while its low-wavenumber content does not illustrate probable isotropic errors that might be present in the result after 10 iterations (figure 2.10b). This strategy of stopping at earlier iterations is analogous to take a model of latter iterations and then apply the smoothing operator, in both cases the aim is to find a smooth initial model for anisotropy. As we did in the first synthetic inversion, in both parametrization we start the anisotropic inversion from the isotropic case, namely $\epsilon = 0$ or $V_v = V_h$, data-weighting matrix is not considered and 15 iterations are performed.

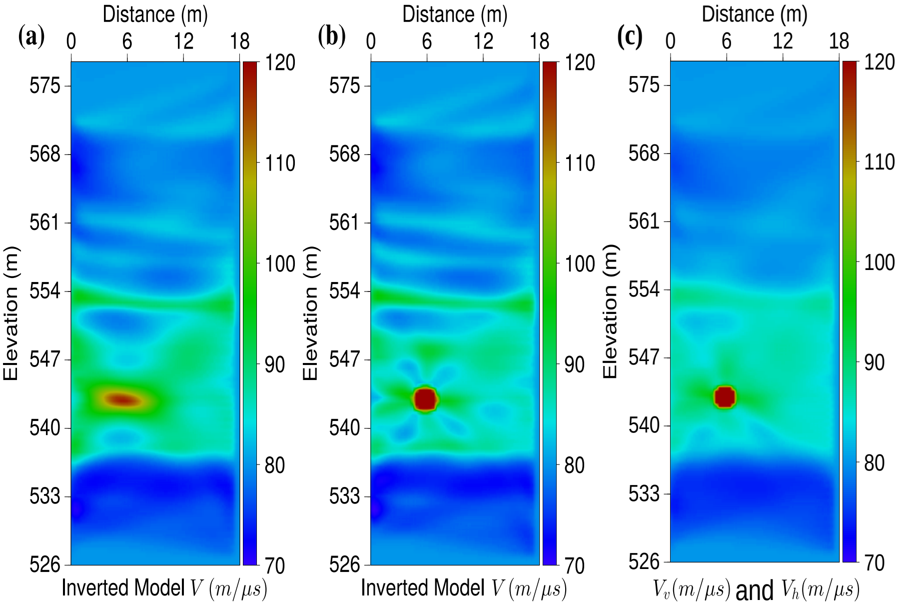

Figure 2.10: Isotropic inversion ($\epsilon = \delta = 0$) of an anisotropic dataset created from the target model of figure 2.4, 10 iterations are performed, while $d_a = 35\,m$ and $d_b = 40\,m$ are used in the data-weighting matrix. Inverted velocity without (a) and with (b) regularization. (c) Inverted velocity after 5 iterations being largely smooth and suitable as an initial model for the anisotropic inversion.

Figure 2.11 shows results using the parametrization set (V_v, ϵ) after a proper scaling whose parameters are different from the first synthetic result (figure 2.8) since scaling investigation is problem-dependent. Although the resolution of the vertical velocity has been improved as well as its amplitude, the final model obtained for the parameter ϵ shows a weak improvement (figure 2.11b). This is a consequence of the fact that the update of ϵ is mainly driven by V_v because of the strong leakage existing between parameters (figure 2.2a-b). Furthermore, figure 2.11a shows similar patterns to figure 2.10b obtained for the isotropic approach: the update of V_v is made in all directions using this parametrization. Finally, the poor reconstruction of ϵ produces a very similar V_h (figure 2.11c) model as V_v (figure 2.11a) thus generating very weak percentages of anisotropy (figure 2.11d) compared to those of the target model (figure 2.4d), while a fitting of RMS= $4.9 \times 10^{-4}\,\mu s$ is reached.

Figure 2.12 shows results obtained using the parametrization set (V_v, V_h). The parameter V_v is barely improved, mainly due to the weak illumination coming from subvertical propagation paths. The final model obtained for V_h seems to show an improvement in terms of resolution compared with the target (figure 2.4c). The Thomsen parameter is computed with the inverted velocities showing a better result (figure 2.12b), we can reach values about 0.05 and the pattern is consistent to that presented in the target (figure 2.4b). The artefacts appearing in the top and the bottom parts are located in zones with poor illumination, this is caused because while V_h is being updated, the other velocity V_v is not due to the absent of near-vertical paths on these zones, consequently it leads to erroneous reconstruction of anisotropy. The final models for parameters V_v and V_h are used to compute the percentage of anisotropy

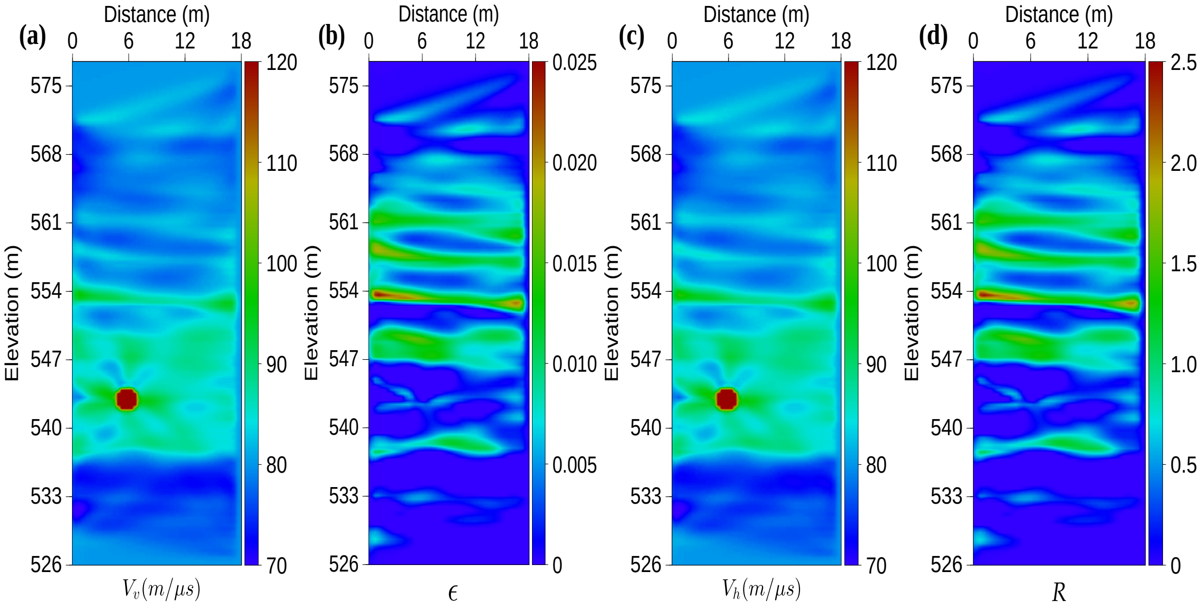

Figure 2.11: Inversion results of synthetic model two with parametrization (V_v, ϵ). (a) V_v and (b) ϵ inverted models, (c) Deduced V_h model using equation (2.4), and (d) Percentage of anisotropy R based on the vertical and horizontal velocities.

R (figure 2.12d). Since the decoupling is better with this parametrization (figure 2.2c-d), the update of one parameter does not influence too much the other, thus leading to the higher expected values of 6% proposed in the target model (figure 2.4d). It must be noted that the results provided by the two parametrizations, both show bad reconstructions around the gallery, a region characterized by large and abrupt velocity and anisotropy contrasts that tomography cannot resolve, we see values close to zero (figures 2.11d and 2.12d), however, the cross pattern located on the gallery in V_v and V_h with the first parametrization (figures 2.11a and 2.11c) is well suppressed with the second parametrization (figures 2.12a and 2.12c). This inversion result is accompanied by a fitting of RMS= $3.0 \times 10^{-4}\,\mu s$ which is slightly lower than with the first parametrization.

The synthetic tests demonstrate that we have a better recovery of anisotropy parameters when the parametrization set V_v and V_h is considered, and when a suitable initial model for V_v (injected also as the initial horizontal velocity) is deduced from an isotropic approach. This step is substantially important due to the angular limitation of the crosshole acquisition which makes challenging the update of V_v, however, in the presence of a full-illumination dataset, the isotropic inversion might be avoided (chapters 3 and 4). Another complexity with parametrization (V_v, ϵ) is to find suitable scaling factors, which is not straightforward and is problem-dependent, i.e., the values found in the first synthetic test are not the same values obtained the second test. The use of (V_v, V_h) avoids that since both parameters have the same dimensionality.

It is worth mentioning that for parametrization (V_v, ϵ), Gholami et al. (2013b) suggest a monoparameter inversion due to the significant trade-off between velocity parameter and the Thomsen parameter. It can be suitable if an accurate background model for the Thomsen parameter is available (Plessix and Cao, 2011). Although these works were applied to FWI, their conclusions are consistent with our analysis: if a good estimation of ϵ is possible, we may fix it and invert only V_v, the result will be satisfactory due to its isotropic-like pattern (figure 2.2a). However, in practice, it is not straightforward to

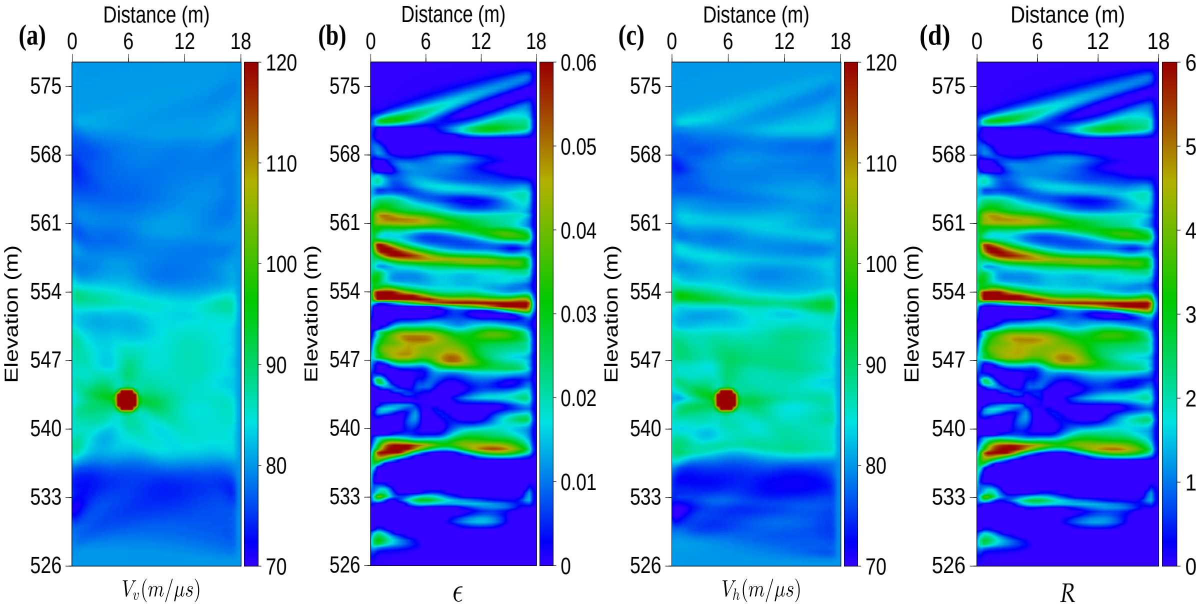

Figure 2.12: Inversion results of synthetic model two with parametrization (V_v, V_h). (a) V_v, (b) ϵ model deduced from (c) the inverted V_h by using equation (2.4), and (d) Percentage of anisotropy R based on the vertical and horizontal velocities.

guarantee a good estimation of ϵ and errors may arise in the inverted V_v if ϵ is wrong. We therefore propose a more realistic approach by inverting the two parameters simultaneously and by starting from the isotropic model. One may underline that thanks to this synthetic analysis, a specific workflow has been designed by tuning data weighting, prior model and initial model for anisotropic reconstruction. Algorithm 2.1 summarizes the anisotropic tomography workflow.

Algorithm 2.1 Matrix-free elliptical-anisotropy tomography workflow for parametrization (V_v, V_h). The model parameters m, the misfit function $\mathcal{C}$ and its gradient $\nabla\mathcal{C}$ are indexed by the iteration number *k*.

```
Use of smoothed isotropic velocity result as an initial model for $V_v$ and $V_h$
Define $W_d$
if Prior information is available then
    Define $\mathbf{m}^p$ and $W_m$
for k=1 to N do
    Compute synthetics on $\mathbf{m}_{k-1}$ $\rightarrow$DG solver
    Calculate the cost function $\mathcal{C}_{k-1} \rightarrow W_d$ is applied. Prior term is considered if it exists
    Compute adjoint field $\lambda(\mathbf{x}) \rightarrow$ FV approach
    Compute the gradients for optimization parameters $\nabla\mathcal{C}_{k-1} \rightarrow$ FV approach
    Smooth $\nabla\mathcal{C}_{k-1} \rightarrow$ Bessel filter
    When $k = 1$, the constant parameter $\beta$ is computed
    Multiply $\beta$ by $\mathcal{C}_{k-1}$ and $\nabla\mathcal{C}_{k-1}$
    call L-BFGS($\mathbf{m}_{k-1}, \mathcal{C}_{k-1}, \nabla\mathcal{C}_{k-1}$)
        $\mathbf{m}_k = \mathbf{m}_{k-1} + \Delta\mathbf{m}_{k-1}$
```

2.3 Anisotropic tomography inversion on a real dataset acquired in carbonates

Based on the synthetic analysis, the parametrization set (V_v,V_h) is selected to perform an anisotropic traveltime tomography on a real crosshole GPR dataset. It was acquired within the Laboratoire Souterrain à Bas Bruit (LSBB) research facilities, which are located within an Urgonian karstic limestone formation in the south of France. As displayed in figure 2.13, the site is equipped with a triangle of three 52-m deep boreholes (F4 to F6). An underground 2-m diameter gallery, whose surface projection is represented with the red dashed line on figure 2.13, is present at a depth of $34\,m$ and constitutes a large electromagnetic contrast. In December 2014, crosshole GPR data were acquired between boreholes F5 and F6 ($17.7\,m$ apart) using 100 MHz borehole antennas of Malå Geosciences. The first 6 meters of the boreholes are not useful for GPR studies due to the presence of metal casing. The global acquisition comprises 44 sources distributed every $1\,m$ in borehole F5 emitting signals recorded by 200 receivers $0.25\,m$ apart located in borehole F6. The source excitation time t_0 is estimated only once before the borehole acquisition, thanks to an air calibration recording. The water table was measured at an average elevation of $537\,m$ on the day of the experiment.

The large contrast induced by the gallery is one of the specificities of the field site. It induces scattering and consequently large first-arrival time variations, as illustrated in figure 2.14a-b displaying two shot gathers for sources located at an elevation of $560\,m$ and $537\,m$, respectively. Pre-processing techniques such as time zero correction, a zero-phase band-pass filter and time amplification have been applied. Figure 2.14a shows a radargram mainly dominated by the direct first arrival exhibiting a satisfying signal to noise ratio, excepted in the lower part (far offsets). On the contrary, figure 2.14b shows a weak diffraction pattern arriving before the main direct arrival on receivers between $540\,m$ and $560\,m$. At far offsets, the picking of this phase becomes more uncertain due to weaker signal to noise ratios. The large amount of source-receiver couples associated to the good signal to noise ratio allows

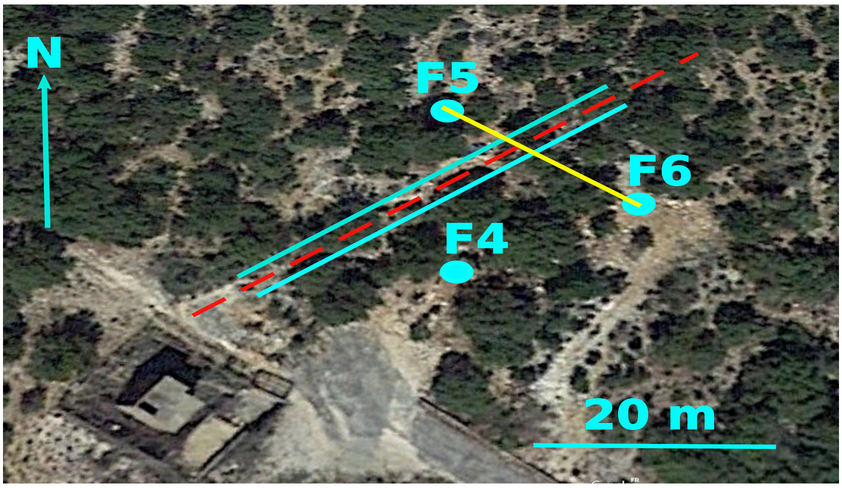

Figure 2.13: The Rustrel triangle borehole configuration. The dashed red line represents the surface projection of the $37\,m$ deep gallery. Our analysis is performed on the dataset acquired between boreholes F5 and F6.

us to pick 6741 first-arrival traveltimes, as displayed on figure 2.15a, which exhibit large variations according to the source-receiver offsets. This dataset is also characterized by the presence of lower traveltimes nearby the location of the gallery. From the dataset, we select the horizontal paths when source and receiver are located at the sale elevation, namely we have 44 traveltimes, and since we know the separation between wells, we can compute a preliminary velocity. A graphical display of the distribution and symmetry of the 44 values can be obtained with a box plot, one may see in figure 2.15b the different velocities, where outliers associated with wrong picking have not been found, and the mean value being $82.37\,m/\mu s$. The velocity information along with the frequency of the antenna allows us to compute the wavelength of the signal being 0.75-0.95 m. We should underline that Eikonal equation is a high-frequency approximation of the wave equation, consequently FATT is only valid if spatial variations in velocity occur over length scales larger than the wavelength, since the separation between boreholes is $17.7\,m$, we have about 18-23 wavelengths that can justify the high-frequency approximation. Moreover, Williamson (1991) demonstrate that the smallest feature that can be expected to be recovered is of the order of the width of the first Fresnel zone radius, given by $\sqrt{\lambda L}$ where L denotes the source-receiver offset and λ the wavelength. This information is crucial when we decide the discretization of the inversion grid, we have tested different grid spacing to find the best compromise between spatial resolution and reliable representation of the velocity structure, we concluded that a grid spacing of $dx = dz = 0.375\,m$ is fine enough to delineate the shape and position of heterogeneities and coarse enough to remain inside the low-wavenumber framework with $Nx = 52$ and $Nz = 139$ being the number of nodes in each direction. Besides, a coarse discretization is particularly important when more than one parameter is inverted because the number of unknowns increase and make the inversion less determined with the danger that many more models can almost satisfy the same data, consequently a very fine discretization in the inversion grid is certainly not a good strategy. Regarding the discretization for the forward modeling at each iteration, Eikonal finite-different solvers suggest to apply a refinement factor to the inversion grid to decide the forward discretization (Zelt and Barton, 1998; Latorre et al., 2004), however, after different tests, we found suitable to use the same grid spacing on the DG spacing which leads to square elements with $dx = dz = 0.375\,m$ being the edges of each element. We have to bear in mind that P^1 approximation with three degrees of freedom is used in each

DG element to describe the solution, consequently $\mathrm{DG}_{ndof} = (Nx - 1) \times (Nz - 1) \times 3$ is the correct estimation of the total number of degrees of freedom when traveltimes are computed, thus we found $\mathrm{DG}_{ndof} = 21114$ fine enough to handle the velocity contrasts and diffraction events induced by the gallery. We have evaluated a finer discretization for the forward modeling and the improvement in the error as well as in the imaging of the structures were not representative. The same analysis needs to be done in other datasets always considering the coarse discretization property required by FATT in the inversion and a DG fine discretization useful to guarantee a high accuracy on the synthetic traveltimes.

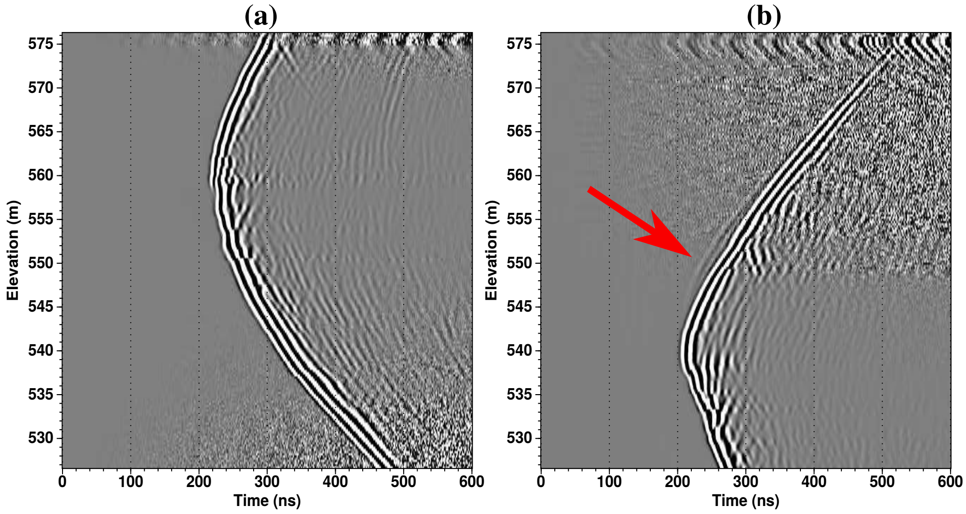

Figure 2.14: Examples of two radargrams obtained after time zero corrections, band-pass filter and time amplification when the source is located at elevations of $560\,m$ (a) and $537\,m$ (b). Red arrow highlights the weak diffraction pattern in (b).

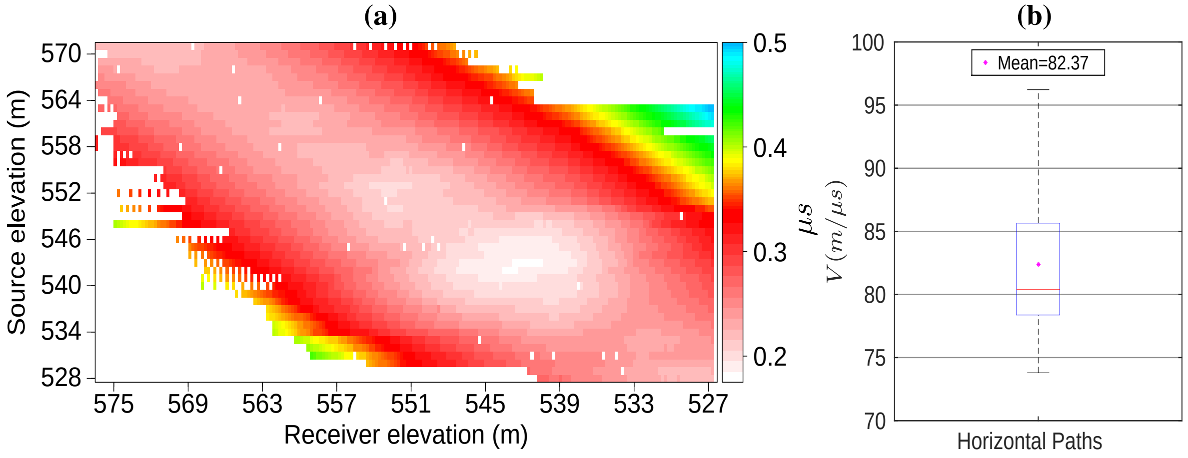

Figure 2.15: (a) Distribution of the 6741 picked first-arrival traveltimes as a function of source-receiver elevations. Note the effect of the gallery at a depth of 543 m, which is highlighted by a zone of low traveltimes. Traveltimes values when source and receiver are located at the same elevation ($17.7\,m$ offset) are extracted from (a) to compute (b) boxplot of velocities, we therefore have 44 values and a mean velocity of $82.37\,m/\mu s$.

The picking was further analyzed considering a double difference analysis (figure 2.16), where traveltimes of each source are subtracted from the traveltimes of the nearest source, starting from the deepest source. figure 2.16a shows the double-difference of the real picked dataset, while figure 2.16b shows the double-difference of synthetic traveltimes obtained using the isotropic velocity model of figure 2.4a. Both figures show large double-difference variations with the same global pattern. The values at far offsets are mostly the same being $\pm 5 \times 10^{-3} \mu s$ to $\pm 10 \times 10^{-3} \mu s$, with few exceptions visible. As expected, the real picked dataset appears rougher, mainly due to uncertainties in the pickings, particularly when the diffraction at the gallery is involved.

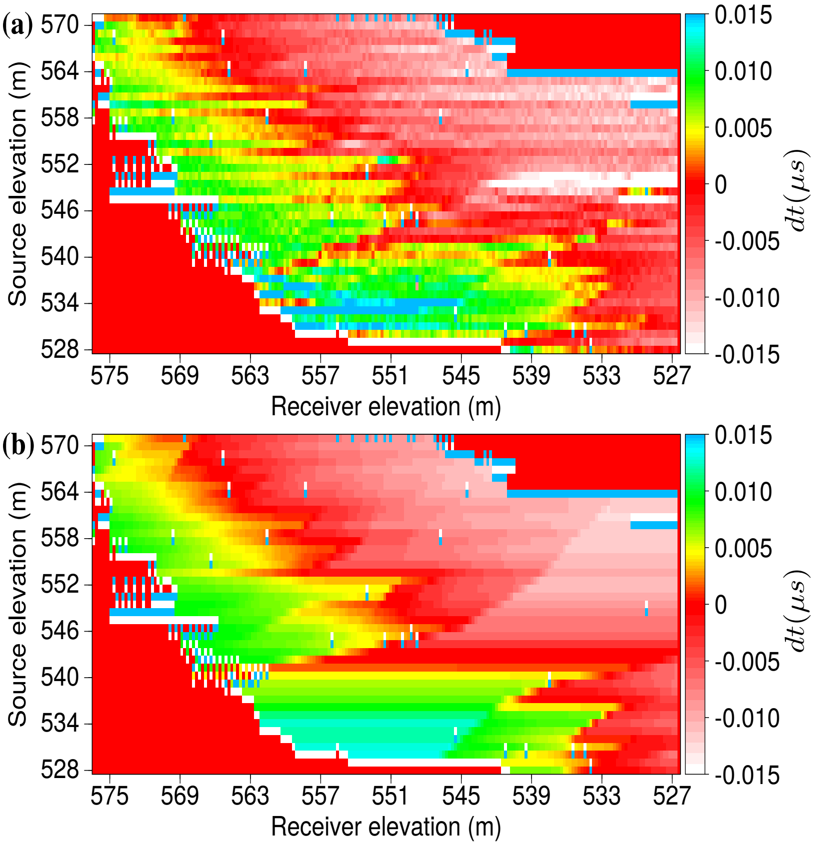

Figure 2.16: Double-difference analysis for (a) picked traveltimes and (b) synthetic traveltimes computed considering the isotropic velocity model of figure 2.4a.

The tomographic workflow proposed from the synthetic analysis is then used: an isotropic inversion stopped after 10 iterations provides a velocity model, which is smoothed (figure 2.17a) and then used as an initial velocity model for the anisotropic inversion. Here, the data-weight function is used for both isotropic and anisotropic inversions, which was unnecessary when very precise synthetic traveltimes were considered before. Indeed, real data face different kinds of errors, such as noise disturbance, instrument errors and traveltime picking errors, mainly observed at large offsets (figure 2.16a-b). Consequently, we have to find a model that attenuates these artefacts while preserving the update of the vertical velocity, which is sensitive to near-vertical offsets. Based on several tests, we found that values of $d_a = 28\,m$ and $d_b = 33\,m$ were efficient, while in our case, the maximum source-receiver offset is slightly larger than 40 m. figure 2.17b shows the isotropic solution without smoothing, while figure 2.17c displays an isotropic velocity model obtained from FWI inversion using the same dataset by Pinard et al. (2016). While tomography results are smoother, the introduction of regularization and of prior model information reduces artefacts around the gallery and increases the quality of the gallery reconstruction. It is worth mentioning that horizontal-like layer velocity obtained in figure 2.17c was used as an *a priori* information to decide a vertical symmetry in the experiments of this chapter, however, in the absence of this information, one may estimate the symmetry by migration (Vigh et al., 2014; Guitton et al., 2012), although we propose a cheaper way based on a data-driven optimization by using our forward engine in chapter 3.

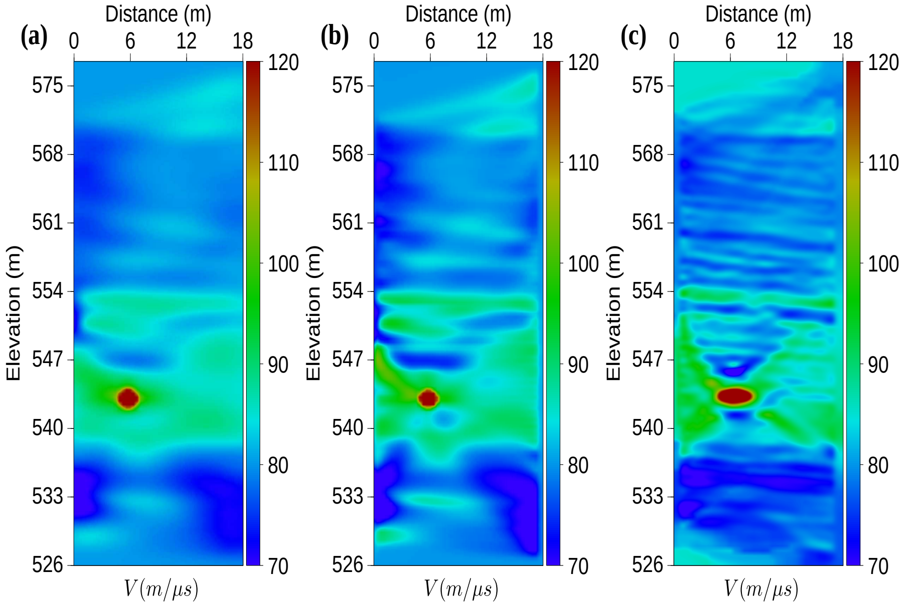

Figure 2.17: Smoothed (a) and raw (b) velocity models derived after 10 iterations of isotropic inversion using an homogeneous initial velocity of $80\,m/\mu s$. (c) Isotropic velocity model derived from FWI, courtesy of Pinard et al. (2016).

The residuals between observed and synthetic traveltimes are plotted for three different cases using the same color bar for comparison (figure 2.18). After the isotropic inversion (figure 2.18a), residuals are higher when waves are sampling zones with high velocity while receivers are located in the low-velocity water table zone. A final root-mean-square (RMS) error of $2.4 \times 10^{-3}\,\mu$s is obtained. When the smooth isotropic velocity model, used as the initial velocity model for anisotropic inversion, is considered, higher residuals are found in several zones, with an RMS error of $3.2 \times 10^{-3}\,\mu$s. After the anisotropic inversion is performed, the final residuals displayed in figure 2.18c are a bit lower, especially in the central part, with an RMS error of $2.3 \times 10^{-3}\,\mu$s obtained at iteration 10. However, one may notice some systematic horizontal patterns of higher residuals, for instance at elevations $531\,m$ and $549\,m$ (figure 2.18c), which could be related to constant time lags of the sources. For each source, one may estimate an average shift δt_0 of the origin time by the expression

$$\delta t_0 = \frac{1}{N_r} \sum_r (t_{obs} - t_{syn}), \tag{2.18}$$

over the N_r receivers (figure 2.19). While values displayed in blue are less than $\pm 1 \times 10^{-3}\,\mu$s, the estimated value of the picking error, those marked by the red asterisks may generate larger modifications in the final model. Consequently, the anisotropic inversion was performed again after shifting origin times, allowing to reduce these horizontal patterns in residuals (figure 2.20).

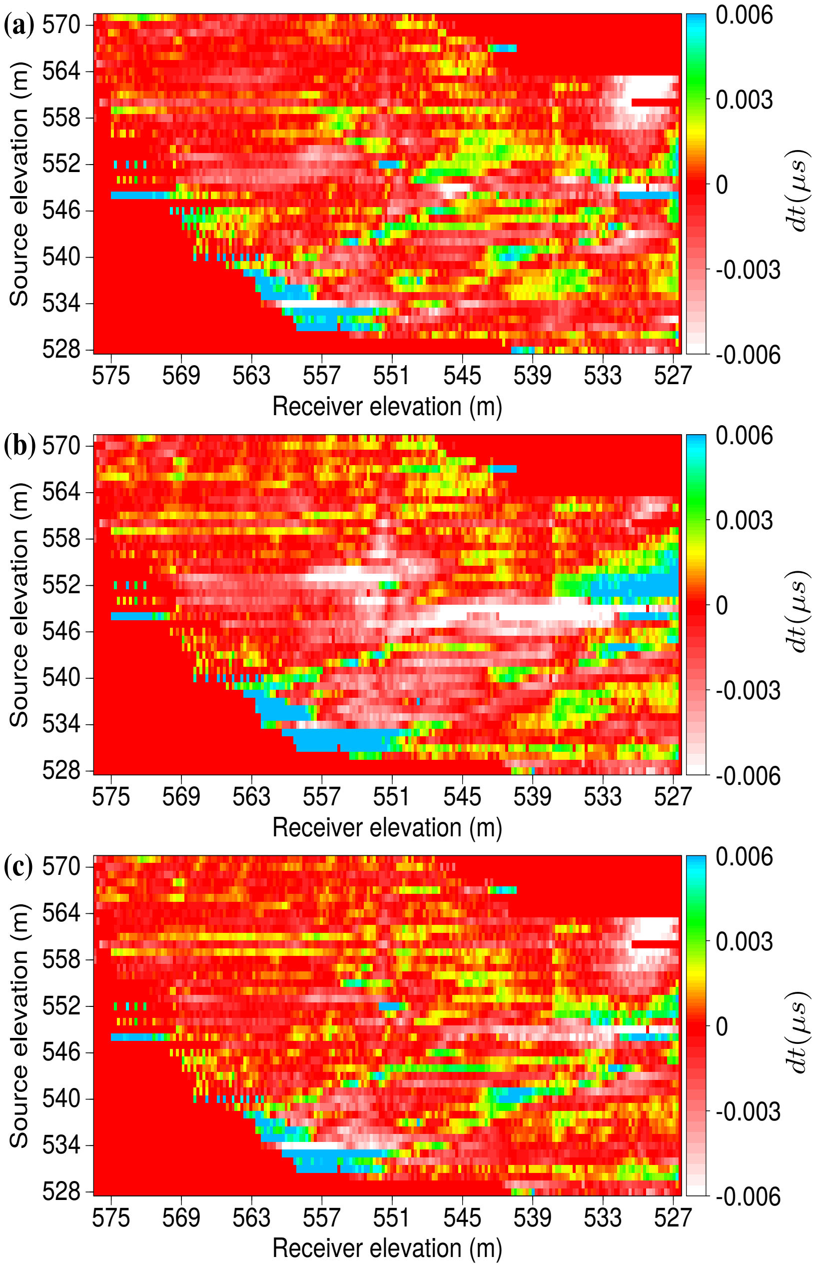

Figure 2.18: Residuals between observed and synthetic traveltimes for three different cases: (a) raw isotropic model obtained after 10 iterations, (b) smoothed isotropic model obtained after 10 iterations (initial velocity model for anisotropic inversion) and (c) anisotropic inversion after 10 iterations.

The convergence of each inversion is displayed on figure 2.21. Data misfit percentage defined by

$$MISFIT(\%) = 100 \times \left(\frac{\frac{1}{2} \sum_{sr} W_d^{sr} (t_{syn}^k - t_{obs})^2}{\frac{1}{2} \sum_{sr} W_d^{sr} (t_{syn}^0 - t_{obs})^2} \right), \tag{2.19}$$

where t_{syn}^k are the traveltimes computed for each iteration, and t_{syn}^0 are computed in the homogeneous

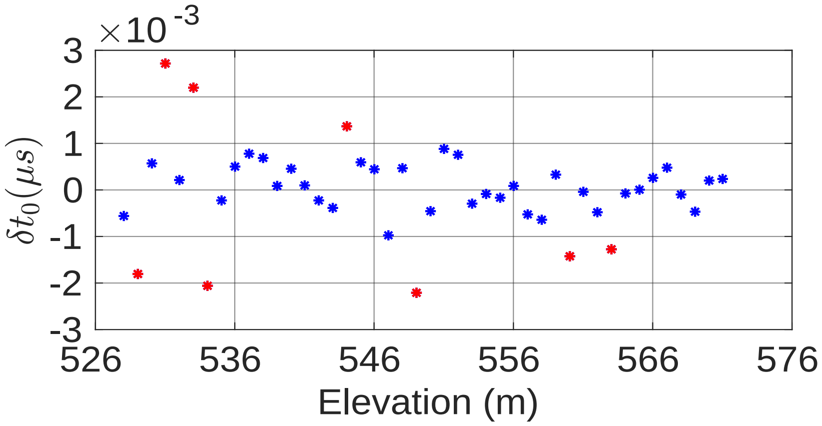

Figure 2.19: Average time shift δt_0 computed for each source, the red asterisks representing the values higher than $\pm 1 \times 10^{-3}\,\mu s$.

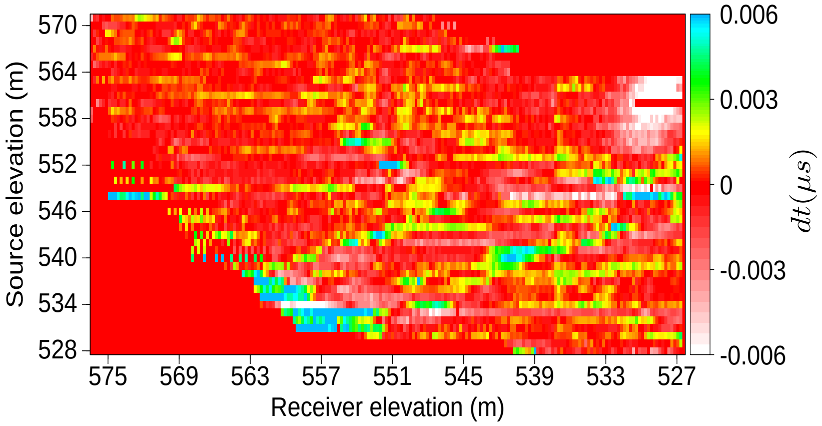

Figure 2.20: Final source-receiver residuals between observed and synthetic traveltimes obtained for the anisotropic inversion after source time shifts have been applied.

initial model for the isotropic approach. Consequently, anisotropic optimization is also normalized with respect to the initial isotropic traveltimes. A misfit of 1.6% is reached after 10 iterations for the isotropic approach. The slow decrease between iterations may be an expression of the assumed isotropic description. When δt_0 corrections were applied, a misfit of 1.4% is obtained, which yields a very small difference (figure 2.21). The anisotropic approach reaches a misfit of 1% after 6 iterations. The final data RMS error for this inversion is $2 \times 10^{-3}\,\mu s$.

The reconstructions of parameters V_v and V_h are shown in figure 2.22a-b, while figure 2.22c shows the relatively weak but notable anisotropic feature expressed by the anisotropic percentage R, which reaches 6% in certain places. Similar to our synthetic experiments, local increase of correlation lengths of Bessel smoothing at left edges has significantly reduced imprints of source locations. Vertical and horizontal velocities provide a slightly smoother image than the one obtained with the isotropic assumption and especially with the one derived from FWI: the gently dipping fine layering structures have been converted into a noticeable spatially varying anisotropy in figure 2.22c. We highlight two boxes that might reveal apparent anisotropy: box A shows a dipping layer with a low degree of anisotropy (figure 2.22a-b), while box B shows a horizontal layer characterized by higher velocity and anisotropy of 4%. One can notice a few artefacts around the gallery due to strong differences between V_v and V_h

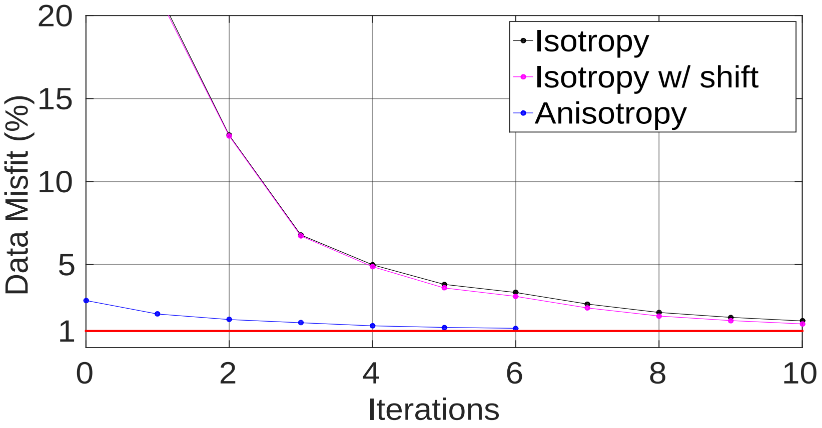

Figure 2.21: Data misfit (in percentage) versus number of iterations for isotropic (black line), and both isotropic (magenta line) and anisotropic (blue line) after the shifting correction. The curves are normalized with respect to the initial homogeneous isotropic model. The one percent of error is highlighted in red.

velocities. The layer between the box B and the gallery shows a higher value of 6% of anisotropy (figure 2.22c), but this could be induced by the presence of the gallery. The water table zone also shows possible anisotropy artefacts, due to the poor illumination in this region, thus reducing the possibility to update the vertical velocity, mainly driven by subvertical propagation paths.

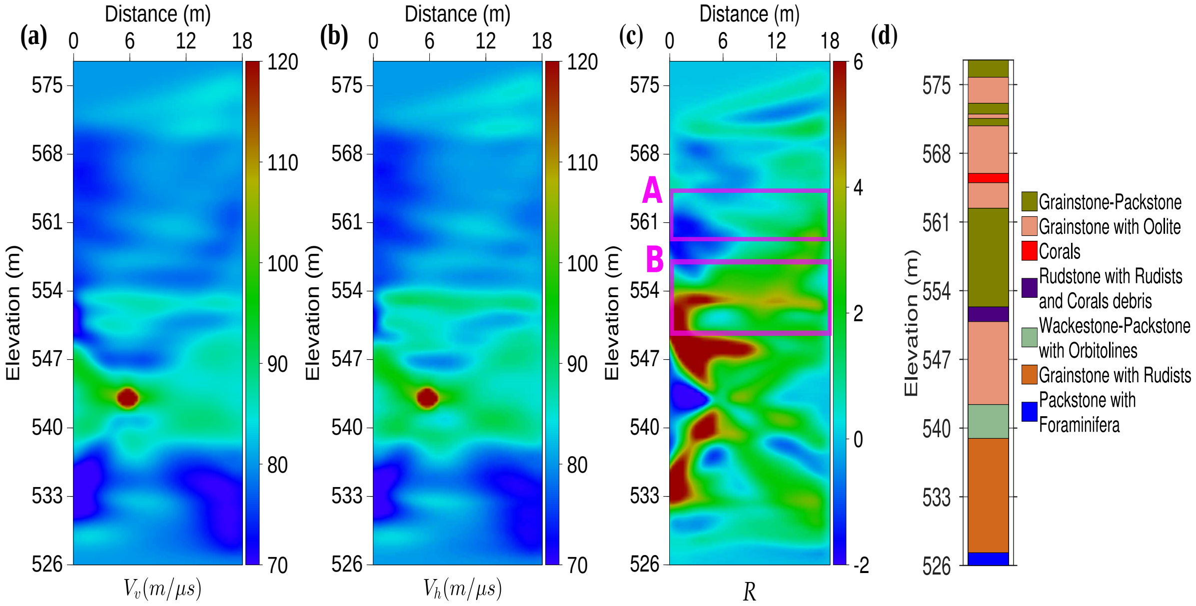

Figure 2.22: .Anisotropic inversion results: (a) vertical and (b) horizontal velocity models. (c) Distribution of the percentage of anisotropy R considering vertical and horizontal velocities. (d) Schematic geology of the area with different carbonate formations adapted from Bouaziz (2015).

Figure 2.22d shows a simplified geological interpretation provided by sample analysis performed by Bouaziz (2015). The correspondence between this rough geology sketch and velocities is relatively clear: higher velocity zones appear to correspond to the Grainstone with Oolite layer, while the upper low-velocity zone seems related to the Grainstone-Packstone layer. As expected, the saturated zone decreases the velocity in the lower part. In terms of anisotropy, the correspondence with geology is not straightforward: it might be blurred by the presence of the gallery and the water table but also by the lack of resolution of the geological sketch. However, spatial variations and the presence of some dipping horizontal anisotropic features appear. The origin of this anisotropy would require additional investigations and complementary rock sample analysis. It could be a marker of fine stratification, as suggested by the high-resolution image provided by FWI, and of localized karstic zones.

2.4 Conclusion

We incorporate an Eikonal/adjoint formulation based on a discontinuous Galerkin scheme into a tomographic method to invert crosshole GPR data under the elliptical vertical transverse isotropic (EVTI) assumption. The discontinuous finite element method for solving the Eikonal equation is based on a Hamilton-Jacobi equation formulation, which allows highly accurate computation of synthetic traveltimes. In addition, the viscous solution of the Eikonal equation accounts for diffraction, which is fundamental when strong contrast are expected, and is not possible with the ray-tracing methods. The adjoint formulation used here not only allows the calculation of the gradient with a reduced complexity limited to the model dimension but is also independent of the chosen parametrization while the model-sized gradient adds analytical expressions of the parametrization. Avoiding the data-sized computation and storage of the Freéchet derivatives would make this method potentially attractive for 3D applications. After different sensitivity kernels of the inversion for multiparameter reconstruction have been analyzed, a synthetic analysis has been performed on two models: the firs showing a high-velocity anisotropic layer, and the second being more realistic with horizontal-like layer variation of velocity, including the presence of a deep gallery creating diffraction. It underlines that data weighting and model regularization are key ingredients of traveltime tomography, especially in highly contrasted environments and that our formulation is efficient to explain first arrival times, even when diffraction is present. Moreover, such a synthetic examples for crosshole experiment confirmed that the preferential parametrization includes vertical and horizontal velocities in this transmission context. Based on such dedicated workflow, a challenging real GPR dataset has been analyzed where the presence of a gallery with high-velocity contrast makes the tomographic reconstruction difficult. With an *ad hoc* workflow based on an initial isotropic inversion followed by an anisotropic one, a horizontal stratification of the carbonate structure even hindered by the presence of the gallery has been recovered. Such a structure reveals the presence of a low degree of anisotropy in this carbonate formation, which might be related to fine stratification, the presence of karstic zones, or angular limitations due to the acquisition configuration. This new anisotropic tomography may be extended to 3D cases without requiring a new methodological formulation. Applications at the lab scale where a full-illumination is possible are presented in the next two chapters.

Chapter 3

Anisotropic acoustic tomography of carbonates at laboratory scale based on seismic first-arrival traveltimes

Contents

Introduction

This chapter is dedicated to the seismic imaging of carbonate blocks through anisotropic tomography based on first arrivals obtained by laboratory measurements. As shown in chapter 2 the inversion of anisotropy strongly depends on the illumination of the studied sample by seismic rays, i.e., the azimuth coverage. Indeed, we illustrated how the crosshole configuration could generate anisotropy artefacts due to the coverage limitation in the vertical velocity. Therefore, one of the advantages of laboratory acquisitions is the possibility to perform a full illumination by locating sources and receivers in different faces of the block. Some of the results shown in this chapter has been presented in Salcedo et al. (2021).

Anisotropy in carbonates has been investigated in laboratory by the three-plug measuring technique (Martínez and Schmitt, 2013; Gordin et al., 2020) assuming a Vertical Transverse Isotropic (VTI) model as we showed in chapter 2. For this, three plugs are cut in three different directions from the main core, and ultrasonic velocities are measured along three different directions at different confining pressures, which are representative of *in situ* conditions. The velocities are used to estimate the five elastic constants for a VTI medium. It must be underlined that no anisotropic inversion is performed here, the obtained anisotropy velocities being assumed homogeneous. Regarding the inversion of anisotropic parameters, other rock formations have been investigated instead of carbonates. For instance, Falls et al. (1992) and Jansen et al. (1993) studied unconfined granite samples extracted from the same location by combining acoustic emission and active ultrasonic measurements. In the former, the sample was subjected to hydraulic stress while in the latter to thermal induction. In both cases the 2D anisotropic model was obtained using the SIRT algorithm (Gilbert, 1972; Dines and Lytle, 1979), modified after according to Stewart (1988) in order to update the anisotropy assuming a weak elliptical anisotropy for VTI anisotropy model and that only straight rays are considered. Pšencık et al. (2018) inverted the 21 anisotropy parameters of a biotite sphere by considering the sample to be homogeneous along with first-order weak-anisotropy aproximation. Under these assumptions, the equations used for the inversion are linear and the inversion procedure becomes non-iterative.

Comparing to the former study, it is worth mentioning that the forward modeling used in the present thesis (Le Bouteiller et al., 2019) directly solves the Eikonal equation in an Eulerian way, therefore we avoid the weak-anisotropy approximation and ray-tracing. Besides, we get rid of the homogeneous assumptions of the medium, as we reconstruct both the velocity heterogeneities and anisotropy using iterative local multiparameter optimization methods. Another interesting approach was provided by Brantut (2018) who proposed a method to invert both the source locations of acoustic emission and the anisotropic parameters. He studied a cylindrical sample of sandstone subjected to triaxial deformation in reservoir conditions, subsequently the anisotropic evolutions was presented. As he used the elliptical approximation in VTI, anisotropy was parametrized with only horizontal velocity and one parameter based on the Thomsen's parameter ϵ. However, there is no discussion about potential leakage between parameters in his work, something we showed that clearly exists (chapter 2). In his approach, the fast marching method (Sethian and Popovici, 1999) is used to solve the Eikonal equation, while the quasi-Newton method is chosen for the inverse problem. Besides, the sensitivity matrix is built by a posteriori ray tracing. This is the main difference with the approach proposed in this thesis: the ray approach involves the parameters when considering the discrete computation of the Fréchet derivatives while in the adjoint approach the parameters are involved in the derivation of the analytical expression of the Eikonal equation.

We study two carbonate blocks from different quarries in France, in both cases the blocks are unconfined, we are not simulating reservoir conditions, nor stress effect on the anisotropy. In contrast, the blocks are investigated through active sonic (20 - 80 kHz) measurements. The first-arrival information along with each source-receiver path (assumed straight) are used to compute an average velocity. This velocity pattern is then studied as a function of the source-receiver angle allowing a qualitative investigation of heterogeneities and anisotropy before any inversion procedure. Such data-driven approach allows to define the properties of the inverted anisotropy model based on data, while in several studies this choice is made after a visual sample inspection or by *a priori* information from the field, generally ending with a VTI model (Martínez and Schmitt, 2013; Abell et al., 2014; Brantut, 2018; Gordin et al., 2020).

In this chapter we dedicate 4 sections to the study of the first block because we participated in the data acquisition and processing while in the last section we present an extension of a dataset in another block already studied by Matonti et al. (2017). The outline of this chapter is the following:

- In section 3.1 we present the acquisition methodology and devices with illustrations of the coverage. The experimental source used implies a time-zero estimation of the source impact which is highlighted. Then, the quality of the recorded data and picking limitations are presented and discussed.
- In section 3.2 we show the dataset based on the average velocity along each (straight) path. This allows, among other things, to qualify the influence of the large diameter of the source and propose several corrections which are applied on synthetics in order to re-evaluate the source-receiver distance according to the source size extension.
- In section 3.3 forward modeling is used to test different theoretical anisotropic curves computed considering various anisotropic models in order to evaluate which one reproduces best the velocity versus angle pattern of the dataset. For this, a homogeneous anisotropy parameters are used. The approximation allows us to define *a priori* anisotropic parameters before the inversion procedure.
- In section 3.4 we present the inversion results. In particular, we highlight the preferred orientations of structures along with the anisotropic velocities recovered, study the residuals between the theoretical traveltimes compared to the observed ones and discuss the results in terms of rock physics.
- In section 3.5, we revisited a highly anisotropic and fractured dataset in another carbonate block, which was widely studied in Matonti et al. (2017), and where no anisotropic inversion was attempted. Therefore it is important to evaluate our approach and possibly extend their conclusions.

3.1 Seismic experimental approach

This section is dedicated to the presentation of the experimental set-up which includes the seismic source-receiver devices, acquisition configuration and the necessary time source (t_0) calibration to correct for the initial temporal offset present in laboratory seismic records. It also includes an illustration of typical recorded seismic waveforms, their properties and their signal to noise ratio.

Block geology The investigated carbonate sample is a $33\,cm \times 33\,cm \times 33\,cm$ cube extracted from the Farrusseng quarry in Beaulieu (South of France). The block is made of bioclastic limestone with siliciclastic grains (quartz) from the Burdigalian age (early Miocene). Besides, the block is partially cemented with an average porosity of $27 - 30\%$ (personal communication, J.P. Rolando from TOTAL), a relative high value in carbonates (Matonti et al., 2015; Bailly et al., 2019).

3.1.1 Seismic source-receiver devices

The signal is generated by a *Keysight*® waveform generator. Among several available functions, we choose a 100 kHz sinusosidal pulse with an initial amplitude of 7 V. The signal is transmitted to a *Falco System*® dynamic amplifier which multiplies the amplitude by a factor of 50.

Subsequently, a piezoelectric transducer (PZT) converts the electrical pulse into a longitudinal wave that propagates into the block. Transducers of a wide range of diameters and frequencies are available in the laboratory which, after several tests of signal/noise ratio in the block for each PZT, we select the Panametrics V1011 PZT from *Olympus*®. Some properties of this PZT: it is a longitudinal (P-wave generation) wave transducer, it has an effective diameter of 38 mm and it has an optimal frequency of 100 kHz, namely at this frequency the PZT gives the strongest amplitude, note that it is the same frequency we choose in the waveform generator.

One of the typical difficulties at laboratory scale arises from the relatively large size of sources and receivers compared to the sample size and considered wavelengths. Consquently, it is genrally not possible to simultaneously deploy a large array of sensors on the block faces. We partially tackle this problem using a Laser Doppler Vibrometer (LDV) as a seismic receiver which allows us to substantially increase the number of recorded traces, since the measurement is performed with a tiny laser beam of less than a 50 μm. We have in the laboratory the OFV-500 single-point sensor from *Polytec*® (Polytec, 2013b), it is accompanied by a OFV-5000 vibrometer controller and an extra DD-300 decoder (Polytec, 2013a), the last ingredient allows us to measure the vibration dispacement (nanometer-scale) while the term single-point refers that we measure only one component of the wavefield, the out-of-plane component. In spite of the recording benefit at one point we still have the size of the PZT which makes the source non-punctual, this is widely discussed in section 3.2. Following the experimental devices, the recorded signal is displayed and recorded in a digital memory oscilloscope *Keysight*® Infiniium (S-Series) at a sample frequency of 5MHz. A detailed review of the seismic experimental set-up is given in Shen (2020).

3.1.2 Acquisition

A schematic design of the experiment is shown in figure 3.1a where each face has its corresponding number, the red asterisk simulates one position of the PZT on face 1 while the laser is recording on face 2, also note that both PZT and laser are located at 16.5 cm leading to a 2D acquisition. The transducer is tightly attached to the block using an elastic band and coupled to the block thanks to gel material (figure 3.1b), in order to get a better transmission of the seismic energy from the PZT to the sample. For the same purpose, each trace recorded by the laser results from the stack of 2500 successive pulses, moreover a reflective band is attached on the measured point in order to reach optimal laser reflection level (figure 3.1c), and each pulse is triggered every 10 ms being long enough for the seismic waves to be completely attenuated in the carbonate. This frequency of triggering is set in the waveform generator which is connected to the oscilloscope, therefore we can extract the trace recorded by the laser and the trigger function.

The laser is displaced every 0.5 cm (inter-trace spacing), so that we recorded 66 traces in each face for each single shot location. 22 shots positioned along two faces, 11 shots on face 1 and 11 shots on

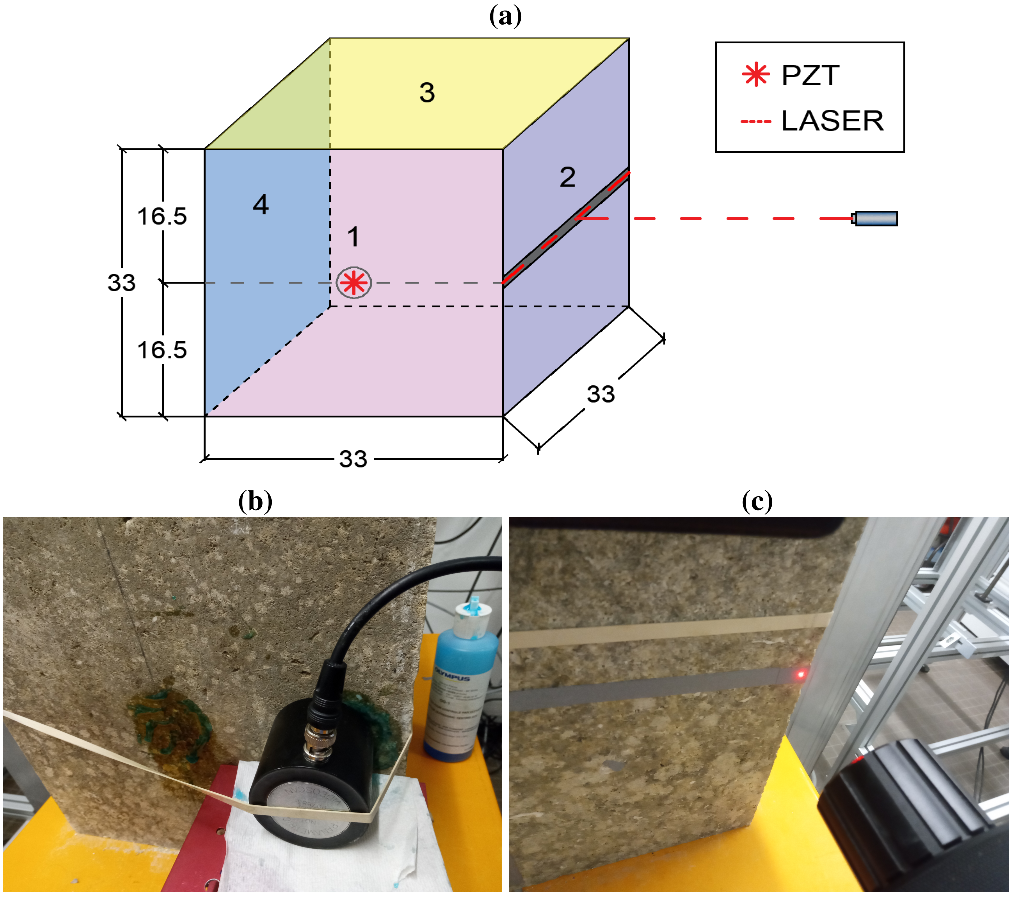

Figure 3.1: (a) Schematic illustration of the experiment where each face has a number, PZT and laser located at the middle of the block. (b-c) Photography of source/receiver acting. (b) The source is located at one corner on face 1 and emitting successive pulses. (c) The laser is located on face 3 and pointing on the reflective tape.

face 2 with an inter-shot spacing of 2.5 cm measured from the center of the PZT. Figure 3.2a shows the laser positions (triangles) associated with the shots (asterisks) on face 1 while figure 3.2b shows the shots located on face 2 and the corresponding faces recorded. For the sake of clarity, the number of receiver locations and thus the number of paths was decimated while the point source i assumed at the center of the transducer surface. It must be underlined that no receiver was recorded on face 1 and that no source was located on faces 3 and 4, due to a lack of experimental availability. This does not prevent a full illumination (figure 3.2a-b). For sake of clarity, acquisition configurations are summarized in table 3.1.

Since we are investigating the anisotropy of the P-wave velocity, one should think about the change of velocity as a function of the angle of propagation in the sample. Based on the acquisition configuration (figure 3.2a-b) we define the source-receiver angle, as displayed on figure 3.3. With this convention, when the source is located on face 1 (figure 3.2a), the range of available angles lies between 0° and 180°, while when the source is located on face 2 (figure 3.2b), the range of angles will be limited between 90° and 225° because the laser did not record the face 1 (table 3.1), otherwise it would reach 270°.

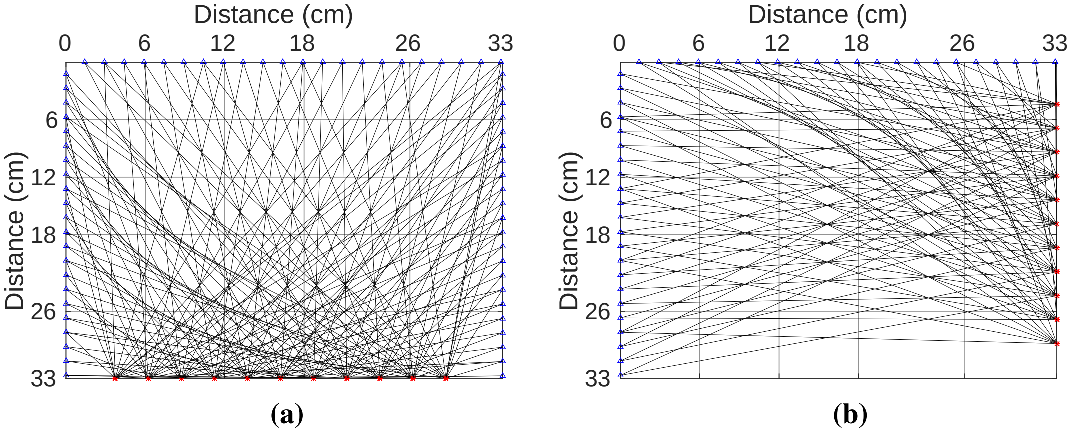

Figure 3.2: Acquisition illustration. (a) 11 shots located on face 1 (figure 3.1a) associated with the other 3 faces, where shot 1 is located on the left bottom corner and it increases until shot 11 located on the right bottom corner. (b) 11 shots located on face 2 associated with faces 3 and 4 (figure 3.1a), where shot 12 is located on the right bottom corner and it increases until shot 22 located on the top right corner. Receivers have been decimated for a better visualization of the illumination.

Face N°	PZT N°	Laser	Laser Init. Pos. (mm)	Record from PZT on face (PZT N°)	Laser disp.	PZT disp.
1	1-11	No	-	-	-	left to right
2	12-22	Yes	2.5	1 (1-11)	bottom to top	bottom to top
3	No	Yes	1	1 (1-11) and 2 (12-22)	right to left	-
4	No	Yes	3	1 (1-11) and 2 (12-22)	bottom to top	-

Table 3.1: Features of each face of the block being each column: the face number (figure 3.1a), the shots positioned on this face (PZT N°), the laser recorded such a face or not, the initial position of the laser along the surface of the block, from which face the P-waves are coming along with the PZT number, the laser displacement direction, and the PZT displacement direction. Use figure 3.2a-b to complement this table.

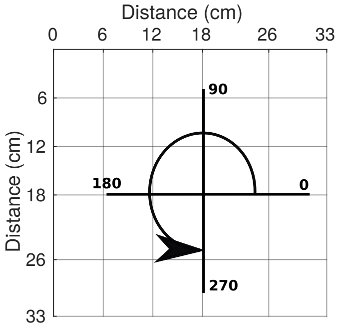

Figure 3.3: Angle convention for a source-receiver couple.

3.1.3 Calibration of the source in the time domain (t_0)

To qualify the source signal, measurements have been made by locating the laser beam directly on the transducer surface (figure 3.4a). Figures 3.4b and 3.4c show the recorded signal and its spectrum, respectively. These figures show the complex time and frequency patterns of the source function exhibiting two different peaks in the frequency domain : one at 58 kHz and a higher one around 120 kHz, which may correspond to a harmonic. Note that here the laser is located at the center of the transducer surface. However, additional measurements performed by moving the laser to different positions on the surface shows identical face and amplitude, suggesting the same energy of the longitudinal wave is spreading all along the surface of the transducer.

In order to check the stability of the source signal all the time of the acquisitions, which lasted several days, the input signal was measured on the transducer each single day allowing to confirm the stability of the spectral source content (figure 3.4c). Figure 3.5 shows the time signal measured directly on the transducer surface until 30 μs, the information of the trigger being added. One can see that the trigger starts at zero, where the sine function is injected, which is not the case for the source function because it takes certain time to be sent. The delay between the trigger and the input signal is the time calibration, which we could estimate as an average $t_0 = 1\ \mu$s, the difference in t_0 for each day being about $0.1\ \mu$s. Such a t_0 value is quite stable since Shen (2020) performed measurements in a homogeneous block of aluminium testing different PZT and obtaining about the same value.

3.1.4 Data quality control

The picking of the first-arrival traveltimes is highly dependent on the quality of the data (i.e., the signal to noise ratio) and on the presence of potential waveform anomalies. In all the measurements, the total recording time is 500 μs while the time sampling is 0.2 μs (sampling frequency of 5 MHz). The traveltime error related to this picking uncertainty is thus estimated around 0.1% for large raypaths and 3% for shorter raypaths. Figure 3.6a shows a sketch of raypaths involved when the source is located at the middle of face 1 (figure 3.1a) and the receivers are located on face 3 (figure 3.1a). Figure 3.6b shows the seismic gather with the 66 traces according to the position of the laser over the face. Each trace has been normalized by its maximum value while the gather is clipped to [-0.4,0.4] to better observe the onset of the first-arrival, which exhibits an expected hyperbola pattern. The onsets of the first-arrivals are located where the negative amplitude begins, in accordance with the polarity of the input signal (figures 3.4b and 3.5).

Figure 3.6c shows the same gather with a wiggle-trace representation and a zoom centered on the first-arrivals. One can identify three traces that are clearly noisy because the laser could not focalize at this position, i.e., distortion of the beam. This effect is random because if we repeat the focalization, it will certainly work, however the laser is being displaced automatically in order to do the acquisition faster while if we record manually one by one and checking the focalization on each record, the acquisition would be endless. The blue line on the top indicates the extension of the 38 mm diameter of the transducer surface. On most of the traces, the signal to noise ratio is very satisfying allowing a confident picking. However, some traces display a strong and localized delay. A visual inspection of the faces of this block, highlights the strong low-scale rugosity of the surface, therefore when the laser beam is diffracted by the boundaries of these holes, it cannot produce a nice focalization, thus generating the observed delays. Similar acquisition has been performed with the same laser on the smooth surface of a cylindrical sample and no traces exhibited any delay (Shen, 2020). In order to identify the delayed traces, one has to assess the continuity of onsets of surrounding traces, and remove the traces with too

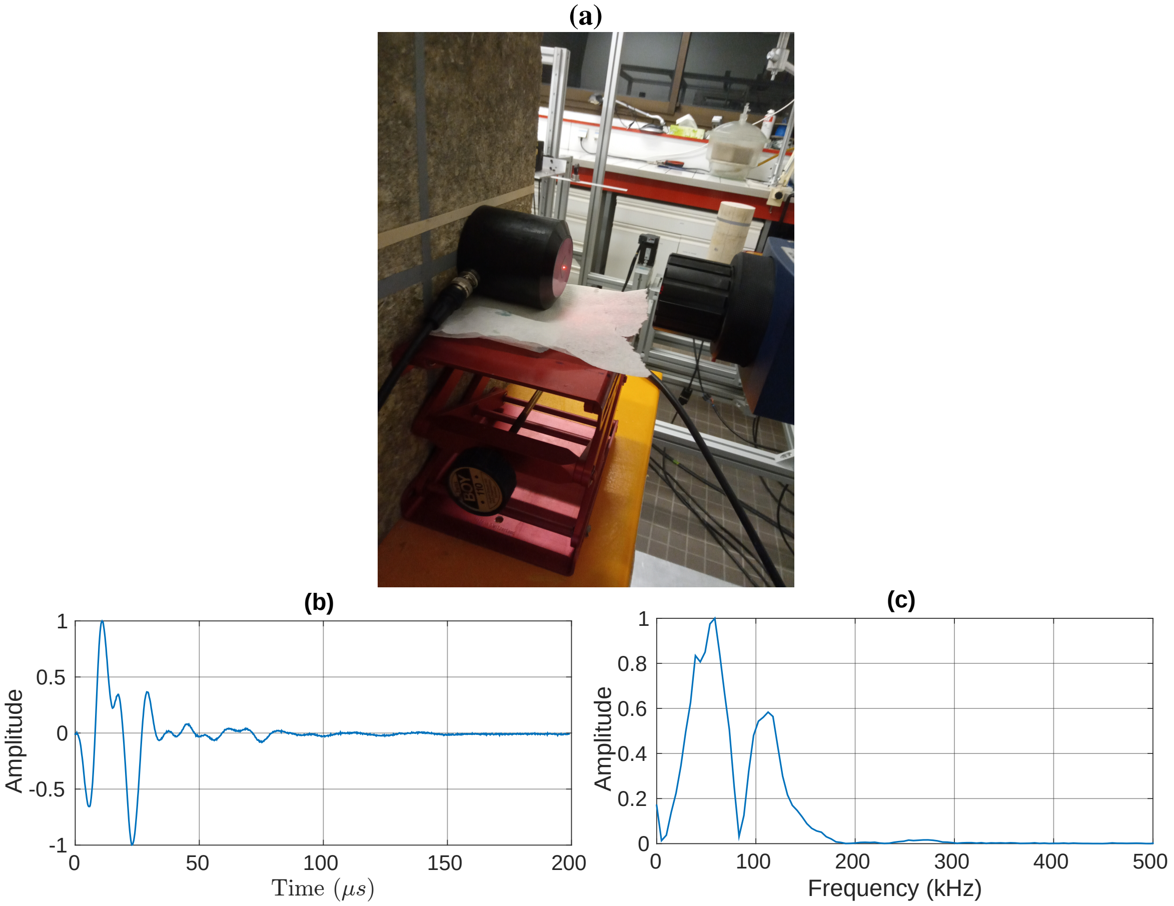

Figure 3.4: (a) Illustration of the experience designed to characterize the input signal by locating the laser directly on the transducer surface. (b) Recorded signal in the time domain after normalization by its maximum amplitude. (c) Normalized frequency spectrum of the input signal, the dominant frequency being 58 kHz.

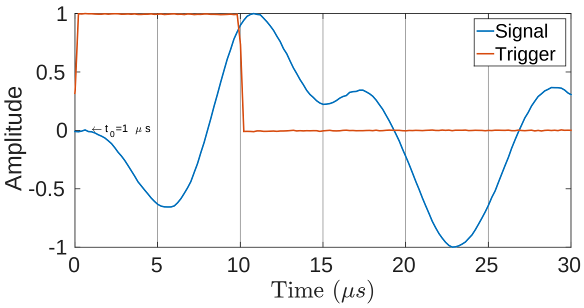

Figure 3.5: Input signal with the trigger superimposed. The delay between the trigger at zero time and the first-break of the sine function is the calibration time.

much delay. In general, this gather displays a large signal/noise ratio, and after discarding both the traces with delay and those very noisy, it was possible to manually pick 54 traces for this particular face and this particular shot being displayed as a red solid line connecting the picked traces. However, due to these limitations, the choice of manually picking has been retained, an automatic strategy would have been complicated to implement. This is all the more true when we look at the following example.

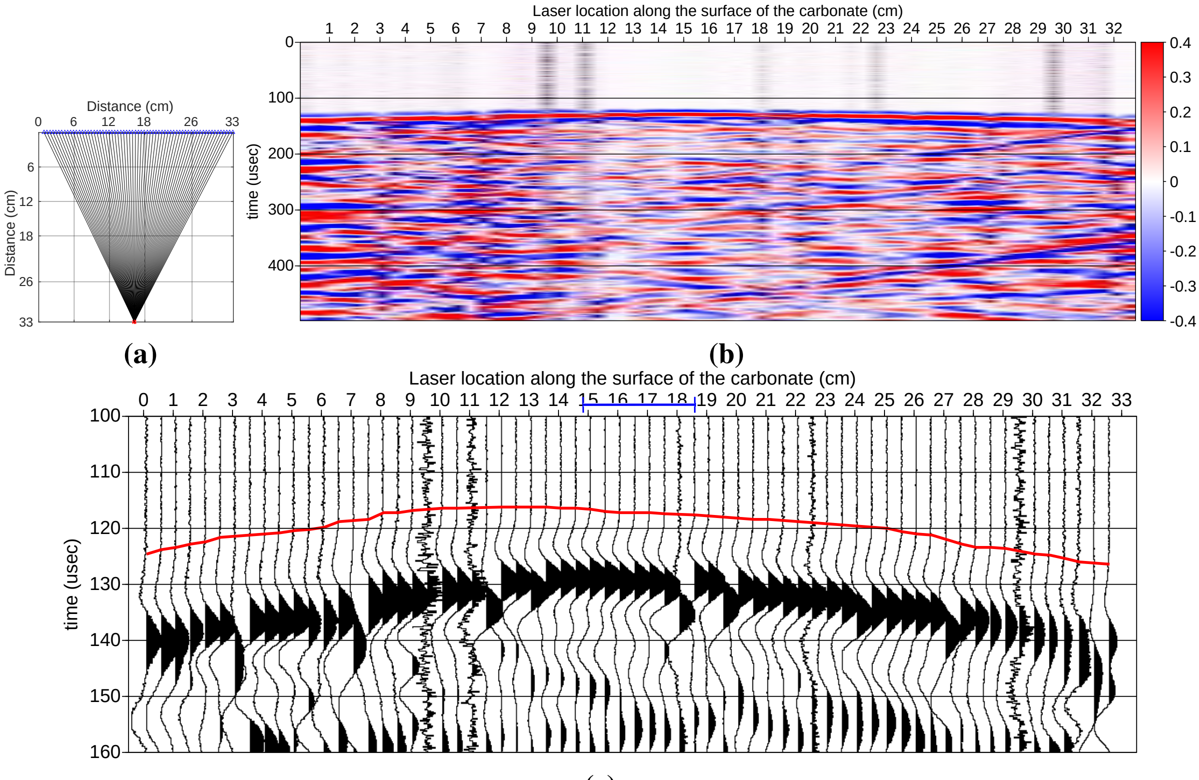

(a) **(b)**

(c)

Figure 3.6: Near-vertical shot gather. (a) Source-receiver configuration. (b) Normalized amplitude image for the 66 traces. (c) Wiggle-trace plot, time axis being limited to the zone of first-break onsets while blue line represents the diameter of the source, namely 38 mm. It is possible to identify traces with delay due to the surface rugosity of the block that affect the laser focalization. A red solid line connects the 54 picked values.

Figure 3.7a shows the acquisition for a more oblique source-receiver configuration. In figure 3.7b, one can see the noisy traces at far offsets, as only a small part of the source energy is transmitted to the receivers, contrary to the previous case illustrated in figure 3.6b. In addition, with this configuration, one can see a strong secondary arrival being the signature of V_s and other subsequent event which are not considered for our tromographic purposes. The energy of first-arrivals is better illustrated in figure 3.7c: besides the noisy traces, we can see very low amplitudes compared with figure 3.6c while traces with delay are also visible. This low energy must be related to the radiation pattern emitted in this particular source/receiver configuration which has 90° of rotation compared to the previous case. All this means only 41 traces were manually picked and being displaced as a red solid line connecting them, most of the traces at far offsets were discarded.

We show in figure 3.8a a selection of pickings performed on face 3 with a decimated number of opposite shots located on face 1 (figure 3.1a), namely the near-vertical paths, while figure 3.8b shows pickings associated with near-horizontal paths since the recorded face is the number 4 (figure 3.1a). In general, both figures show a smooth pattern of picking with some localized heterogeneites but the main observation is certainly the fast hyperbolas obtained in the near horizontal paths compared to the vertical ones which is a first insight of anisotropy, i.e., dependency of one property on the propagation

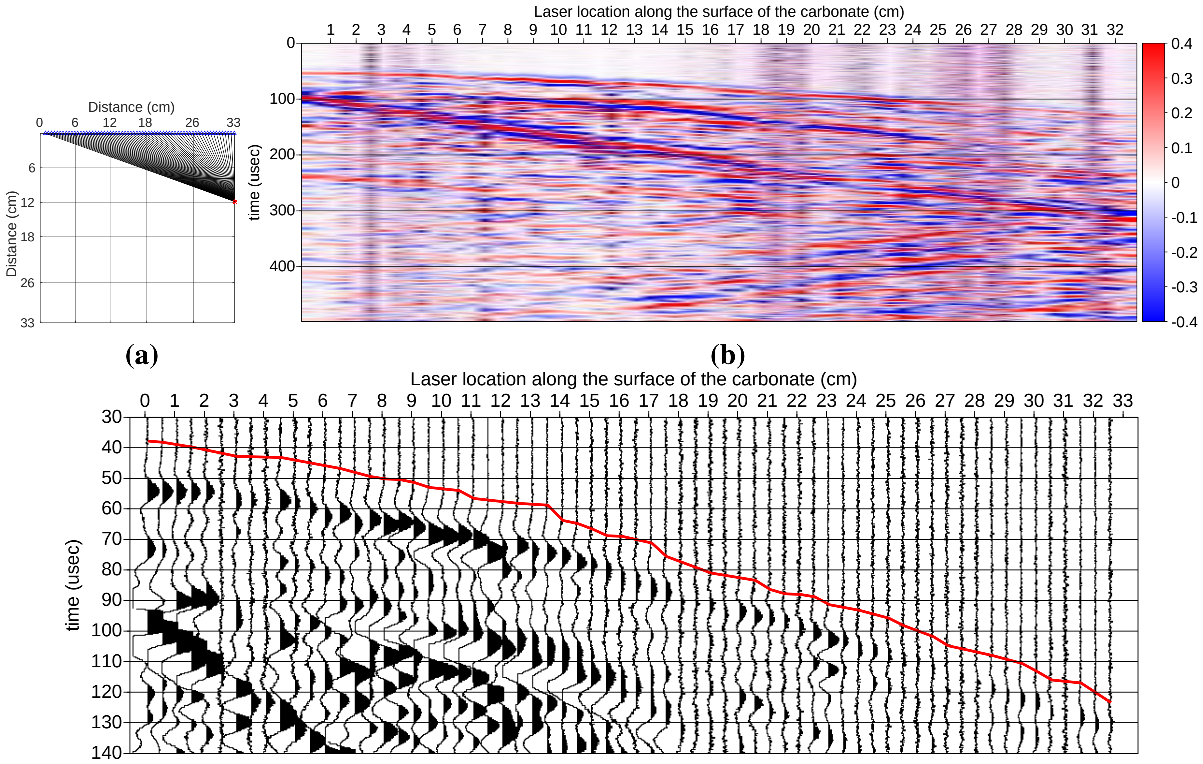

(a) **(b)**

(c)

Figure 3.7: Oblique seismic shot gather. (a) Source-receiver configuration. (b) Normalized amplitude image for the 66 traces. (c) Wiggle-trace plot, time axis being limited to the zone of first-break onsets with a red solid line connecting the 41 picked values. Besides the traces with delay, a general trend of low signal/noise ratio is visible.

direction.

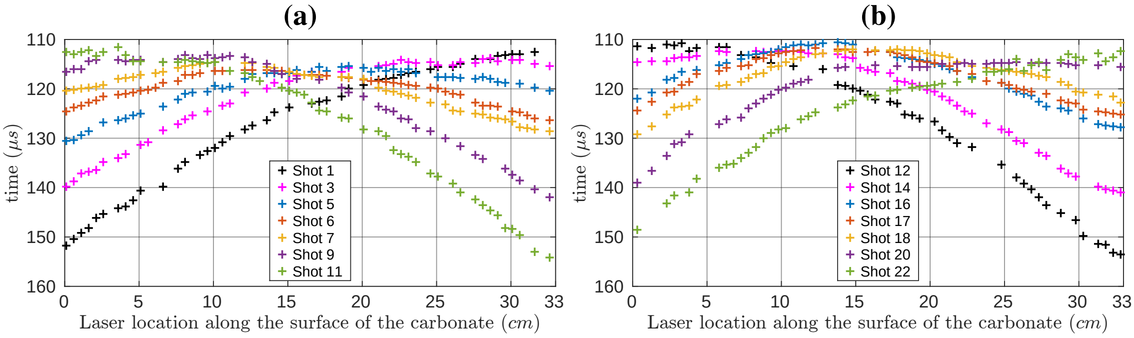

Figure 3.8: (a) Picking of face 3 (top face) associated with some shots on face 1. (b) Picking of face 4 (left face) associated with some shots on face 2. Use figure 3.2a-b and table 3.1 to identify the location of source/receiver.

Wavelength estimation Based on the picked traveltimes, a preliminary estimation of velocity was performed using the straight distance between source-receiver pairs, thus velocities ranging between

$0.27-0.31\ cm/\mu s$ were obtained. On the picked traces we apply a window, figure 3.9a is an example of a raw trace while figure 3.9b is the same trace after applying the window, it includes the the first negative amplitude and the first positive amplitude of the signal as we saw in the source measurement (figure 3.5), while the remaining of the trace is filled with zeros, therefore this isolation on the trace allows us to guarantee that we are working with the first events. Subsequently, we compute the frequency content of each windowed trace, figure 3.10a and figure 3.10b are the spectra of figure 3.6c and 3.7c, respectively. Each trace was normalized by its maximum frequency amplitude while vertical traces in blue were not picked. Unlike the dominant frequency of the input signal is 58 kHz (figure 3.4c), we can see in figure 3.10a-b that the dominant frequency varies depending on the propagated distance. figure 3.10a shows higher dominant frequencies when the receivers are near the source $(14 - 18\,cm)$ while the frequency decreases at far offsets as expected when attenuation is considered. In contrast, figure 3.10b for the oblique configuration (figure 3.7a) shows a slight increase in frequency at large offsets where some traces show the gap in frequency, namely the same pattern we observed in the spectrum obtained from the source measurement (figure 3.4c). Following this analysis for each shot gather, an average dominant frequency of 51 kHz was estimated which is not substantially far from the dominant frequency when the laser records directly on the transducer surface. Subsequently, a range of wavelength obtained for this experiment is shown table 3.2, as we discussed in section 2.3, the wavelength information gives an idea about the expected resolution of velocity/anisotropy in the block (Williamson and Worthington, 1993), and it is also associated with the assessment of the discretization in FATT. We will now focus on issues related to the use of an extended source and propose some corrections necessary to be applied to overcome it.

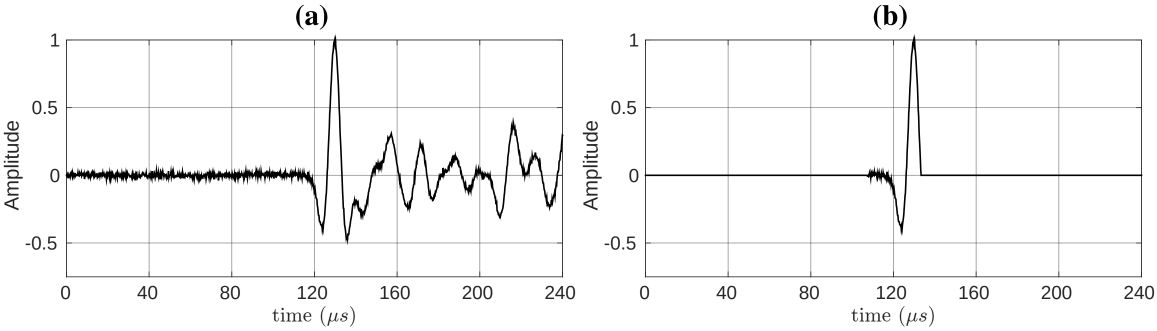

Figure 3.9: (a) Example of a raw trace acquired in the block. (b) Window is imposed on (a) to isolate the first events and then compute the frequency content in figure 3.10.

f [Hz]	$\lambda = \dfrac{V_{carbonates}}{f}$ [cm]
51×10^3	5.3-6.1

Table 3.2: Estimated wavelength using the range of velocities $0.27-0.31\ cm/\mu s$ measured in the block under the straight source-receiver propagation hypothesis.

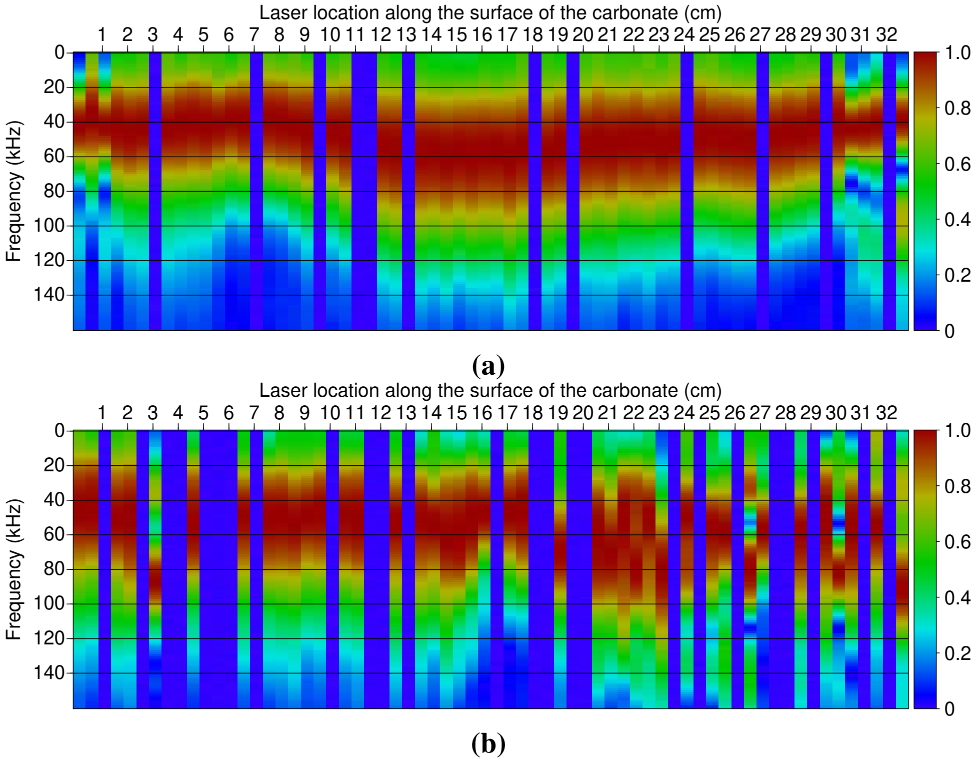

Figure 3.10: Normalized frequency spectrum. A window is imposed on the picked trace to limit the frequency content to only first-arrival events (figure 3.9b). (a) Frequency spectrum of shot gather of figure 3.6. (b) Frequency spectrum of the oblique shot gather of figure 3.7. The traces with zero information mean that they were not picked, thus the noisy oblique shot gather display less traces.

3.2 On the necessity of source location corrections

Contrary to field scale measurements where sources can be considered as punctual sources, the piezoelectric source has a rather large extension (3.8 cm) relative to the dimension of the block (33 cm). In this part, we will illustrate the consequences and possible artefacts that this spread source can generate, and propose different discretizations of the source to obtain a better representation of the dataset. We will then evaluate the effect of this source modeling on the tomographic inversions based on synthetics models.

3.2.1 Computing an average velocity

From 3630 available traces, only 2384 were picked due to bad signal/noise ratio and delays discussed in section 3.1.4 affecting the remaining traces. These traveltimes have been used to compute velocity on each path assuming a straight distance between source-receiver, also known as average velocity since the raypath is crossing several heterogeneities and thus the velocity is being averaged, while the source is assumed to be located at the middle of the PZT. In the computed velocities, an accuracy of $\pm 0.2\,cm$ for the source location is assumed, thus combining this error with the traveltime uncertainty of $\pm 0.2\,\mu s$, we obtain an error in velocity of 0.29% for large raypaths and the error can reach 10.7% for the shortest raypath. Velocities are displayed as a function of the angle in figure 3.11a (angle convention in figure 3.3), indeed, several studies have presented this plot (Vasco et al., 1998; Bereš et al., 2013; Matonti et al., 2017) mainly to qualitatively study the degree of heretogeneities and anisotropy in the data domain. In an isotropic homogeneous model we would see a straight horizontal line, i.e., the same velocity regardless of the angle. However, before considering anisotropy or heterogeneity, one can see several outlier values where the velocity is overestimated. For instance, note that velocity seems constant between 180° and 225°, while under 180° we can see some outliers. This is the same around 90°, where we do not see major outliers. The values of 90° and 180° correspond to vertical and horizontal paths, respectively. At these angles, the receiver is located on the front, so that considering the source as a point source located at the middle of the PZT is a good assumption and allows to compute a reliable average velocity. Using only 90° and 180° source/receiver paths, the maximum velocity value we found is about $0.305\,cm/\mu$s. Figure 3.11b shows the source-receiver paths where the velocity is above $0.305\,cm/\mu$s highlighting that despite potential local heterogenities, globally a bad location of the effective source generates strong over-velocity estimations and this effect mainly affects the angles where outliers were detected in figure 3.11a, which indeed are basically the short paths.

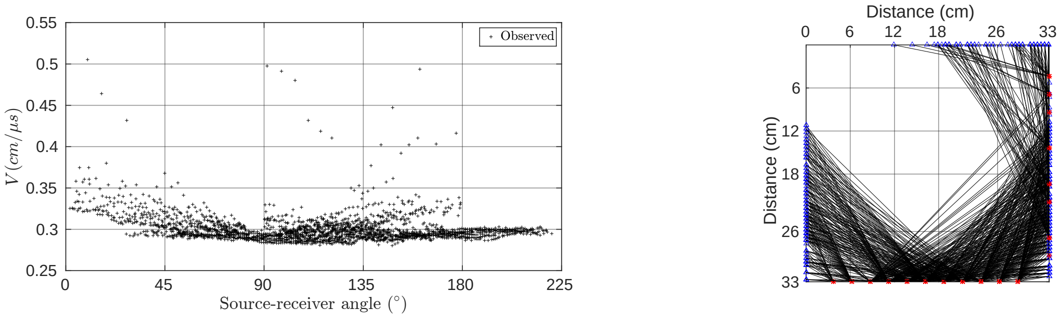

(a) **(b)**

Figure 3.11: (a) Average velocity as a function of the source-receiver angle (figure 3.3). Picked traveltimes and the assumption of straight distance between source-receiver are used to compute the velocity, the source being supposed to be located at the middle of the PZT. (b) Source-receiver paths where velocity was overestimated in (a), i.e., they correspond to values higher than the maximum value of $0.305\,cm/\mu s$ computed from near vertical/horizontal paths.

3.2.2 Models of source correction

The picked traveltimes represent the fastest arrival between two points, therefore the location of these two points has to be perfectly known. For a diameter of $3.8\,cm$ and knowing that each receiver position is every $0.5\,cm$, 8 traces are always located in front of the source. One option is to associate each of these traces with one virtual source located on the front. Figure 3.12a illustrates this discretization model, i.e., when receivers are located within the lateral limits of the extended source, the shortest path is considered (the vertical one in figure 3.12b), while the traces that are outside of the extended source are systematically associated with the nearest path, i.e., the virtual source being located on the edge of the PZT. Using this discretization, each trace is always associated with the nearest source location. Figure 3.12b shows the new path distribution, where 9 virtual source locations are considered they cover the diameter of the PZT. This modeling is denoted as the correct discretization for the rest of the chapter. This kind of modeling where the total PZT diameter is covered has been also proposed by Shen et al. (2021) for a PZT of 0.5 MHz being smaller than the PZT we are using.

The proposed source discretization is evaluated with velocity models where the local heterogeneities

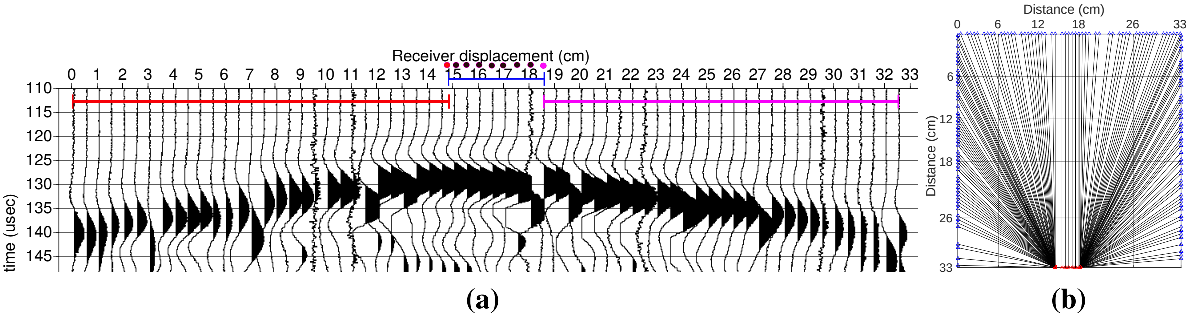

Figure 3.12: Illustration of the simple source discretization model. (a) The blue line is the total diameter of the source, each trace is associated with one virtual point source, in order to cover the total diameter, traces with red color are associated with the red source located on the edge, the same being done for the magenta group. (b) The new path distribution (one source is missing because that trace was not picked).

are known. For this, a synthetic dataset is created using the previously mentioned source discretization of 9 virtual sources and considering the 2384 paths that were picked in the real dataset, in order to be consistent between real and synthetics. The forward traveltime computation (Le Bouteiller et al., 2019) was performed on the isotropic velocity model of figure 3.13a which has been designed inspired by the real inversion results being presented afterwards, and a discretization of 80 × 80 elements is chosen to represent the model. The computed traveltimes along with the correct discretization source-receiver locations (figure 3.12a-b) are used to compute the average velocity of figure 3.13b as a function of the angle assuming straight paths. In order to identify the heterogeneities in an ideal isotropic situation, some shots have been colored whose acquisition can be deduced from figure 3.2a-b and table 3.1.

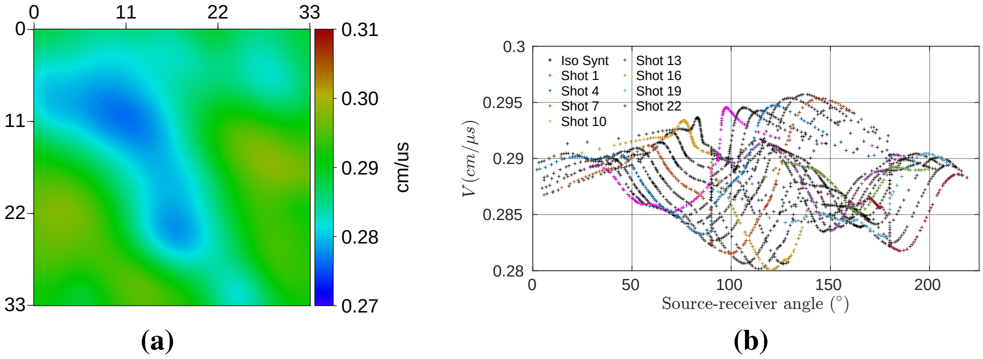

Figure 3.13: (a) Isotropic velocity model used to perform a forward modeling with the Eikonal solver. The source-receiver configuration is identical to the experimental one. Each source is discretized along 9 points. (b) Average velocity obtained by the computed traveltimes and the source locations of the 9 points discretization (figure 3.12a-b) considering straight paths between source-receiver pairs. Some shots are colored which can be localized using figure 3.2a-b and table 3.1

We present in figure 3.14, 5 source discretization models designed to approximate the real PZT source, figure 3.14a assumes a single source at the middle of the PZT, figure 3.14b-c three sources and figure 3.14d-e using 5 sources, in both cases the sources being equally distributed with always one located in the center of PZT. Besides, the three and five points models are divided in two sub-models, the first is with virtual sources near the edges (figure 3.14b and d) and the second is with sources located on the edges (figure 3.14c and e).

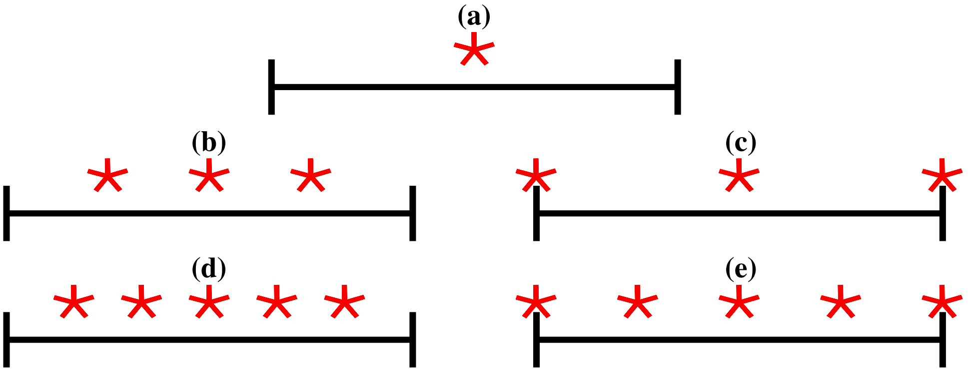

Figure 3.14: Source discretization modeling. (a) One single source at the middle of the PZT. (b) Three sources which are near the edges. (c) Three sources with sources located on the edges. (d) Five sources with sources near the edges. (e) Five sources with sources located on the edges. Point sources are equally spaced.

We show in figure 3.15a the case of figure 3.14b, each source is associated with one color, note that the red and magenta sources are not located on the edges. Figure 3.15b shows the path distribution for this choice. The proposition of figure 3.14c for three sources is shown in figure 3.16a, the difference is that now the sources are located on the edges so that traces are always associated with the nearest source and the path distribution displayed in figure 3.16b exhibits that the 3.8 cm length of the extended source is now covered. To better approximate the PZT surface with 5 sources, the first option of figure 3.14d is the same of figure 3.15a but with two more sources, therefore the sources are getting closer to the edges, figure 3.17a shows the path distribution highlighting the coverage is higher than in figure 3.15b. The second model of 5 sources (figure 3.14e) is shown in figure 3.17b, similar to figure 3.16b but with two more sources, both covering the total PZT surface.

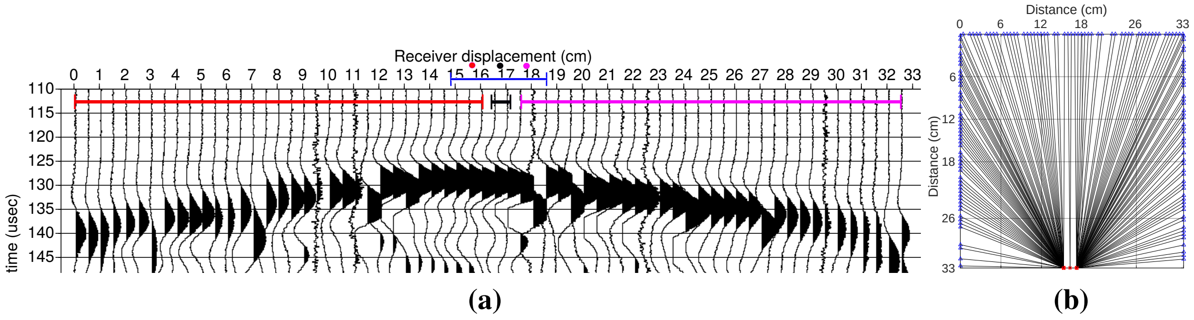

Figure 3.15: Illustration of the 3-sources discretization. (a) The blue line is the total diameter of the source, the source is divided in three points equally distributed. The color of the traces are associated with the corresponding color of the source. The total diameter is not covered. (b) The path distribution for this shot discretized.

The next step is to quantify the effect of the mentioned discretizations. For each proposed discretization, from the traveltimes obtained in the model of figure 3.13a, differential source-receiver distances are computed according to each source discretization allowing to obtain both the average velocities and angles. Figure 3.18a (identical to figure 3.13b) is the true solution, the RMS for apparent velocity in

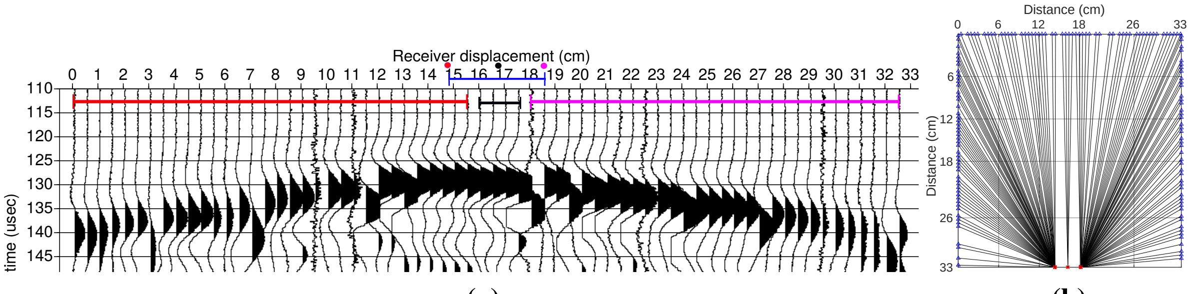

(a) **(b)**

Figure 3.16: Illustration of the second 3-sources discretization. (a) The blue line is the total diameter of the source, the source is divided in three points equally spaced. The color of the traces are associated with the corresponding color of the source. The total diameter is covered. (b) The path distribution for this shot discretized.

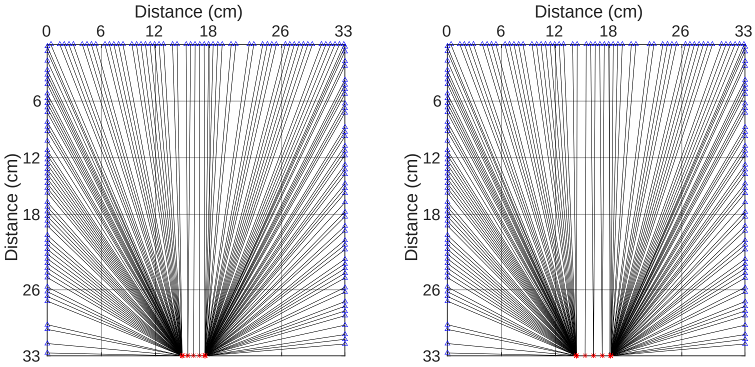

(a) **(b)**

Figure 3.17: Source discretized with 5 points. In both the points are equally distributed. In (a) the diameter of the source is not covered. In (b) one source is placed on each edge of the PZT, therefore the total diameter is covered.

percentage is given by

$$RMS(\%) = 100 \times \sqrt{\frac{1}{N}\sum_{sr}\left(\frac{v_{approx} - v_{true}}{v_{true}}\right)^2}, \tag{3.1}$$

where v_{approx} is the average velocity computed for each model and N is the total number of source-receiver paths. The first one is locating only one source in the middle of the PZT (figure 3.14a), the effect is shown in figure 3.18b. Velocities are overestimated (source-receiver distances are larger) when the source is not in front of the receiver leading to a RMS error of 7.7%, values at 90° and 180° not suffering major changes. We can observe an improvement using the first option of three sources (figures 3.14b and 3.15a-b) in figure 3.18c, where some outliers still exist leading to RMS of 3.8%. The second option of three sources (figures 3.14c and 3.16a-b), namely with sources placed on the edges suppresses all the outliers (figure 3.18d), leading to a RMS of 0.19%. The first model with five sources (figures 3.14d and 3.17a) is displayed in figure 3.18e, and gently improves the velocity computation compared with the similar option by three sources (figure 3.18c) providing a RMS of 2.43%. Finally, figure 3.18f shows the effect of adding two more sources inside the transducer and remaining with sources on the edges (figure 3.14e and 3.17b). The result is very similar to both the true values and the values of figure 3.18d, the RMS reaching 0.19%. It is clear with this analysis that the source has to be discretized at least considering three sources including locations on the PZT edges.

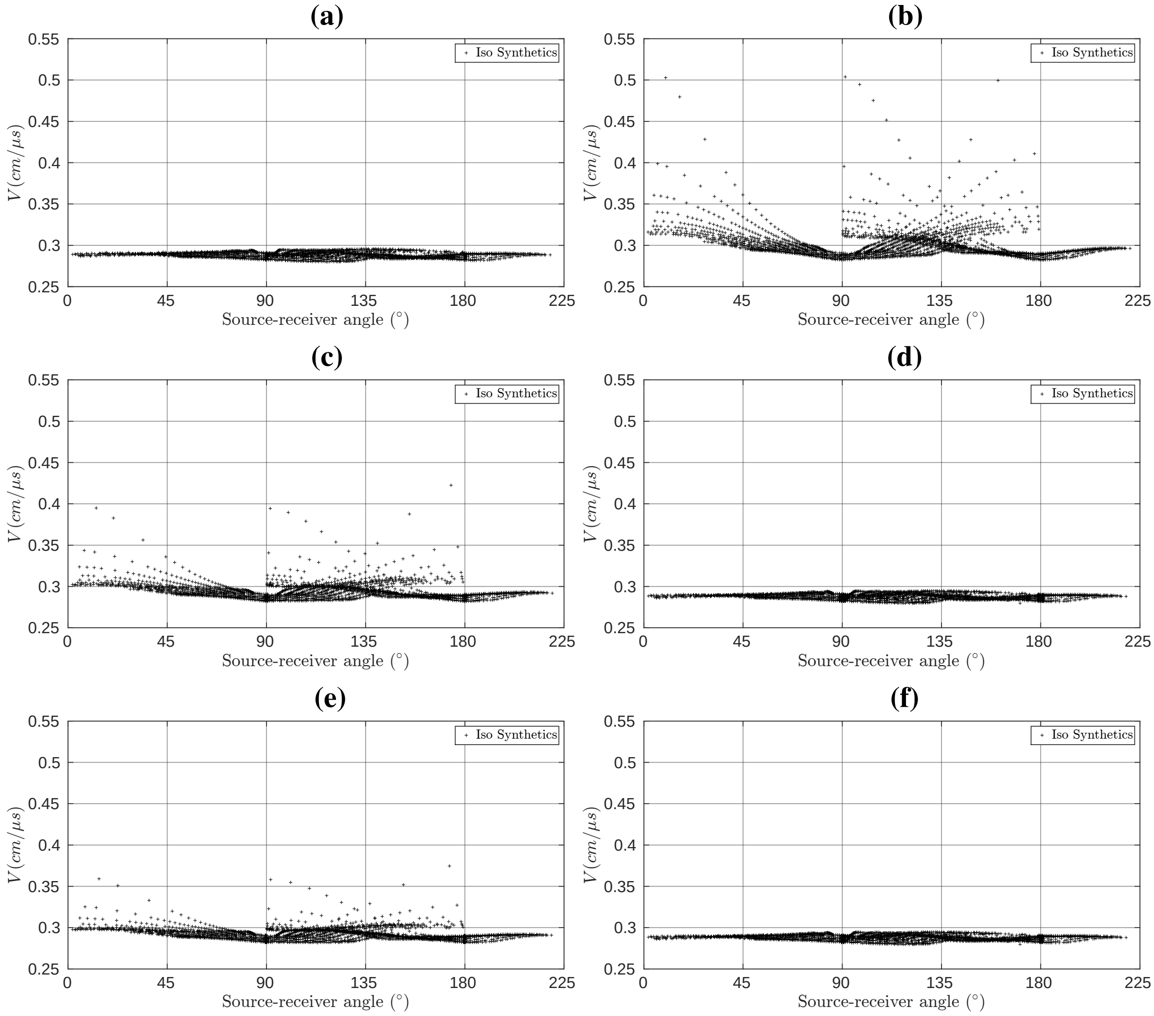

Figure 3.18: Average velocity pattern according to the different source discretization studies. Velocities obtained according to: (a) the true model with the correct discretization of 9 sources. (b) One middle source assumption, RMS=7.7%. (c) The first option of three sources, RMS=3.8%. (d) The second three sources discretization, RMS=0.19%. (e) The first model of five sources, RMS=2.43%. (f) Using five sources, second model, RMS=0.19%.

3.2.3 Sensitivity of tomography to source discretization: a synthetic approach

The goal of this study is to evaluate how different source discretizations affect inversion results. At each iteration, the forward discretization to compute synthetic traveltimes is the same discretization we used to create the synthetic dataset in figure 3.13b. For the inverse grid we represent the model on a 34×34 grid points, with 1 cm between points. All inversions are stopped at iteration number 15 and we use a homogeneous initial model of $0.29\,cm/\mu s$. In order to compare the inversions, we use the RMS in percentage for the traveltimes

$$RMS(\%) = 100 \times \sqrt{\frac{1}{N}\sum_{sr}\left(\frac{t_{cal} - t_{obs}}{t_{obs}}\right)^2}, \tag{3.2}$$

where t_{obs} is the dataset created with the true model of figure 3.13a and t_{cal} is the one obtained in the final model of each inversion, we use this RMS formulation for the rest of the chapter. Figure 3.19a is the true model, figure 3.19b shows the inverted model obtained after source corrections were made with the true discretization model: it is quite similar to the true model, it does not present any artefacts and exhibits a low RMS of 0.23%. Figure 3.19c is the tomography image obtained considering only one source located in the middle of the transducer: it shows several large artefacts with localized high velocities located nearby the sources and certainly caused by the short paths, the RMS being 5.7%. Figure 3.19d is the inversion result obtained considering the first option of the three sources model (figures 3.14b and 3.15a-b). A slight improvement is visible but high velocity artefacts nearby the sources are still present, leading to a RMS of 2.85%. Finally, the second option of the three sources model (figures 3.14c and 3.16a-b) results in figure 3.19e. The obtained velocity model is very similar to the one derived with the true discretization, and consequently also very similar to the true model, the RMS being 0.27%. Considering this result, we felt that an inversion considering 5 sources was not necessary, the conclusions being the same of figure 3.18. This sensitivity analyses suggests that the extension of the source can be correctly modelled with a three-point source model, with 2 sources located on the edges and one at the middle of the PZT (figures 3.14c and 3.16a-b).

The same sensitivity analysis has been performed when anisotropic multiparameter inversion is considered, in order to identify the effect of source discretization corrections on vertical and horizontal velocities. For that purpose, we first created an anisotropic dataset using the same source discretization as in the isotropic example. The same velocity model is used for the vertical velocity (figure 3.20a), while imposing an elliptical anisotropy with the Thomsen's parameter ϵ shown in figure 3.20b. In addition, we decide to tilt the axis of symmetry by changing the parameter θ which as we defined in section 1.1.3, it is $\theta = 0^\circ$ in VTI and $\theta = 90^\circ$ in HTI model. We show in figure 3.21 the angle convention difference between θ and the source-receiver angle. The angle we impose to tilt the model is $\theta = 135^\circ$ which is close to the orientation of the low velocity structure identified in figure 3.20a, thus simulating an elliptical TTI model (ETTI). A detailed analysis of the effect of θ will be presented in section 3.3. The computed traveltimes are then used to estimate the average velocity as a function of the angle (figure 3.20c). One can see the effect of this smooth anisotropic model with the tilted symmetry, the low velocities corresponding to the low velocity structure. For the other angles, the average velocity increases due to the effect of ϵ. We compare in figure 3.20d these average velocities with those obtained in the isotropic velocity model of figure 3.13b. We can observe the expected horizontal pattern of the isotropic average velocity compared with the anisotropic dataset of figure 3.20c. The conclusions about the anisotropic average velocity patterns for different source discretizations are the same than in the isotropic case: the same pattern of outliers shown in figure 3.18 is visible and these outliers fade when a correct source discretization is used. We go directly to the inverse results to evaluate the effect of the different proposed source modeling in the anisotropic reconstructed models.

For the anisotropic inversion, we follow the workflow proposed in chapter 2. A smooth initial model is built from the isotropic inversion. Following the elliptical approximation, we invert the vertical and horizontal velocities. We show in figure 3.22a the true model of vertical velocity, we use ϵ of figure 3.20b to compute the horizontal velocity, namely $V_h = V_v\sqrt{1+2\epsilon}$ in figure 3.22b. The latter has two smooth zones of higher velocity near the edges of the model. We used both velocities to compute

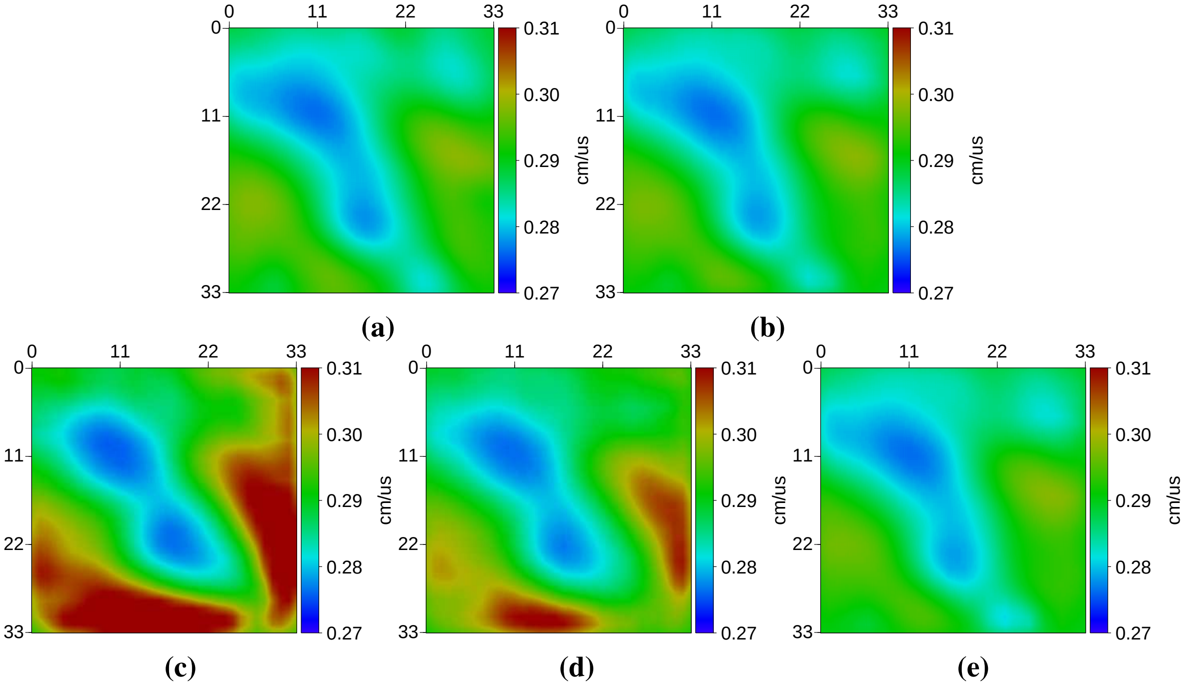

Figure 3.19: Inversion result considering an isotropic synthetic model and different source discretizations. (a) True velocity model. (b) Velocity model obtained after inversion when the correct source discretization is used, RMS=0.05%. (c) Velocity model obtained after inversion when one source is considered, RMS=5.7%. (d) Velocity model obtained after inversion when three sources, first option is considered, RMS=2.85%. (e) Velocity model obtained after inversion when three sources, second model is applied, RMS=0.15%.

the percentage of anisotropy R=$[(V_h/V_v) - 1] \times 100$ in figure 3.22c. For the inversion, we follow the same discretizations used for the isotropic inversion, while the parameter θ is fixed to the true value, i.e., $\theta = 135°$.

The first case, displayed in figures 3.23a-c is assuming only one source located at the middle of the PZT. It shows the very bad reconstruction of the structures with overestimated values of velocity in left and right faces, and a low velocity anomaly is created due to the wrong source assumption. This leads to a highly contrasted percentage R in figure 3.23c, a RMS of 5.1% is obtained. The addition of two more sources not located on the edges partially reduces the artefact in figure 3.23d-e, the percentage R in figure 3.23f shows that the artefact are strong on the corners because in these short offset zones, the inverted velocities are very sensitive to wrong source locations, we can however observe slight improve in the RMS to 2.5%. Using three sources, but with two point sources located on the edges of the transducer, the inversion significantly improves as displayed in figure 3.23g-h. All the previously discussed artefacts are removed in the velocity models, providing a better percentage R (figure 3.23i) being quite similar to the true percentage (figure 3.22c). A slight smearing is produced on the right side because of the reduced vertical illumination in this zone, we should recall that sources were not located exactly on the corners, there is a space between the corner an the source located on the edge of the source device, consequently the edges are always less illuminated, this causes some inversion drawbacks associated with the edges of the block, in addition, we did not record the bottom face with the sources located on the right (figure 3.2b) which might help to fix this smearing. Moreover, when using the true model of either V_v or V_h as a passive parameter and performing a monoparameter inversion of

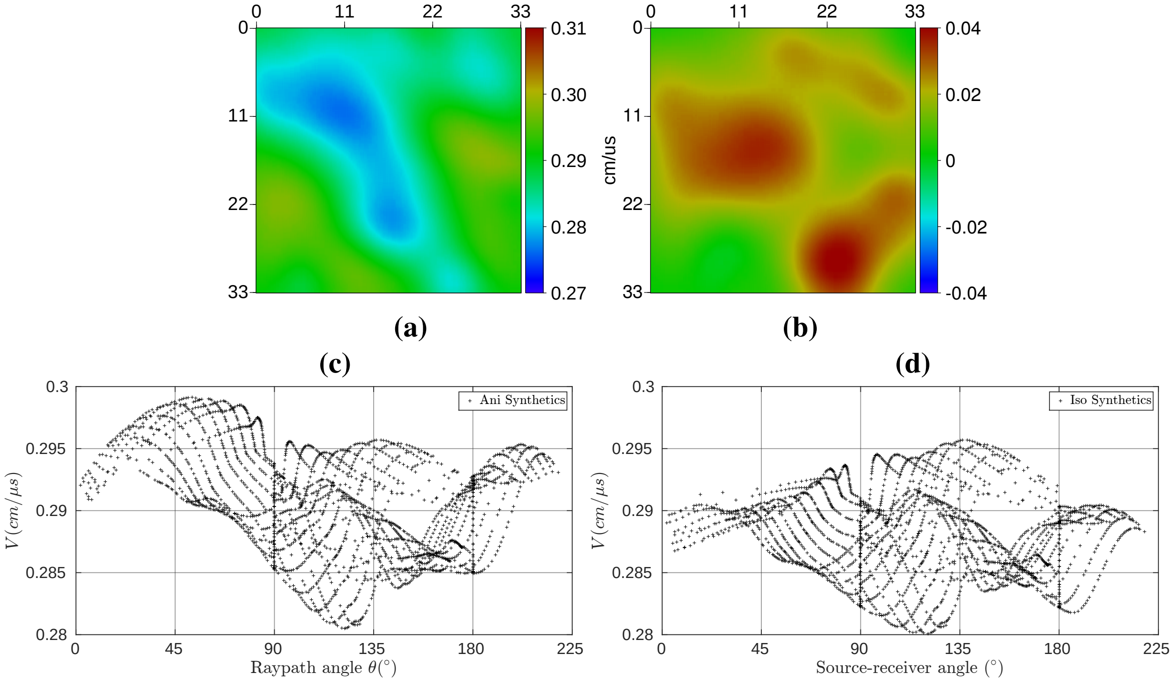

Figure 3.20: Anisotropic models used to create a synthetic dataset. (a) Vertical velocity. (b) Thomsen's parameter ϵ being identical to δ. The axis of symmetry was tilted to $\theta = 135°$, therefore we have an ETTI model. (c) Average velocity computed with the anisotropic traveltimes obtained in (a-b), and angles computed with the correct source discretization. (d) Average velocity obtained with the model of (a) assumed isotropic and the correct source discretization, note that (d) is identical to figure 3.13b.

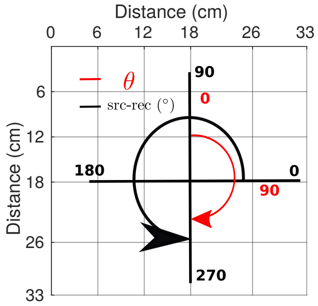

Figure 3.21: Angle convention for the anisotropic parameter θ and its difference with the source-receiver angle.

the other velocity, the outcome is that the final R model does not present this smearing. The inversion of figure 3.23g-i reach a satisfactory RMS of 0.12%. The last inversion displayed in figure 3.23j-l is performed using the true discretization of the transducer, namely 9 sources, it basically shows the same result of figure 3.23g-i, with an improvement in the RMS to 0.03%. Note that the two last results have a small failure in the center of V_v (figures 3.23g and 3.23j) which is a full-illumination zone, while the same velocity under the isotropic case (monoparameter inversion) is basically equal to the true model (figure 3.19b and 3.19e), this highlights the added complexity on the non-linearity of the inversion when two parameters are inverted. However, this smooth anisotropic example with full-illumination clearly shows that our approach is capable to reconstruct the two parameters simultaneously with very small

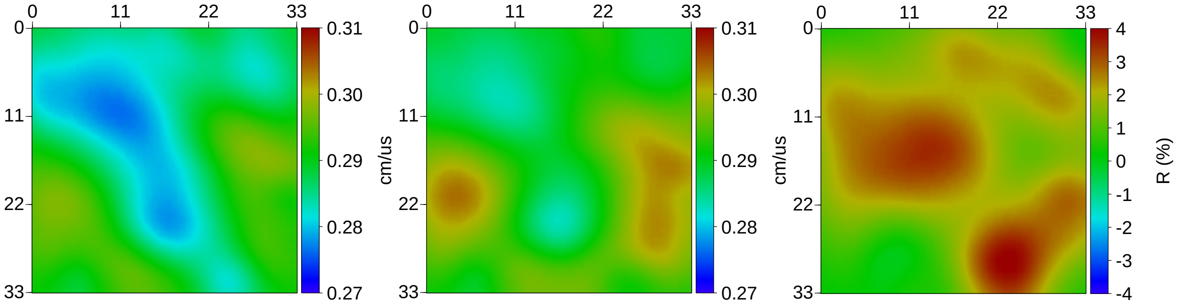

(a) **(b)** **(c)**

Figure 3.22: True models of (a) vertical velocity and (b) horizontal velocity. They are used to compute the percentage of anisotropy R in (c).

localized differences. To sum up about the source discretization, the same conclusions can be drawn as in the isotropic inversion, the exact diameter of the transducer has to be covered locating sources on the edges or, failing this, strong artefacts in both inverted velocities would arise.

Following the synthetic results, we select for the real dataset the discretization of figures 3.14c and 3.16, namely one source in the middle and sources located on the edges. Figure 3.24a shows the dataset without correction, with several outliers of high velocity. When the correction is applied, figure 3.24b shows that most of them have been suppressed. One can see that a few velocities are now underestimated. In general, we have shown the importance of the source size at this experimental scale, where a source of $3.8\,cm$ is used to investigate a medium of $33 \times 33\,cm$ dimensions, synthetic examples were used to validate different options to discretize the diameter of the source. Now, the study will focus on the potential anisotropic characteristics of the block.

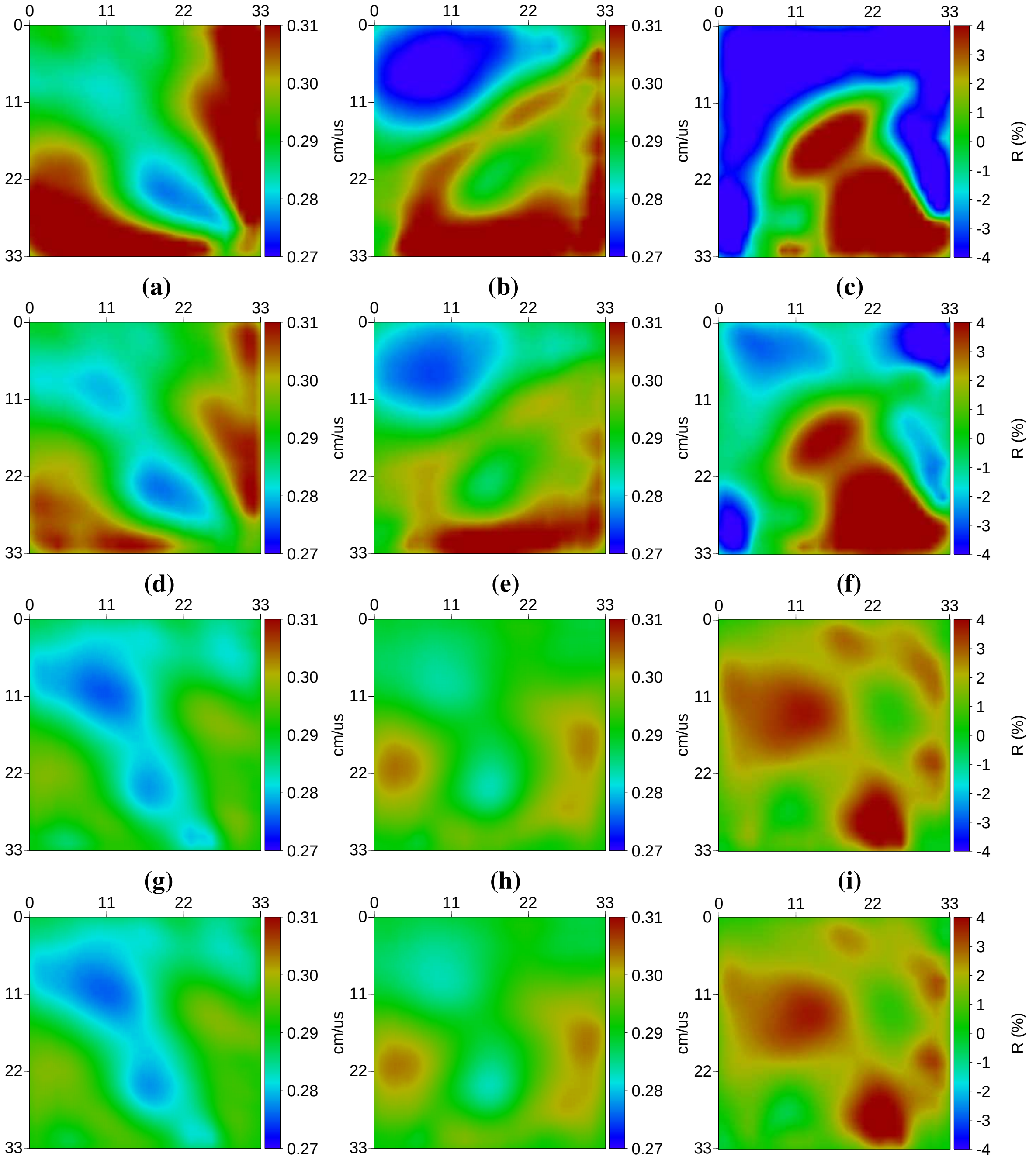

(a) (b) (c)

(d) (e) (f)

(g) (h) (i)

(j) (k) (l)

Figure 3.23: Source discretization effects on inversion results of anistropic synthetic dataset. (a) Vertical velocity, (b) horizontal velocity and (c) percentage of anisotropy R models obtained when a single source is considered, RMS=5.1%. (d) Vertical velocity, (e) horizontal velocity and (f) R models when three point discretization with sources near the PZT edges are considered, RMS=2.5%. (g) Vertical velocity, (h) Horizontal velocity and (i) R models when three point discretization with sources at the edges of the transducer are considered, RMS=0.18%. (j) Vertical velocity, (k) horizontal velocity and (l) R models when the correct discretization is considered, RMS=0.08%.

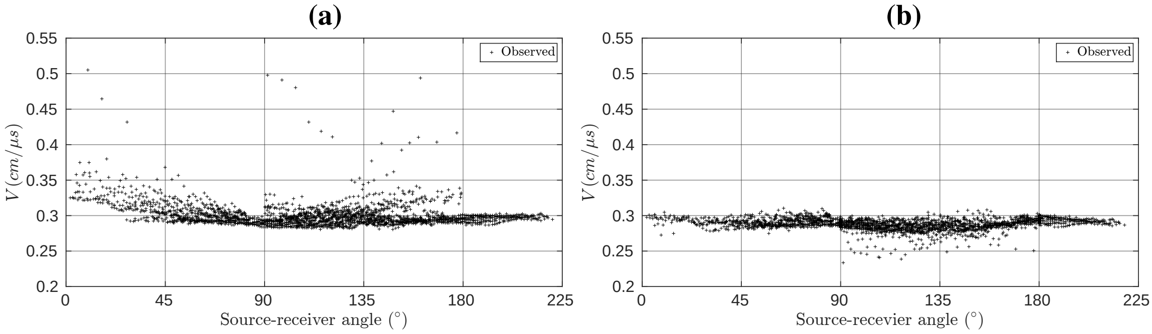

Figure 3.24: Average velocity of the real dataset as a function of the source-receiver angle. It is presented assuming (a) one source located in the middle of the transducer and (b) 3-sources discretization based on one source in the middle and sources located on the edges.

3.3 Anisotropy investigations

Unlike isotropic inversion, anisotropy implies more than one parameter to invert which makes the problem less determined, this can be mitigated by a suitable anisotropic approximation to represent the observations. We propose in this section a data-driven approach based on the velocity versus angle pattern which allows us to justify the chosen anisotropic model for the inversion.

3.3.1 Anisotropic model selection

The real dataset with the suitable source approximation discussed in section 3.2 is presented in figure 3.25 (same of figure 3.24b with a zoom imposed) under the form of apparent velocity versus source-receiver angle, with a straight path assumption. The angles and velocities have been computed according to the three point approximation of each source, as discussed before (figures 3.14c and 3.16). One classical approach to analyse this pattern is to try to fit it with some analytical anisotropic functions which reproduces the pattern. For instance, Bereš et al. (2013) used a cosine function to fit a dataset acquired in a fractured karstic limestone massif between underground galleries. According to the cracks orientation they assumed a HTI model, which was then tilted to the angle found in the cosine fit. This angle was fixed in an TTI anisotropic inversion to obtain a maximum anisotropy of 15%. Matonti et al. (2017) performed a seismic acquisition at a fractured block of limestone located in a quarry. As the block was excavated, full illumination like in our experiment was possible. They also used a cosine fit to approximate the average velocity versus angle pattern where the estimated angle of rotation was consistent with the orientation of reactivated fractures. According to the dataset, an average 8% of anisotropy was found. This interesting dataset will be revisited at the end of the chapter with an anisotropic tomography inversion. It is worth mentioning that the cosine fit assumes homogeneous anisotropy, it defines an intermediate point of the velocity curve, subsequently the velocity increases or decreases depending of the angle, this homogenous assumption is well justified since the objective is not to fit each value (heterogeneities) but rather to fit the global pattern, therefore it is possible to claim about the presence of anisotropy. In this section, we also assume homogeneous anisotropy in the laboratory dataset and applied a methodology to derive velocity versus angle values. For that, we

1. rely on the elliptical assumption ($\epsilon = \delta$) and run a forward modeling with three homogeneous parameters being V_v,ϵ and θ;

2. several combinations of parameters are used and RMS of velocity (equation (3.1)) is computed between the observed points (figure 3.25) and the velocity values computed from the synthetic traveltimes.
3. the combination of parameters with the lowest RMS is the optimum model that will be crucial for tomographic decisions.

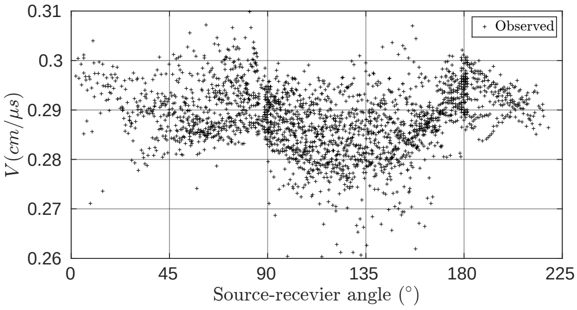

Figure 3.25: Average velocity of the real dataset as a function of the source-receiver angle. Velocity and angles are estimated with the assumption of three point sources in each PZT, one at the middle and sources located on the PZT edges.

Before presenting the optimization of the three parameters, it is important to understand the effect of each parameter on the velocity versus angle pattern, thus a value of $V_v = 0.284\, cm/\mu s$ is used while the other parameters are tested. For the parameter θ, figure 3.26a shows how is defined the orientation and the difference with the source-receiver angle. We first illustrate three synthetic computations in figure 3.26b, obtained i) where no anisotropy is present ($\epsilon = \delta = 0$, black curve) showing the same velocity for all angles. It must be noted that here, the symmetry axis is vertical, namely $\theta = 0°$, however in absence of anisotropy, the angle of symmetry does not have any effect on the traveltime, and so the same horizontal line would be obtained in an isotropic HTI media ($\theta = 90°$); ii) a degree of anisotropy was added imposing $\epsilon = 0.03$ and $\epsilon = -0.03$ where both represent a 3% of anisotropy, and the forward modeling is run assuming a EVTI model, thus two different curves are displayed in figure 3.26b. According to the analytical expression of anisotropy $V_h = V_v\sqrt{1+2\epsilon}$, if ϵ is positive we have a maximum velocity in the horizontal direction (V_h), perpendicular to the symmetry axis, while the minimum velocity (V_v) would be parallel to the symmetry axis, this is the case for the the blue curve in figure 3.26b, while in the orange curve ($\epsilon < 0$), the roles of the minimum and maximum velocity are inverted. The latter case is unrealistic according to laboratory measurements in carbonates (Martínez and Schmitt, 2013; Gordin et al., 2020) where ϵ was always higher than zero, and this is also obtained by Bereš et al. (2013) at the field scale in the same kind of medium, consequently this option of $\epsilon < 0$ is not considered for the parameter optimization. Moreover, looking carefully at the dataset of figure 3.25, the values around the angle of 180° (near-horizontal paths) are in general higher than the values obtained at 90° (near-vertical paths) which is clearly a signature of anisotropy. Therefore, the next approximation is to fit the pattern with EVTI and EHTI models using $\epsilon = 0.03$ in both, the results displayed in figure 3.26c shows that the preferred orientation of anisotropy features is not well approximated with these assumptions, and thus θ needs a better approximation.

The three parameter optimization has been computed considering a range of V_v, θ and ϵ, therefore we select the range of 3 different V_v where the RMS is close to the minimum and display the evolution of the other two parameters in figure 3.27a, 3.27b and 3.27c being $V_v = 0.283\, cm/ns$, $V_v = 0.284\, cm/ns$ and $V_v = 0.285\, cm/ns$, respectively. The minimum was obtained in figure 3.27b showing an RMS =

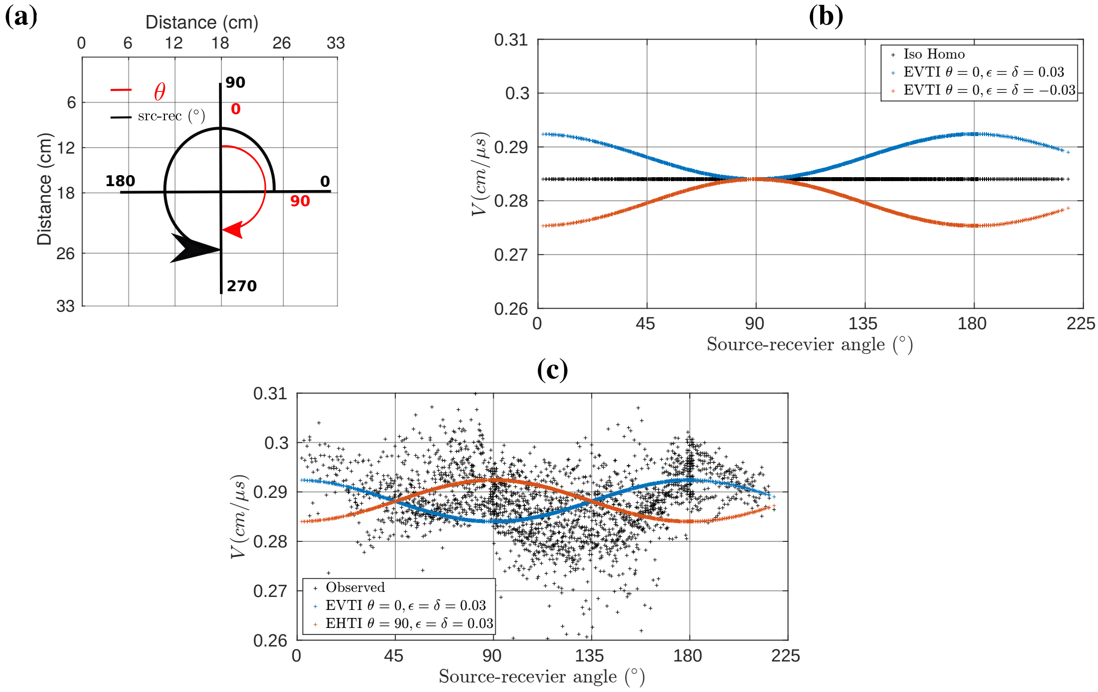

Figure 3.26: Synthetic homogeneous examples to investigate anisotropy effects of the velocity pattern. The value of the imposed Thomsen' parameters represents 3% of anisotropy while the value of vertical velocity is $0.284\,cm/\mu$s. (a) Angle convention for the anisotropic parameter θ and its difference with the source-receiver angle. In (b) the black horizontal line is the velocity in a homogenous isotropic media of $0.284\,cm/\mu$s while two elliptical VTI curves are added to show the effect of sign changes in Thomsen' parameters. (c) An elliptical HTI and an elliptical VTI curves are superimposed on the dataset.

2.491% while the optimum parameters are $\theta = 145$ and $\epsilon = 0.03$. However, the optimum parameters and the RMS are not substantially different with $V_v = 0.283\,cm/ns$ (figure 3.27a) being the RMS $=$ 2.494% and $\epsilon = 0.04$, while using $V_v = 0.285\,cm/ns$ (figure 3.27c) we reach an RMS $= 2.517\%$ and $\epsilon = 0.03$, moreover $\theta = 145°$ was always obtained in the three images. It is important to underline that the choice of $V_v = 0.284\,cm/ns$ and $\epsilon = 0.03$ to compute the velocity curves in figure 3.26b-c was not arbitrary, it was based on the optimization results of figure 3.27b.

We plot in figure 3.28a three curves varying the value of θ in order to visualize the effect of this parameter, the optimum combination of parameters (figure 3.27b) is shown in magenta while the other two curves are shifted. It must be noted that $\theta = 145°$ is reciprocal to $125°$ for the source-receiver angle (figure 3.26a), and therefore the minimum velocity $V_v = 0.284\,cm/ns$ being located at that angle. The last parameter to be evaluated is δ, related to the NMO velocity by $V_n = V_v\sqrt{1+2\delta}$, whose influence affects the diagonal directions with respect to the symmetry axis ($\theta = 145°$). We perform an optimization fixing the parameters obtained in figure 3.27b and only δ is evaluated, thus an optimum $\delta = 0.05$ leads to an RMS $= 2.468\%$ being displayed in figure 3.28b and we also use $\delta = 0$ which gives an opposite effect on the velocity curve and RMS $= 2.59\%$. The optimum value obtained for δ is not realistic since most measurments made for transversely isotropic formulation at seismic frequencies indicate that $\epsilon > \delta$ (Thomsen, 1986; Sayers, 1994; Tsvankin and Thomsen, 1994). For instance, in the case of weak anisotropy caused by thin layering of isotropic media, Berryman (1979) and Helbig et al.

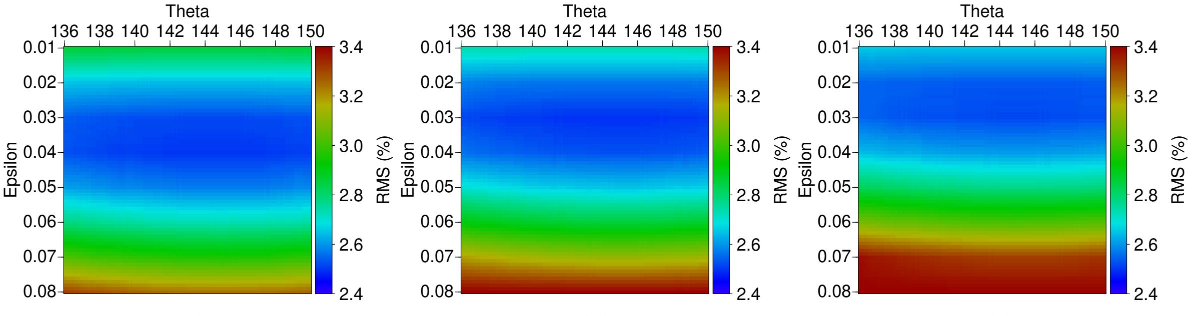

(a) **(b)** **(c)**

Figure 3.27: Misfit of the three parameter optimization assuming constant values. (a) $V_v = 0.283\,cm/\mu s$, the minimum found at $(\epsilon = 0.04, \theta = 145°)$, RMS $= 2.494\%$. (b) $V_v = 0.284\,cm/\mu s$, the minimum found at $(\epsilon = 0.03, \theta = 145°)$, RMS $= 2.491\%$. (c) $V_v = 0.285\,cm/\mu s$, the minimum found at $(\epsilon = 0.04, \theta = 145°)$, RMS $= 2.517\%$. RMS in percentage computed from equation 3.1.

(1979) showed that in all cases $\epsilon \geq \delta$, and this was mathematically proven by Brittan et al. (1995). Moreover, the optimization of δ allows us to identify two things: i) the weak effect of this parameter on the data, note that a very small portion of the data is fitted when δ varies (figure 3.28b), while a change of V_v or ϵ will produce a strong shift on the curves (figure 3.26b-c). This is consistent with the circular full-illumination experiment of section 1.2.2, where we showed the gradient of both V_n and δ whose amplitude was smaller than the other parameters. ii) The optimum $\delta = 0.05$ (figure 3.28b) is not substantially far from the optimum elliptical case $\epsilon = \delta = 0.03$ (figure 3.27b and 3.28a). These two factors allow us to consider the elliptical case as a suitable model to approximate the medium. In spite that we have the benefits of a full illumination coverage, the inclusion of a third parameter in the optimization increases the ill-posedness and non-uniqueness of the solution, one option is to consider a hierarchical scheme designed to invert the third parameter (Waheed et al., 2016) but this strategy is beyond the scope of this work, which now consider an elliptical assumption (magenta curve in figure 3.28b) being previously justified.

(a) **(b)**

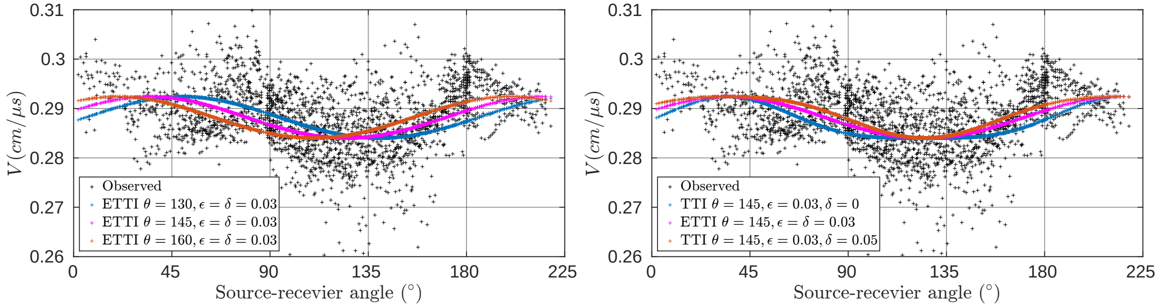

Figure 3.28: Synthetic homogeneous examples using $V_v = 0.284\,cm/\mu s$ and varying the values of (a) θ and (b) δ to illustrate the effects. (a) Results obtained by varying the parameter θ, an optimum $\theta = 145°$ was found with $\epsilon = 0.03$, RMS $= 2.491\%$ (figure 3.27b). (b) Results obtained by varying the parameter δ leading to an optimum value of $\delta = 0.05$, RMS $= 2.468\%$. In both, the magenta curve is the optimum under the elliptical assumption.

To sum up, by a simple optimization based on homogeneous parameters injected in our forward engine, we can approximate the global pattern of the observations, which clearly shows anisotropy.

An optimization of (V_v, ϵ, θ) shows that we have about 3% of anisotropy which will be validated by multiparameter inversion along with the heterogeneities. There are two finding with our approach: i) the dataset in the block cannot be explained by a VTI nor HTI model, there is a rotation of the symmetry axis given by $\theta = 145^\circ$ and ii) the elliptical assumption is a fair approximation for most of the observations. These two results allow us to reduce the number of parameters in the inversion which is desired due to the non-uniqueness in multiparameter traveltime tomography.

3.4 Inversion of the real dataset

In this section we extend the inversion procedure to the laboratory dataset using a multiparameter approach restricted to an elliptical anisotropic model. Special attention is given to certain source-receiver offsets in order to reduce potential artefacts linked to a incorrect source discretization correction. The results will then be discussed in terms of rock properties and discontinuities.

3.4.1 Isotropic inversion

We perform an isotropic inversion of the real dataset that clearly exhibit a degree of anisotropy (section 3.3). Besides, we validate in this section the conclusions obtained in synthetic examples about the source correction. The inverse grid for all the inversion tests is set as 23×23 nodes, with a separation of $1.5\,cm$ between nodes, consequently we have $(23-1) \times 1.5 = 33\,cm$ being the total length of the block faces and this gives us 1156 as the total number of degrees of freedom. The decision is motivated by the estimated wavelength in section 3.1.4 which imposes a physical limitation on the spatial resolution we could achieve, we expect large length scales of velocity variations (high-frequency approximation) that can be described with this discretization, while a finer discretization has been also evaluated with any numerical improvement. We should recall that the laser is recodirding every $0.5\,cm$, being useful in terms of illumination with satisfactory results in synthetics (section 3.2.3), however, it is not possible to reach that level of relolution with the chosen PZT source. For the forward modeling, we also evaluated different discretizations comparing the error and the model reconstruction of each result, we found that square elements with $0.625\,cm$ on the edges was optimum for a good accuracy in the computation of traveltimes, while decreasing the length of the edges (finer discretization) led to the same error.

We begin the analysis by performing an isotropic inversion, we use an homogeneous initial model of $V = 0.284\,cm/\mu s$ being justified by the previous data-driven optimization (section3.3.1), the inversion is stopped after 8 iterations and the whole the dataset is considered, namely 2384 traveltimes. The first inversion considering one source located at the middle of each transducer is shown in figure 3.29a. As expected, several artefact of high-velocity structures are visible, while the RMS reaches 5.1% (computed from equation 3.2). The corresponding result of the isotropic inversion on synthetics is shown in figure 3.29b (same of figure 3.19c) which exhibits the same arfefacts generated by a bad source location. The second inversion presented in figure 3.29c is obtained using the correct source discretization of 9 points (figure 3.12). Most of the high-velocity artefacts are suppressed, although there is still a small anomaly on the right bottom corner where only short offset paths are present. However, the RMS has been reduced to 2.1%. The last inversion is obtained assuming three point sources (figure 3.14c and 3.16). Qualitatively it is very similar to figure 3.29c with a RMS of 2.14%, while in terms of traveltime units, the RMS is $1.63\,\mu s$ for this assumption and $1.60\,\mu s$ when using 9 points, consequently the same conclusion than those obtained on synthetics: we can approximate the surface of the transducer using only three sources, one located on the left edge, one at the center and one on the right edge. It must be noted that this source approximation was used to investigate the anisotropy in section 3.3. Finally, after testing different initial models for the anisotropic inversion, we choose the model shown in figure 3.29d, it was designed by taking the isotropic result at the iteration 4 and then the smooth operator is applied, one may see that it is almost homogeneous.

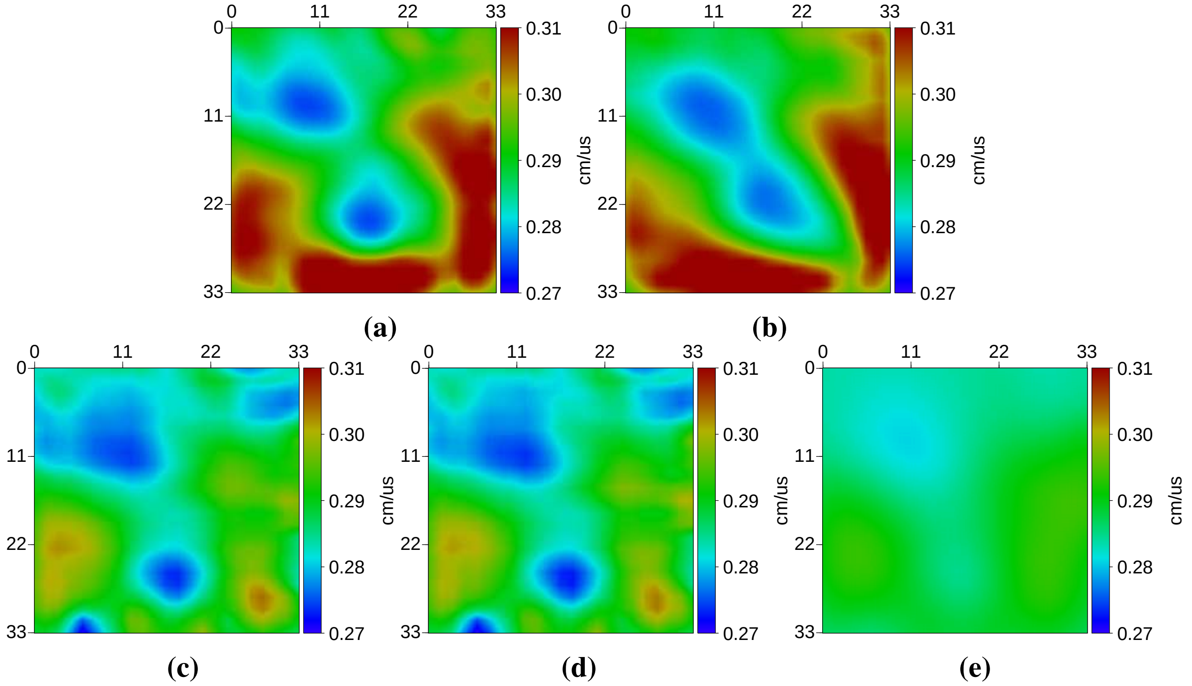

Figure 3.29: Inversion results of the real dataset with an isotropic model. (a) Velocity obtained using one source located at the middle of each transducer, RMS $= 5.1\%$. (b) Isotropic synthetic result obtained using one source located at the middle of each transducer. (c) Velocity model obtained assuming the 9 points source discretization, RMS $= 2.1\%$. (d) Inverted velocity assuming three points source discretization, sources being located at the middle and on the edges of the transducer, RMS $= 2.14\%$. We extract a model at the iteration 4 and apply the smooth operator to design (e) initial model for V_v and V_h in the anisotropic inversion.

3.4.2 Multiparameter anisotropic inversion

In the absence of a multiparameter inversion workflow, one option is to invert V_v and freezing a degree of anisotropy during all the optimization. For instance, Menningen et al. (2018) did ultrasonic measurements in marble samples, the ray-based approach of Jackson and Tweeton (1996) under the elliptical assumption was used in a single-parameter inversion of V_v while a degree of anisotropy remained constant ($\epsilon = const$) and knowing that $V_h = V_v\sqrt{1+2\epsilon}$, they presented a model with 20% of anisotropy that explained the observation better than the isotropic inversion. Although we could also do the same, we go directly to our multiparameter workflow because the fixing of anisotropy is a big assumption that might certainly introduce errors.

Before the multiparameter inversion, a look at the dataset of figure 3.25 shows some velocity values that are well below the general pattern and other values are above. To identify the source-receiver pair associated to these outlier values, figure 3.30a illustrates the paths that produce values lower than 0.275

cm/μs and higher than 0.305 cm/μs, moreover the velocity versus angle after filtering these traces is shown in figure 3.30b. Note that figure 3.30a is analogous to figure 3.11b which highlighted the source-receiver pairs with overestimated values. From figure 3.30a, we can conclude that most of the paths are associated to short offsets that were overcorrected when the source discretization approach was applied or in the case of values higher than 0.305 cm/μs, the correction was not enough. This can be explained because these offsets are very sensitive to: 1) positioning error of the source, which means a human error introduced during the acquisition, a very small error of millimeters can cause these velocity values to suffer large decrease/increase; 2) the picking uncertainty, which at these offsets a minimum variation of traveltime can produce drastic changes of velocity; and 3) the source discretization that can lead to a overcorrection or might be not enough for the case of some still overestimated values. Moreover, we can see 5 traces with large offsets in figure 3.30a, such an offsets have a very low signal/noise ratio, thus higher uncertainties arise during the picking.

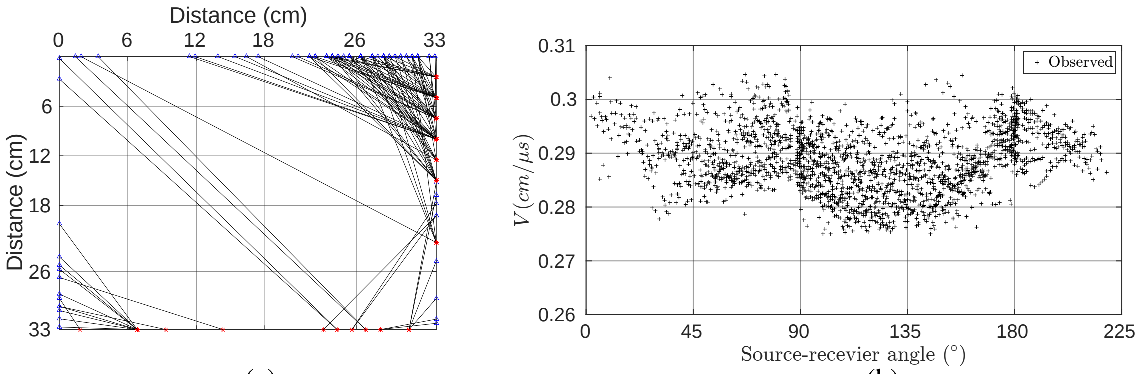

(a) (b)

Figure 3.30: (a) Paths where an average velocity lower than 0.275 cm/μs and higher than 0.305 cm/μs are identified. (b) Average velocity versus angle after removing the data from (a).

To assess the impact of the velocity outliers, we perform two inversions, one considering all the dataset (figure 3.31a-c) and the other after removing the paths of figure 3.30a (figure 3.31d-e). Following the workflow presented in chapter 2, we use the smooth model of figure 3.29e as an initial model for V_v and V_h, i.e., we start from the isotropic case and the anisotropy is recovered at latter iterations, moreover $\theta = 145°$ is fixed based on the optimization shown in figure 3.27a-c, and the inversions are stopped after 8 iterations as we did for the isotropic case (figure 3.29c-d). The main velocity features appear relatively consistent between the two approaches: vertical velocity variations (figures 3.31a and d) are rather localized in different parts of the block with some dipping, while horizontal velocities (figure 3.31b and e) appear a bit more homogeneous. The inverted velocities are used to compute the percentage of anisotropy R, which shows a general anisotropy of 5-7% in parts, mostly associated with low vertical velocity zones. The major difference between the inversions is the presence of a very low velocity anomaly localized at the upper-right corner of the block in V_v (figure 3.31a) which also produce a higher anisotropy percentage in the same zone (figure 3.31c), however the other structures are basically the same pattern in both inversions. Regarding the RMS (equation 3.2), the inversion of all the dataset reaches 1.73% while the filtered dataset leads to RMS $= 1.39\%$. We draw in figure 3.31d dash lines to illustrate the tilted symmetry of $\theta = 145°$ in whose direction V_v is being updated, and the same is done in V_h (figure 3.31d) where the lines are perpendicular to V_v. Such a lines are useful to have an idea of how is distributed the layering in the sample block, we should recall that the tilted case is similar to VTI but with a rotation of the layering, one may see the VTI results of chapter2 where the horizontal layering is normal to the vertical axis. Moreover, we recall that a smooth initial model obtained from the isotropic code was used (figure 3.29e), however, the anisotropic inversion of the filtered dataset by using a homogeneous initial model $V_v = V_h = 0.284\, cm/\mu s$ produced an error of RMS $= 1.43\%$ which is slightly higher than in figure 3.31d-e and the structures of both results being quite similar, thus the isotropic step could have been avoided, this is due to the benefits of having a full illumination, while in the crosshole experiments of chapter 2, the limited illumination of V_v required a good model starting. Since the error by using an initial model from isotropic is slightly lower (RMS $= 1.39\%$), we continue the analysis with the results of figure 3.31d-e. In order to make a fair comparison, isotropic inversion is repeated using the dataset filtered (figure 3.30b) and displayed in figure 3.31g which reaches RMS $= 1.67\%$, note that qualitatively it is not substantially different from the use of all the dataset (figure 3.29c-d). Finally, the synthetic traveltimes obtained from the isotropic inversion (figure 3.31g) and anisotropic one (figure 3.31d-e) are used to compute the velocity versus angle pattern. The observed pattern displayed in figure 3.32a is compared with the wrong isotropic assumption shown in figure 3.32b and the multiparameter approach shown in figure 3.32c. The most notorious difference is related to the absence of a tilted pattern in the isotropic result. The observations cannot be explained only by heterogeneities while our approach recovers the heterogeneities and anisotropic features. For this reason, in the presence of an anisotropic dataset, the wrong isotropic assumption leads to velocity results that can be misinterpreted afterwards. In general, the multiparameter inversion (figure 3.31d-e) provides interesting changes compared to the isotropic one (figure 3.31g) and both the heterogeneities and anisotropy need to be discussed.

3.4.3 Discussion

Laboratory studies have shown that anisotropy is the signature of intrinsic properties of the rocks such as the texture of all the rock-forming minerals, crack population, or pores (Siegesmund et al., 1996). Therefore, we have to understand the origin of the anisotropy observed in the block where the inverted velocities clearly exhibit a directional dependence (figure 3.31d-e). The main pattern is the tilted low-velocity structure observed in the vertical velocity model V_v (figure 3.31d), while the horizontal one, V_h presents more homogeneous values around 0.29 cm/μs in the half upper zone, and some lateral variation in the lower zone appears, which shows certain degree of alignment with the dash tilted lines (figure 3.31e). After visual inspection of the surface of the block, we could observe several heterogeneities on the surface characterized by millimetric holes/cracks, such heteregoneities being consistent with the high porosity measured (27-37%). The effect of porosity on velocities depends of the saturation, a pore filled with air will decrease the velocity, while porous saturated by fluids will tend to increase the acoustic velocities (Berryman et al., 1988; Batzle et al., 2006). In our case, the block can be considered as dry, or with a very small degree of water saturation. In such a porous dry rock dry we can presume the low-velocity pattern of V_v (figure 3.31d) to be caused by a larger porosity. Moreover, large variations in size and shape of pores (geometry of pores) also influence the velocity. Hamilton et al. (1956) were the first to observe a positive correlation between pore size and velocity in carbonate sediments. O'Connell and Budiansky (1974) have shown the reduction of velocity due to the presence of very flat pores. In addition to the geometry, if the pore type is inter-crystal, it will favor a strong decrease in velocity (Baechle et al., 2008; Fournier et al., 2011). The mentioned pore properties could certainly contribute for the low values exhibited in V_v (figure 3.31d).

The particular low-velocity pattern of V_v might be also related with high fracture density in the block (number of crosscutted fractures per length), fractures being known to decrease the global mechanical moduli of rocks, thus to reduce the velocity (Hudson, 1981; Moos and Zoback, 1983). For instance,

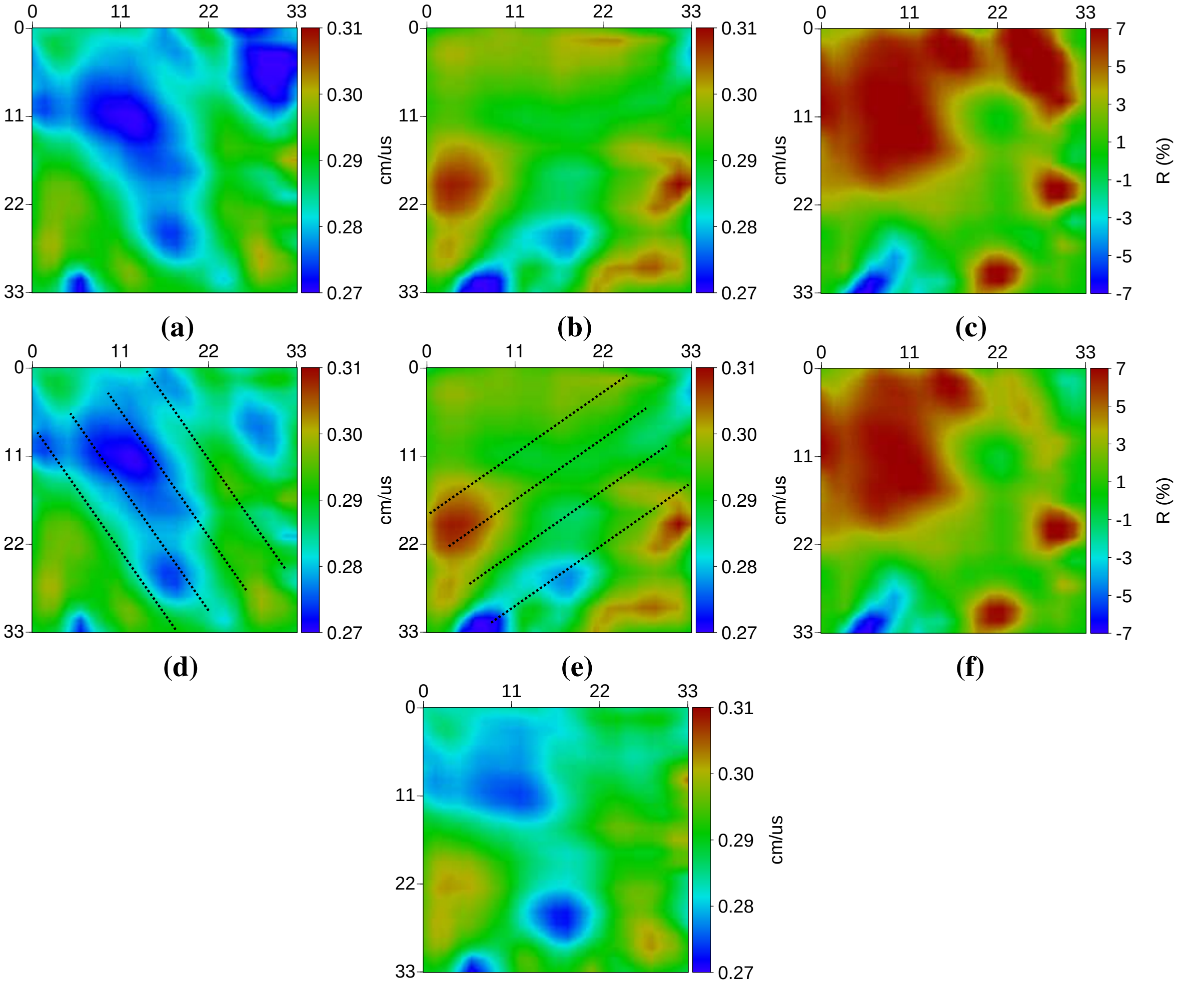

(a) **(b)** **(c)**

(d) **(e)** **(f)**

(g)

Figure 3.31: Multiparameter anisotropic inversion results. (a-c) All the daset is considered to obtain (a) V_v and (b) V_h, which are both used to compute (c) the percentage of anisotropy R, RMS $= 1.73\%$. (d-e) Outlier values are filtered to obtain (d) V_v and (e) V_h, which are used to compute (f) R, the obtained RMS being 1.39%, dash lines are added in V_v and V_h to illustrate the propagation paths that favour the update of each velocity. (g) Isotropic inversion considering the filtered dataset, RMS $= 1.67\%$.

Pyrak-Nolte et al. (1990a,b) showed a decreased of velocity of about 50% caused by multiple synthetic fractures and observed a delay in the first-arrival transmitted through a single fracture. Watanabe and Sassa (1996) highlight the effect of fractures on seismic waveforms which can suffer of destructive interferences between transmitted and reflected waves in a fractured medium, which could generate a decrease in velocity. At the field scale, crosshole experiments also detected a velocity decrease in the presence of fractures, King et al. (1986) found a velocity reduction of about 55-65% while Lubbe and Worthington (2006) detected a decrease of $1000\,m/s$ due to the presence of partially open fractures with density up to 9 fractures per meter. Consequently, we can suspect that the low-velocity values of V_v are due to the large amount of fractures being crossed by propagation paths parallel to the symmetry axis (dash lines in figure 3.31d). In contrast, the more homogeneous pattern obtained along V_h might be associated with lower fracture density in this direction. Other property of fractures is the infilling

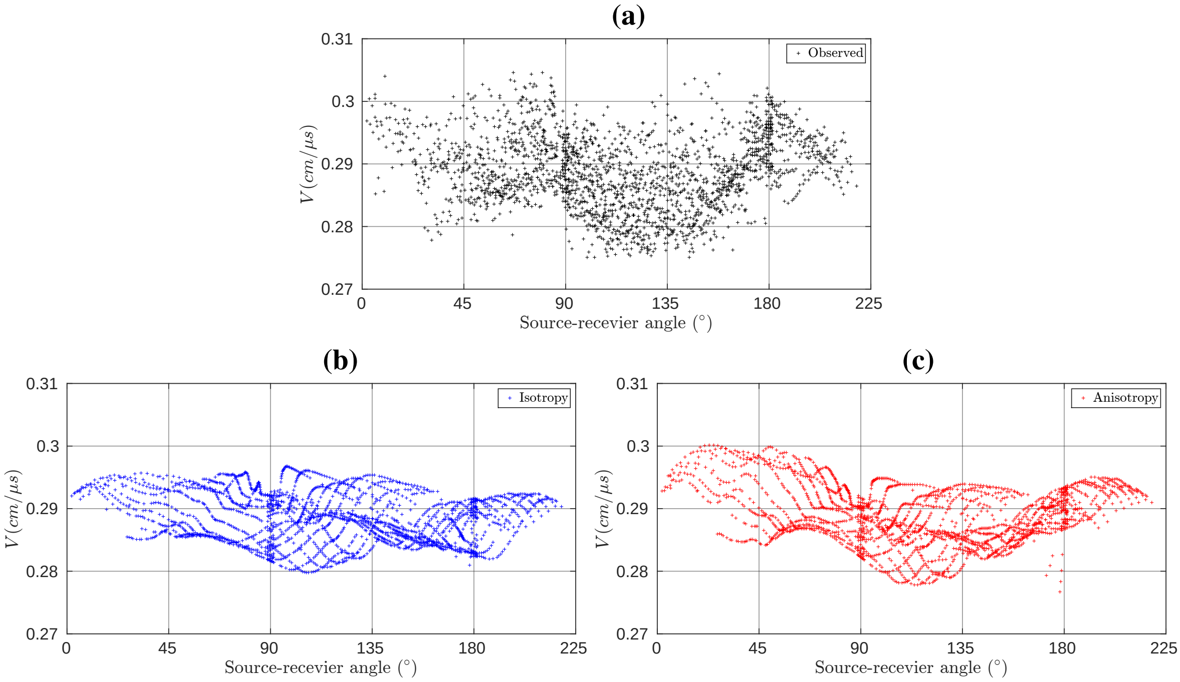

Figure 3.32: Average velocity as a function of the source-receiver angle under the straight path assumption for (a) the real dataset; (b) Isotropic inverted model (synthetic times computed in figure 3.31g); and (c) multiparameter inversion by an elliptical TTI model (synthetic times computed in figure 3.31d-e).

material that can modulate the impact on wave propagation and velocity (Boadu and Long, 1996; Leucci and De Giorgi, 2006; Matonti et al., 2015). The laboratory study of Ass'ad et al. (1993) showed an increase of velocity in cracks that are filled by rubber, regardless of the fracture density. Such feature could explain the zones where V_v surrounds the tilted structure exhibiting increased velocities of about 0.29 $cm/\mu s$, while V_h also increase the values where the tilted structure of V_v is not located. Moreover, the block is partially cemented, if fractures are present, the cementation could explain the higher values in both velocities, a process associated with the burial in the exhumation history as suggested by Matonti et al. (2017). Other authors have underlined the role of fracture aperture or fracture rugosity (wide aperture is caused by high rugosity) and its coupling to fracture compliance which impact the velocities (Pyrak-Nolte and Morris, 2000; Kahraman, 2002; Worthington and Lubbe, 2007; Wei and Di, 2008). Regarding these results, the low velocity patterns in V_v could be associated with a propagation crossing a wide fracture, while the increased velocity values surrounding the tilted structure may be due to small aperture fractures. Finally, we have to consider the presence of karst or large voids which are known to decrease the velocity in carbonates (Hall et al., 2000; Gu et al., 2006; Samyn et al., 2014), Matonti et al. (2017) studied a block similar to our study, and found very low velocity values in zones characterized by the presence of karst. Consequently, the top-right corner of V_v that we suppressed by filtering of data might be a signature of karst instead of overcorrected values, although not visible from the surface.

Comparison of isotropic and anisotropic approaches showed that our experimental data are better explained with an elliptical tilted anisotropic model. Outlier velocity values were removed which indeed do not affect drastically the inversion results leading to a global anisotropy of 5-7% in most of the block. Our approach highlights the importance of taking into account the anisotropy, even when the datatset presents a low to moderate degree of anisotropy. We could then observe a clear localized dipping anisotropy pattern characterized by a low vertical velocity while the horizontal velocity exhibits an effective homogeneous pattern with small lateral variations. Although several processes could explain such pattern the presence of oriented fractures remains the most likely explanation.

3.5 Anisotropy in fractured carbonate

Our anisotropic approach was applied to an anisotropic dataset acquired in-situ on a larger block of carbonates by Matonti et al. (2017). Although the anisotropy observed in the data has been widely discussed and interpreted in their paper, only an isotropic velocity inversion was performed since no anisotropic tomography algorithm was available at the time within the research group. Consequently, we decided to revisit the dataset and to compare the resulting images obtained with our code by considering or by omitting the anisotropy in the inversion process.

3.5.1 Acquisition procedure

The seismic acquisition was performed on a densely fractured parallelepiped carbonate block of dimensions 237 cm × 151 cm × 110 cm. Matonti et al. (2017) used a piezoelectric transducer which emits a P-wave at 55 kHz peak frequency (similar to the frequency used in the porous block of section 3.1), while the receiving transducers receive the seismic signals which are recorded with a 1 MHz frequency sampling. Sources and receivers were located 15 cm from the top of the block along an horizontal 2D plane. The acquisition configuration is presented in figure 3.33, highlighting that sources (red asterisks) and receivers (blue triangles) are located on all the faces thus providing a full illumination. The acquisition has been decimated on the figure and split in near horizontal paths (figure 3.33a) and near vertical paths (figure 3.33b) to better illustrate the raypath coverage.

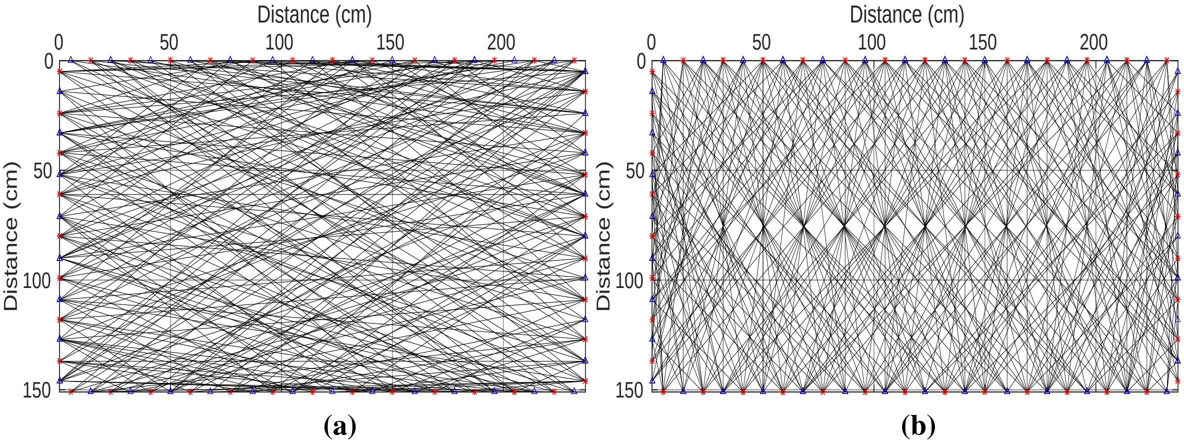

(a) **(b)**

Figure 3.33: Seismic acquisition configuration with straight paths between source-receiver couples. (a) Near-horizontal paths. (b) Near-vertical paths. Data have been decimated for sake of clarity.

Geological properties of the sampled block Matonti et al. (2017) made a detailed description of the block, which was extracted from the Orves quarry located in the Beausset basin (South-East of France). The sedimentary microfacies of the block are characterized by a rich rudist fauna (mainly Radiolitidae in "life position"), embedded in a non-porous wackestone to packstone matrix exhibiting a very low

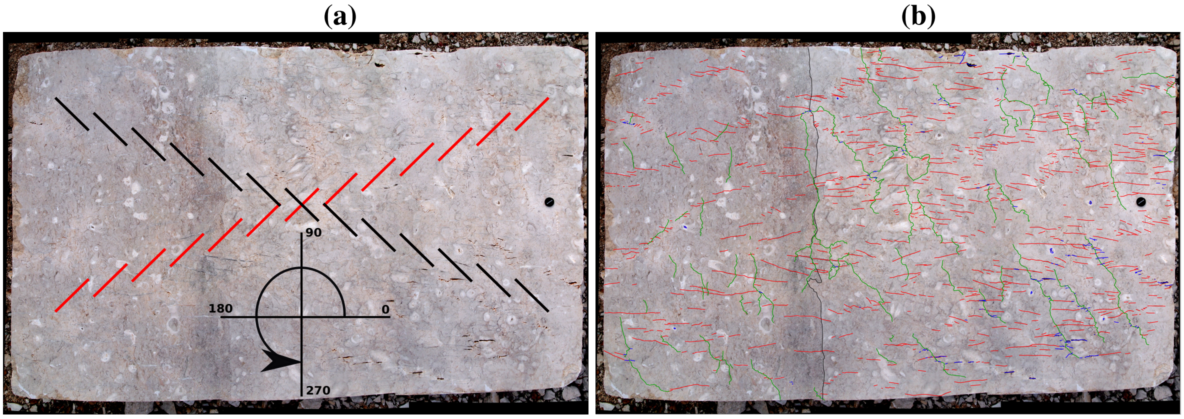

Figure 3.34: High resolution photograph of the block. (a) Two *en-échelon* clusters affecting the block (reactivated cluster in red and non-reactivated in black). Angle convention for source-receiver couples is added to identify the clusters' orientation. (b) Structural features map with cemented fractures (red), stylolites (green) and karsts (blue). Images courtesy of Christophe Matonti.

porosity ($< 1.5\%$). The fracturing process took place during the basin subsidence, the principal stress created fractures of opening mode 1 (tensile stress normal to the plane of the crack), most of them are completely sealed by calcite cement, thus making the fractures non-permeable, these fractures are denoted as non-reactivated since they are initially created. Subsequently, during the tectonic inversion, a rotation of the principal stress (strike-slip movement) caused the reactivation of fractures at one specific dip, one may understand reactivation as the changes of the infilling material. The two *en-échelon* clusters (reactivated and non-reactivated) have different dips, around $35°$ and $145°$ according to the source-receiver angle definition (figure 3.34a). The fracture densities are comparable in both clusters, but only the cluster dipping at 35° shows a reactivation (in red in figure 3.34a). Structural features of the block (cemented fractures, stylolites, and karstified fractures) are shown in figure 3.34b. The fractures exhibit kinematic/mechanical apertures (distance between fractures walls) between 1 and $2\,mm$. It is worth mentioning that the clusters drawn on figure 3.34a are simply to illustrate the dipping, it does not mean that we have only two big fractures, the block is densely fractured and depending of the dipping we can identify to which group are associated, either non-reactivated or reactivated.

3.5.2 Anistropy characteristics of the dataset

Matonti et al. (2017) manually picked 1298 seismic traces. After omitting the first-arrival traveltimes presenting inconsistent delays, a dataset of 1220 traveltimes is finally obtained and used to compute the average velocity versus angle distribution (Figure 3.35). The estimated wavelength of the signal is about $11\,cm$, therefore, contrary to the previous experiment, the large dimensions of the block compared to the wavelength explains why there is no observed bias in apparent velocity due the size of the sources. In addition, we showed in section 3.2 that short paths located on the corners of the sample are more sensitive to source location, in this experiment the shortest distance between source-receiver is about $20\,cm$, and we did not find velocity outliers at these offsets, thus the assumption at the center of source/receiver PZT is still valid. The velocity pattern in figure 3.35 is far from being an homogeneous isotropic velocity (horizontal pattern), and the sinusoidal shape suggests a significant anisotropy. The latter was modelled with our forward modelling code following the procedure described in section 3.3 assuming an elliptical model. After the data-driven optimization, the best combination of parameters leads to $V_v = 0.590\,cm/\mu s$, $\epsilon = 0.08$ (7.7% of anisotropy) and $\theta = 46°$ (magenta in figure 3.35). It results in a RMS error value of 2.58% (equation 3.1) between the observed velocities and the synthetic ones. Note that the optimum angle $\theta = 46°$ corresponds to 44° for the source-receiver angle (figure 3.34a), and therefore we can observe the minimum velocity (parallel to the symmetry axis) $V_v = 0.590\,cm/\mu s$ located at 44° and 226° (44° + 180°) in figure 3.35.

A similar analysis of the dataset was done by Matonti et al. (2017) considering a trigonometric fitting approach performed with MATLAB. They found an average percentage of anisotropy of 8% and an angle $\theta = 45°$, thus quite close to the values we estimated. As they mention, the dip of 44° (or 226°) where the low values are located in the dataset (figure 3.35) are associated with the dip of the reactivated fractures (around 35° dip, red in figure 3.34a) while the higher velocity values are associated with the non-reactivated fractures (with a 145° dip, black in figure 3.34a).

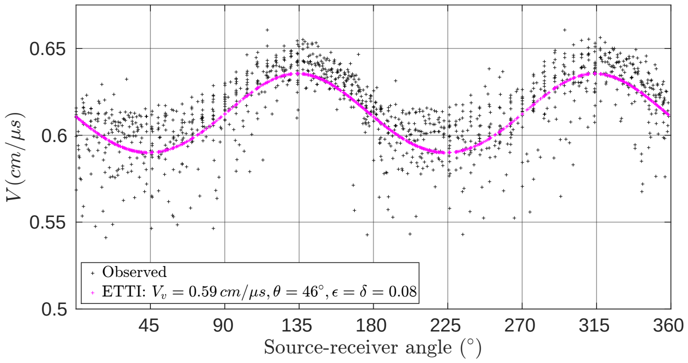

Figure 3.35: Average velocity as a function of source-receiver angle. A fitting of the dataset pattern is found with a elliptical TTI anisotropy model characterized by a homogeneous $V_v = 0.590\,cm/\mu s$, $\theta = 46°$, and $\epsilon = \delta = 0.08$, which represents 7.7% of anisotropy and it gives a $RMS = 2.58\%$ between the observed and synthetic velocities.

3.5.3 Inversion results

We performed several preliminary tests to evaluate the inversion grid: i) the resolution for this dataset is about 15-55 cm given by $\sqrt{\lambda L}$ (Williamson and Worthington, 1993), where λ and L are the wavelength and the different offsets, respectively. ii) Due to the ill-posed nature of traveltime tomography, a very fine discretization comes with the risk of having many models that fit the same data. Consequently, after testing different grid spacing, we found 7 cm suitable to delineate the different structures, and the number of nodes being $nz = 23$ and $nx = 35$ in each direction, this is certainly coarse to partially suppress the ill-posedness of the inversion and to remain in the low-wavenumber framework required by FATT. A discretization analysis was also performed for the forward modeling, suggesting the use of square elements with sides of 3.24 cm, as finer discretizations did not produce any numerical improvement. In the following, all inversions are stopped after 7 iterations.

We compare the isotropic inversion presented by Matonti et al. (2017) with the isotropic inversion using our code and then with the multiparameter elliptical anisotropic approach. Although we suggest to build an initial model from the isotropic code to be used in the anisotropic inversion, we did not find any significant improvement compared to the use of an homogeneous initial model, this is not surprising since we have the benefits of a full illumination dataset. Therefore, in the two inversions, isotropy and anisotropy, we use a homogeneous model of $0.590\,cm/\mu s$ being justified by the optimization shown in figure 3.35.

We begin with the isotropic comparison, figure 3.36a shows the velocity tomography obtained using the Sardine software (Demanet, 2000), which relays on a finite-difference Eikonal solver forward modeling and a Simultaneous Iterative Reconstruction Technique (Dines and Lytle, 1979) with $a\,posteriori$ ray tracing. The isotropic DG-adjoint approach provides the tomography presented in figure 3.36b. Both RMS, computed according to equation 3.2, are comparable ranging from 5.1% with the SIRT method to 4.3% with our method. It is noticeable that both results show a big high-velocity structure which has the same dipping of the non-reactivated fractures, followed by several artefacts on the boundaries of the block. We recall that the homogeneous anisotropic curve in figure 3.35 describes quite well the global pattern, we can suspect that V_v and V_h are largely homogeneous and largely different (high anisotropy), therefore the presence of a localized big structure at the center of the the block cannot be seen as a satisfactory result, it is certainly created because the isotropic modeling is trying to compensate the different directions of velocity.

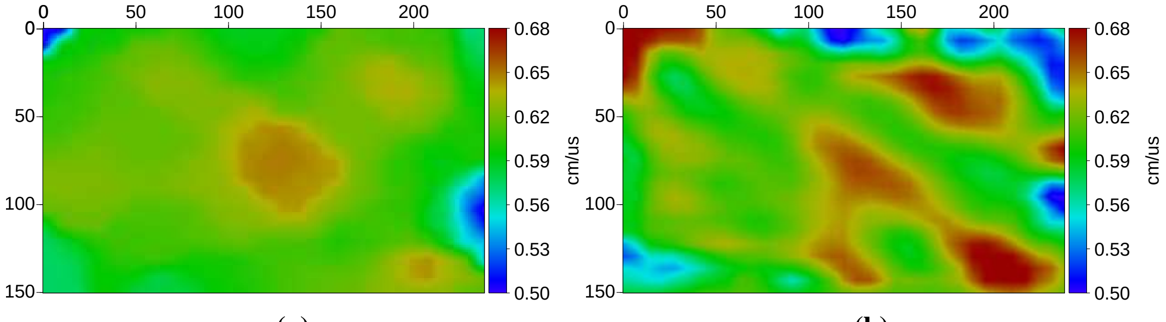

(a) **(b)**

Figure 3.36: (a) Isotropic result with ray-based approach presented in Matonti et al. (2017), RMS=5.1%. (b) Isotropic result with our approach, RMS=4.3%.

The multiparameter anisotropic results are shown in figure 3.37a-b representing the distribution of V_v and V_h, respectively. The dash lines on V_v illustrate the tilted symmetry axis, namely the directions where this velocity is well updated, conversely the dash lines on V_h are normal to the symmetry axis. Such a lines help us to understand how is expected to be distributed the layering inside the block when model is tilted. In the inversion θ was fixed to a value of $46°$ based on the fitting shown in figure 3.35. We reach a RMS $= 1.82\%$ in this inversion being quite low compared to our isotropic result (RMS $= 4.3\%$ in figure 3.36b). The result is quite consistent with the fitting performed in figure 3.35, both velocities are mostly homogeneous and highly different in terms of amplitudes, about $0.59\,cm/\mu s$ in V_v and $0.66\,cm/\mu s$ in V_h. As explained by Matonti et al. (2017), during the subsidence, the cementation of all the fractures (the two clusters) probably produced a high isotropic velocity near the pure calcite velocity value of $0.64\,cm/\mu s$, then during the tectonic inversion, a strike-slip movement caused the reactivation of one of the clusters, i.e., the one oriented in the direction of the (tilted) symmetry axis where the vertical velocity has the major influence. Consequently, the low values observed in V_v (figure 3.37a) are associated with the reactivation, the dominant mechanism that induces anisotropy since it allowed for multiple cementation/dissolution phases and crushing of cement asperities, while in the case of V_h (figure 3.37b) being oriented parallel to the non-reactivated fractures, the values remain high and close to the pure calcite velocity.

Although both velocities are mostly homogeneous, it seems that some localized heterogeneities can be identified in V_v and not so easy in V_h. Therefore, we constraint the range of values in V_v

until a maximum value of $0.65\,cm/\mu s$ in figure 3.37c and now a tilted high-velocity structure appears, probably due to the fracture's filling material in these particular locations. Indeed, for non-porous material, if the fracture has a degree of sparite higher than micrite, the stiffness (proportional to velocity) is increased (Vanorio and Mavko, 2011; Matonti et al., 2017), this might explain this localized increase of velocity. Moreover, on the top left zone of V_v, we see a decrease of velocities compared to the rest of the domain, it can be associated with an increase in the fracture density for these particular locations or maybe the rays crosscut more perpendicular these fractures, both cases lead to a decrease of velocity. Therefore, although the conclusions of Matonti et al. (2017) relating the increase and decrease of velocities are well justified by the presence of two different clusters, the observations we present are only possible when each velocity is inverted locally. Regarding V_h (figure 3.37b), although it is quite homogeneous, there is a vertical structure well defined at $110\,cm$ in the horizontal direction with an increase in the velocity, at this location the rays intersect fractures of the two cluster, therefore, it is not straightforward to interpret this increase. Besides, note the increase of V_h on the bottom right corner which although it has the same orientation of the non-reactivated fractures, there are some kasrst that should produce a decrease, this highlights the directional dependency of karst for different illumination angles.

The two inverted velocities are then used to compute the percentage of anisotropy R (figure 3.37d), which reaches values of 20 to 25% in certain zones, while our data-based simple analysis (and the one of Matonti et al. (2017)) performed considering homogeneous anisotropic parameters suggested a maximum anisotropy of 16%. One may see the increase of anisotropy due to the karst in the bottom right corner (figure 3.34b) while the general pattern of anisotropy seems to have the dip of the reactivated fractures (red in figure 3.34a and dash lines in figure 3.37a), this being suggested by Matonti et al. (2017) as the main responsible of the anisotropy. However, there is a zone (black rectangle in figure 3.37d) showing low values of anisotropy about 3% being possible to extend the analysis in certain locations of the block. This highlights the importance of performing a multiparameter inversion when different low-scale features are present.

To better understand the inversion results, we propose a return to the data domain by comparing the calculated apparent velocities according to angle distributions for the observed (figure 3.38a), isotropic (figure 3.36b) and anisotropic (figure 3.38c) cases. Such representation highlights the presence of several outliers in the isotropic case, which generate significant artifacts within the velocity model. It is well observed that the initial isotropic assumption, which prevents to reproduce some azimuthal periodicity present in the data, results in high values at some angles, this support our view about the big tilted structure in figure 3.36b. A great improvement is naturally obtained with the multiparameter inversion, it shows a sinusoidal pattern quite similar to the observations while the heterogeneities are also consistent in both.

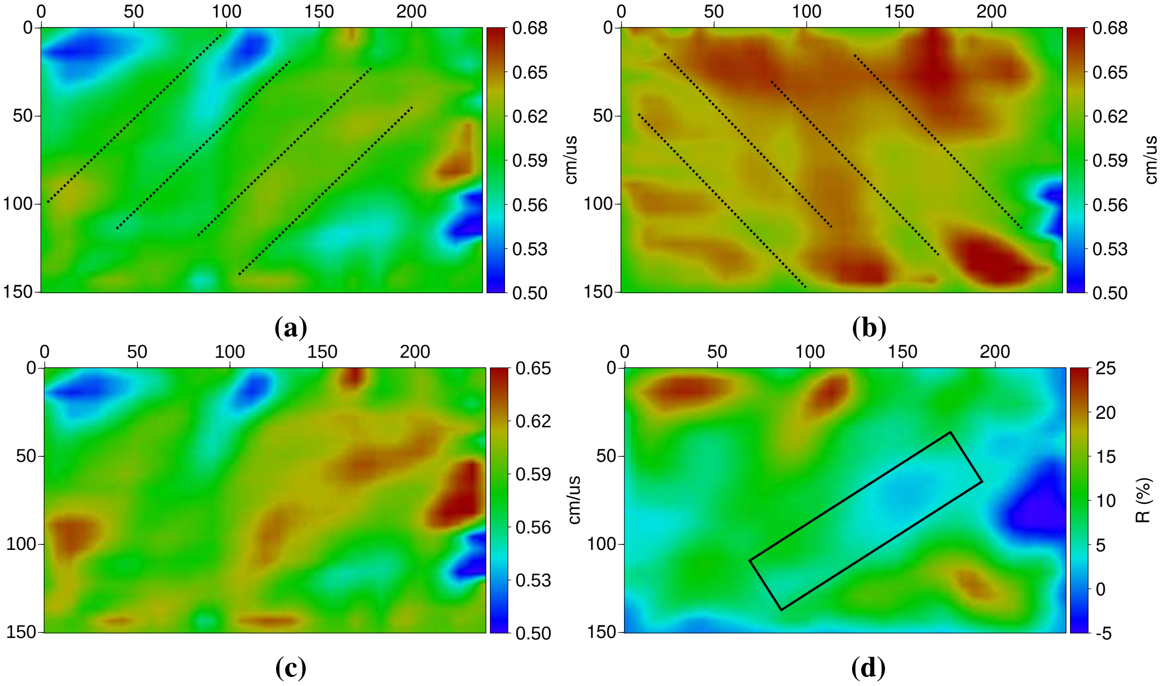

Figure 3.37: Multiparameter anisotropic inversion with $\theta = 46°$ fixed based on the fitting of figure 3.35. (a) V_v model with dash lines showing the tilted $\theta = 46°$, namely where V_v is sensitive and following the orientation of the reactivated fractures (red figure 3.34a). (b) V_h model with dash lines illustrating sensitivity angles normal to $\theta = 46°$ and following the orientation of the non-reactivated fractures (black in figure 3.34a). (c) Same of (a) but with a decrease in the colorbar to highlight heterogeneities. (d) Percentage of anisotropy R computed from V_v and V_h, black rectangle identify a zone where anisotropy decreases. We reach a RMS $= 1.82\%$ in this inversion.

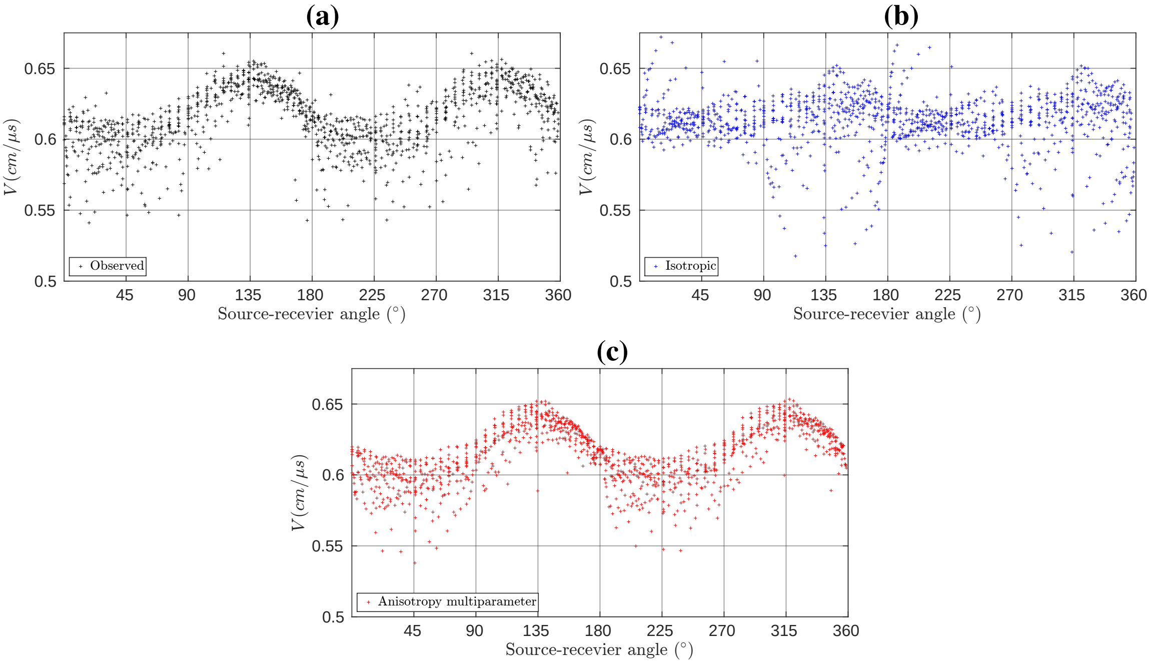

Figure 3.38: Average velocity as a function of the source-receiver angle for each inversion result. Traveltimes and straight distance between source-receiver are used to compute the velocity for (a) observed dataset, (b) isotropic result (figure 3.36b), and (c) multiparameter anisotropic approach with $\theta = 46^\circ$ fixed (figure 3.37).

3.6 Conclusion

The multiparameter approach to invert both anisotropy and heterogeneities was applied at the laboratory scale. Two blocks made of limestone (carbonates) extracted from different quarries of France were subjected to a full illumination acquisition with similar source frequency content. The acquisition in the first block was performed recently as a experience part of this PhD work, while in the second block we went directly to the inversion part as an extension of the work widely developed in Matonti et al. (2017). Regarding the first block, it is a cube characterized by a high porosity about 27-30% and partially cemented, we presented details about the source-receiver devices, data pre-processing as time delay estimation, and the raw data was exhibited to underline some considerations before the picking procedure whose pattern considering near-vertical and near-horizontal paths showed a first insight about anisotropy. The processing part was extensively developed because of the transducer's diameter, thus the picked dataset was presented by the average velocity as a function of the source-receiver angle assuming one source in the center of the transducer, it displayed several outliers of overestimated velocities which gives us the initiative about source representation at this scale. We proposed different discretizations for the diameter of the source assigning the nearest distance between the transducer's surface and the receiver location, we use synthetic examples to evaluate the discretizations, the effect of wrong discretizations was presented in the average velocity versus angle pattern which exhibited the same outliers of the real dataset, and subsequently in the inversion results of both isotropic and anisotropic. We showed that the source can be approximated by three point sources equally spaced along the total diameter of the transducer. An isotropic inversion of the real dataset without source correction produced the same artefacts shown in synthetics while the use of the source discretization suppressed the outliers in the average velocity and also the artefacts in the inversion.

Afterwards, anisotropy of the real dataset was investigated by the velocity versus angle pattern, our forward modeling was used to produce homogeneous anisotropic curves varying the anisotropic parameters, we showed the effect of each Thomsen's parameter and the angle of symmetry axis θ. We found that there is a degree of tilt in the dataset and therefore it is wrong to assume VTI or HTI models, moreover the dataset is well explained by 3% of anisotropy under the elliptical approximation. Following this elliptical tilted assumption, we performed an inversion with our multiparameter approach, the result was compared with inversion under the isotropic assumption. Our approach gave the lowest error of RMS and it exhibited several differences regarding the anisotropy and heterogeneities, the most predominant was a tilted low velocity structure in the vertical velocity that was absent in the isotropic inversion result, moreover the horizontal velocity with our approach had nearly homogeneous values with some small lateral variations, in general most of the block exhibit 5-7% of anisotropy. We gave some suggestions about the origin of this anisotropy, one is regarding the high porosity of the block which is related with the size, shape and geometry of pores, the second is the possible presence of fractures that impact the velocity by the shape, fracture density, rugosity and filling material.

The second block is non-porous with high amount of fractures that are completely sealed by calcite cement, it has two clusters depending of the angle, therefore fractures can be non-reactivated or reactivated. We follow the same procedure of the first block, anisotropy of the dataset pattern was estimated, we found a good approximation with elliptical 7.7% of anisotropy and the parameter θ has the same inclination of the reactivated fracture, indeed our estimation is very close to the one presented by Matonti et al. (2017). The inversion of the dataset by the isotropic assumptions displayed several artefacts, this highlights that in presence of very strong anisotropy, the isotropic result hides structures like in the first block and it also produce artefacts, therefore it cannot be used for interpretation. The inversion using our multiparameter approach showed that the block is mostly high-homogeneous anisotropic with some localized heterogeneities, the result was quite different compared to the isotropic version and a satisfactory decrease in the RMS was obtained. We computed the average velocity as a function of the angle for each inversion result, where the worst was obtained from the isotropic result with several outliers and far from a sinusoidal shape, while our approach produced a velocity pattern quite close to the observation. A tilted anisotropy of 10% or more is found in several parts of the block, the anisotropy is mainly caused by the reactivated fractures which is consistent with the analysis of Matonti et al. (2017), however thanks to our approach we can see some parts of the block that exhibit high an low anisotropy, the difference of these zones allows us to extend the discussion about the anisotropy, which might be associated with the filling material of fractures in certain parts of the block. This dataset was important to evaluate our approach in the presence of high anisotropy, moreover the inverted velocities can be used to design realistic and complex synthetic models with both high amount of anisotropy and densely fractured, thus it gives us the motivation to extend our approach to fractures imaging.

Chapter 4

GPR laboratory investigations of the carbonate block

Contents

Introduction

The block analysed in chapter 3 is subject to a ground-penetrating radar acquisition (GPR) based on transmission data in a multiphysics framework. GPR at laboratory scale has been applied on several materials besides carbonate samples, most of the applications being performed in reflection mode. For maintenance and monitoring of civil engineering structures, Capozzoli and Rizzo (2017) designed a pool with different inclusions, rebar and utilities (metallic and non-metallic pipes), where several GPR antennas were tested. They showed a better detection of the targets compared to electrical resistivity tomography (ERT). A similar study is presented by Cataldo et al. (2014) to detect a water leak within underground pipes. They designed a box where they controlled the level of leaking on the pipes, and compared GPR data ERT and time domain reflectometry (TDR) measurements suggesting the latter as the most convenient for a quick assessment on the possible presence of leaks. In rock physics studies, De Donno et al. (2017) used GPR and ERT on masonry samples before and after the application of shear and compression stress which created fractures and weakness zones, thus GPR provided a better resolution while in terms of acquisition they showed the benefits of using a dielectric layer between the GPR antenna and the investigating medium since it improves the signal penetration in the case of shallow high-conductive layers. Fracture properties are also studied by Arosio et al. (2016), they added sheets of different thickness and known filling material between marble blocks to simulate the presence of fractures, then two approaches based on common-offset and common-midpoint reflections are compared in order to estimate the correct thickness and permittivity, the benefits and shortcomings of each method are discussed.

Hydrological applications are presented by Hagrey et al. (2000) who built a box of sand where GPR was used for detecting and quantifying the water content and salinity in the unsaturatd vadose zone. In a time-lapse framework, Mangel et al. (2020) proposed reflection tomography as a new approach for hydrologic monitoring by estimating the water content, while Orlando and Palladini (2019) designed a small cell where grained glass beads simulate a porous medium with layers of different permeabilities. Subsequently, contaminants that are known to affect the groundwater quality were injected and GPR was used along with ERT and TDR during several days, the use of different geophysical methods allowed to describe the interaction of the contaminant with a saturated and unsaturated medium and thus reducing the uncertainty in data interpretation. GPR has been also tested in wood, Martínez and Schmitt (2013) using the two-way traveltime of a 1.6 GHZ antenna varying the position with respect to the grain direction of wood in several samples. They showed that the GPR velocity was always greater when the electrical field was transverse to the grain of the wood, i.e., highlighting a dominant anisotropy effect. Li et al. (2018) proposed to use reflection tomography to investigate the internal part of tree trunks for health control and to prevent collapses of trees in urban areas or around roads.

It is worth underlining that all the mentioned works at lab scale, in spite of their substantial results, are limited to reflection data, and this is due to the main limitation we have in GPR with transmission data on small samples, i.e., the effect or the high velocity of air. This problem is identified by Peterson (2001) in a crosshole dataset acquired between wells separated by 7 m. He noticed that the waveforms from a source gather presented a change of polarity for the traces located near the soil/air interface. Average velocities as a function of the source-receiver angle, computed from the first-arrival time pickings under the straight path assumption, were too large when aperture angles were higher than 50° leading to a hyperbolic pattern. According to Peterson (2001), one explanation to these higher velocities is that at high angles, the direct arrival of the signal traveling through the earth is distorted by a faster arrival traveling within the boreholes. However, although his hypothesis makes sense, it was not validated numerically.

In a similar way to what we would like to do in our experiences, Kana (2015) studied the influence of other events on the first arrivals by transillumination surveys in a limestome boulder, the field data was compared with full modelling simulations leading to a good agreement between the two based on an analysis of amplitude as a function of propagation direction, particularly at high angles: interferences in the amplitude pattern were found, while in time domain, lateral waves (major influence of air) were identified, this suggest that a special careful needs to be taken, i.e., avoiding the sample edges to reduce the interference from the air waves. Regarding velocity tomography, Hanafy and Al Hagrey (2005) performed a transmission acquisition with a 0.9 GHz antenna in a wooden sandbox of 90 × 90 × 35 cm, locating the transmitter and receiver in opposite faces. He investigated the potential of tomography to image different objects with different water saturations and shapes. It is worth mentioning, they used Eikonal solver as a forward engine but the gradient is build by a posteriori ray-tracing and anisotropy was not considered. In a second experiment, they dug trenches until a depth of 50 cm around a poplar tree forming a trapezoid area of 6.3 m^2 that they investigated using a full illumination acquisition by locating 0.5 GHz transmitters and receivers on all faces. In both experiments, they followed the suggestion of Peterson (2001) of discarding all the traces with incident angles higher than 50°, thus they omitted to discuss probable air effects on the data, for instance, when Tx-Rx are located on the same corner (short offset), or when Tx-Rx are located on opposite corners (large offset), although only low-angle data is considered, the images were capable to identify the targets under this isotropic assumption framework. We should mention that Alumbaugh et al. (2002) also suggest to discard traces at angles greater than a particular threshold value from a crosshole acquisition where the wells were separated by 3 m.

An significant effort has been undertaken by Irving and Knight (2005) to understand the effect of the air in a crosshole environment with a GPR full waveform forward modeling approach considering a homogeneous medium and a 100 MHz antenna, usually the chosen antenna for crosshole field experiments. They studied three factors: the ratio between the velocity inside the borehole (v_{ant}) and the medium v_{med}, the borehole separation and the length of the antennas. Picked first arrivals were used to compute the apparent velocity versus angle distribution assuming straight raypaths. It showed that large angles values were sensitive to the velocity ratio ($v_{ant} >> v_{med}$), particularly and to the large length of the antennas, particularly for small borehole separation (less than 8 m). Their raypath estimations, based that the sources and receivers can be considered as points located at the center of antennas, is no longer valid. They could not however propose an alternative.

Such effects were not noticed in the Rustrel dataset presented in chapter 2, certainly because the boreholes were separated by a larger distance of 18 m. This favourable condition is no longer respected in our laboratory experiment, described in section 5.1: we work in transmission at around 1 GHz on a cubic block of 33 cm side, where all sides of the investigated material are surrounded by air, similar to Hanafy and Al Hagrey (2005). Therefore, instead of processing the block data in a blind manner, we performed an air experiment first to test an automatic picking strategy inspired from Irving et al. (2007), described in section 5.2, but also to analyze the picking distribution as a function of source-receiver angle in the homogeneous and known air material (section 5.3). We could then characterize the effect of using non-point antennas in the air at this scale and propose some potential corrections. Identical processing and analysis was performed on the carbonate block acquisitions and is discussed section 5.4. Indeed, instead of discarding traces at moderate angles which are important to consider for resolution purposes, we design a strategy to consider them based on the correction of the source/receiver positions coming from a data-driven optimization. Our approach is analogous to the one presented by Irving et al. (2007) where they apply a traveltime correction at large angles instead of antenna position correction. Another study complementing air and field measurements is presented by Millard et al. (2002) in the framework of amplitudes in order to estimate the beam width of the antennas, this is essential to define the resolution capabilities in the antennas, corrections based on the spatial attenuation are proposed and they concluded that the effective beam on the surface of a dielectric medium decreases as the relative permittivity increases.

The corrected dataset is then incorporated into isotropic inversion attempts (section 5.5), carried out to evaluate the impact on the tomographic images by comparing the results coming from traces potentially influenced by the presence of air around the block. An anisotropic approach is also proposed and discussed. All the different results are compared but they all present unexpected very low degree of heterogeneities compared to the acoustic investigations (chapter 3), which will remain the highlight of this study.

4.1 Experimental approach

In this section we first briefly present the characteristics of the GPR antennas and the acquisition configuration used for the electromagnetic (EM) imaging of the block of carbonates already presented and studied in the previous chapter with an acoustic approach. Because of the specificity of GPR acquisitions, we will focus on air acquisitions, which have been proved necessary initially to study the stability of absolute time calibration but also to better understand the behavior of GPR antennas, which cannot be considered as point-sources at this scale. Contrary to the acoustic analysis, the large number of signals recorded and the precision required, a reliable and quasi-automatic picking strategy of first-arrivals based on the cross-correlation (CC) technique, will be presented.

4.1.1 GPR antennas

We are using the ”GroundVue 3” antennas from Utsi electronics mainly due to their theoretical central frequency of 4 GHz, which were particularly adapted to our laboratory application in terms of resolution and penetration. They have never been used to our knowledge for rock tomography. Figure 4.1a shows a photography of the source shielded box in which a source antenna Tx and a receiver antenna Rx are integrated to perform constant offset acquisitions in reflection mode. For our tomography purposes performed in transmission, only the source part of the box is used and is highlighted by a red arrow. Another receiver antenna is positioned in a second shielded box (figure 4.1b) and can be offset according to the desired configuration, on the opposite side of the block in our case. The design and dimensions of each antenna were provided by the supplier company *Geomatrix*®. Figure 4.2 shows sketches of the side and the front parts of each antenna. Focusing on the front part of the Tx antenna in figure 4.2a, it

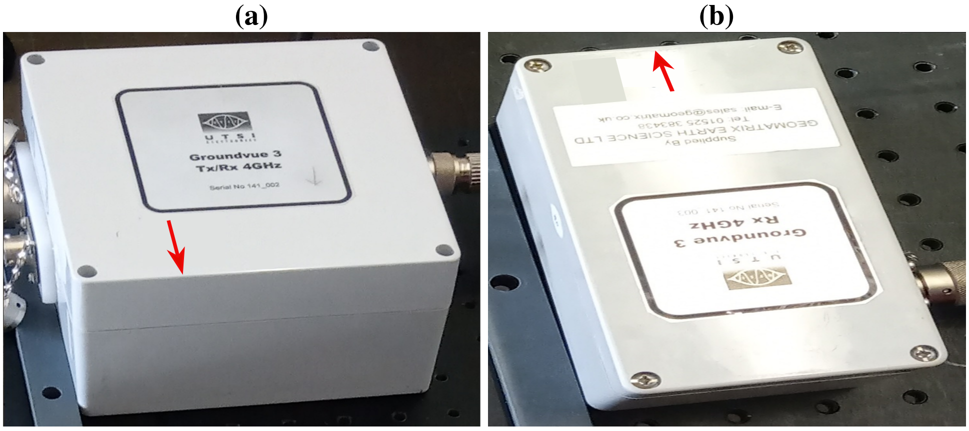

Figure 4.1: Photography of the shielded boxes for (a) the source and (b) the receiver antennas. Red arrows illustrate the location of each antenna.

shows that from the left edge of the box there are 2 cm of screws and the center of Rx is located 3 cm further on. The symmetrical Rx antenna is incorporated in a 8 cm wide box and measures 5 cm with a middle point located at 4 cm from the edge of the box (figure 4.2b). Other box dimensions, height and side length are identical, being 9 cm and 16 cm respectively.

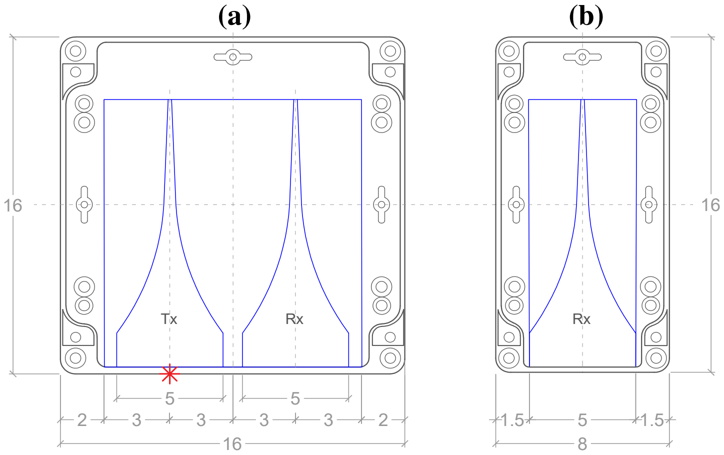

Figure 4.2: Sketches of the antennas with (a) the source box which includes the Tx source and (b) the receiver antenna Rx. Figure has been created considering the information provided by *Geomatrix*®. Dimensions are given in centimeters.

4.1.2 Acquisitions in carbonates

To compare GPR and acoustic results (Chapter 3) in a multiphysics approach, we locate the antennas at the same elevation, namely at 16.5 cm (middle of the block). Figure 4.3 shows the experiment performed on the block. The receiver antenna (Rx) is static and the source antenna (Tx) is moved thanks to a calibrated car (arrow in figure 4.3a) in order to record a gather on the opposite face of the block. Then, the receiver position is displaced and another gather is recorded. For the two devices, the plastic surface of the antenna is in direct contact with the block.

The final transmission acquisition is summarized in figure 4.3b-c where the red asterisks represent the different locations of the source antenna while the blue triangles are the positions of the receiver. At this stage, we have assumed antennas can be simplified as a single point located at the middle of each device, which will be evaluated afterwards. Our acquisitions were conducted with a separation of 2.5 cm between receivers locations and 0.24463 cm between each source, a value deduced from the car distance calibration. Consequently, we could record 119 traces along the 33 cm of the block for each receiver gather. This configuration in transmission enables us to obtain the near-vertical paths (figure 4.3b) and the near-horizontal paths (figure 4.3c) needed for anisotropy estimations. Tests carried out with Tx/Rx forming diagonal angles as we did in the seismic acquisition showed problems of noise and really fast arrivals due to the air effect at this particular scale, we illustrate this afterwards in section 4.4.

Before analyzing the data acquired on the carbonate block, an experiment was conducted in air for calibration of the antenna behavior. In all these experiments, signals were recorded on a 10 ns time window with 512 samples, so a frequency sampling of 51.1 GHz. They have been then re-sampled at 819.2 GHz with 8192 samples, leading to a time sampling (picking uncertainty) of 0.001221 ns.

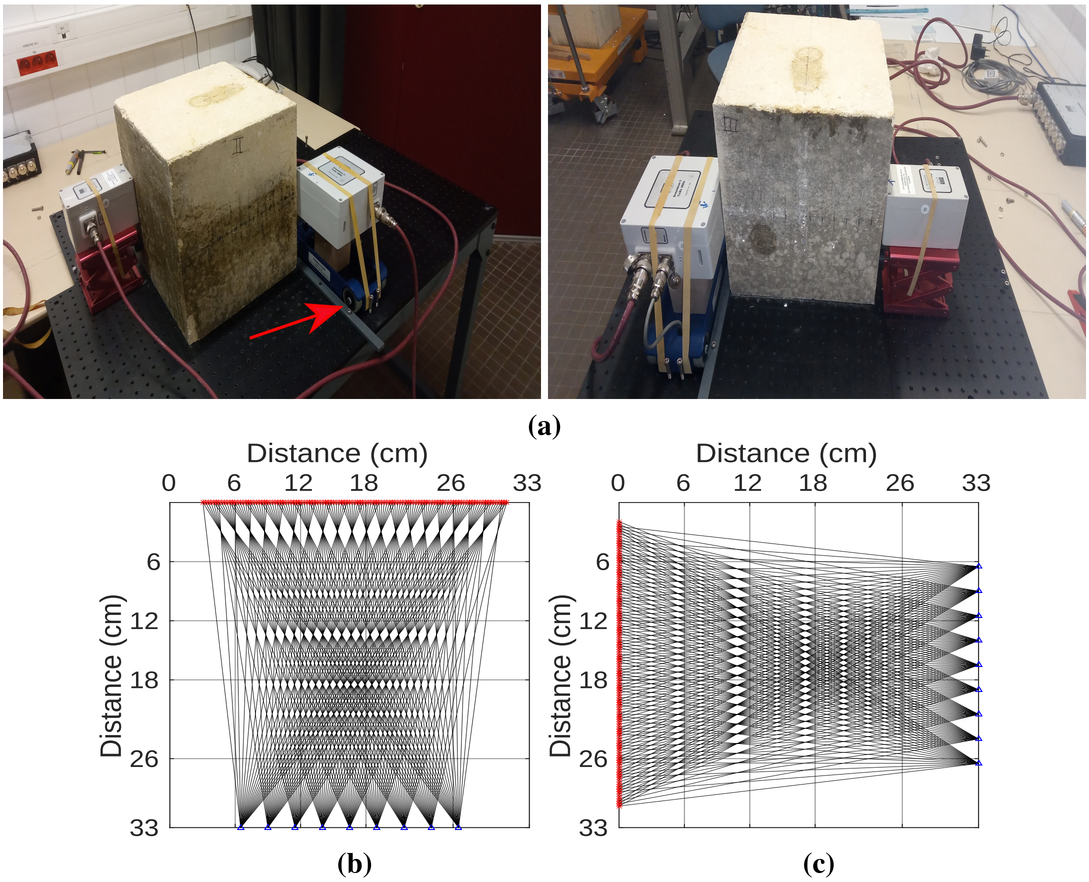

(a)

(b)

(c)

Figure 4.3: (a) Photographies of the GPR acquisition performed on the block, with the source moving along a face located in front of the fixed receiver. The red arrow highlights the wheels of the moving car. (b-c) Illumination properties of the whole experiment assuming straight raypaths for (b) the near-vertical paths, and (c) the near-horizontal paths. The red asterisks are the positions of the source and the blue triangles the positions of the receiver, assuming they are located at the middle of the antennas (figure 4.2).

4.1.3 Air experiment

Besides the experiment in the block, a comparable experiment conducted in air was performed in order to study the characteristics of the recording signals and the stability of the source. This dataset has also be used to test the quasi-automatic picking technique. A photography of this experiment is presented in figure 4.4 where the source antenna is moved using a car from position 1 to position 2 over a distance of 120 cm while the receiver, located 35.5 cm away when facing the source, remains static. Then the receiver is displaced horizontally (arrow in figure 4.4) and the car returns to position 1 in order to repeat the recording with other angles, leading to 6 receiver gathers.

Figure 4.5a-b shows the raw data of two gathers with their spectrum, after DC shift removal. The radargrams show some low amplitude flat events between 0 and 1.5 ns that may be related with electronic noise. Then, a large hyperbola, with a Ricker-type waveform, dominates the recordings and is characterized by an apex arriving a bit before 2 ns when antennas face each other. This arrival is followed by other hyperbolas, more or less disturbed by possible reflections on the sides, suggesting that

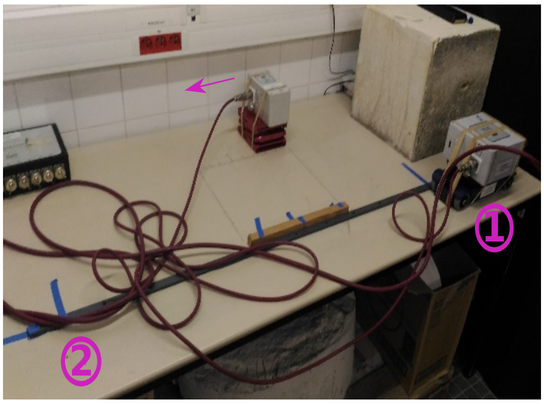

Figure 4.4: Photography of the experiment in air, the source moves from position 1 to position 2 while the receiver remains static. The receiver is then displaced to the left (arrow) and the experiment is repeated covering the same distance for each receiver position.

the source emits a rather complex signal that spreads out in time.

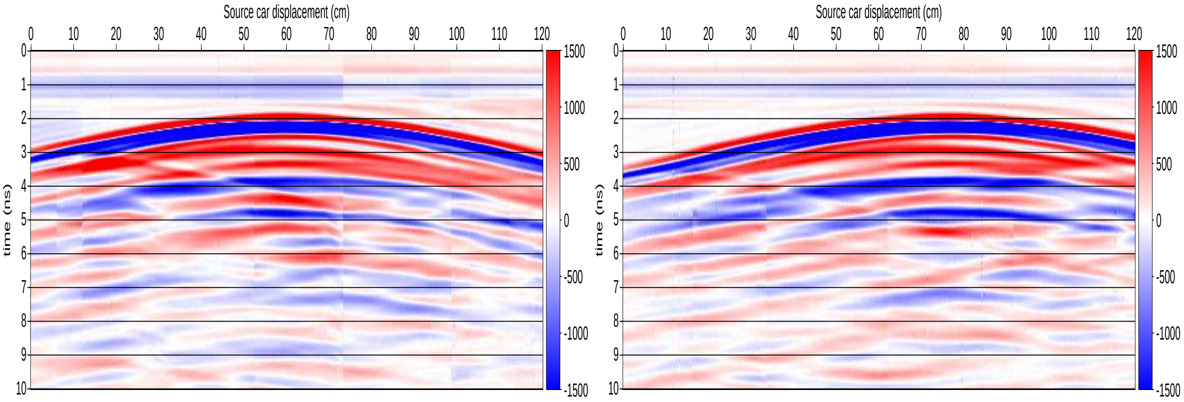

(a) **(b)**

Figure 4.5: Examples of two different receiver gathers acquired in air. (a) Gather 2, and (b) gather 6.

After trace by trace normalization and amplitude amplification, zooms of the first arrivals are provided in figure 4.6a-b as a function of horizontal offset separating the source and receiver. The latter was computed assuming the source and receiver are point sources located at the middle of the antennas, also note that in the 6 recorded shots the source is located in front of the receiver, and the first recordings are always with the source antenna located at the left of the receiver antenna (fig 4.4), therefore they correspond to negative horizontal values and being the opposite when the source is located at the right of the receiver (positive values). The gathers clearly shows the first positive onset of the hyperbola, whose period is a bit lower than the negative second onset. We can also observe small amplitude events arriving just before the dominant first-arrivals and might also result from a source time spreading. This could affect the quality of the picking.

Besides the horizontal offset, we also define the angle convention in figure 4.7a, which is defined as the angle between receiver/source position since it is the receiver the static antenna while the car (source) is moving, consequently traces located at the left of the receiver correspond to angles higher than 90°, conversely when the car is at the right of the receiver, we have angles lower than 90°, one

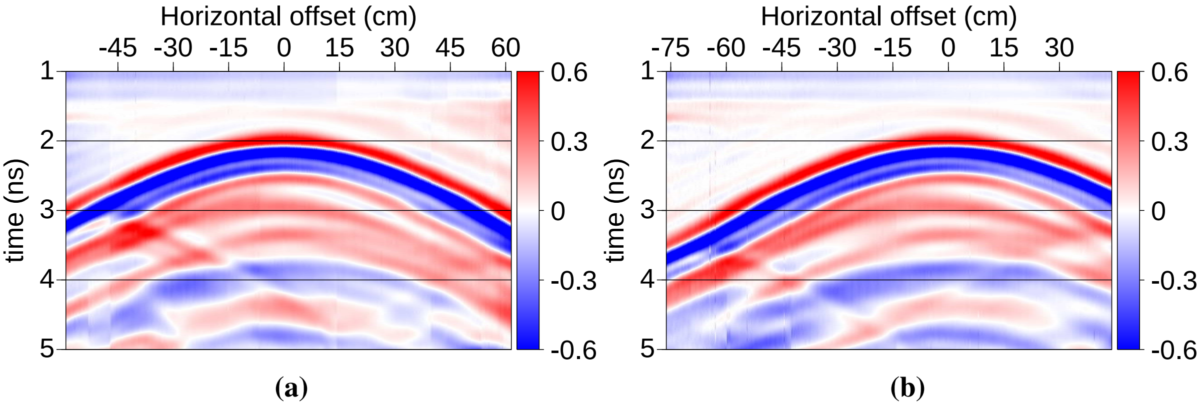

(a) **(b)**

Figure 4.6: Close-up views of (a) figure 4.5a and (b) figure 4.5b after trace by trace normalization and amplitude amplification.

may note that for this air experiment we do not reach 180° since the car is always in front of the receiver (figure 4.4 and analogous to figure 4.3b), while in the carbonate experiment when receiver is located on the right and the car on the left (figure 4.3c), we can reach angles higher than 180°, this angle convention being used in rest of the chapter. In order to extent the investigation of the traces, figure 4.7b-e shows the waveforms of four different traces extracted from the gather displayed in figure 4.6a with the corresponding horizontal offset and receiver/source angle. The dominant first arrival signals are relatively stable although some weak amplitude changes are observed. They are systematically preceded by small amplitude and rather constant noise regardless the offset, which could be electronic noise coming from the acquisition devices. The first dominant onsets present some variability in term of period, indicating a certain amount of signal dispersion maybe due to antenna radiation pattern effects. What is reassuring is that the arrival times of the symmetrical traces are the same, in addition, we can conclude that the dominant waveform which includes the first-arrival onset is made of two events: one increase on the amplitude followed by a negative peak, therefore we propose to isolate all the traces by imposing a window as shown in figure 4.8 being the same trace of figure 4.7b, subsequently we compute the frequency content with the confidence that the main waveform is considered, we should recall that similar window was applied on the seismic dataset acquired in the same block (section 3.1.4). Figure 4.9a-b are the spectral domain of the gathers in figure 4.6a-b, respectively, and after applying the window of figure 4.8, note that the dominant energy is much lower than originally imagined, between 1 and 2 GHz. The spectrum reaches values of 4 GHz but only when the antennas face each other, the frequency of the iso-amplitudes decreasing gradually with distance. Finally, the picking of the first onset of these dispersive signals will be realized using a cross-correlation technique.

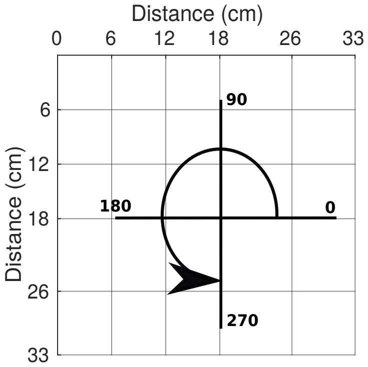

(a)

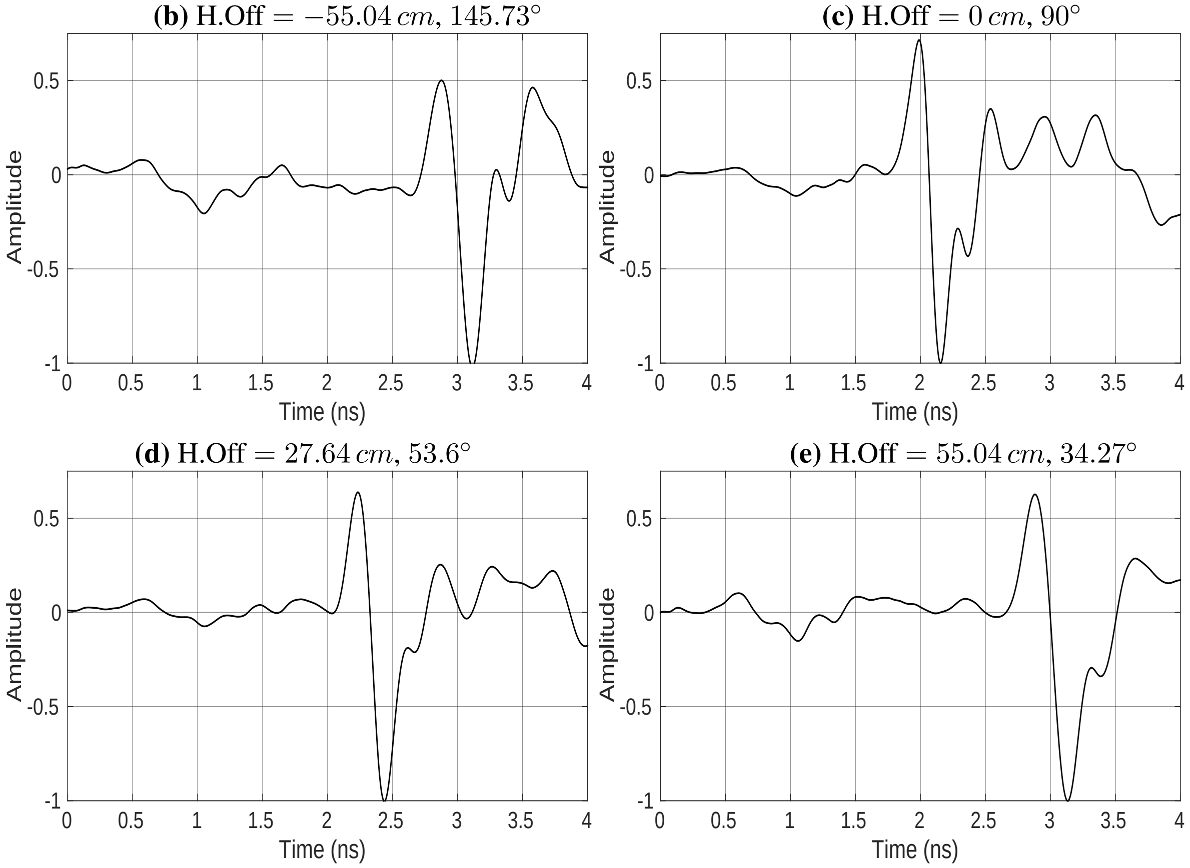
(b) H.Off $= -55.04\,cm$, $145.73°$

(c) H.Off $= 0\,cm$, $90°$

(d) H.Off $= 27.64\,cm$, $53.6°$

(e) H.Off $= 55.04\,cm$, $34.27°$

Figure 4.7: (a) Angle convention between receiver and source position since the receiver is the static antenna and the source is displaced, the antenna positions assumed as a point located at the center of the devices. (b-e) Time signature of four air traces extracted from gather of figure 4.6a with different horizontal offset and angles: (b) $-55.04\,cm$, $145.73°$; (c) $0\,cm$, $90°$; (d) $27.64\,cm$, $53.6°$; and (e) $55.04\,cm$, $34.27°$

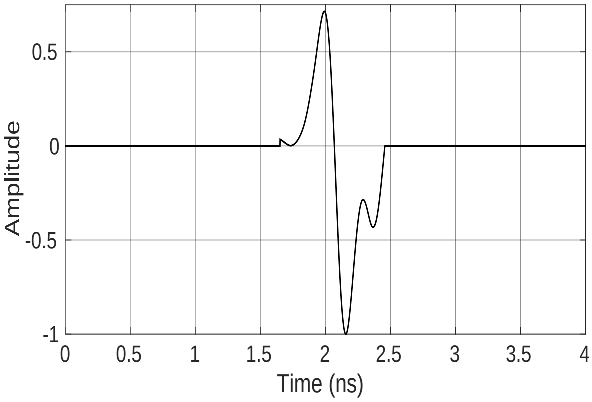

Figure 4.8: Window imposed in trace of figure 4.7c to isolate the main waveform carrying the first-arrival, same window applied in all the traces of the air experiment to compute the frequency content.

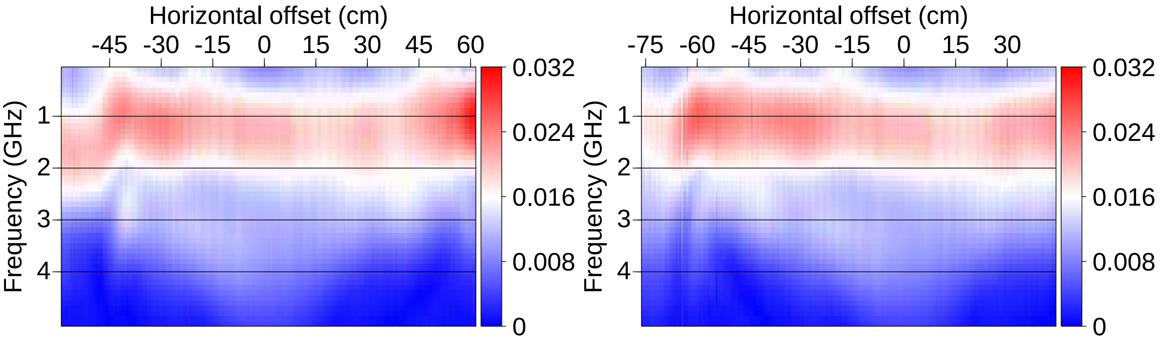

(a) **(b)**

Figure 4.9: (a-b) Frequency content of the gathers in figure 4.6a-b, respectively, and after applying the window shown in figure 4.8 in all the traces.

4.2 Cross-correlation picking approach

In the last few decades, efforts have been done to develop automatic or semi-automatic picking techniques, as reviewed by Sabbione and Velis (2010) and Akram and Eaton (2016b). In our case, we choose to modify the semi-automatic cross-correlation (CC) picking strategy originally proposed by Irving et al. (2007). CC methods have been classified as a multilevel algorithm because it makes simultaneous use of information on multiple receivers while a reference pilot signal has to be defined. One of the first attempts to produce a computer-based picking algorithm using CC of adjacent traces was proposed by Peraldi and Clement (1972) in order to find the time delay between first-breaks and construct intercept time curves on seismic data acquired for oil exploration purposes. A similar strategy was proposed by VanDecar and Crosson (1990) for teleseismic events recorded by local or regional networks. In this approach, for each pair of traces, the peak of CC gives the relative time shifts which are then used to produce a system of over-determined linear equations. Subsequently, a least-squares optimization process is applied in order to find the best fitting station delay. Following this work, Bagaini (2005) focused on the estimation of the pilot signal concluding that it is better to update the pilot iteratively. De Meersman et al. (2009) designed a workflow based on CC for the refinement of arrival-time picks. In this approach, the initial arrival times (either manually picked or using any other picking algorithm) are used to align the waveforms and compute the pilot. The procedure is repeated until the time delay converges to a user-defined threshold value, which represent the optimal re-alignment of the input data. However, this procedure may fail in the presence of bad S/N ratio and polarity fluctuations which affect the pilot waveform computation. To overcome this, Akram and Eaton (2016a) improved the workflow of De Meersman et al. (2009) by adding conditions on S/N and polarity weighted stacking.

Instead of refining the arrival-time picks, we rely on CC to directly pick the arrival times on the waveforms based on the algorithm of Irving et al. (2007). However, we found some steps where the technique could be improved, consequently we designed the algorithm 4.1 whose steps will be discussed. The air gather of figure 4.6a is used to evaluate the potential of the method.

After preliminary data processing, the angle sorting step (2 in algorithm 4.1) is an important one when dealing with GPR data, because it allows to gather small groups of traces where the changes of waveforms are not expected to be large. Indeed, as already noted in air but probably even more important in carbonates, the combined effect of attenuation and potential antenna radiation patterns means that the signals will not be stable with respect to the angle between source and receiver. Therefore, the use of a single pilot signal is illusory. An example of angle sorting is provided for air data in figure 4.10a-b, where two different symmetrical groups have been sorted by angles with the corresponding horizontal offset. It shows that the traces inside each group share similar patterns with no large differences in waveforms, only time delays can be noted. On the contrary, it is clear that there are large waveform differences according to group angle, i.e., the pilot estimated from one angle gather will not efficiently work in other gathers.

The next step directly concerns the cross-correlation computations devoted to align the traces of each group of traces independently. For that, a location on each trace must be found where the time window will be imposed. To define a starting time position in each trace, we modified the approach of Irving et al. (2007):

1. Based on the first trace of the gather, we manually pick a reference time position which is near the correct first-arrival position.
2. Cross-correlation is iteratively computed between adjacent traces and no window is imposed: for instance the first trace with the second trace, the second trace with the third trace, etc.

Algorithm 4.1 Cross-correlation (CC) technique workflow inspired by the approach of Irving et al. (2007), where several improvements have been added.

```
1: Data processing: remove DC shift from each trace, normalize each trace by signal maximum, and discard data where signal is clearly absent.
2: Sort data into common-ray angle gathers
3: Manual picking of one trace near the first-arrival position, followed by cross-correlation of adjacent traces and considering all the recorded trace.
4: The time picked along with the time delay found in (3) are used to locate the position, where the suitable time window can be defined, i.e., a preliminary first-arrival in each trace.
5: Select the trace having the highest signal-to-noise ratio as the pilot in each common-ray-angle gather
6: Define a smart window by considering only first event of both the pilot and the other traces in each common-ray-angle gather. For this particular dataset, it is associated to the positive amplitude zone. This window being used for all the CC performed afterwards.
7: Align the traces of each angle gather by applying CC between the pilot and the corresponding traces.
8: Compute a mean trace considering the alignment of (7) for each angle gather.
9: Use the mean trace of (8) as the pilot to perform refinement in the alignment by CC.
10: Compute a mean trace from the aligned traces in (9), this will be the final pilot for each angle gather.
11: From all the estimated pilots, choose one where the first-arrival will be manually picked, we suggest the pilot formed by traces where the source and receiver are facing each other, this pilot being called the super-pilot.
12: Apply CC between the super-pilot and the adjacent pilots to find the time delay.
13: Use the manual picking of the super-pilot and the time delays to determine the first-arrival of all the pilots.
14: Perform CC of each trace in data set with appropriate pilot for that angle, and use to determine the first arrivals.
15: Manually inspect the picks
```

3. The derived time delays as well as the time reference obtained in 1) are used to estimate an initial time position for each trace. In this position we can now define the time window (step 4 in algorithm 4.1).

Note that at this stage we have not perform any alignment yet. The selection of the window duration is also a crucial step as CC computations will be strongly sensitive to it. Contrary to Akram and Eaton (2016a) who suggest to use a window sufficiently large to contain a few cycles of the waveform, preliminary tests indicated that in our case we must restrict the time window to the first cycle due to the abrupt cut coming from the window. This effect and suggested modification is illustrated in figure 4.11 for a trace from figure 4.10a located at -56.26 cm. The constant time window duration is a bit too large for this signal to only include the first cycle, creating a large negative spike at the end. To avoid this, we

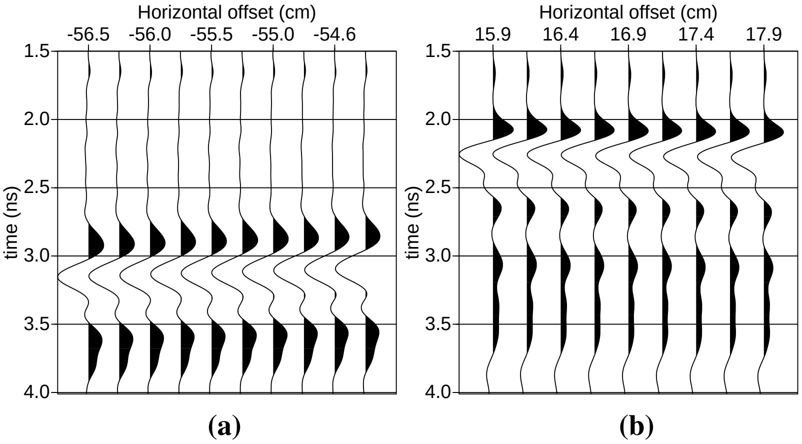

Figure 4.10: After applying the angle sorting, two groups of traces are extracted from figure 4.6a with the associated horizontal offset. (a) 10 traces located on the left and (b) 9 traces located on the right of the receiver. No alignment has been performed in both figures.

simply impose that after the first cycle, the signal is filled with zeros as shown in figure 4.11b. Then, for

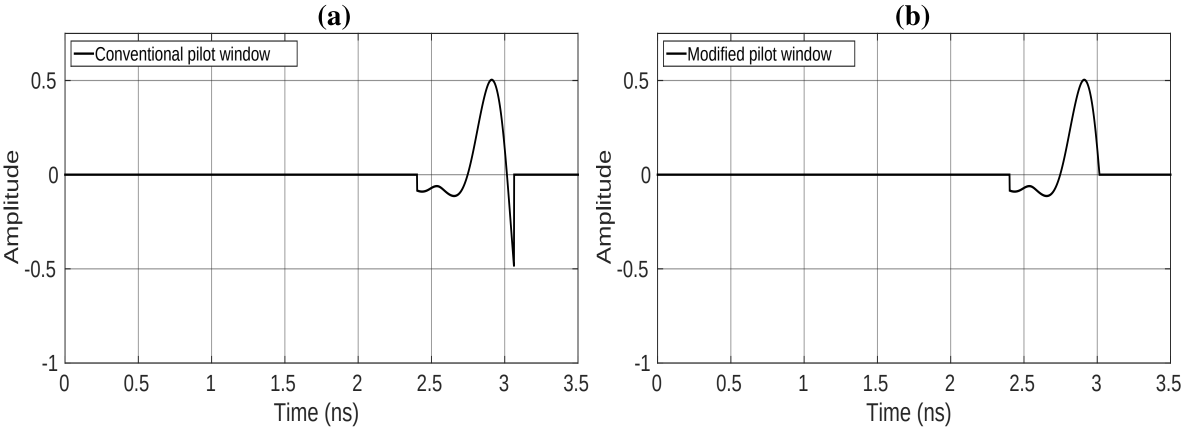

Figure 4.11: Pilot trace used to crosscorrelate the traces of figure 4.10a, it correspond to the trace located at $-56.26\,cm$ and chosen since it has the highest S/N. (a) Pilot with the conventional approach using a constant cross-correlation window. (b) The same pilot where the window has been modified in order to remain with the first cycle and remove the negative interference displayed in (a).

each gather, the signal with the highest S/N is selected as the pilot trace and CC are performed between the pilot traces and other traces of the group, for instance the discussed pilot in figure 4.11 is the trace with the highest S/N within the corresponding angle gather (figure 4.10a). The CC and the use of our window strategy provides the relative time delays for all the traces in each gather (steps 5 to 6). Using these delays, the traces are then aligned and stacked in order to create a new mean pilot trace paving the way for a second computation and updated re-alignment (steps 7 to 9). As mentionned by Irving et al. (2007), the need for this second process depends on the S/N ratio of the traces: in our case, for a total array of 493 traces, only 8 traces needed a second alignment.

Figure 4.12a illustrates the satisfying result of the process by superimposing the 10 traces presented in figure 4.10a after the time delays were applied: the first cycles are perfectly superimposed. Once we arrive to the proper alignment, we compute a mean trace (figure 4.12b), which will acts as the pilot trace for the gather. This process is repeated for all the different angle gathers leading to a decimated mean receiver gather displayed in figure 4.13.

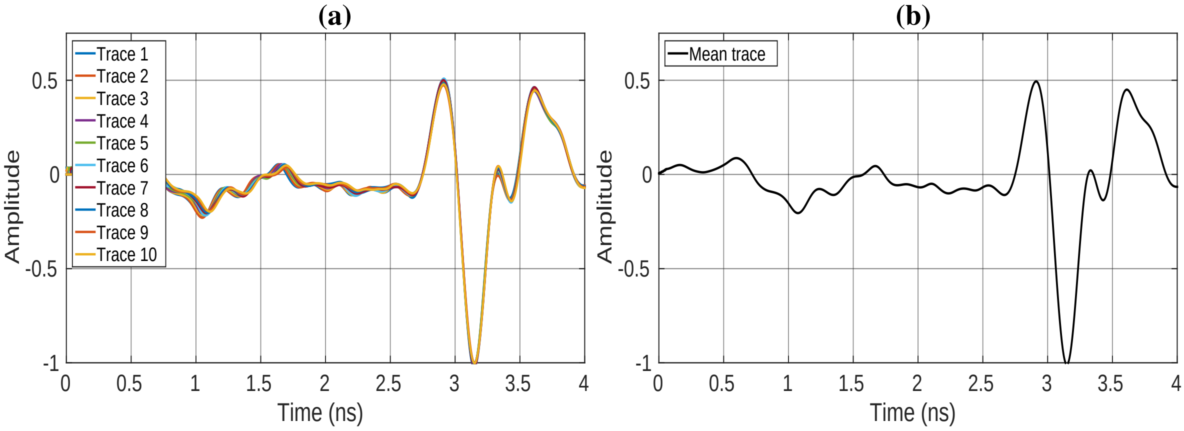

Figure 4.12: (a) The 10 traces of figure 4.10a after the alignment obtained by using the pilot presented in figure 4.11b. (b) A mean trace computed with the 10 traces of (a).

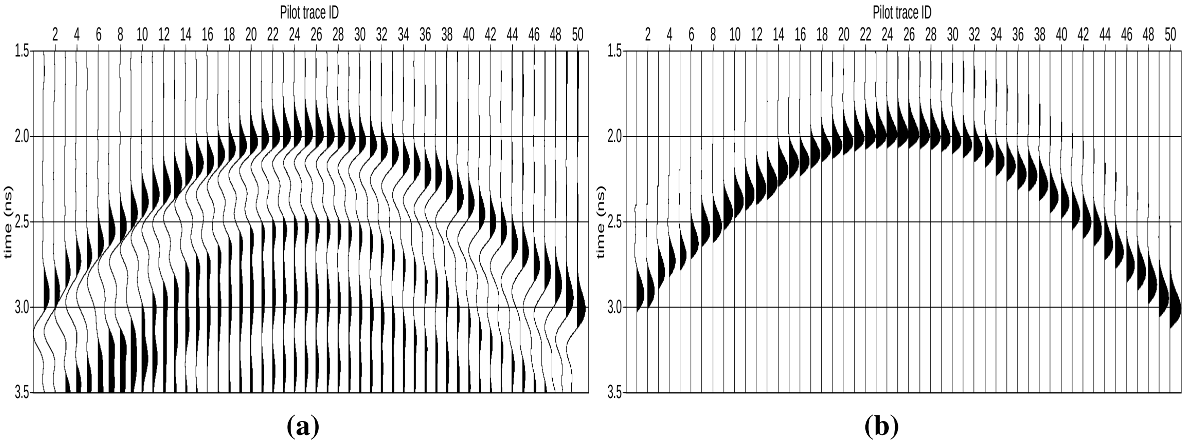

Figure 4.13: (a) The 50 pilots obtained by CC approach from the gather in figure 4.6a. (b) Same pilots of (a) after applying the window strategy of isolating the first cycle.

From there, the original approach of Irving et al. (2007) suggested to manually pick all these pilot traces, a process which can be cumbersome in the presence of a large dataset. In addition, this strategy can lead to biased and inconsistent picks because it relies on the picking-operation subjectivity (Sabbione and Velis, 2010). Therefore we choose to continue with the automated strategy through the CC approach by first selecting a “super-pilot” reference trace and then compute CC between the reference and the 50 pilots of a receiver gather after the time windowing strategy (figure 4.13b). For the six receiver gather recorded, the “super-pilot” chosen is the one corresponding to the smallest angles, i.e. when the antennas face each other. As an example, the pilot 25 covers a horizontal offset range of [-0.98,1.22] cm, lower than the dimensions of the antennas (figure 4.2.

This process provides relative time lags between each pilot trace representative of different angle gathers and the “super-pilot” trace. As relative time delays have already been obtained for each angle gathers compared to the pilot trace, we have now access to relative times of all the traces of a receiver gather relative to the super-pilot reference.

This process was done for the 6 acquisitions performed in air. The 6 super-pilots are shown in figure 4.14a and each of them requires the manual picking, however, we can reduce to the maximum the picking, we decide to apply CC to find the time delay between the super-pilots instead of picking 6 times which can lead to potential inconsistencies, consequently only 1 super-pilot in figure 4.14a needs to be manually picked, in this case we picked the super-pilot 4 which is illustrated in figure 4.14b with a vertical blue line highlighting the picking. Subsequently, the first-arrival of super-pilot 2 is easily estimated by using the time delay previously computed between super-pilots, this first-arrival is used to obtain the first arrival of the 50 pilots in figure 4.13. Finally, the first-arrival of each pilot is used to estimate the first arrivals of the associated traces in each angle gather.

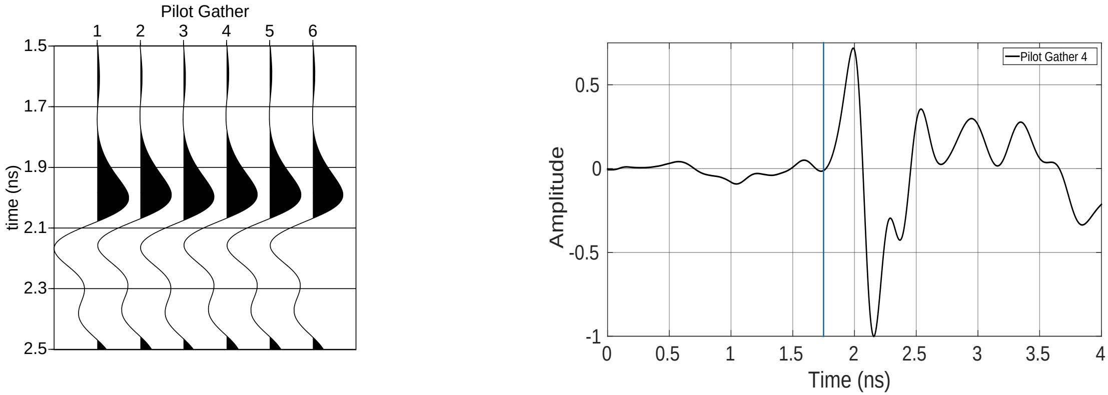

(a) **(b)**

Figure 4.14: (a) Super-pilot traces for the six receiver gathers. (b) Super-pilot number 4 extracted from (a), where the manual picking is represented by the vertical blue line.

Examples of final pickings are superimposed in figure 4.15a-b for two receiver gathers. They show that there is no particular problem and that no picking needs to be reviewed, certainly thanks to the careful time window selection and the good S/N ratio of the data. The picking database will now be analyzed.

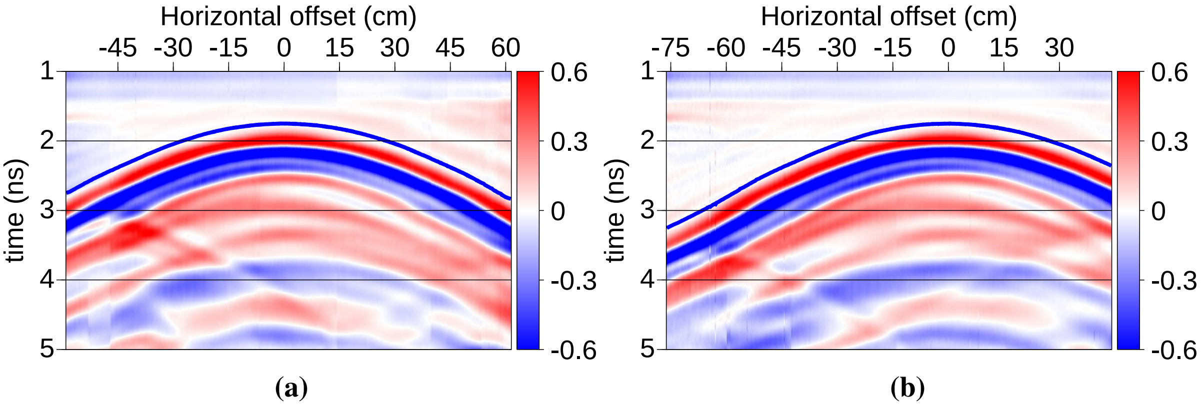

Figure 4.15: Picked traveltimes obtained by crosscorrelation have been added to (a) the gather number two (figure 4.6a), and (b) the gather number six (figure 4.6b).

4.3 Source/receiver effects and corrections from air data

4.3.1 Time zero calibration and stability

The precise estimation of the source time is a recurrent problem in GPR. For surface acquisitions, we generally use the arrival time of the air wave to adjust the initial time (t_0) of the source. For this experiment carried out in the air, this approach is also possible while it is more complex in the case of the acquisition on the carbonate block. To get rid of potential antenna length effects, as discussed in the previous chapter, we used small offset data, i.e. when the antennas face each other. For each gather, 11 traces with horizontal offsets lower than $1.22\,cm$ have been used so that they always are limited inside the Tx/Rx diameters according to the design of the antennas (figure 4.2). The corresponding pickings shown in figures 4.16a-b for gathers 2 and 6 (figures 4.15a-b), respectively, exhibit a limited variability equal to the time sampling (1.22 picoseconds). Their flat pattern, not expected if sources were point-sources, is due to the spatial extend of the antennas so that it seems that the traces appear to have propagated on identical vertical lengths of $35.5\,cm$. Using a velocity of $30\,cm/ns$, we can estimate an average t_0 for each gather as the difference between the picked traveltimes and the theoretical one ($1.18\,ns$).

The 11 t_0 values have been estimated for each of the 6 available gathers (figure 4.17a), many being identical due to the resolution of the sampling, for instance in gather 4 we only see three points but indeed 11 points were plotted. The average t_0 from the 6 gathers ($11 \times 6 = 66$ traces) is highlighted with a horizontal line being $0.569292\,ns$. This mean value can be compared with the average t_0 of each gather in order to estimate a variability, i.e., how far is the mean value from the t_0 of each gather, a variability of $2.67\,ps$ is obtained. Another representation of the $66\,t_0$ values can be given by a box plot (figure 4.17b), this kind of plot allows a clear summary of large amounts of data in five parts: 1) the minimum value, the bottom and top of the box are 2) the 25th and 3) 75th percentiles of the sample data, the distance between 2) and 3) is defined as the interquartile range, 4) the red line in the middle of the box is the sample median, and 5) the maximum value of the sample. The main observation is that our estimated average t_0 is within the interquartile range, thus it is a value inside a confident range, in addition, outliers were not detected, which are obtained when a value is more than 1.5 times the interquartile range away from the top or bottom of the box. The emitting time of the source can consequently be considered as rather stable, although $\pm 2.67\,ps$ of uncertainty remains.

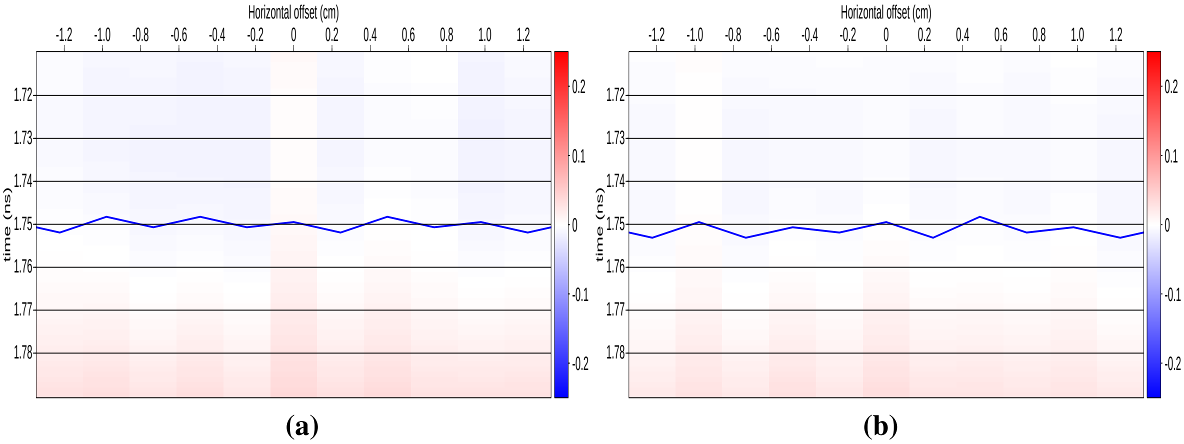

Figure 4.16: Picking variability for the 11 traces located at short horizontal offset. (a) Close-up of figure 4.15a. (b) Close-up of figure 4.15b.

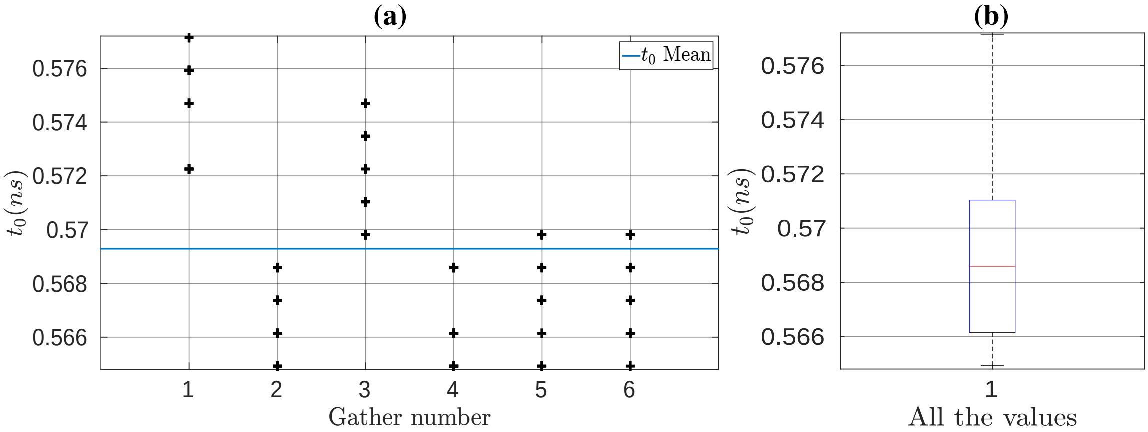

Figure 4.17: (a) t_0 values obtained in each air gather. The mean of all the values is superimposed with a blue line. (b) Boxplot representation of all the t_0 values, outliers were not found.

4.3.2 The need for antenna corrections

From figure 4.17a we know that an average t_0 correction can be computed in each gather, such a correction followed by the assumption of Tx/Rx locations at the center of the antennas and knowing that the vertical separation in the experiment is $35.5\,cm$, the six recorded gathers can be plotted in figure 4.18. The theoretical curve under the same Tx/Rx location assumption, considering the velocity of air and the vertical separation of the experiment is also superimposed (solid line in figure 4.18). The picking curves have a good agreement with the theoretical curve at small horizontal offsets (lower than 4 cm), they then gradually move apart to reach a stable gap for large offsets. This also agrees with the observation made earlier on the short offsets which did not show a hyperbolic shape (figure 4.16). Note that these non-linear observations are the same for all picked shots, moreover the picking of the six gathers is quite stable since all the curves are well superimposed. The incorrect match between the picked values and the theoretical curve seems to indicate that the hypothesis of Tx/Rx point at the center of the devices is not satisfactory and we have to find a model that could explain these discrepancies. This is understandable considering the size of the antennas (5 cm diameter) and the propagation distances involved in our experiments.

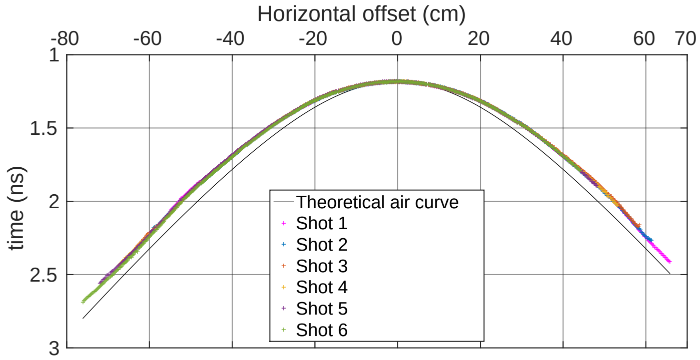

Figure 4.18: The six picked gather, where each gather received the corresponding average t_0 correction obtained from figure 4.17a, and Tx/Rx locations assumed at the center of the antennas. In solid the theoretical curve computed with the air velocity, the vertical separation of the experiment ($35.5\,cm$) and the same assumption for locations of Tx/Rx.

We propose in the following a methodology to retrieve the actual (effective) positions of Rx and Tx taking advantage of the *a priori* knowledge of the air velocity. We perform the analysis on the gather 2 of figure 4.18 (same picking of figure 4.15a after applying the average t_0 associated to the gather 2), the picked traveltimes along with the Tx/Rx location assumed at the center of the antennas are used to compute the velocity and the receiver-source angle in figure 4.19a, the angle being defined according to the angle convention of figure 4.7. The angles higher and lower than 90° respectively represent the negative and positive horizontal offset values in figure 4.18. Only at angles close to 90° a velocity close to 30 cm/ns is achieved, while at other angles the velocity is overestimated. Figure 4.19c shows offset versus angle patterns of the uncorrected and apparent positions, the latter being estimated to force the retrieval of air velocity. Such representation shows clearly that the two curves meet at very short offsets but also that they tend to meet at very long offsets. This is reassuring because it indicates that the antennas can be considered as point-like as soon as the propagation is far away. Unfortunately we are in the area where the effects of non-point sources and receivers will be maximum.

Since we know the needed offset that satisfy the air velocity from figure 4.19b, the positions of Tx/Rx can be shifted equally in both antennas in order to obtain such an offset. It is worth mentioning that Tx/Rx are always located in the center of the device, and the obtained shift that satisfy the air velocity will be applied from this initial location. The shifts are shown in figure 4.19c, it shows that the maximum radius of $2.5\,cm$ of the antennas is never reached, so that we cannot consider a three-point model (sources at the middle and on the edges of the antennas) like in the acoustic case. We can also observe that the Tx/Rx effective point progressively increases until a large angle is reached. In the near-offset range, as discussed before when looking at the 11 near-vertical traces (near 90°) used to estimate t_0, the flat pickings were already indicating that the lengths of the 11 paths were identical. For these traces, we impose that only the receiver position is shifted and located exactly in front of the source assumed to be at the center of the antenna. This assumption implies that the main energy of the source arises from the center while the receiver can record the waves at different position besides the center. This simple procedure will guarantee that velocity of air is always located at $30\,cm/ns$ regardless of the angle. Finally, we compare in figure 4.19d the picked traveltimes versus the Tx/Rx offset we have by assuming no correction and the offsets after applying the shifts from figure 4.19c, the pattern shows the progressive increase of the correction at large offsets, it must be noted that the picked traveltimes are the same in both curves.

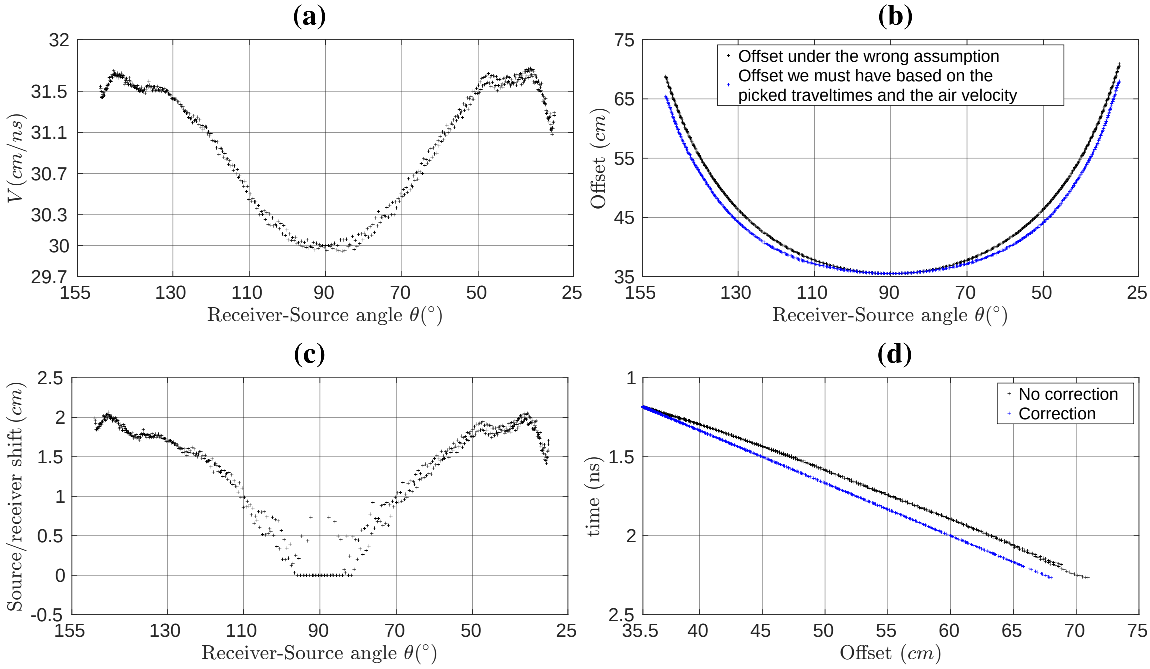

Figure 4.19: (a) Velocity versus angle based on the picked values of gather number two (blue in figure 4.18) and Tx/Rx assumed as points located at the middle of the antennas. (b) Uncorrected (black) and adjusted (blue) offsets versus angle distributions.(d) Deduced Tx/Rx shift derived from the difference between the black and the blue curves in (c), the shifts are applied equally in both antennas and from the no correction assumption, i.e, center of the devices. (d) Picked traveltimes versus Tx/Rx offsets computed before (black) and after (blue) applying the shift of (c) corrections.

Other views of the effect of these corrections for this gather are provided in figure 4.20. They first show a comparison between new effective and original horizontal offsets (a) and angles (b), the latter shows that if we want the velocity of air, angles lower than 90° need to increase while angles higher than 90° need to decrease, this is important to note for future computations on the block experiment. In terms of illumination changes, the slight changes are illustrated using straight raypaths before (c) and (d) after corrections.

By extending this approach to the 6 acquired gathers, we are able to generate an average correction pattern (figure 4.21), whose degree of averaging depends on the available angles present in each gather. These corrections will generate positions changes of sources and receivers. This averaged correction model was then quantitatively tested for each individual receiver gather using a comparison between the modeled velocity v_{syn} and the expected 30 cm/ns velocity in a RMS sense:

$$RMS_v(\%) = 100 \times \sqrt{\frac{1}{N}\sum_{sr}\left(\frac{v_{syn}-30}{30}\right)^2}, \tag{4.1}$$

N being the number of traces per gather. The results, presented in figures 4.22a-b for the gather 2 and 6 (figure 4.18), show low RMS values of 0.23% and 0.32% respectively. Values in the velocity range of [29.7,30.3]cm/ns lead to a RMS of less than 1% which is quite acceptable considering picking uncertainties.

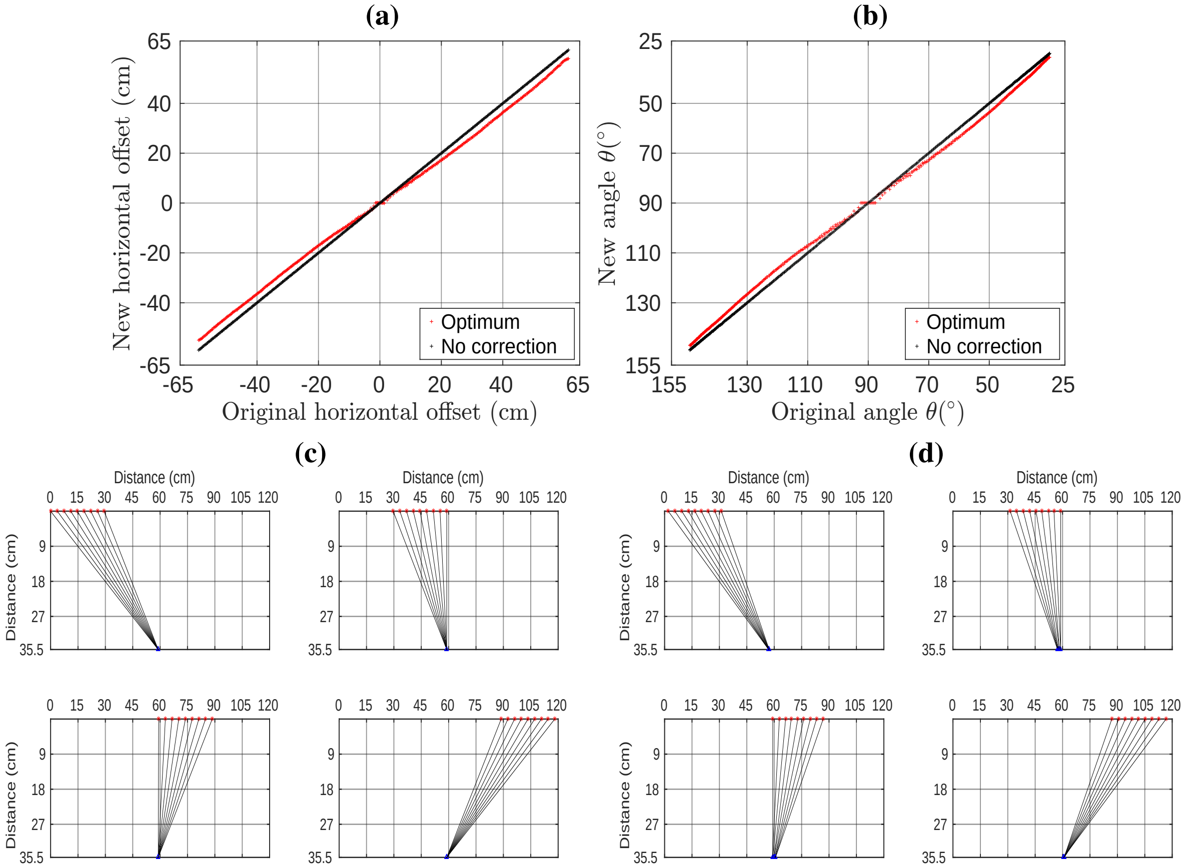

Figure 4.20: Differences between new and original horizontal offsets (a) and angles (b). In both figures, the no correction points in black are computed under the source/receiver assumption at the center of the antennas. Raypath changes for the same gather before (c) and after (d) the corrections.

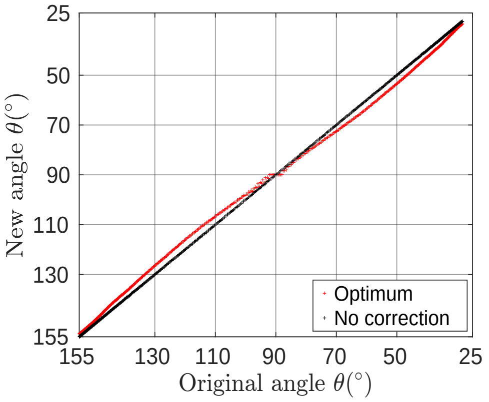

Figure 4.21: Optimum angle corrections for the air experiment obtained after averaging the information of the 6 recorded gathers.

This study clearly indicates that at this scale, even when waves propagate in a non attenuating and homogeneous material, the kinematic behavior of antennas is more complex than expected even if there are no contact problems between antennas and a material. Something to highlight is the fact that at large offsets, the tip-to-tip antenna path (point on the edges of the devices) is not a correct assumption, this somehow violates the Fermat's principle when the nearest path between two points is required, while in the seismic experiment such an approximation worked well to represent the source. These complexities within the antennas were known at the level of amplitudes because of the radiation patterns that can be modeled in general but their effect on arrival times was a bit unexpected. It can be expected that these effects are very different in the presence of contact with a material of different EM properties, and that the corrections obtained in air are not directly transposable to the experiment on the carbonate block.

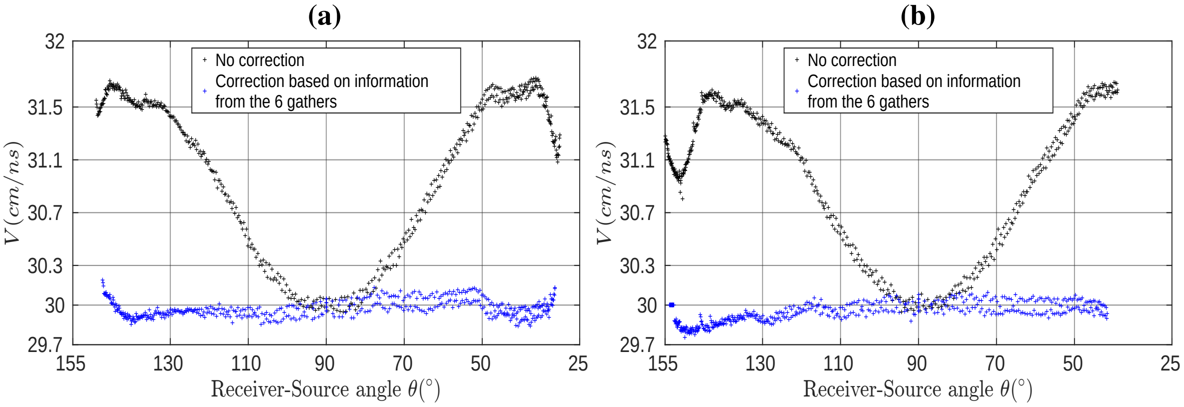

Figure 4.22: Corrected (blue) and uncorrected (black) apparent velocity estimations for (a) gather 2 and (b) gather 6 (figure 4.18).

4.4 Source-receiver effects on carbonates data - potential correction

4.4.1 Global view of the picking

Before showing the picking we should recall how is distributed the acquisition in the block, 9 receiver positions on the bottom are recording the car moving on the top face and both antennas are displaced from left to right (figure 4.3b), these gathers being numbered as shot 1 until shot 9. Subsequently, the receiver is located on the right face and the car on the left, both antennas being displaced from the bottom to the top (figure 4.3c), thus forming the shot 10 until shot 18. Table 4.1 helps to understand the order of the acquisition, the column of initial position for both antennas in gather 1-9 is measured from the left corners, then we know that the receiver is displaced by 2.5 cm to the right and the car produce another gather also from left to right. Regarding gather 10-18, the initial position is measured from the corners at the bottom and then both antennas displace to the top.

The cross-correlation technique (algorithm 4.1) presented in the air experiment was chosen to pick the data acquired in the carbonate. Similar to air, the picking is performed on the raw data, i.e., before the t_0 correction. From the first 9 gathers forming the near-vertical angles, we illustrate some of them in figure 4.23 with the picking added, in general, the picking follows perfectly the first arrivals with no sharp discontinuities. According to table 4.1, gather 1 (figure 4.23a) has at the beginning the source almost facing the receiver and then it moves to the right increasing the offset and the traveltimes, note that we have the opposite for gather 9 (figure 4.23e). Moreover, figure 4.23c is the gather with the receiver located at the center of the block, one may note the hyperbola shape, however, it looks quite symmetric, something not desired since we are looking for velocity changes and not for a homogeneous result.

Gather N°	Source Init. Pos. (cm)	Receiver Init. Pos. (cm)	Receiver separation (cm)	Receiver disp.	Source disp.
1-9	3.04	6.5	2.5	left to right	left to right
10-18	2.19	6.5	2.5	bottom to top	bottom to top

Table 4.1: Distribution of each gather, source is always emitting in front of the receiver. Initial position of antennas is assumed as a point at the center of the devices and measured from the nearest corner, from the left corner for gathers 1-9 and from the bottom for gathers 10-18. Use figure 4.3 to complement this table.

We also show some gathers for the near-horizontal paths (shots 10-18) in figure 4.24, in general they look quite similar to the near-vertical shots, this is notorious if we compare the gather 14 (figure 4.24c) with the gather 5 (figure 4.23c) since both have the receiver at the center of the face, if the pickings of near-horizontal gathers are similar to the vertical ones, we may start thinking about a poor detection of anisotropy, we validate this afterwards, the main message in this section is to illustrate the performance of our semi-automatic picking technique which clearly detects the first arrivals, the total dataset has 2106 traveltimes which was obtained really fast since we reduce at the maximum the manual picking.

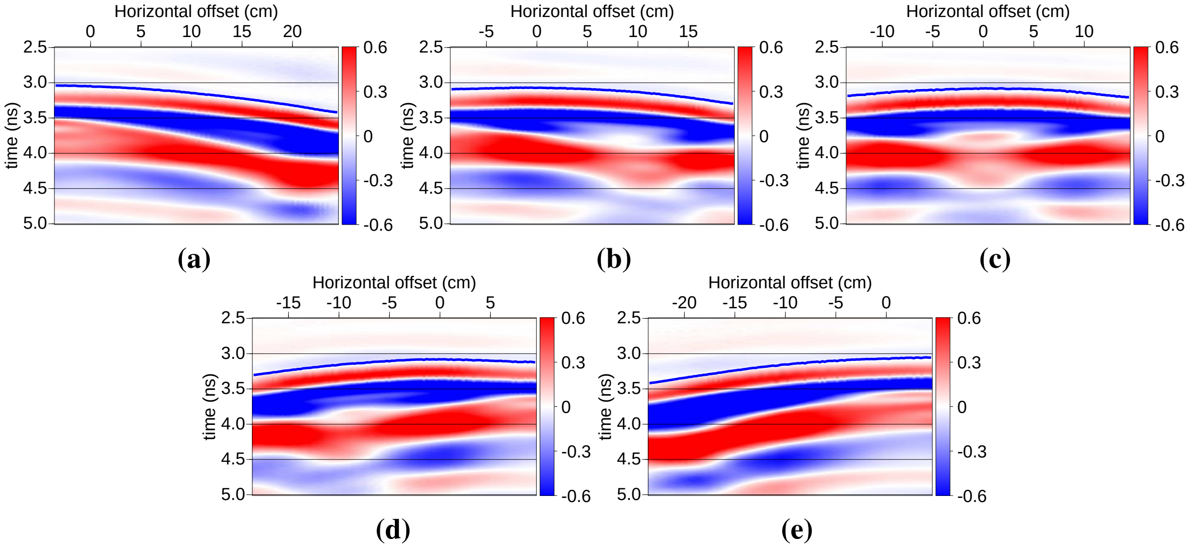

Figure 4.23: From the 9 gathers when the receiver is located on the bottom face and source on the top, we show gathers: (a) 1, (b) 3, (c) 5 which has the receiver at the center of the block, (d) 7, and (d) 9. Horizontal offset computed assuming point location at the center of the antennas. Picking obtained by cross-correlation is added in each gather.

One may note from the gathers that the waveform carrying the first arrivals has a similar shape to the air experiment, namely there is a slight increase in the amplitude followed by a decrease showing a minimum peak, therefore we may apply the same window used in the air experiment (figure 4.8) to compute the frequency content of some gathers in figure 4.25. As expected, the patterns from the block are very different compared to the air experiment which showed a more constant shape, for instance, we may analyze the shot 1 (figure 4.25a) which although it has low amplitudes at small offsets, the dominant frequency is about 2GHz and it decreases when the source is leaving until it reaches about

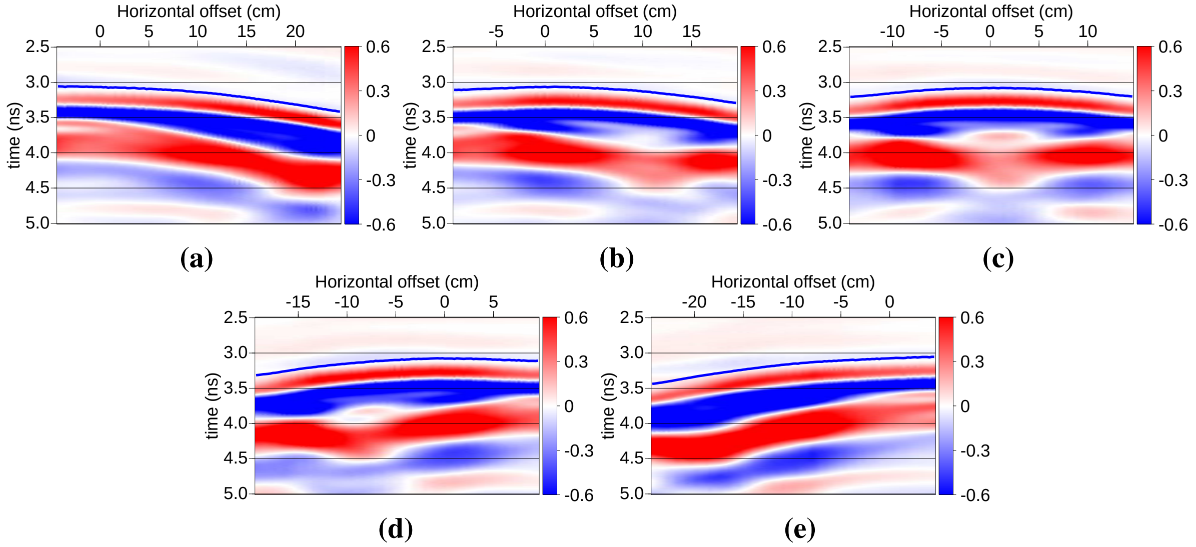

Figure 4.24: From the 9 gathers when the receiver is located on the right face and source on the left, we show gathers: (a) 10, (b) 12, (c) 14 which has the receiver at the center of the block, (d) 16, and (d) 18. Horizontal offset computed assuming point location at the center of the antennas. Picking obtained by cross-correlation is added in each gather.

1GHz, the shot 5 with the receiver at the center of the face shows a more symmetric pattern with frequencies about 2GHz at small offsets, followed by some decreasing about $10\,cm$ and finally an increase at the largest offsets. One may note in all the gathers that at large offsets where the influence of the air is high, they are also the offsets where we see the increase in the frequency reaching about 2GHz. After computing the spectra of all the gathers, we may conclude that our dataset remains in a frequency range of 1.5-2GHz, important information when estimation of the signal wavelength is required.

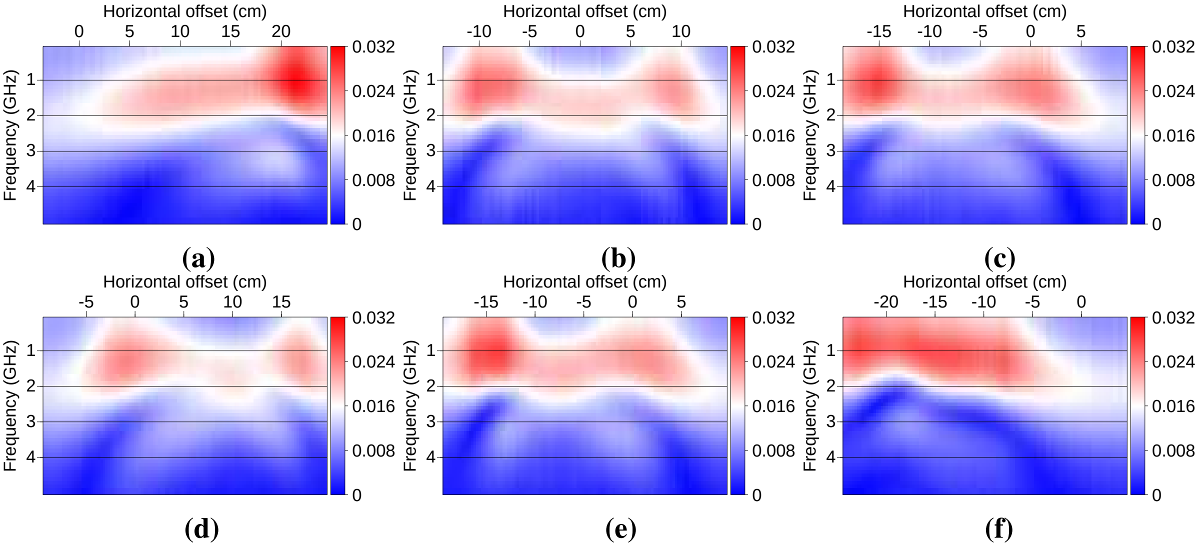

Figure 4.25: Frequency content of some gathers after imposing the same window of the air experiment (figure 4.8), average dominant frequency is computed for each gather. Gathers: (a) 1, 1.46GHz; (b) 5, 1.46GHz; (c) 7, 1.42GHz; (d) 12, 1.48GHz; (e) 16, 1.4GHz; and (f) 18, 1.36GHz.

We know justify the decision of our acquisition design, the reasons why we only record with the car moving in the opposite face to the receiver. Figure 4.26 shows one tentative of recording diagonal paths, the receiver is static on the right face at $4\,cm$ measured from the bottom corner while the car is on the top moving from left to right, the first observation is the large amount of noise compared with the gathers of our acquisition (figures 4.23 and 4.24) where the signals were quite clean before the first arrival. Besides, the main waveforms are distorted, we do not see the same shapes as in the air or block experiment, and note that at short offsets, there is a strong and very fast arrival. These observations are probably due to major impact of the air for this particular acquisition, the air and block contact certainly causing some refractions. Although we have an efficient picking tool, it requires the user to identify the first onset, however in this gather is quite challenging to identify it and it is not clear if we are picking a transmitted wave through the block or an air wave, while in our gathers the pickings are consistent and well positioned before the main waveform. These difficulties made us to decide an acquisition where the air can be partially suppressed, namely transmitter and receiver always at opposite sides. Same acquisition was adopted by Hanafy and Al Hagrey (2005) at this centimeter scale in a wooden box to evaluate an isotropic tomography code, although they do not discuss the reasons of the acquisition, we believe they also noticed the same difficulties.

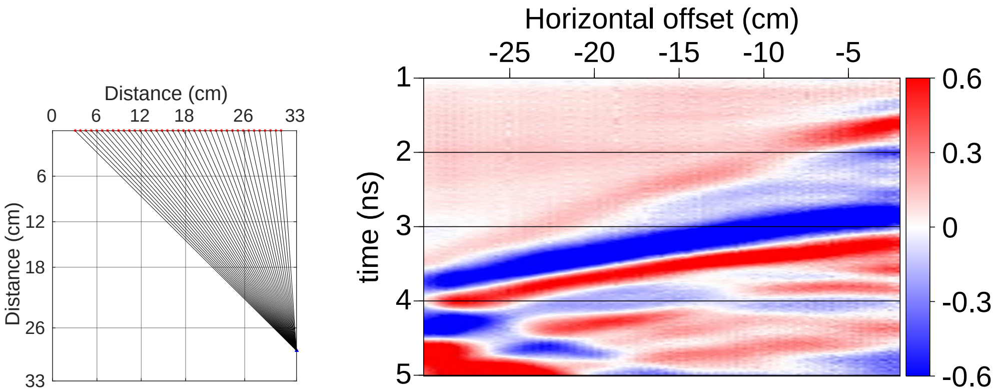

(a) **(b)**

Figure 4.26: (a) Acquisition sketch of Tx (red) and Rx (blue) forming diagonal paths, position assuming one point at the center of the antennas. (b) Time domain gather as a function of the horizontal offset, receiver is static and the car (source) is approaching it.

4.4.2 Air correction applied on the carbonate dataset

As part of the processing, we apply the correction of $t_0 = 0.56929\,ns$ obtained in the air experiment to all the picked times of the block, therefore all the discussion and analysis are based on the correct times from the block in what follows. However, we should recall the presence of some variability on t_0 estimated as $2.67\,ps$, thus for all the picked times we computed the relative error in percentage due to this variability, the maximum error being 0.11% that we consider really small and not able to change drastically our tomography results.

Since we obtained a correction from the air experiment, we may use it in the block to see the improvements compared with the no correction choice. We use the gather 1 whose acquisition sketch is shown in figure 4.27a assuming no correction, namely point Tx/Rx at the center of the devices, in this gather receiver is located at $6.5\,cm$ from the corner (table 4.1). Subsequently, we plot the picked traveltimes as a function of the horizontal offset when no correction is used (black in figure 4.27b), although we invert the velocities with our tomopraphy code, first we may compute synthetic traveltimes under the homogeneous assumption in order to evaluate how far we are from the picked traveltimes. The procedure is simple: we evaluate different velocities, for each velocity we compute the synthetic traveltimes and we compute the percentage error given by

$$RMS_t(\%) = 100 \times \sqrt{\frac{1}{N}\sum_{sr}\left(\frac{t_{syn} - t_{pick}}{t_{pick}}\right)^2}, \tag{4.2}$$

where t_{syn} are the synthetic traveltimes, t_{pick} are the picked traveltimes and N the number of traces. The velocity that produce the minimum error is displayed as magenta in figure 4.27, the obtained error being 2.51% and the modeled hyperbola is not fitting our picked times.

As a next step, we apply the correction found in air to the picked traveltimes, namely we only edit the positions and not the picked values (blue in figure 4.27b), note that we start to see the shape of an hyperbola. Since we know the positions given by the air correction, the error analysis is repeated, we evaluate different velocities in order to find the best fitting hyperbola (orange in figure 4.27b), although the error is improved to reach 1.14%, we believe that the model obtained in the air experiment is not completely valid when antennas are in contact with the carbonate block.

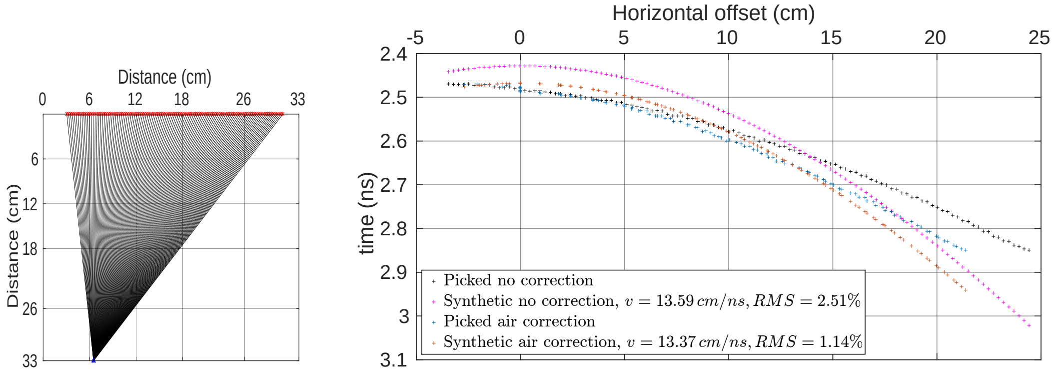

(a) **(b)**

Figure 4.27: (a) Acquisition sketch of shot 1 assuming straight raypaths whose ends are located at the the middle of the antennas. (b) Time versus horizontal offset for the picked traveltimes with no correction on the position (black), and after applying the correction obtained in the air experiment (blue). Synthetic traveltimes are computed under the homogeneous assumption, the one with the minimum error is added for both the no correction case (magenta) and with the air correction (orange). The RMS time difference in percentage is obtained from equation 4.2.

We have repeated the analyis for another gather, the number 14 which has the receiver located on the middle of the right face (figure 4.28a). The corresponding time versus horizontal offset for this gather is shown figure 4.28b, picked traveltimes as well as the optimum modeled hyperbola show an error of 1.18%, although it is clear that the approximation is not good, the picked traveltimes show a better hyperbola shape compared with the gather 1 whose receiver is located near the corner (figure 4.27). After applying the air correction, the picked times show a consistent hyperbola shape and the modeled hyperbola fits quite well the picked one with 0.57%. We may conclude that the model found in air works better when the receiver is not located near the corners, however, we should investigate the possibility of a better model.

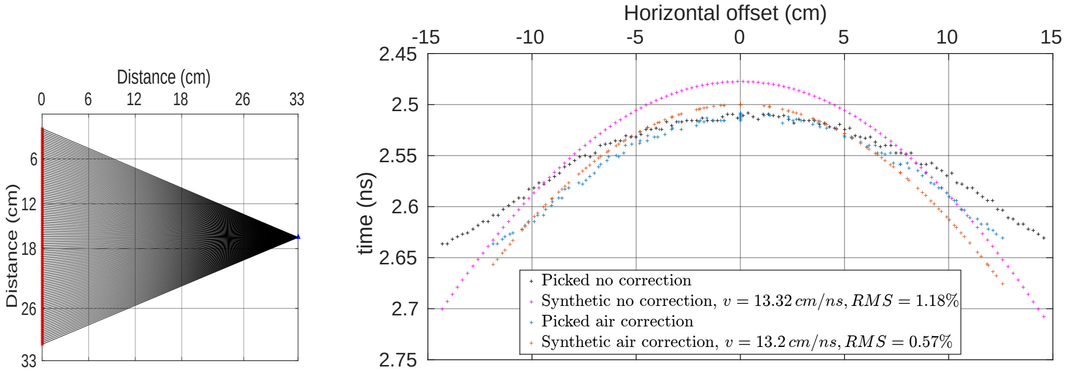

(a) **(b)**

Figure 4.28: (a) Acquisition sketch of shot 14 assuming straight raypaths whose ends are located at the the middle of the antennas. (b) Time versus horizontal offset for the picked traveltimes with no correction on the position (black), and after applying the correction obtained in the air experiment (blue). Synthetic traveltimes are computed under the homogeneous assumption, the one with the minimum error is added for both the no correction case (magenta) and with the air correction (orange). The RMS time difference in percentage is obtained from equation 4.2.

Since all the dataset is available, the apparent velocity versus Rx/Tx angle distribution can be obtained considering straight raypaths whose extremities are located at the middle of the antennas (figure 4.29a). We see a high sensitivity to offset, both in the vertical and horizontal acquisitions, with overestimated velocity values at large offsets. Similar pattern has been presented by Peterson (2001) in a crosshole acquisition at the meter scale, his first observation is that for each gather there is a symmetry on the velocity about the angle where Rx/Tx are facing each other (90° or 180°), and such a symmetry cannot be attributed to anisotropy, his explanation to this pattern is that for large offsets the direct arrival of the signal traveling through the earth is distorted by a faster arrival traveling within the borehole, however, no numerical analysis is given to validate his conclusions. Irving and Knight (2005) go further to investigate this pattern, GPR full modelling was performed in a crosshole environment at the meter scale, and varying three parameters: distance between boreholes, length of the antennas which in GPR a large antenna also means lower frequency, and the ratio between the velocity surrounding the antenna in the borehole and the velocity of the medium. For the latter they used 2 as a maximum velocity ratio, while in our case is even worst because if we assume a velocity of $13\,cm/ns$ in the block and the velocity of the air being $30\,cm/ns$, a ratio of 2.3 is obtained. They concluded that under these three factors, it is not correct to assume the propagation of EM waves between the center of the antennas, which is basically the same conclusion we arrive after looking the velocity pattern of both the air and the block experiment.

Applying the angle correction derived from air data in the limited angle range available (figure 4.29b), we obtain the new velocity distribution of figure 4.29c where the velocity variability is largely decreased especially as large offsets. However, it is obvious that this correction is not enough, always showing a hyperbolic behavior of the apparent velocity distribution. The extraction of the two gathers discussed before, namely the gathers 1 and 14 from figure 4.27 and figure 4.28, respectively is displayed in figure 4.29d. The correction appears to me more effective for the gather 14 (angle range of [150,205]°) while this is not the case for the gather 1 located near the corner (angle range of [50,100]°), where overestimated velocity values remain.

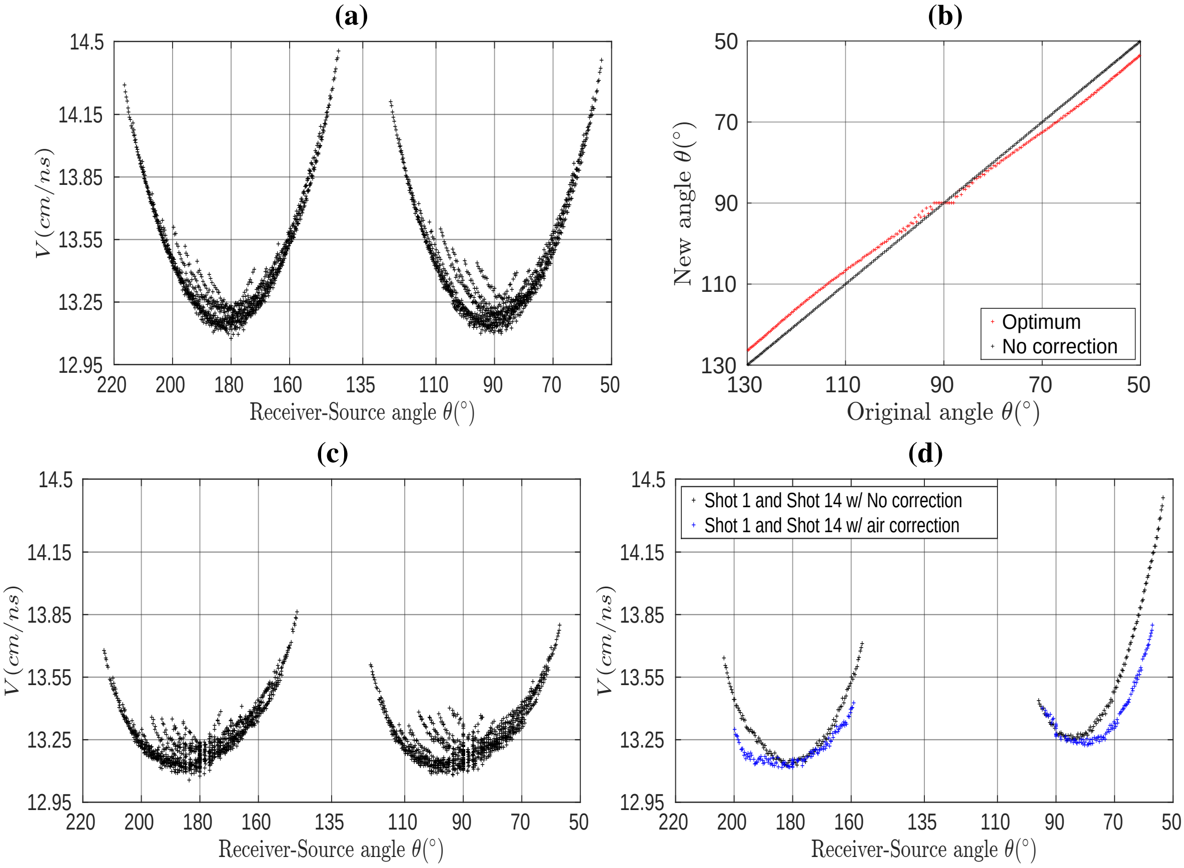

Figure 4.29: (a) Velocity versus angle for all the dataset acquired in the block assuming straight raypaths and position of point source/receiver located at the middle of the antennas. (b) Angle correction proposed from the air experiment in the limited angle range available. (c) Velocity versus angle for all the block dataset after applying the optimum angles of (b). (d) Two gathers are extracted from (a) and (c), which are indeed the same gathers we analyzed in figures 4.27 and 4.28.

4.4.3 A procedure for antenna correction for the carbonate dataset

In order to find the optimum positions of the antennas for the block experiment, we follow the air approach using the pattern of figure 4.29b as an initial point and consider a data-driven optimization to establish a new correction model appropriate for the block. In order to illustrate the optimization, we continue the analysis with the two gathers presented before, the number 1 and 14. From the velocity versus angle pattern of gather 1 (figure 4.29d), one may see that angles before 90° need to increase in order to suppress this hyperbolic shape while angles higher than 90° need to decrease, same conclusion is evident from gather 14 with the only difference that we are referring to 180°. We therefore propose to create two scalar values associated with each angle zone, one being associated with angles lower than 90° while the other is associated with angles larger than 90°. Contrary to the air experiment, the velocity is unknown in the block, and we rely on the homogeneous assumption for the correction analysis by roughly fitting modeled and picked traveltimes.

A first strong hypothesis concerns the particular case where the source is almost facing the receiver (angle range of [88,92]°). Like in the air experiment, in this case, which corresponds to an horizontal offset of [-1.1,1.1] cm, we consider that the receiver is always facing the source antenna which emits at the middle of the antenna, or in other words, it is only the receiver position that shifts and leads to a horizontal offset of $0\,cm$, note that the chosen range is behind the physical size of the antennas ($5\,cm$ diameter). Consequently, all angles for this range are reduced to a single angle of 90°. For the other angles, starting from the new optimum angles found in air, we perform an optimization where three parameters are involved:

1. F2 which is in charge of the angle values lower than 90°, note that this value has to be higher than 1 in order to increase the initial angles.
2. F1 which is in charge of the angle values higher than 90°, note that this value has to be lower than 1 in order to decrease the initial angles.
3. Velocity of the block.

As we have to respect the physical dimensions of the antennas, which means that the extension of source and receiver cannot exceed the maximum radius of the antennas of 2.5 cm, we add in the optimization process this limitation, basically if the optimum factor either F1 or F2 leads to an extension higher than 2.5 cm, our approach imposes the maximum radius to be the correction limit.

We perform a least-square fitting with the three parameters as follows: for a specific combination of F1 and F2, new sources and receivers positions are computed allowing to compute theoretical traveltimes for a given propagation velocity. The modeled traveltimes are then quantitatively compared with the picked traveltimes. For gather 1, the optimization result of the three parameters is shown in 3D in figure 4.30a, it indicates that the best combination of parameters in terms of RMS is F1=0.97, F2=1.04 and $v = 13.21\,cm/ns$ being located as magenta on the faces of the optimization cube. Note that the optimization is not sensitive to F1 for this shot, this is because there are almost no picked traveltimes for angles higher than 90°, therefore the optimization will be mostly driven by F2 and velocity. With these new angles and velocity, we can compute the new theoretical traveltimes, as displayed in figure 4.30b and it can be compared with the traveltime curve obtained with no correction. The improvement of the fitting is visible although not perfect, certainly due to the homogeneous velocity assumption, reaching a RMS value of 0.78% while the no correction curve reaches a minimum RMS of 2.31%, we may also compare the optimum correction with the air correction of figure 4.27b (F1=F2=1) which reached a RMS of 1.14%. It must be noted that the limit of the source extension is reached here at very large offsets (about $15\,cm$ offset) where the edge to edge path between antennas is used but the picked traveltimes cannot be fitted. We believe that this pattern is mainly due to the strong effect of the air that we have at this scale for those particular large offsets and for this edge receiver.

Another example is provided from gather 14 of figure 4.28, whose receiver is located at the middle of the face with a horizontal illumination. The resulting 3D image is displayed on figure 4.31a where the optimized values are F1=0.99, F2=1.04 and $v = 13.12\,cm/ns$. The optimization is much more accurate with clear minima for all the parameters and therefore there are not many trade-offs. The optimum theoretical traveltime curve (orange) is compared in figure 4.31b with the picked traveltimes after using the F1 and F2 values on the air correction, it reaches a very low RMS of 0.19% while the no correction curve we can only reach 1.18%, same comparison can be done after with the use of only the air correction which reached a RMS of 0.57% (figure 4.28). We should mention that here the maximum extension of the antennas that we reached was $2.1\,cm$, lower than the radius of the antennas, this is somehow not physically consistent because we should expect to localize the position of Rx/Tx on the edges of the devices when they are at large offsets as we did in the seismic source modeling for the same block, this certainly explain the complexities behind the radiation pattern of GPR antennas at this

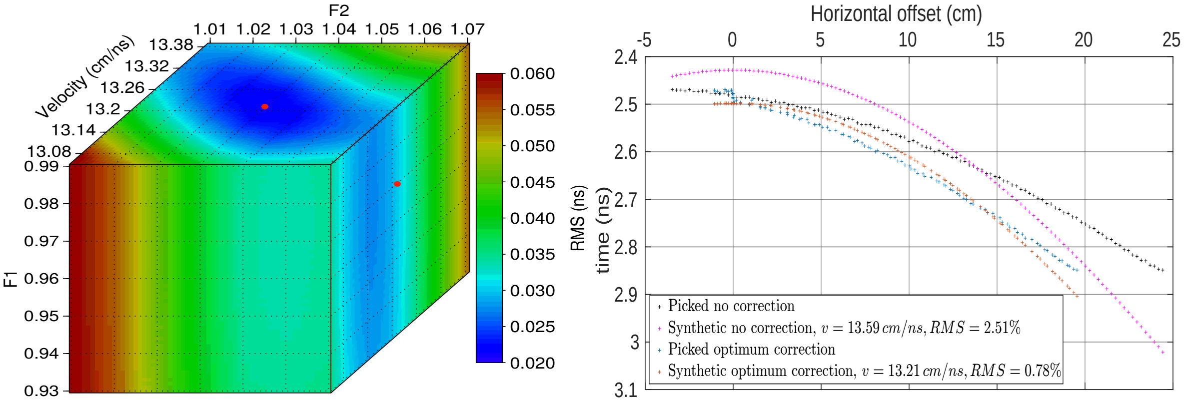

(a) **(b)**

Figure 4.30: Optimization result for gather 1 of figure 4.27. (a) 3D image of the three parameter optimization, with the lower RMS found for F1=0.97, F2=1.04 and $v = 13.21\, cm/ns$ (magenta point). (b) Time versus horizontal offset for the no correction picked traveltimes (black), best no correction modeled traveltimes (magenta), picked traveltimes after using the optimum values of F1 and F2 from (a) on the air correction (blue), and the theoretical curve after using the optimum values of F1, F2 and the best fitting velocity (orange).

particular scale and frequency. The edge to edge path was suggested by Irving and Knight (2005) at the meter scale and using a 100MHz antennas, however we may see that this is not a correct approximation at this centimeter scale.

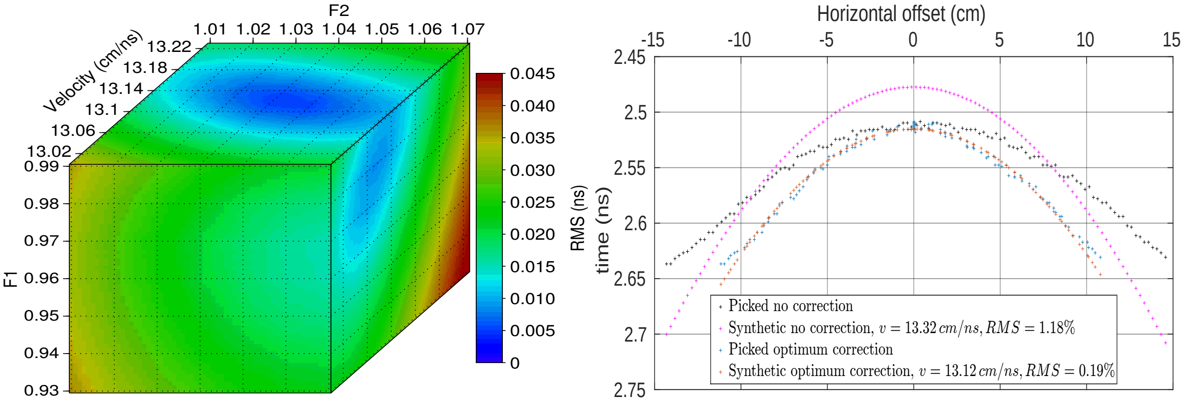

(a) (b)

Figure 4.31: Optimization result for gather 1 of figure 4.27. (a) 3D image of the three parameter optimization, with the lower RMS found for F1=0.99, F2=1.04 and $v = 13.12\, cm/ns$. (b) Time versus horizontal offset for the no correction picked traveltimes (black), best no correction modeled traveltimes (magenta), picked traveltimes after using the optimum values of F1 and F2 from (a) on the air correction (blue), and the theoretical curve after using the optimum values of F1, F2 and the best fitting velocity (orange).

This optimization has been generalized to the 18 available gathers resulting in a distribution of values for F1, F2 and velocities. Since we have our tomography code to invert the velocities, we focus on the values of F1 and F2. Their variability is analyzed based on a boxplot representation (figure 4.32a-

b) for F1 and F2, respectively. For F1 the mean value is within 75% of the estimated values with a variability of 0.04 (0.99-0.95 in figure 4.32a) without any outlier values. For F2, there is a lower variability of 0.03 (1.06-1.03 in figure 4.32b) in spite of the two outliers which were not considered for the estimation of the F2 mean value, such outliers are associated to gathers when receiver is located near the corners, i.e, large impact of air in EM waves. Since the two mean values are inside the interquartile range, we can consider them as optimum values that will be used to modify the angles previously estimated in the air experiment.

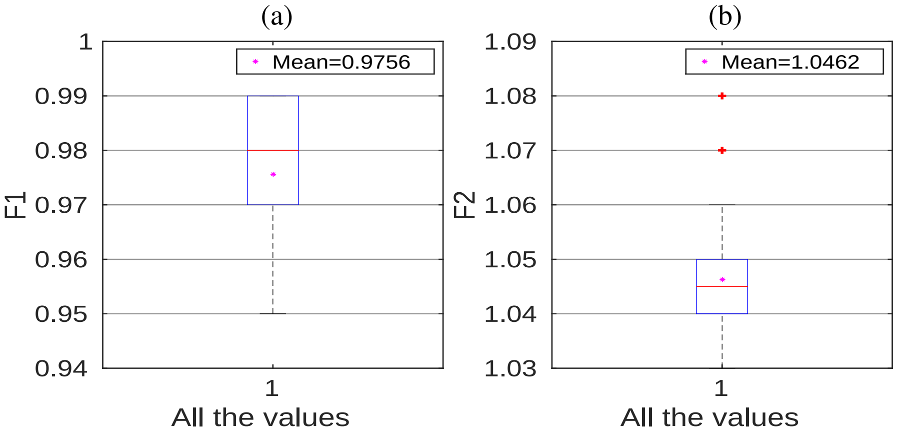

Figure 4.32: Boxplot of the parameters obtained in each gather optimization (a) F1 with a mean equal to 0.9756 and (b) F2 with mean equal to 1.0462.

4.4.4 Consequences of the proposed Tx/Rx correction model

The optimum angles obtained from the air experiment, shown in figure 4.29b, are then subsequently corrected in the defined angle range using the mean optimum parameters F1=0.9756 and F2=1.0462 (figure 4.32). This angle correction (shown in figure 4.33a) is equivalent to a shift of the source and the receiver positions, generating new offsets as we may see for all the dataset in figure 4.33b, it must be noted that around 0 the new offset is also 0 since we impose a shift on the receiver to be located in front of the source (90°). A new velocity versus angle distribution can then be proposed in figure 4.33c, which must be compared to the original one displayed in figure 4.33d. This Rx/Tx model strongly decreases the overestimated values originally detected at large offsets.

The effects of the Tx/Rx correction model on the acquisition geometry is illustrated on gathers 1 and 14 (figure 4.34), with a decimated number of rays for the sake of clarity. These sketches are dominated by the extension of the receiver size (blue triangles), this is even more pronounced for gather 1 presenting larger offsets (figure 4.34a). Indeed, for this gather, the correction reaches the maximum possible antenna extension of 2.5 cm, while shot 14 with lower offsets, only reaches a maximum correction of 2.1 cm. These representations also highlight the change in illumination generated by the horizontal shifts applied to both source and receiver, which are represented in figure 4.34c for both gathers. The changes in horizontal offsets generate changes of raypath lengths which are shown in figure figure 4.34e for all the dataset and increase naturally with offset.

These corrections induce large changes of apparent velocities, especially at large offsets, as illustrated in figure figure 4.34d. It shows that the shape of gather 14 is largely improved with an almost full

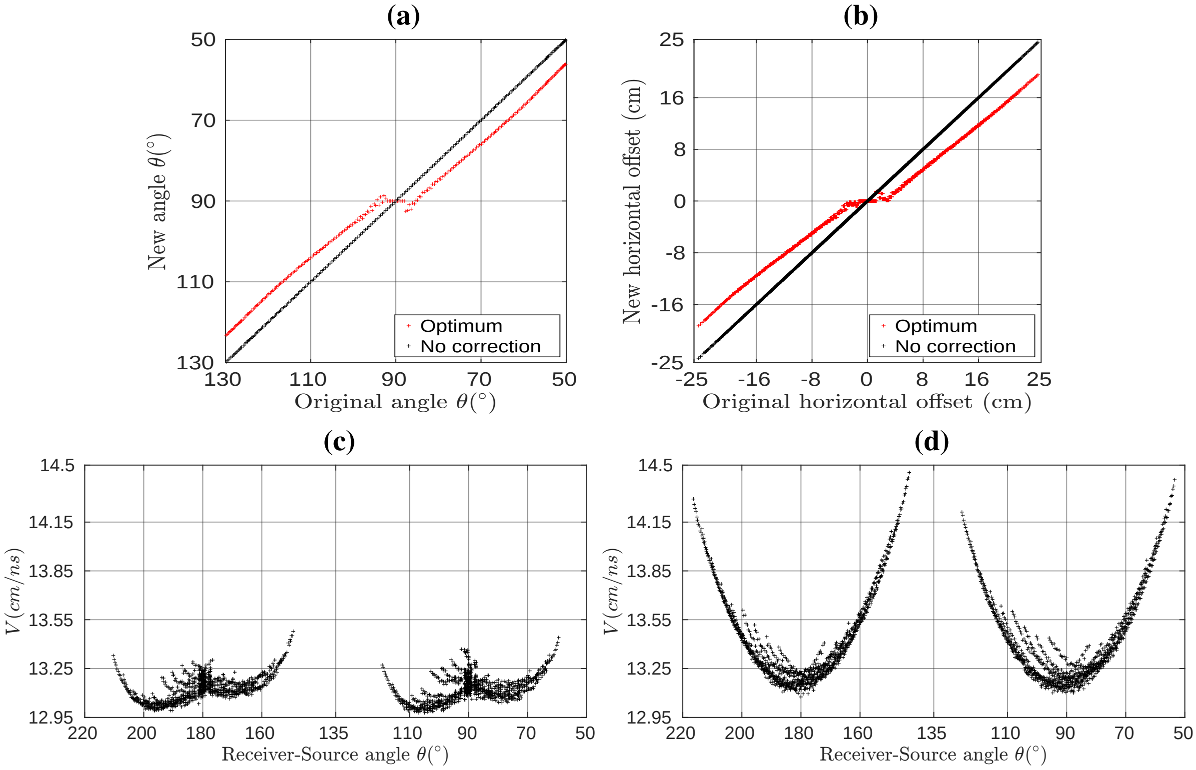

Figure 4.33: (a) Angle correction proposed for the block dataset, (b) horizontal offset for all the dataset after applying the angles of (a). Based on the picked traveltimes and the straight path assumption, the updated block velocity versus angle distribution (c) is compared to the initial one (d) with no correction.

removal of the hyperbolic pattern generated by the extended antenna effect. For gather 1, some overestimated values are still present although the correction involves the maximum radius of the antennas. It seems that while the correction appears efficient for most of the gathers located near the center of the block, it struggles a bit with the shots located near the corners, which might be influenced by the presence of the air boundary.

This simple data analysis assuming a homogeneous block and straight raypaths was able to detect and partly correct possible artefacts generated by the use of non-point source and receiver antennas relative to the block dimensions. This data-driven approach enables to obtain a source/receiver model showing that the GPR antennas are much more complex than the piezoelectric source used in acoustic experiment. It seems that if we refer to a single point of transmission and reception, these gradually shift from the center of the antennas outwards, reaching the edge of the antenna at large offsets. These corrections, already visible in the absence of a material between the antennas (air experiment), are even more pronounced when the antennas are in contact with a material, whose properties can affect the corrective pattern. The impact of these difficulties will now be assessed at the level of the tomographic results.

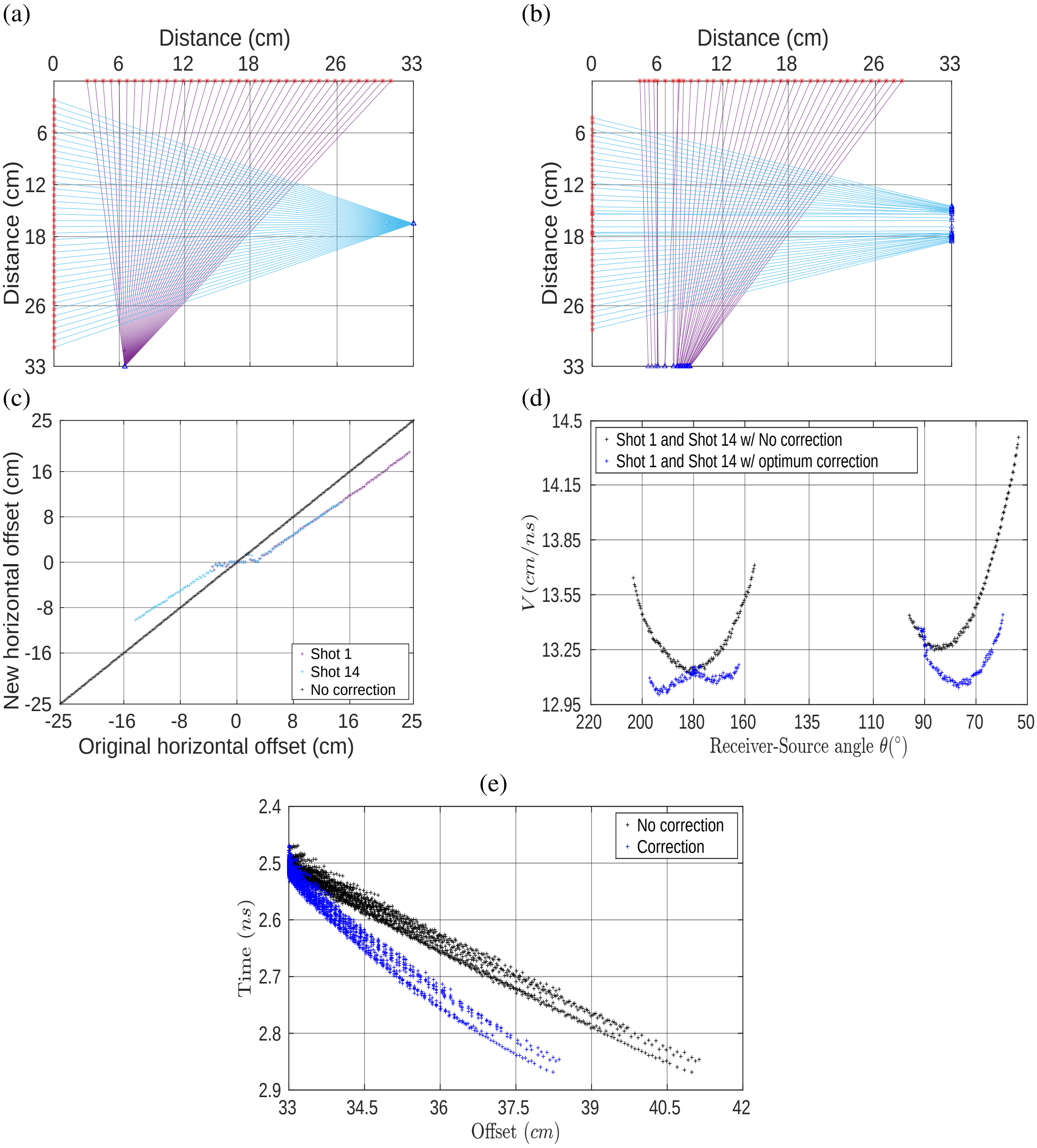

Figure 4.34: Effects of the Tx/Rx location correction for gathers 1 and 14 with (a) the initial and (b) final raypath geometries, (c) the horizontal offsets with the uncorrected black and corrected blue/purple points, (d) the velocity versus angle distributions and (e) the traveltime versus offset for all the dataset.

4.5 Isotropic and anisotropic traveltime tomographies

4.5.1 Impact of the Tx/Rx location correction - Isotropic approach

In order to evaluate the impact of the Tx/Rx correction on the tomography and to evaluate the possibility to image heterogeneities within the block with the available acquired data, we first use an isotropic approach before evaluating the possibility to detect and image electromagnetic anisotropy in the carbonate block.

For the initial model, we select the traces that have Tx/Rx facing each other (vertical offset $33\,cm$) and the corresponding picked traveltimes, thus an average of the different apparent velocities leads to $13.1\,cm/n$ being the initial homogeneous model for all the subsequent inversions. From this velocity, wavelength of the signal is computed in table 4.2, which although it is larger than the one obtained in the seismic experiment, we believe that tomography results can still be compared between the two physics applied on the block. The wavelength information is crucial for estimation of resolution in tomography, which is expected to be some scales larger than the signal wavelength. In addition, from the expected resolution, discretization can be evaluated, after testing different options, we consider suitable to use the same discretization applied in the seismic experiment: i) $1.5\,cm$ as a node separation for the inverse grid, and ii) for the forward modeling, square elements of $0.625\,cm$ on the edges.

$v\ [cm/ns]$	$\lambda = \dfrac{V_{carbonates}}{f}$ [cm]
13.1	$6.55 - 9.36$

Table 4.2: Estimated wavelength using the range of frequencies $1.4 - 2$GHz, such a range computed from the spectrum of all the picked traces (e.g., figure 4.25) and after isolating the main waveform (figure 4.8).

For the first inversion, the initial dataset without any Tx/Rx correction (figure 4.35a) is used considering an isotropic approach. The tomography in figure 4.35b was obtained after 11 iterations leading to a RMS of 0.41% (equation 4.2) while the initial RMS obtained in the initial homogeneous model was 3.17%. It shows expected results dominated by the influence of large velocities observed at large angles in figure 4.35a, that results in large velocities visible along diagonal paths. To compensate them and explain low velocities observed along near-vertical or near-horizontal raypaths, low velocities zones are present at the center of each face. This rather satisfactory result in terms of traveltime RMS error is uninterpretable, completely distorted by the bad positions of sources and receivers which dominate at this investigation scale.

In a second step, we inverted the corrected dataset using the new Tx/Rx locations leading to the apparent velocity versus angle distributions of 4.36a, the velocities being zoomed to the minimum and maximum values compared to the now-correction velocities where we reached up to $14.5\,cm/ns$ (figure 4.35a), moreover some gathers are highlighted with different colors, gathers with the receiver on the corners, i.e., 1, 2, 10 and 18, and two gather whose receiver is located on the center of the face, i.e., 5 and 14. The tomography presented in figure 4.36b) is obtained after 6 iterations showing a traveltime RMS error slightly decreasing from 0.59% when the homogeneous initial velocity was used to 0.35%. In general, the result is far better than the cross-shaped result when no-correction is considered (figure 4.35a), however, it is not easy to see some velocity continuation on the structures, it is dominated by velocity patches and although more iterations were tried, the same global result was obtained, the difference being that the amplitude of the patches was increased, either very low or very high velocities, this is understood as over-fitting on the inversion, thus 6 iterations was found as enough to evaluate the inversion in order to see some realistic velocity continuation on the structures. In addition, it must be noted the rather limited velocity variability of 4.5% given by the maximum and minimum velocity values ($[v_{max}/v_{min} - 1] \times 100$) in the tomography, while there are always high-velocity values located on the corners, i.e., large offsets. This relative homogeneity was already present

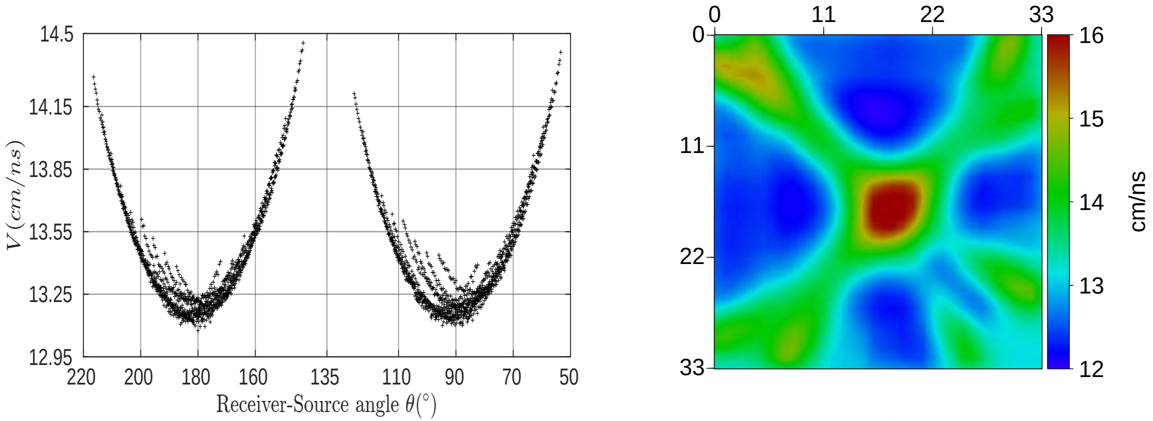

(a)

(b)

Figure 4.35: (a) Apparent velocity versus angle when no correction is considered, i.e., Tx/Rx located at the center of the antennas for all the offsets. (b) Resulting Isotropic tomography obtained after 11 iterations decreasing the traveltime RMS error from 3.17% to 0.41%.

if we consider the very low initial value of traveltime RMS error obtained with the homogeneous model. Therefore, it is difficult to exclude that the observed variability can come from the bad corrections still present, especially at large offsets, rather than from the material itself. From the velocity model we computed the synthetic traveltimes and the apparent velocity versus angle distribution assuming straight raypaths (figure 4.36c). This confirms that most of the observed pattern is well reproduced (figure 4.36a), excepted at large offsets near 120° and 210°.

4.5.2 Impact of the air boundary - isotropic approach

To better assess the impact of the air/carbonate boundary on the results, we selected 5 shots whose respective acquisition configurations are different and are shown in figure 4.37a. Figures 4.37b-f compare the observed and theoretical traveltime curves according to the new horizontal offsets obtained after Tx/Rx correction (figures 4.33a-b). The theoretical traveltime curves were separately computed using an optimized homogeneous velocity value producing the lowest traveltime RMS error. They are drawn keeping the color representation of the acquisition sketch. When the receiver is located at the middle of the block as in figure 4.37d, there is a good fit between the theoretical hyperbola and the picked traveltimes, with the lower RMS of 0.22%. The rather small differences might be associated with velocity heterogeneities that we want to image by tomography.

On the contrary, figures 4.37b and 4.37f, which correspond to gathers whose receiver are located nearby the block corners, clearly show large inconsistencies between observations and predictions. First, while the arrival times should be theoretically almost constant or slightly increase with increasing offset, we observe a decreasing in picked arrival time. In addition, where the largest horizontal offsets are present (about 19 cm with source near the corner), our model for Tx/Rx locations considered the maximum radius of the antennas, however, the theoretical hyperbola cannot fit the picked traveltimes which indeed have a linear trend instead of a hyperbolic one, i.e, picked traveltimes do not increase properly, they remain very fast at large offsets. These two gathers also have large RMS values. We can also notice smaller problems in gathers concerned by the corner in figures 4.37c 4.37e at low offsets

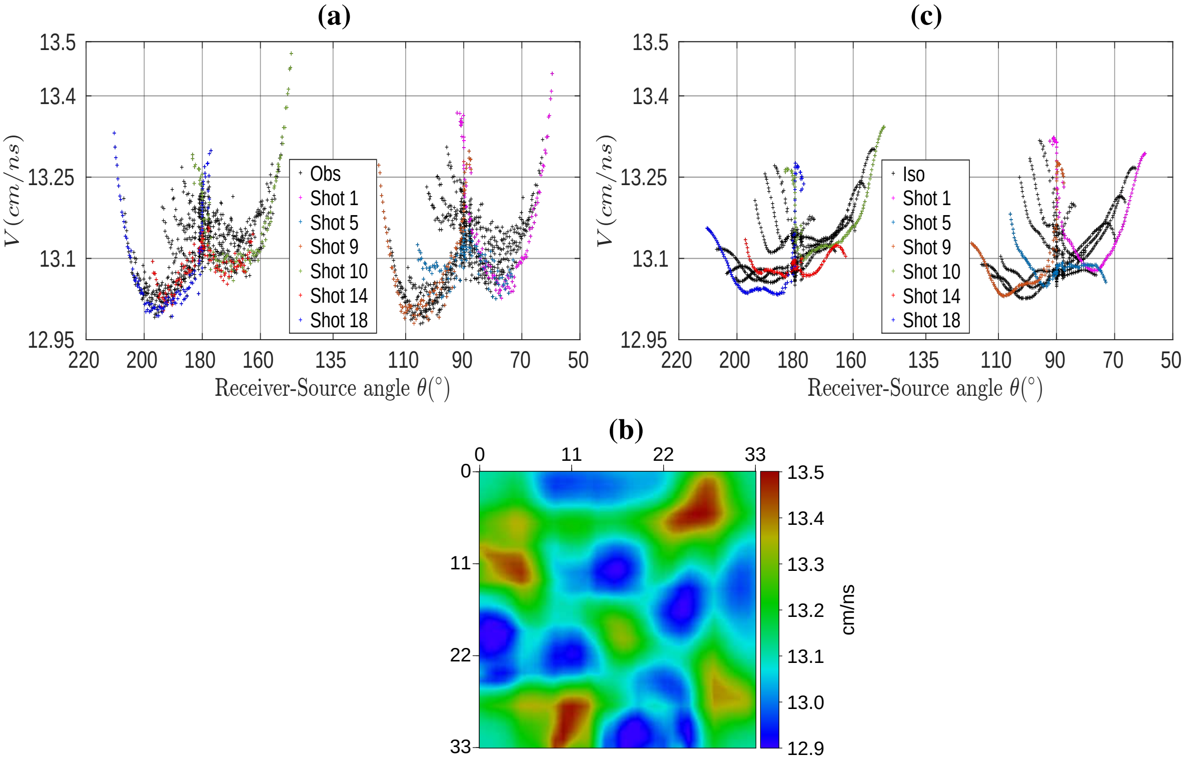

Figure 4.36: (a) Apparent velocity versus angle for all the picked dataset after using the Tx/Rx correction model of figures 4.33a-b. (b) Resulting Isotropic tomography obtained after 6 iterations decreasing the traveltime RMS error from 0.59% (initial velocity of $13.1\,cm/ns$) to 0.35%. (c) Synthetic apparent velocity versus angle distribution obtained from the velocity model of (b). Some shots are highlighted in (a) and (c)

when source is near the corner, if source is leaving, we should expect an increase in time, however the time decreases. Since we know that EM waves are highly sensitive to air, we believe that the contact block/air when Tx/Rx are located near the corners, it is the responsible of these no consistent physical patterns. It is worth recalling that most of our gathers are with the receiver located near the center, for instance, gather 3 to 7 (near-vertical paths) and 12 to 16 (near-horizontal paths), consequently it is not surprising that our model proposal for Tx/Rx locations fit better these gathers that have a hyperbolic shape (e.g. figure 4.37d) and the model fails with gathers whose shape is linear (corners). Another model proposal can be considered only for shots on the corners, we could decide a homogeneous velocity for the block and apply the procedure presented in the air where the velocity of $30\,cm/ns$ was known, therefore we do not start from the model found in air and there would not be F1 or F2, on the contrary we would arrive to a specific correction for each gather on the corner, however it is clear that the model found will fail for shots with the receiver on the center due to the discussed different patterns (figure 4.37), we thus discard this option also because it is not physically meaningful to have one model correction for shots on the corners and another model for shots on the center.

These discussed inconsistencies of some traces are causing the artefacts in the tomography result of figure 4.36b. Consequently, we propose to decimate the dataset by removing the traces too much diverging from the theoretical hyperbola shape, at low and large offsets, when needed. There are two criterias to select the discarded traces for gathers whose receiver is located near the corners: i) at short offsets when the source is leaving to the corner and the picked time decreases while an increase is

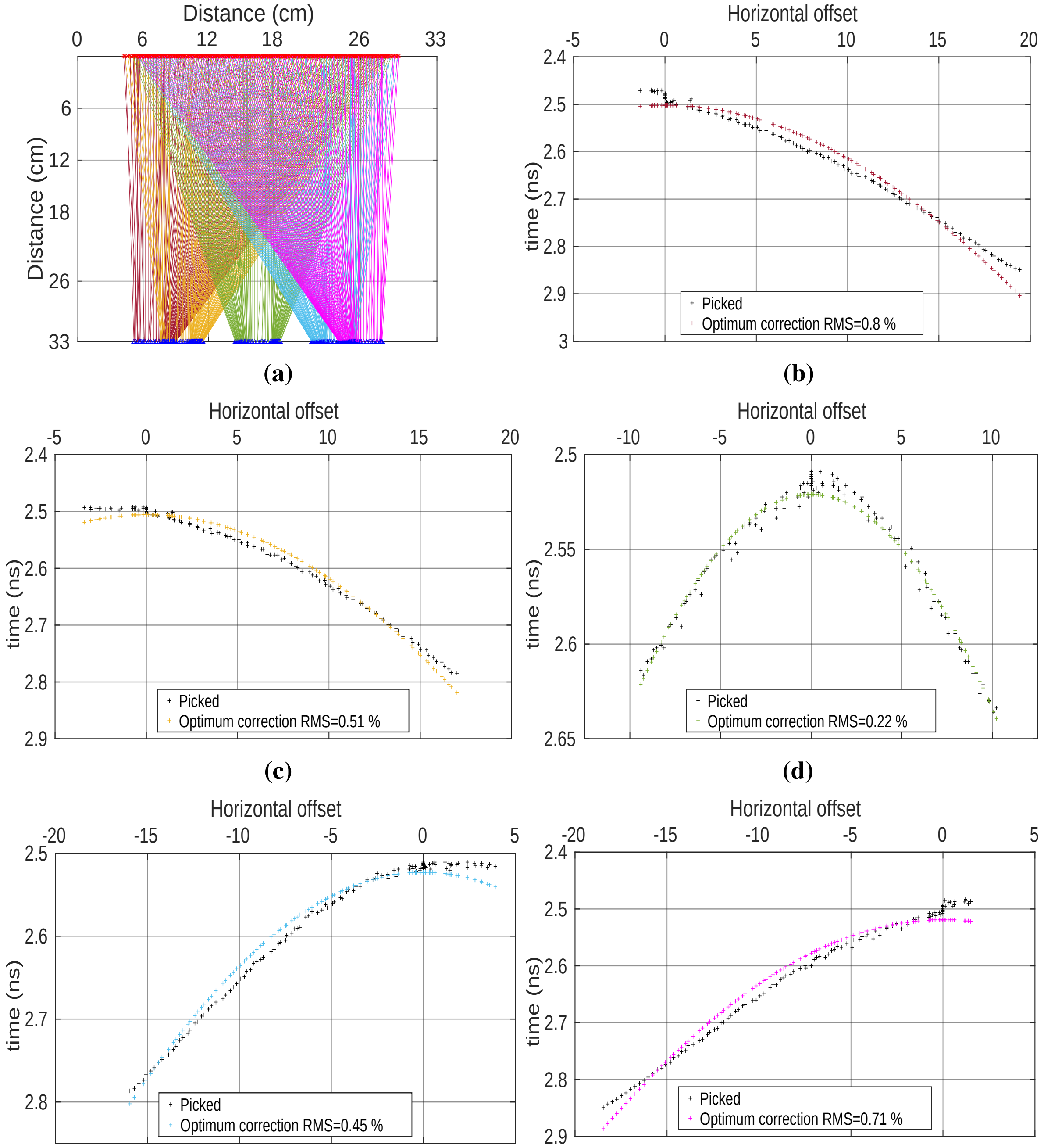

(a) **(b)** **(c)** **(d)** **(e)** **(f)**

Figure 4.37: Traveltime analysis of some gathers. (a) Sketch of the 5 gathers acquisition configuration. (b-f) Traveltime versus corrected horizontal offset for picked traveltimes (black) and theoretical one computed assuming a homogeneous and best fitting velocity. Use the color of (a) to locate the gathers in the time/offset analysis.

expected, this is clear in gather 2 and 8 of figures 4.37c and e, respectively; ii) when the source is very far (largest offsets) and the tip-to-tip antenna approximation fails, as illustrated in gather 1 and 9 of figures 4.37b and f, respectively. These particular traces are highlighted in figure 4.38a, they are 199 traces which correspond to 9.45% of the total dataset, moreover the remaining paths after discarding those traces are shown in figure 4.38b (paths are decimated to improve the illustration), we still have a large illumination within the block.

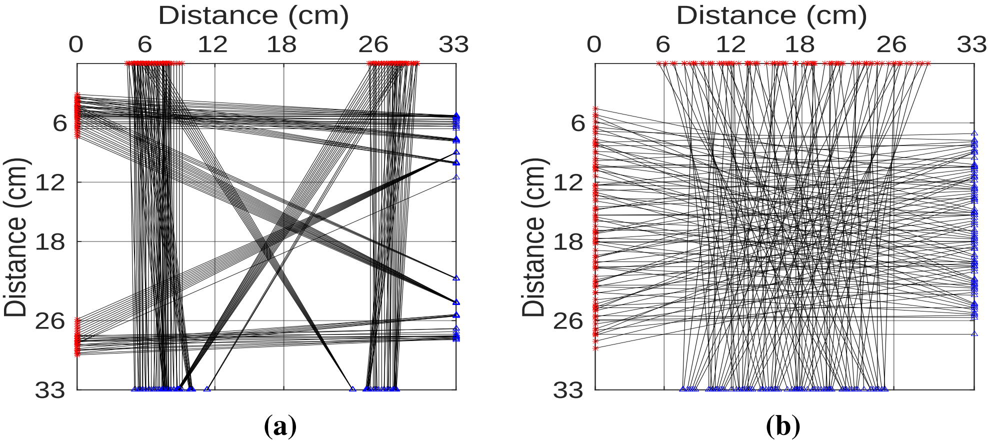

Figure 4.38: (a) Sketch of discarded raypaths. (b) Tx/Rx paths after discarding the traces of (a), paths are decimated to have a better illustration.

This decimated dataset is used to obtain a final isotropic tomography after 13 iterations (figure 4.39a), with traveltime RMS error slightly decreasing from 0.46% (initial model) to 0.33%. The previous high-velocity patches have disappeared and the model shows more structural continuity, although the amplitude of the velocity variability remains weak and reaching 3.71%. Figure 4.39b shows the isotropic result obtained from the seismic experiment, the variability from this model being 14%, such a large difference compared to the GPR result might be associated to the differences in the wavelength size propagated. However, we highlight 3 zones from the GPR result and they can be compared with the seismic tomography: the zone 1) of the seismic result was interpreted as a filling material of fractures leading to this slight increase of velocity, while for GPR the same property might be acting in an opposite form; zone 2) is interesting since it shows a nice low-velocity continuation pattern for GPR but it is completely homogeneous in seismic, if fractures are aligned vertically, the pattern from GPR might be caused by high fracture density but it is not easy to understand the absence in seismic; zone 3) was discussed as a zone with high anisotropy in seismic (about 7%) due to the high presence of crosscuted fractures, since the GPR tomography also shows the decrease of velocity, this zone might be consistent because at high-fracture density we expect a decrease of velocity regardless of the physics.

Another comparison is done by the apparent velocity, after discarding the inconsistent traces of figure 4.38a, the new decimated apparent velocity versus angle distribution is shown in figure 4.40a, note that the high-velocity values at large offsets are removed. From the isotropic GPR tomography (figure 4.39), synthetic traveltimes are used to compute the apparent velocity versus angle distribution, in general the global pattern of the observations is well approximated, some shots are highlighted afterwards when anisotropic tomography is performed.

4.5.3 Preliminary concluding remarks

Despite all the analytical efforts made on the data in order to take into account the problems related to extended antennas and edge effects related to the presence of air which has a very fast velocity in

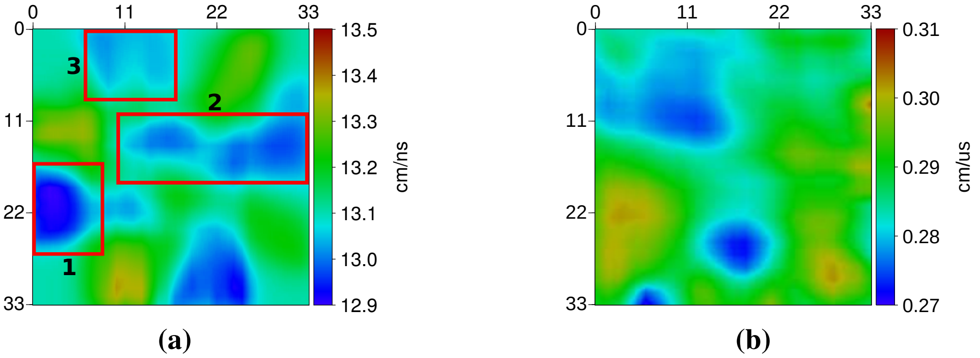

Figure 4.39: Isotropic inversion results. (a) GPR after discarding the inconsistent traces of figure 4.38a, we run 13 iterations leading to an error of 0.33% where an initial homogeneous model of $13.1\,cm/ns$ is used and it produced an error of 0.46%. (b) Seismic after 8 iterations reaching a RMS of 1.67%, an initial homogeneous model of $0.284\,cm/\mu s$ was used and it caused an error of 2.64%. Three zones are highlighted in (a) and discussed according to (b).

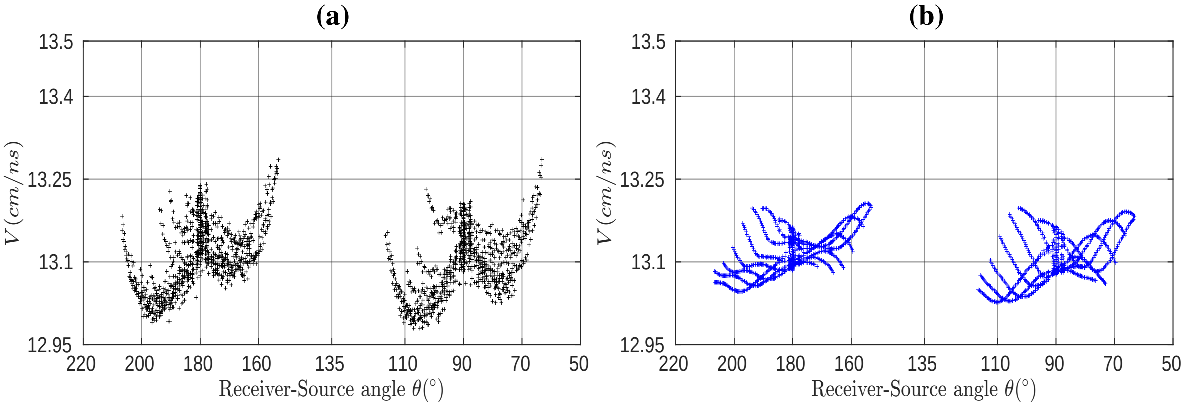

Figure 4.40: (a) Velocity versus angle pattern computed after discarding the traces of figure 4.38a. (b) Based on the modeled traveltimes obtained from the isotropic velocity model of figure 4.39a.

electromagnetism, we obtained a dramatically homogeneous tomographic image. Indeed, the percentage of velocity variability exhibited in the final isotropic model (figure 4.39a) is about 3.71% while we obtain 14% in the acoustic experiment performed on the same 2D plane (figure 4.39b). According to the estimated wavelength on table 4.2 and after considering a nominal frequency range of [1.4-2GHz] (figure 4.25), unfortunately only 3.5 to 6 wavelengths propagate within the block and consequently we might expect less sensitivity to small structures. These values are not ideal but are also not completely different than in the acoustic case from which certain velocity differences were possible to discuss for our multi-physics analysis. The question arises about the sensitivity of electromagnetic waves to heterogeneities generated by the presence of fractures. Do the differences in fracture filling and/or fracture density, which seem to generate variations in mechanical properties, produce sufficient electromagnetic contrasts? It seems that at this scale and with the frequency involved, the answer is unfortunately negative. We will now try to evaluate whether these fractures or the formation of the block at the grains creates electromagnetic anisotropy.

4.5.4 Can we reasonably detect and image some electromagnetic anisotropy?

Looking at the differences between the horizontal and the vertical velocities of figure 4.40c tends to indicate a rather low-level of anisotropy if any, in terms of EM traveltimes along different directions. It must be noted that the similarities in traveltimes are not coming from the antennas' position correction we performed, as they are also present in the picked raw data, e.g., near-vertical gathers of figure 4.23 look very similar to the near-horizontal in figure 4.24, consequently the no correction apparent velocity (after applying t_0 calibration) versus Rx/Tx angle also shows similar patterns regardless of the orientation (figure 4.35a). Following the forward approach presented in section 3.3.1, we can compare the apparent velocity versus angles curves with different theoretical elliptical anisotropic curves considering EVTI and EHTI anisotropic models with homogeneous velocity. In addition, since we have as an *a priori* information the tilted angle from the acoustic experiment, we can compute an ETTI curve. Figure 4.41 shows such comparison using a vertical velocity of $13\,cm/ns$ and 1.5% of anisotropy, it is clear that any curve can reproduce the observed pattern.

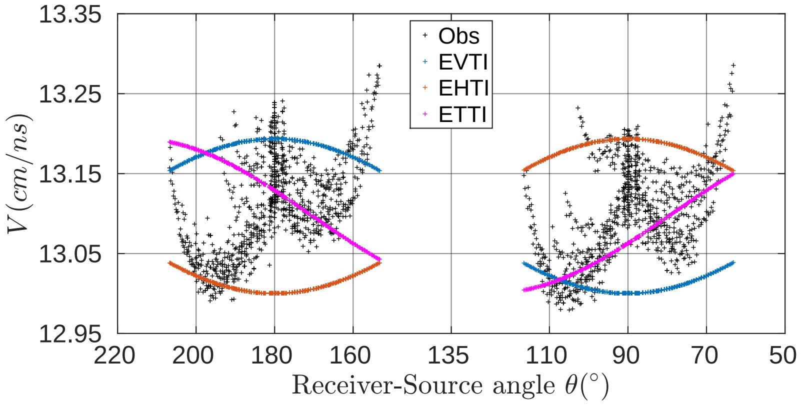

Figure 4.41: Average velocity versus angle distributions for the corrected dataset acquired in the block (black points) and theoretical distributions obtained from elliptical VTI (blue) and horizontal (red) anisotropic models. The latter were computed with an homogeneous velocity of 13.0 cm/ns and 1.5% of anisotropy.

To confirm the absence of anisotropy, we compare the pickings obtained on two gathers of comparable acquisition configuration performed at the middle of the block face, different in angles by 90° (figure 4.42a). Showing similar patterns, the pickings displayed on figure 4.42b differs in traveltime RMS by a value of $0.00617\,ns$ or $6.17\,ps$ which is extremely low in a dataset whose picking uncertainty was estimated to $1.22\,ps$. This seems to confirm that the vertical and horizontal velocities are very similar.

A final attempt consists in inverting our decimated and corrected dataset considering a multiparameter anisotropic approach with a vertical symmetry (EVTI) under the elliptical assumption. For this, we use the same homogeneous initial model of 13.1 cm/ns for V_v and V_h, which was already the initial velocity of the isotropic inversion. A EHTI tomography was tried but it basically gives the same result of EVTI but with velocities rotated by 90°, i.e., V_v from EVTI is equal to V_h in EHTI, therefore we do not show the EHTI case.

Figure 4.43 sums up the final isotropic and EVTI anisotropic results. The inverted anisotropic velocities display some continuity on the structures, regarding the vertical velocity (figure 4.43b), we cannot identify the tilted low velocity structure we found in seismic, such an absent structure seems to be

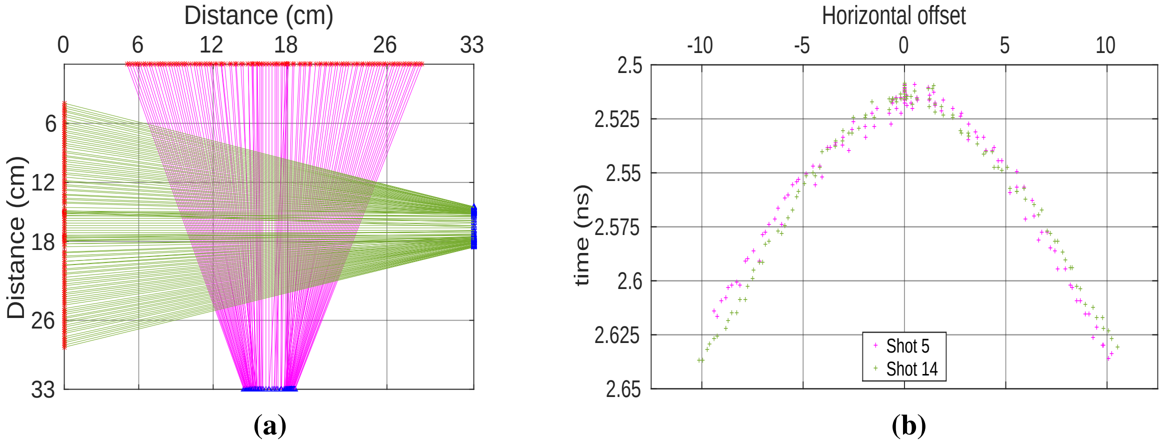

Figure 4.42: (a) Acquisition configurations of two gathers located at the middle of the block. (b) Traveltime versus horizontal offset curves, the RMS time difference being 6.17 picoseconds.

imaged in the GPR horizontal velocity result (figure 4.43c). From the V_v and V_h models, the percentage of anisotropy given by $[(V_h/V_v - 1)] \times 100$ is around zero (figure 4.43d), if we focus our attention to the center of the block where most of the raypaths are crossing, it is clear that 0% is computed. There are a few places where the anisotropy slightly increases, these locations are also consistent with the locations in the isotropic result (figure 4.43a), consequently, we may conclude that in this low-anisotropic dataset, the inverted anisisotroic velocities are simply split from isotropic result. We can see from the anisotropic percentage (figure 4.43d) a few zones where the anisotropy increases but with no evident continuation pattern that could be associated with dip structures as karst or fractures, something we could find from the seismic data obtained in the same block (section 3.4). The zones where V_v and V_h (figure 4.43b-c) show a slight increase might be associated with an increase of porosity as EM waves propagate faster in a dry porous media (contrary to mechanical waves). This increase only reaches 2.29%.

The error convergence curve of figure 4.44 show a faster convergence when anisotropy is considered indicating that in spite of the low-level of anisotropy, our data can be better explained with an anisotropic parametrization. From each tomographic result, the synthetic traveltimes are used to obtain the apparent velocity versus angle in figure 4.45, where some shots are highlighted, shots with the receiver near the corners (1,9,10,18) and with the receiver located at the center of the block (5 and 14). The anisotropic apparent velocities show some improvement compared to the isotropic case. The similarities between the horizontal and the vertical paths in the observed apparent velocities (figure 4.45a), indicate very low values of anisotropy, which is consistent with the anisotropic results where most of the structures have values around 0% (figure 4.43d).

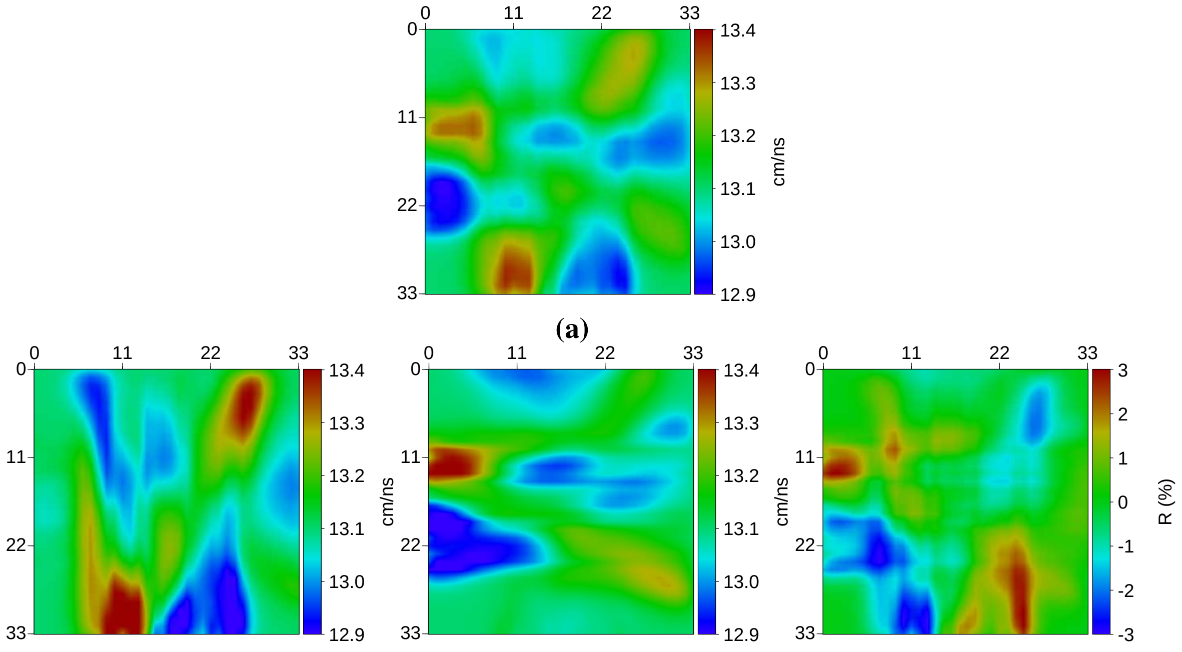

(a)

(b) **(c)** **(d)**

Figure 4.43: (a) Isotropic result (same of figure 4.39a). (b-d) Anisotropic EVTI obtained after 9 iterations with V_v on the left, V_h in the middle and percentage of anisotropy on the right. The latter was obtained using $[(V_h/V_v - 1)] \times 100$.

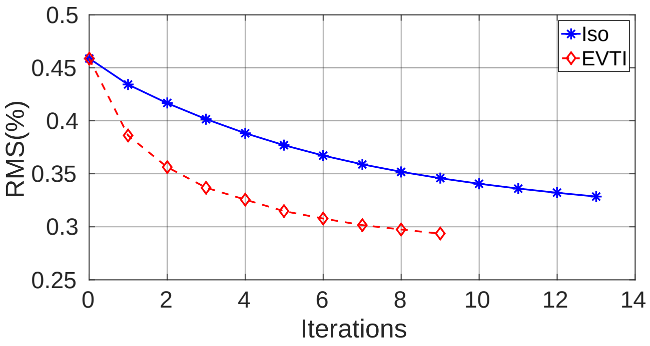

Figure 4.44: Evaluation of the percentage of error (equation 4.2) as a function of the number of iterations for each approach: isotropic in blue (final RMS=0.33), and EVTI in red (final RMS=0.29).

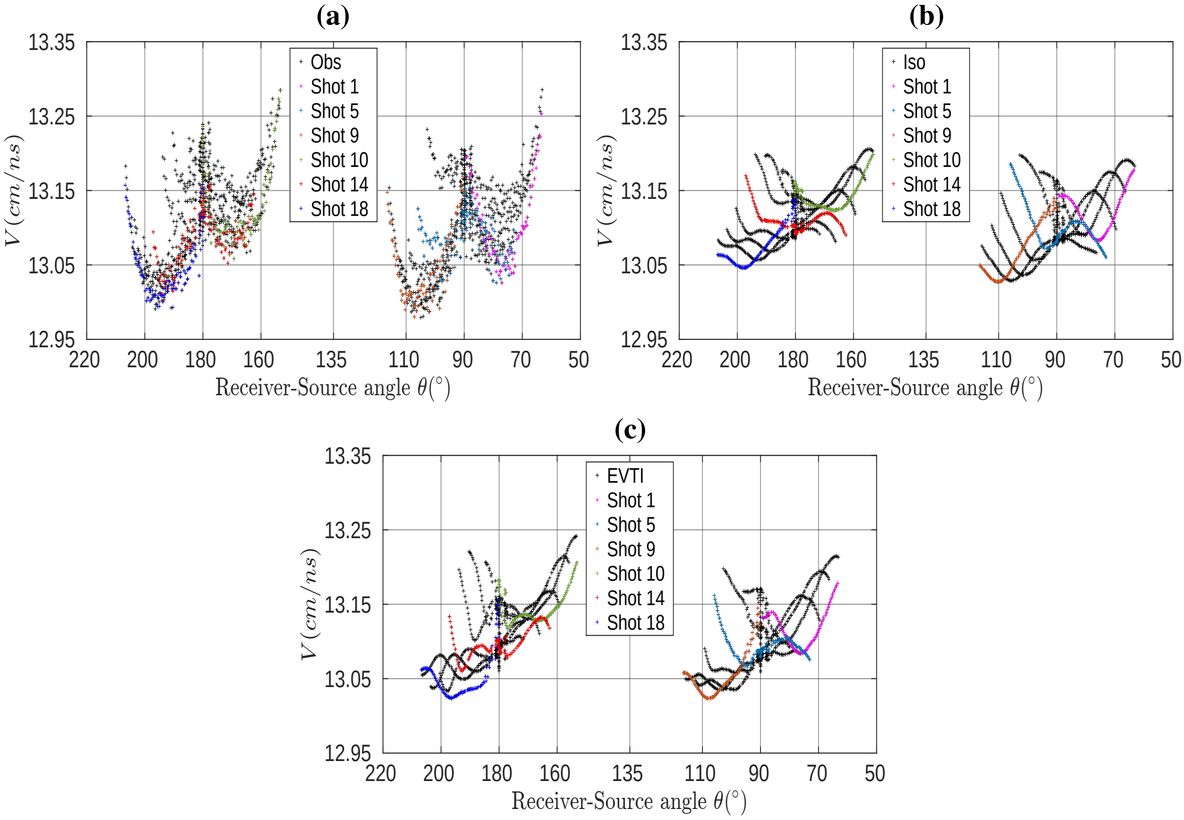

Figure 4.45: Velocity versus angle pattern obtained from the synthetic traveltimes of each tomography result and the position of the antennas under the straight path assumption. (a) Observed pattern based on the picked traveltimes, (b) Isotropic pattern obtained from the model of figure 4.43a, (c) EVTI pattern obtained from the model of figure 4.43b-c. Some shots are highlighted.

4.6 Conclusion

Unlike the seismic part, the experiment presented here in the laboratory did not benefit from any prior feasibility study. Furthermore, the chosen commercial GPR antennas, which appeared to be suitable in terms of frequency content, had not been tested in transmission experiments either. These tests were thus carried out and described within the framework of this chapter. We were able to release a methodology of acquisition and analysis, as well as the difficulties related to this experiment, that will allow for the acquisition of more appropriate data in the future. In this context, two experiments were performed, one in air that can be assimilated to calibration or quality control and a second for imaging the carbonate block studied in acoustic tomography (chapter 3).

Regarding the air experiment, we could performed a detailed analysis looking at the waveforms to quantify the frequency content - lower than expected - to identify first arrivals, which presents slight dispersion with a satisfying signal to noise ratio. This dispersion, which was also unexpected as the waves propagate only in the air, is probably due to the complex radiation pattern of the antennas. From these considerations, we choose to implement a crosscorrelation (CC) technique designed to perform an automatic picking of the first arrivals. The workflow is an adaptation of the one proposed by Irving et al. (2007) with two main modifications: i) the choice of a very narrow time window centered on the half period of the first arrival where CC is computed, a choice which is not that of Akram and Eaton (2016a) who suggested a large window, ii) a CC picking of the pilot traces to completely cancel the manual and subjective intervention, source of error. In the end, only one pilot trace is manually picked on the whole dataset to get the absolute times from the relative pickings. This approach resulted in a continuous traveltime dataset without abrupt variation.

The database of 6 gathers was first used to analyze the temporal stability of the transmission time of the antennas: it resulted in an averaged temporal time shift t_0 used to obtain absolute GPR travel times in transmission mode between antennas, as well as its variability. Then the comparison of these traveltimes with the theoretical one calculated by considering straight raypaths assuming that they connected the middles of the transmitting and receiving antennas showed that this assumption did not work as soon as the antennas moved too far away from each other. This approach allowed us to propose a simple corrective model in the air that relocated the effective transmitter and receiver points of the antennas from a traveltime perspective. These new positions were used to compute new effective angles for each raypath of a single gather and a generalization to the six gathers was performed allowing to obtain an average correction pattern for the Tx/Rx set-up in air.

In a second step, we worked on the electromagnetic imaging experiment of the same carbonate block previously studied in acoustic. The specificity of the boundary conditions in electromagnetism have influenced and restricted the acquisition configuration. Indeed, the air being in this case of largely higher velocity, only the acquisitions in transmission between opposite faces could be carry out to avoid the presence of refracted waves in the air when the 2 faces were adjacent. After applying the automated picking technique validated in the air, we benefited from a traveltime dataset of 18 gathers, 9 vertical and 9 horizontal. The comparison with the theoretical times calculated assuming a homogeneous carbonate velocity showed that the corrective model proposed for the air data, while going in the right direction, was not sufficient, probably due to the specificity of the radiation pattern of the antennas when in contact with a marked interface. Considering the same type of Tx/Rx point location model than in the air, we adjusted by a RMS fitting the apparent velocity versus angle curves assuming an homogeneous velocity and allowing to obtain an adapted model of effective point-source locations for the source and receiver. This model could however not explain satisfactorily the whole dataset, the low offsets (shots nearby the edges) and large offsets datasets being quite far from the proposed modeling.

Finally, we used the corrected dataset to perform an isotropic GPR tomography. We should underline that most of the GPR tomography attempts presented in the literature are performed at the field scale without problems of antenna sizes relative to the material dimension. Here, as already detected prior to any inversion, the resulting EM velocity image exhibits only slight variations, whose validity can be questioned in relation to the numerous corrections carried out, in particular with the source and receiver location model. In addition, the large similarities between horizontal and vertical traveltimes also question the existence of any anisotropy present in the studied carbonate block. We have nevertheless tried to perform a multiparameter anisotropic tomography, whose convergence appears faster than in the isotropic case. It showed us several zones where there is no anisotropy and a few zones with a maximum of 3% in anisotropy.

The homogeneity of the GPR images contrasts strongly with the heterogeneous/anisotropic images obtained in acoustic tomography (chapter 3) and raises several questions. That difference between between EM and acoustic could be explained by a difference in sensitivity of the physical parameters. However, several other factors may also explain these results. First, the lower than expected frequency content in GPR results in slight longer wavelengths, which are less sensitive to small, localized heterogeneities. Second, the complexity of the radiation pattern of the antennas required the use of a transmitter-receiver correction location model, constructed assuming point sources varying with angle. It is probably too simplistic at this stage. While it has corrected some first-order effects, probably imperfectly, it may also have led to errors that mask the signatures of local heterogeneities in the arrival times observed within the block. In the future it will be necessary to use either larger blocks or smaller, probably non-commercial, higher frequency antennas. From an experimental point of view, our preliminary study will have to be pursued more deeply by including consideration of amplitudes when antennas are in contact with a carbonate block and numerical modelling of the antenna pattern. This could help to design a more complex and appropriate correction model.

Conclusions and perspectives

Conclusions

The growing demand for high resolution imaging of complex subsurface structures has led to the development of several methods such as wave equation-based tomography and full waveform inversion. They have shown promising results by handling complex geologies but at the expense of being extremely demanding in terms of computational resources. In this context, the high-frequency approximation of first-arrival traveltime tomography (FATT) might be an efficient, robust and flexible alternative, at the expense of decreasing the resolution of the derived images, providing smooth velocity models. We have added in this problem the taking into account and the inversion of the anisotropy. Although several approaches are discussed in the literature for computing traveltimes in the presence of anisotropy, the extension to the inverse part is still investigated due to the complexity to recover simultaneously two or more parameters. This complexity can be amplified depending on the illumination of the domain. This low-resolution approach can be perceived as a first step of a more ambitious imaging strategy, where more sophisticated multiparameter imaging methods can be applied, if necessary, in a second step. In addition, the results of the anisotropic tomography will help in the choice of the model and the need to include or not the anisotropic in the parametrization, and according to which anisotropic model. In this context, the main contribution of this thesis lies in the development of a robust approach that can simultaneously invert velocity and anisotropy from first-arrival traveltimes. A number of applications on real data, at field scale or in the laboratory, with seismic or electromagnetic methods, have led to other contributions that we detail below:

- In chapter 1 a detailed review was provided about the physics behind the Eikonal equation and the main techniques that have been proposed to obtain its solution. The discontinuous Galerkin method was introduced as well as the new implementations proposed here. This solver has some advantages over the ray-based and finite-difference solvers that were highlighted. For the inverse part, we discussed about the classical tomography workflow, which in general relies on a Eikonal solver to compute synthetics but usually computes rays from receiver to source in order to built the Fréchet matrix. This approach is somehow not physically consistent since rays are avoided in the forward part while they appear in the inverse part. We proposed an alternative mathematical formulation of the inverse problem using the adjoint-state method to avoid the computation of rays, and thus the computation of the related matrix. The gradient of the misfit function is expressed by two terms, the solution of the adjoint transport equation and the analytical derivative of the anisotropic Eikonal equation. As the first term in not dependent on the second, different parametrizations can be evaluated with the same adjoint field.
- A preliminary sensitivity analysis is provided at the end of chapter 1 by showing the first gradient of each parameter involved in the problem parametrization, which is obtained using a synthetic

test with a circular acquisition. The full-illumination case gave us a clear view of the sensitivity in each parameter involved in an elliptical anisotropy model, which is important to evaluate the possible leakage between parameters during the inversion. This sensitivity analysis was extended in chapter 2 to a crosshole configuration and leaded to the same previous conclusions. Two synthetic examples were used to evaluate the efficiency of the multiparameter inversion of velocity and anisotropy, considering a VTI model. The first pedagogical example showed a good agreement with our sensitivity conclusions, while the second example was more realistic as it was deduced from a FWI image and included a large contrast gallery at depth to mimic the real field acquisitions presented afterwards. This allowed us to introduce the regularization term designed from *a priori* information and the weight-data matrix to handle picking uncertainties. The results in synthetics validated that parametrization (V_v, V_h) is more convenient than (V_v, ϵ) and has also highlighted the limitations in the reconstruction of V_v due to the crosshole configuration.

- After presenting the final workflow of our tomography code, we tested it on 100 MHz GPR data acquired in a crosshole configuration within carbonate formations. The particularity of the investigated site is the presence of a gallery locally generating a large velocity contrast between air/carbonates, which causes diffraction events that were identified in the raw data. Interestingly, such events are not part of the ray solution, while they are part of the viscosity solution given by our discontinuous Galerkin solver. The pattern of the picked dataset was carefully compared with the synthetic one obtained from a realistic model constructed from FWI results. The tomographic isotropic result was compared with a previous isotropic result obtained from FWI where the regularization term was not considered. The anisotropy result showed some artefacts near the gallery which was also the case in the analysis of synthetics, thus highlighting the high-wavenumber content generated by the gallery that tomography cannot resolve. Other artefacts were localized in zones where the illumination was not balanced, making it impossible the correct update of V_v. In spite of these artefacts, the anisotropy tomography result highlighted the presence of some weak and localized anisotropy, suggesting that it might be caused by the fine metric stratification being also observed in the borehole cores.

  We then applied our tomography workflow to multiphysics laboratory measurements performed on carbonate blocks. Unlike from chapter 2, the data acquisitions were almost completely part of this work being an important step for the formation and experience in a laboratory framework.

- In chapter 3 acoustic data were acquired with a piezolectric source and recorded with a laser. The analysis of manually picked traveltimes, displayed under the form of the average velocity versus the source/receiver angle exhibited outliers for short offsets. This allowed to highlight the effects of an extended source and to propose a correction of the source, which cannot be considered as a single point located at the center of the device at this investigation scale.

- The corrected apparent velocities versus angle are then analyzed fitted using synthetic data computed assuming an homogeneous material, in order to assess the choice of the anisotropic model and its degree of anisotropy. We then fixed the tilt angle of the model and the two corresponding velocities were inverted allowing to obtain tilted structures in the vertical velocity and very small variations in the horizontal velocity, leading to a percentage of anisotropy reaching 7% in some areas. The potential origin of this anisotropy might be related to the large amount of porosity of this block and/or to the presence of tilted fractures. However, it must be noted that an isotropic approach of the same dataset does not dramatically change the results, as the degree of anisotropy was moderate.

- We then applied our workflow on a higher anisotropic dataset already published, which could not benefit from an anisotropic inversion approach at the time. We could first confirm that the fitting model is a tilted one. This example illustrate well the large differences in velocity results depending on whether or not anisotropy is taken into account. While the isotropic inversion showed some large tilted structures, the anisotropic inversion provides rather homogeneous but different vertical and horizontal velocities with a general pattern of 10% to 15% of anisotropy. The global pattern of the data from the inversion results showed in the isotropic case several outliers randomly distributed and very far from the real pattern. On the contrary, the anisotropic pattern was very close following the desired sinusoidal shape present of the real data. This highlights two features: i) the initial analysis of the data is a crucial part in order to identify the level of anisotropy and to define the adapted model, and ii) the importance of having a multiparameter code to better explain the data in case of high anisotropy. In this case, the use of an isotropic code will generate false heterogeneities that can lead to wrong interpretation.

- In chapter 4, before performing a GPR transmission acquisition around our laboratory carbonates block, we present a preliminary experiment done in air to evaluate the characteristics of the antennas and particularly the potential effect of their sizes. We also developed a semi-automatic picking approach based on crosscorrelation. The picking and the *a priori* knowledge of the velocity of the air for electromagnetic waves allowed to show the large effects generated by the extended sizes of the Tx/Rx antennas, which cannot be considered as points located at the center of the antennas. We proposed an empirical correction that modifies the position of the antennas in order to reach the air velocity value regardless of the angle, leading to a satisfactory approximation with an error of less than 1%. We should underline that even when Tx is located far of Rx the obtained position shifts were not large enough to reach the edges of the devices. In addition, the air experiment allowed to analyze the source t_0 correction and its variability.

- The raw radargrams acquired in the carbonate block have been picking with the semi-automatic process, the traveltimes were then corrected from the t_0 delay and displayed as a function of the average velocity versus the receiver/source angle. Hyperbolic patterns were identified at large offset on apparent velocity versus receiver/source angle representation, confirming the necessity to apply source/receiver position corrections. For that, we modified the air approach with a new fitting procedure between the data and the synthetic time. The correction suppressed most of the outliers although some velocity values were still above the normal trend of the dataset. These values correspond to large offsets traces or when Tx/Rx are located close to the edges of the block. After discarding these values, an isotropic inversion was performed showing that the level of heterogeneity was almost negligible. This unexpected result might be due to the larger wavelength available compared to the acoustic case, so that not enough wavelengths interact within the block.

- Besides all the discussed limitations in GPR, we tried to investigated the dataset for some degree of anisotropy, without any satisfying outcome. We moved to the anisotropic inversion and found that at the center of the domain where most of the illumination is present 0% of anisotropy was found, while there small heterogeneities that reach 3% could be detected, but without any clear continuity. It seems that only the use of smaller antennas with a higher frequency content could help imaging the block.

Perspectives

The advances summarized above and their limitations point to short and longer term perspectives that could broaden the application areas of anisotropic tomography in the future.

Assessing the heterogeneity/anisotropy trade-off in more complex environments. Although we have not benchmarked our code with an anisotropic ray-based tomography being usually developed under the weak anisotropy assumption, we showed in chapter 3 that our numerical algorithms developed during this thesis were efficient retrieving high anisotropic structures in rather homogeneous environments. A classical ray-based algorithm would have probably give a spurious image of the anisotropic structures. Therefore, it would be interesting to test our tomographic approach in more complex materials in order to assess its limitations and also to better study the potential trade-off between heterogeneities and anisotropy, with the considered scale information. For example, synthetic numerical cases should be conducted to study the signature of various fractures with different characteristics (scales, velocity contrasts): would the inversion lead to more heterogeneous or more anisotropic media?

Towards a more general anisotropic inversion framework. The inversion of the four parameters involved in TTI has been proposed as a hierarchical scheme in several works due to the angle limitations in the acquisitions and the chosen parametrization. Waheed et al. (2016) showed synthetic examples in a surface acquisition and using the parametrization (V_n, η, δ) for VTI. The third parameter δ was fixed to the true model, while V_n since it has the major influence on the data is inverted first with η fixed to a smooth initial model, then the obtained V_n is fixed and η is inverted. The idea behind the hierarchical approach is well explained by Vigh et al. (2014) for parametrization (V_v, ϵ, δ): we need to invert first V_v that strongly controls the data, keeping the weak parameters fixed to an approximate guess, then we invert V_v and ϵ and δ remains fixed. The tilt angle model is obtained by migration and fixed during all the procedure. In general, if the range of angles is limited like in surface experiments, this strategy is valid for the two mentioned parametrizations because the wave velocity is sensitive to a wide range of angles. However, if the initial guess of the second parameter is quite inaccurate, it will hamper the reconstruction of the wave velocity by creating perturbations (Gholami et al., 2013b), thus it is not intuitive the idea of fixing one parameter.

We validated that (V_v, V_h) is better under the elliptical assumption (V_h=V_n). In our case the third parameter is either δ or V_n which have the same sensitivity pattern driven by diagonal angles. Therefore in both cases there is a good decoupling with the other two velocities V_v and V_h. If δ is chosen as the third parameter, (Gholami et al., 2013b) showed that it has a very minor influence on the data, as was previously validated by Jiang and Zhou (2011), while Meléndez et al. (2019) recently performed different inversion tests suggesting that although it is the weakest parameter, it cannot be neglected and at least one homogeneous value should be used. Consequently, we should first evaluate which parameter is convenient to use, although the use of V_n is attractive since we avoid the scaling normalization. We propose that in a full-illumination framework, the hierarchical approach can be avoided, and in case we have complexities, we should isolate the diagonal paths to design an initial model for the third parameter and run a simultaneous inversion of the three parameters with the tilt angle fixed and being obtained by the data-driven approach (chapter 3).

Extension to a 3D anisotripic tomography The extension to 3D is needed in order to work with more general datasets that have sources and receivers distributed on a 3D volume. Regarding anisotropy in

3D, it has been investigated by different approaches. One is the ray-based azimuthal anisotropy which solves for anisotropy that varies azimuthally in the horizontal plane. In this case, the traveltime inversion is parametrized with an isotropic component and two azimuthal anisotropy parameters (e.g., Eberhart-Phillips and Mark Henderson, 2004; Dunn et al., 2005). An alternative is to remain in the transverse isotropy (TI) framework, as proposed for instance by Meléndez et al. (2019), who rely on the VTI case after considering the weak anisotropy formulation of Thomsen (1986) to compute rays. Zhou and Greenhalgh (2008b) change the formulation to compute rays in strong anisotropic situations and invert anisotropy in arbitrary TTI media. There are applications assuming 3D TTI models in earthquake seismology or deep seismic sounding (Takeuchi and Saito, 1972; Anderson and Dziewonski, 1982). Considering the VTI case, the 3D VTI Eikonal becomes

$$V_v^2(1+2\epsilon)(T_{,x}^2+T_{,y}^2)+V_v^2T_{,z}^2-2V_v^4(\epsilon-\delta)(T_{,x}^2+T_{,y}^2)T_{,z}^2-1=0. \tag{4.3}$$

The particularity in 3D is that the plane normal to the symmetry axis behaves as isotropic as it was shown in figure 2a. If we want to get the 3D TTI case, two angles need to be included in the formulation, the inclination angle $\theta(\mathbf{x})$ and the azimuth angle $\phi(\mathbf{x})$. Although Le Bouteiller et al. (2019) provided the solution of the Eikonal in orthorhombic medium which is an appropriate model for the description of one or several systems of cracks, there are 9 parameters involved in this formulation and consequently it is quite challenging in terms of inversion.

However, before moving to orthorhombic models, they developed the solver of Eikonal equation for 3D TTI media that we can continue using. The parts missing in terms of computational implementations are the adjoint solver and the projection of the traveltime time derivatives from the forward problem to the inverse part. Both are crucial for the formulation of the gradient, the adjoint being independent of the parametrization while the traveltime derivatives are needed for the analytical expressions derived from a chosen parametrization as showed in 2D (chapter 1). The conclusions about the sensitivity of the parameters in each parametrization will be the same.

After the implementation, synthetic tests as we did in 2D need to be repeated in a 3D framework. As we discussed previously, if a surface acquisition is considered, the inversion of anisotropy parameters will be difficult, and probably the hierarchical approach should be used. On the contrary, if the illumination is good like in laboratory experiments, the inverted anisotropy parameters are expected to be accurate and we can enter to macro-model building which is a crucial step in seismic imaging workflows as it provides the necessary background model for migration Etgen et al. (2009) or full waveform inversion Hadden et al. (2019).

Source inversion in seismology There is a strong trade-off between earthquake source positions, initial times and velocities during the tomographic inversion. Thus, seismic velocity reconstruction can be largely distorted when there is inaccuracy in earthquake locations (Thurber, 1992). In the framework of Eikonal-adjoint FATT there are a few attempts to invert velocity and source parameters. Virieux et al. (2013) performed some tests in 2D by inverting simultaneously the parameters and comparing different optimization algorithms. The truncated Newton algorithm which requires the second-order adjoint formulation was proved to mitigate scaling and trade-offs between parameters. Recently, Tong (2021) developed an iterative approach to invert earthquake hypocenters and velocity models in 3D, following two steps: first earthquake locations are updated and then the velocity model. The mathematical derivations to obtain the adjoint equation and to include earthquake parameters in the inversion appear compatible with our approach and should be implemented in our code, first in 2D and then in 3D. Depending on the results, we might think about the inclusion of anisotropy, where the elliptical case might be preferred for initial tests.

Improvements in laboratory experiments We identified some difficulties regarding the modeling of the source due to the relative large size of the devices compared to the wavelength (Dellinger and Vernik, 1994). In the acoustic part, we have in our laboratory facilities other piezoelectric sources whose effective diameter varies depending on the central frequency, for instance the PZT of 0.5MHz has an effective diameter of $10\,mm$, which indeed some measurements were done with that source but since the S/N was not so large we discarded that PZT, however this was decided before the findings about the source size modeling. Since we have designed a semi-automatic picking tool, we can reconsider the option of using PZTs with higher frequency where maybe the point source at the center of the diameter is enough as an approximation and the extension can be avoided. In addition, the use of higher frequencies allows us to perform an analysis at different scales, similar to the work Bailly et al. (2019) where datasets of different frequency content were obtained and concluding that sonic measurements acquired on outcrop surfaces seems to fit wit the field scale, however anisotropy was not studied, what we know for several studies is that velocity increase when the frequency increases, however, what about the anisotropy?, how would be the evolution of anisotropy?, the analysis can be done until 2MHz which is the the PZT with maximum central frequency available in the lab.

We have also in the lab a pulsed-laser source with a central frequency of 1MHz, and previously used by Shen (2020), thus it could be used in order to avoid the source extension. However, Shen (2020) reported two key point when using the pulsed-laser, large amount of noise on the data and the source is somewhat abrasive which could harm the sample, thus special training is needed to use it. Other point to discuss, is the feasibility to perform measurements *in situ* like the experiment in Matonti et al. (2017), they used PZT for both sources and receivers, and problems about the device size were not reported certainly due to the size of the sample compared to the devices. We could follow the same principle, however if the receiver laser is needed, the installation in the field is not straightforward, the laser in the laboratory is moved by motors and the amount of measurements is programmed by the user, however we cannot move these motors to the field, consequently we will need to perform the measurements displacing manually the position of the laser which will certainly increase the time of the acquisition. Regarding the GPR measurements, we do not have at this stage other antennas, thus the only option we have now is to change the sample and use a block with higher dimensions, however we have in the lab another block with the same dimension of the block analyzed in this work and extracted from the same quarry, consequently a quick test that can be done, is to locate the blocks next to each other in order to increase the size of the domain to $33 \times 33 \times 66\,cm$, subsequently we need to perform measurements and the data can be compared with the current data we have analyzed in this work, the main evaluation is for the measurements at large offsets and see how large is the suppression of the air effect in this increased domain. Moreover, the GPR equipment is very easy to carry and measurements on the field with larger blocks is not a difficulty.

Bibliography

Abell, B. C., Shao, S., and Pyrak-Nolte, L. J. (2014). Measurements of elastic constants in anisotropic mediaelastic constants in anisotropic media. *Geophysics*, 79(5):D349–D362.

Aki, K., Christoffersson, A., and Husebye, E. S. (1977). Determination of the three-dimensional seismic structure of the lithosphere. *Journal of Geophysical Research*, 82(2):277–296.

Aki, K. and Richards, P. (1980). *Quantitative Seismology: Theory and Methods*. W. H. Freeman & Co, San Francisco.

Akram, J. and Eaton, D. W. (2016a). Refinement of arrival-time picks using a cross-correlation based workflow. *Journal of Applied Geophysics*, 135:55–66.

Akram, J. and Eaton, D. W. (2016b). A review and appraisal of arrival-time picking methods for downhole microseismic dataarrival-time picking methods. *Geophysics*, 81(2):KS71–KS91.

Aldridge, D. F. (1994). Short note: Linearization of the eikonal equation. *Geophysics*, 59(10):1631–1632.

Alkhalifah, T. (2000). An acoustic wave equation for anisotropic media. *Geophysics*, 65:1239–1250.

Alkhalifah, T. and Plessix, R. (2014). A recipe for practical full-waveform inversion in anisotropic media: An analytical parameter resolution study. *Geophysics*, 79(3):R91–R101.

Alkhalifah, T. and Tsvankin, I. (1995). Velocity analysis for transversely isotropic media. *Geophysics*, 60:1550–1566.

Alumbaugh, D., Chang, P. Y., Paprocki, L., Brainard, J. R., Glass, R. J., and Rautman, C. A. (2002). Estimating moisture contents in the vadose zone using cross-borehole ground penetrating radar: A study of accuracy and repeatability. *Water Resources Research*, 38(12):45–1.

Anderson, D. L. and Dziewonski, A. M. (1982). Upper mantle anisotropy: evidence from free oscillations. *Geophysical Journal International*, 69(2):383–404.

Anselmetti, F. S., Von Salis, G. A., Cunningham, K. J., and Eberli, G. P. (1997). Acoustic properties of neogene carbonates and siliciclastics from the subsurface of the florida keys: implications for seismic reflectivity. *Marine Geology*, 144(1-3):9–31.

Arosio, D., Deparis, J., Zanzi, L., and Garambois, S. (2016). Fracture characterization with gpr: A comparative study. In *2016 16th International Conference on Ground Penetrating Radar (GPR)*, pages 1–6. IEEE.

Asnaashari, A., Brossier, R., Garambois, S., Audebert, F., Thore, P., and Virieux, J. (2013). Regularized seismic full waveform inversion with prior model information. *Geophysics*, 78(2):R25–R36.

Ass'ad, J., Tatham, R., McDonald, J., Kusky, T., and Jech, J. (1993). A physical model study of scattering of waves by aligned cracks: Comparison between experiment and theory 1. *Geophysical Prospecting*, 41(3):323–339.

Backus, G. E. (1962). Long-wave elastic anisotropy produced by horizontal layering. *Journal Geophysical Research*, 67:4427–4440.

Baechle, G. T., Colpaert, A., Eberli, G. P., and Weger, R. J. (2008). Effects of microporosity on sonic velocity in carbonate rocks. *The Leading Edge*, 27(8):1012–1018.

Bagaini, C. (2005). Performance of time-delay estimators. *Geophysics*, 70(4):V109–V120.

Bailly, C., Fortin, J., Adelinet, M., and Hamon, Y. (2019). Upscaling of elastic properties in carbonates: A modeling approach based on a multiscale geophysical data set. *Journal of Geophysical Research: Solid Earth*, 124(12):13021–13038.

Batzle, M. L., Han, D.-H., and Hofmann, R. (2006). Fluid mobility and frequency-dependent seismic velocity—direct measurements. *Geophysics*, 71(1):N1–N9.

Becht, A., Tronicke, J., Appel, E., and Dietrich, P. (2004). Inversion strategy in crosshole radar tomography using information of data subsets. *Geophysics*, 69(1):222–230.

Bereš, J., Zeyen, H., Sénéchal, G., Rousset, D., and Gaffet, S. (2013). Seismic anisotropy analysis at the low-noise underground laboratory (lsbb) of rustrel (france). *Journal of Applied Geophysics*, 94:59–71.

Berryman, J. G. (1979). Long-wave elastic anisotropy in transversely isotropic media. *Geophysics*, 44(5):896–917.

Berryman, J. G. (1989). Weighted least-squares criteria for seismic traveltime tomography. *IEEE Transactions on Geoscience and Remote Sensing*, 27(3):302–309.

Berryman, J. G., Thigpen, L., and Chin, R. C. (1988). Bulk elastic wave propagation in partially saturated porous solids. *The Journal of the Acoustical Society of America*, 84(1):360–373.

Biondi, B. (1992). Solving the frequency dependent eikonal equation. In *Expanded Abstracts*, pages 1315–1319. Soc. Expl. Geophys.

Bleistein, N. (1984). *Mathematical methods for wave phenomena*. Academic Press Inc., London.

Boadu, F. K. and Long, L. T. (1996). Effects of fractures on seismic-wave velocity and attenuation. *Geophysical Journal International*, 127(1):86–110.

Born, M. and Wolf, E. (1970). *Principles of optics*. Pergamon Press.

Bouaziz, I. (2015). Etude d'une carotte de la plateforme urgonienne du vaucluse: Approches sédimentologie, pétrophysique et numérique. Master's thesis, Université de Pau et des Pays de l'Adour.

Bracewell, R. N. (1990). Numerical transforms. *Science*, 248(4956):697–704.

Brantut, N. (2018). Time-resolved tomography using acoustic emissions in the laboratory, and application to sandstone compaction. *Geophysical Journal International*, 213(3):2177–2192.

Bretaudeau, F., Brossier, R., Métivier, L., and Virieux, J. (2014). First-arrival delayed tomography using 1st and 2nd order adjoint-state method. In *Expanded Abstracts*, pages 4757–4762. Society of Exploration Geophysics.

Bretaudeau, F., Métivier, L., Brossier, R., and Virieux, J. (2013). The truncated newton using 1st and 2nd order adjoint-state method: a new approach for traveltime tomography without rays. In *AGU Fall Meeting Abstracts*, volume 2013, pages S33A–2388.

Brittan, J., Warner, M., and Pratt, G. (1995). Anisotropic parameters of layered media in terms of composite elastic properties. *Geophysics*, 60(4):1243–1248.

Bruns, H. (1895). *Das eikonal*, volume 35. S. Hirzel.

Cai, W., Qin, F., and Schuster, G. T. (1996). Electromagnetic velocity inversion using 2-D Maxwell's equations. *Geophysics*, 61(4):1007–1021.

Capdeville, Y. and Marigo, J.-J. (2007). Second order homogenization of the elastic wave equation for non-periodic layered media. *Geophysical Journal International*, 170(2):823–838.

Capozzoli, L. and Rizzo, E. (2017). Combined ndt techniques in civil engineering applications: Laboratory and real test. *Construction and Building Materials*, 154:1139–1150.

Carcione, J. and Cavallini, F. (1995). On the acoustic-electromagnetic analogy. *Wave motion*, 21:149–162.

Cataldo, A., Persico, R., Leucci, G., De Benedetto, E., Cannazza, G., Matera, L., and De Giorgi, L. (2014). Time domain reflectometry, ground penetrating radar and electrical resistivity tomography: a comparative analysis of alternative approaches for leak detection in underground pipes. *Ndt & E International*, 62:14–28.

Cerveny, V. (1985). Ray synthetic seismograms for complex two-dimensional and three-dimensional structures. *J. geophys*, 58(2):26.

Cerveny, V. et al. (1982). Direct and inverse kinematic problems for inhomogeneous anisotropic media-linearization approach. *Contrib. Geophys. Inst. Slov. Acad. Sci.*, 13:127–133.

Červeny, V., Jech, J., et al. (1982). Linearized solutions of kinematic problems of seismic body waves in inhomogeneous slightly anisotropic media. *Journal of Geophysics*, 51(1):96–104.

Červený, V. (2001). *Seismic Ray Theory*. Cambridge University Press, Cambridge.

Chapman, C. (2004). *Fundamentals of seismic waves propagation*. Cambridge University Press, Cambridge, England.

Chapman, C. t. and Pratt, R. (1992). Traveltime tomography in anisotropic media—i. theory. *Geophysical Journal International*, 109(1):1–19.

Cheng, X., Jiao, K., Sun, D., and Vigh, D. (2014). Anisotropic parameter estimation with full-waveform inversion of surface seismic data. In *SEG Technical Program Expanded Abstracts 2014*, pages 1072–1077. Society of Exploration Geophysicists.

Cheng, Y. and Shu, C.-W. (2007). A discontinuous Galerkin finite element method for directly solving the Hamilton-Jacobi equations. *Journal of Computational Physics*, 223(1):398 – 415.

Cheng, Y. and Wang, Z. (2014). A new discontinuous Galerkin finite element method for directly solving the Hamilton–Jacobi equations. *Journal of Computational Physics*, 268:134–153.

Cholet, J. and Richard, H. (1954). A test on elastic anisotropy measurement at berriane (north sahara). *Geophysical Prospecting*, 2(3):232–246.

Courant, R. and Hilbert, D. (1966). *Methods of Mathematical Physics*. John Wiley, New York.

Crandall, M. G. and Lions, P. L. (1983). Viscosity solutions of Hamilton–Jacobi equations. *Transactions of the American mathematical society*, 277(1):1–42.

Dafflon, B., Irving, J., and Barrash, W. (2011). Inversion of multiple intersecting high-resolution cross-hole gpr profiles for hydrological characterization at the boise hydrogeophysical research site. *Journal of Applied Geophysics*, 73(4):305–314.

De Donno, G., Di Giambattista, L., and Orlando, L. (2017). High-resolution investigation of masonry samples through gpr and electrical resistivity tomography. *Construction and Building Materials*, 154:1234–1249.

De Meersman, K., Kendall, J.-M., and Van der Baan, M. (2009). The 1998 valhall microseismic data set: An integrated study of relocated sources, seismic multiplets, and s-wave splitting. *Geophysics*, 74(5):B183–B195.

Dellinger, J. and Vernik, L. (1994). Do traveltimes in pulse-transmission experiments yield anisotropic group or phase velocities? *Geophysics*, 59(11):1774–1779.

Demanet, D. (2000). Tomographies 2d et 3d à partir de mesures géophysiques en surface et en forage. *Unpublished PhD thesis. Université de Liège, Belgium.*

Dey-Barsukov, S., Dürrast, H., Rabbel, W., Siegesmund, S., and Wende, S. (2000). Aligned fractures in carbonate rocks: laboratory and in situ measurements of seismic anisotropy. *International Journal of Earth Sciences*, 88(4):829–839.

Dijkstra, E. W. (1959). A note on two problems in connection with graphs. *Numerische Mathematik*, 1:269–271.

Dines, K. and Lytle, R. (1979). Computerized geophysical tomography. *Proceedings of the IEEE*, 67(7):1065 – 1073.

Dunn, R. A., Lekić, V., Detrick, R. S., and Toomey, D. R. (2005). Three-dimensional seismic structure of the mid-atlantic ridge (35 n): Evidence for focused melt supply and lower crustal dike injection. *Journal of Geophysical Research: Solid Earth*, 110(B9).

Eaton, D. (1993). Finite difference traveltime calculation for anisotropic media. *Geophysical Journal International*, 114:273–280.

Eberhart-Phillips, D. and Mark Henderson, C. (2004). Including anisotropy in 3-d velocity inversion and application to marlborough, new zealand. *Geophysical journal international*, 156(2):237–254.

Etgen, J., Gray, S. H., and Zhang, Y. (2009). An overview of depth imaging in exploration geophysics. *Geophysics*, 74(6):WCA5–WCA17.

Falls, S., Young, R., Carlson, S., and Chow, T. (1992). Ultrasonic tomography and acoustic emission in hydraulically fractured lac du bonnet grey granite. *Journal of Geophysical Research: Solid Earth*, 97(B5):6867–6884.

Farra, V. (1989). Ray perturbation theory for heterogeneous hexagonal anisotropic media. *Geophysical Journal International*, 99:723–737.

Farra, V. (1992). Bending method revisited: a hamiltonian approach. *Geophysical Journal International*, 109:138–150.

Farra, V. and Madariaga, R. (1987). Seismic waveform modeling in heterogeneous media by ray perturbation theory. *Journal of Geophysical Research*, 92:2697–2712.

Farra, V., Virieux, J., and Madariaga, R. (1989). Ray perturbation theory for interfaces. *Geophysical Journal International*, 99:377–390.

Fawcett, J. A. and Clayton, R. W. (1984). Tomographic reconstruction of velocity anomalies. *Bulletin of the Seismological Society of America*, 74(6):2201–2219.

Fichtner, A., Kennett, B. L., and Trampert, J. (2013). Separating intrinsic and apparent anisotropy. *Physics of the Earth and Planetary Interiors*, 219:11–20.

Fomel, S. and Claerbout, J. F. (2003). Mutlidimensional recursive filter preconditioning in geophysical estimation problems. *Geophysics*, 68(2):1–12.

Fomel, S., Luo, S., and Zhao, H.-K. (2009). Fast sweeping method for the factored eikonal equation. *Journal of Computational Physics*, 228:6440–6455.

Fournier, F., Leonide, P., Biscarrat, K., Gallois, A., Borgomano, J., and Foubert, A. (2011). Elastic properties of microporous cemented grainstones. *Geophysics*, 76(6):E211–E226.

Fullagar, P. K., Livelybrooks, D. W., Zhang, P., Calvert, A. J., and Wu, Y. (2000). Radio tomography and borehole radar delineation of the mcconnell nickel sulfide deposit, sudbury, ontario, canadaradio and radar delineation. *Geophysics*, 65(6):1920–1930.

Gaffney, C. (2008). Detecting trends in the prediction of the buried past: a review of geophysical techniques in archaeology. *Archaeometry*, 50(2):313–336.

Gajewski, D. and Pšenčík, I. (1990). Vertical seismic profile synthetics by dynamic ray tracing in laterally varying layered anisotropic structures. *Journal of Geophysical Research: Solid Earth*, 95(B7):11301–11315.

Gholami, Y., Brossier, R., Operto, S., Prieux, V., Ribodetti, A., and Virieux, J. (2013a). Which parametrization is suitable for acoustic VTI full waveform inversion? - Part 2: application to Valhall. *Geophysics*, 78(2):R107–R124.

Gholami, Y., Brossier, R., Operto, S., Ribodetti, A., and Virieux, J. (2013b). Which parametrization is suitable for acoustic VTI full waveform inversion? - Part 1: sensitivity and trade-off analysis. *Geophysics*, 78(2):R81–R105.

Gilbert, P. (1972). Iterative methods for the three-dimensional reconstruction of an object from projections. *Journal of theoretical biology*, 36(1):105–117.

Giroux, B. and Gloaguen, E. (2012). Geostatistical traveltime tomography in elliptically anisotropic media. *Geophysical prospecting*, 60(6):1133–1149.

Giroux, B., Gloaguen, E., and Chouteau, M. (2007). bh_tomo—a matlab borehole georadar 2d tomography package. *Computers & Geosciences*, 33(1):126–137.

Gloaguen, E., Marcotte, D., Chouteau, M., and Perroud, H. (2005). Borehole radar velocity inversion using cokriging and cosimulation. *Journal of Applied Geophysics*, 57:242–259.

Goldstein, H. (1980). *Classical Mechanics*. Addison-Wesley Publishing Compagny, Reading.

Gómez, J. V., Álvarez, D., Garrido, S., and Moreno, L. (2019). Fast methods for eikonal equations: an experimental survey. *IEEE Access*, 7:39005–39029.

Gordin, Y., Hatzor, Y. H., and Vinegar, H. J. (2020). Anisotropy evolution during early maturation of organic-rich carbonates. *Journal of Petroleum Science and Engineering*, 188:106946.

Gordon, R., Bender, R., and Herman, G. T. (1970). Algebraic reconstruction techniques (art) for three-dimensional electron microscopy and x-ray photography. *Journal of theoretical Biology*, 29(3):471–481.

Grechka, V. (2009). On the nonuniqueness of traveltime inversion in elliptically anisotropic media. *Geophysics*, 74(5):WB137–WB145.

Gremaud, P. A. and Kuster, C. M. (2006). Computational study of fast methods for the Eikonal equation. *SIAM Journal on Scientific Computing*, 27(6):1803–1816.

Gu, H., Cai, C., and Wang, Y. (2006). Investigation of fractures using seismic computerized crosshole tomography. *Journal of Environmental and Engineering Geophysics*, 11(2):143–150.

Guitton, A., Ayeni, G., and Díaz, E. (2012). Constrained full-waveform inversion by model reparameterization. *Geophysics*, 77(2):R117–R127.

Gutenberg, B. (1914). Über erdbenwellen viia. beobachtungen an registrierungen von fernbeben in göttingen und folgerungen über die konstitution des erdkörpers. *Nachrichten von der Könglichen Gesellschaft der Wissenschaften zu Göttinge, Mathematisch-Physikalische Klasse*, pages 125–176.

Hadden, S., Gerhard Pratt, R., and Smithyman, B. (2019). Anisotropic full-waveform inversion of crosshole seismic data: A vertical symmetry axis field data application. *Geophysics*, 84(1):B15–B32.

Hagedoorn, J. (1954). A practical example of an anisotropic velocity-layer. *Geophysical Prospecting*, 2(1):52–60.

Hagrey, A. et al. (2000). Gpr study of pore water content and salinity in sand [link]. *Geophysical Prospecting*, 48(1):63–85.

Hale, D. (2007). Local dip filtering with directional laplacians. Technical report, Centre for Wave Phenomena, Colorado School of Mines.

Hall, S. A., Kendall, R. R., Kendall, J.-M., and Sondergeld, C. (2000). Analysis of anisotropic velocities in a core sample and avoa from a fractured vuggy carbonate reservoir. *Anisotropy 2000: Fractures, Converted Waves, and Case Studies*, pages 257–269.

Hamilton, E., Shumway, G., Menard, H., and Shipek, C. (1956). Acoustic and other physical properties of shallow-water sediments off san diego. *The Journal of the Acoustical Society of America*, 28(1):1–1.

Hanafy, S. and Al Hagrey, S. (2005). Ground-penetrating radar tomography for soil-moisture heterogeneity. *Geophysics*, 71(1):K9–K18.

Hanyga, A. (1982). The kinematic inverse problem for weakly laterally inhomogeneous anisotropic media. *Tectonophysics*, 90(1-2):253–262.

He, W. and Plessix, R. (2017). Analysis of different parameterisations of waveform inversion of compressional body waves in an elastic transverse isotropic earth with a vertical axis of symmetry. *Geophysical Prospecting*, 65:1004–1024.

Helbig, K. (1956). Die ausbreitung elastischer wellen in anisotropen medien. *Geophysical Prospecting*, 4(1):70–81.

Helbig, K. (1994). *Foundations of anisotropy for exploration seismics*. Handbook of geophysical exploration: Seismic exploration. Pergamon.

Helbig, K. et al. (1979). Discussion on" the reflection, refraction, and diffraction of waves in media with an elliptical velocity dependence", by franklin k. levin (geophysics, april 1978, p. 528-537).

Helbig, K. and Thomsen, L. (2005). 75-plus years of anisotropy in exploration and reservoir seismics: A historical review of concepts and methods. *Geophysics*, 70(6):9–23.

Hesse, A. (1999). Multi-parametric survey for archaeology: how and why, or how and why not? *Journal of Applied Geophysics*, 41(2-3):157–168.

Hole, D. and Zelt, B. (1995). 3-D finite difference reflection traveltimes. *Geophysical Journal International*, 121:427–434.

Hudson, J. A. (1981). Wave speeds and attenuation of elastic waves in material containing cracks. *Geophysical Journal International*, 64(1):133–150.

Hunziker, J., Laloy, E., and Linde, N. (2017). Inference of multi-gaussian relative permittivity fields by probabilistic inversion of crosshole ground-penetrating radar data. *Geophysics*, 82(5):H25–H40.

Ikelle, L. T. (2012). On elastic-electromagnetic mathematical equivalences. *Geophysical Journal International*, 189(3):1771–1780.

Irving, J., Knoll, M., and Knight, R. (2007). Improving crosshole radar velocity tomograms: A new approach to incorporating high-angle traveltime data. *Geophysics*, 72(4).

Irving, J. D. and Knight, R. J. (2005). Effect of antennas on velocity estimates obtained from crosshole gpr data. *Geophysics*, 70(5):K39–K42.

Iyer, H. M. and Hirahara, K. (1993). *Seismic tomography: theory and practice*. Chapman & Hall, London.

Jackson, M. J. and Tweeton, D. R. (1996). 3dtom, three-dimensional geophysical tomography. Technical report, United States. Government Printing Office.

Jansen, D., Carlson, S., Young, R., and Hutchins, D. (1993). Ultrasonic imaging and acoustic emission monitoring of thermally induced microcracks in lac du bonnet granite. *Journal of Geophysical Research: Solid Earth*, 98(B12):22231–22243.

Jech, J. and Pšenčík, I. (1989). First-order perturbation method for anisotropic media. *Geophysical Journal International*, 99(2):369–376.

Jiang, F. and Zhou, H.-w. (2011). Traveltime inversion and error analysis for layered anisotropy. *Journal of Applied Geophysics*, 73(2):101–110.

Jongmans, D. and Garambois, S. (2007). Geophysical investigation of landslides: a review. *Bulletin de la Société géologique de France*, 178(2):101–112.

Kahraman, S. (2002). The effects of fracture roughness on p-wave velocity. *Engineering Geology*, 63(3-4):347–350.

Kaipio, J. and Somersalo, E. (2007). Statistical inverse problems: discretization, model reduction and inverse crimes. *Journal of computational and applied mathematics*, 198(2):493–504.

Kana, A. A. (2015). Field measurements of gpr antenna pattern for ava data correction. *British Journal of Earth Sciences Research*, 3(2):18–34.

Kao, C. Y., Osher, S., and Qian, J. (2004). Lax-friedrichs sweeping schemes for static hamilton-jacobi equations. *Journal of Computational Physics*, 196:367–391.

Keller, J. B. (1962). A geometrical theory of diffraction. *Journal of the Optical Society of America*, 52:116–130.

King, M., Myer, L., and Rezowalli, J. (1986). Experimental studies of elastic-wave propagation in a columnar-jointed rock mass. *Geophysical prospecting*, 34(8):1185–1199.

Klimeš, L. and Kvaskička, M. (1994). 3-D network ray tracing. *Geophysical Journal International*, 116:726–738.

Kline, M. and Kay, I. W. (1965). *Electromagnetic theory and geometrical optics*. Interscience, New York.

Kneisel, C., Hauck, C., Fortier, R., and Moorman, B. (2008). Advances in geophysical methods for permafrost investigations. *Permafrost and periglacial processes*, 19(2):157–178.

Knight, R. and Dvorkin, J. (1992). Seismic and electrical properties of sandstones at low saturations. *Journal of Geophysical Research*, 97:17425–17432.

Knight, R. and Endres, A. L. (1990). A new concept in modeling the dielectric response of sandstones; defining a wetted rock and bulk water system. *Geophysics*, 55(5):586–594.

Lambaré, G., Lucio, P. S., and Hanyga, A. (1996). Two-dimensional multivalued traveltime and amplitude maps by uniform sampling of ray field. *Geophysical Journal International*, 125:584–598.

Latorre, D., Virieux, J., Monfret, T., Monteiller, V., Vanorio, T., Got, J. L., and Lyon-Caen, H. (2004). A new seismic tomography of Aigion area (Gulf of Corinth, Greece) from the 1991 data set. *Geophysical Journal International*, 159:1013–1031.

Le Bouteiller, P. (2018). *Eulerian approach of Hamilton–Jacobi equation with a discontinuous Galerkin method in heterogeneous anisotropic medium: Application to seismic imaging*. PhD thesis, University Grenoble Alpes.

Le Bouteiller, P., Benjemaa, M., Métivier, L., and Virieux, J. (2018). An accurate discontinuous Galerkin method for solving point–source Eikonal equation in 2-D heterogeneous anisotropic media. *Geophysical Journal International*, 212(3):1498–1522.

Le Bouteiller, P., Benjemaa, M., Métivier, L., and Virieux, J. (2019). A discontinuous galerkin fast-sweeping eikonal solver for fast and accurate traveltime computation in 3d tilted anisotropic media. *Geophysics*, 84(2):C107–C118.

Lecomte, I. (1993). Finite difference calculation of first traveltimes in anisotropic media. *Geophysical Journal International*, 113:318–342.

Lehmann, I. (1936). P'. *Publications du Bureau Central Séismologique International*, A14:87–115.

Leucci, G. and De Giorgi, L. (2006). Experimental studies on the effects of fracture on the p and s wave velocity propagation in sedimentary rock ("calcarenite del salento"). *Engineering Geology*, 84(3-4):130–142.

Leung, S. and Qian, J. (2006). An adjoint state method for three-dimensional transmission traveltime tomography using first-arrivals. *Communications in Mathematical Sciences*, 4(1):249–266.

Li, W., Wen, J., Xiao, Z., and Xu, S. (2018). Application of ground-penetrating radar for detecting internal anomalies in tree trunks with irregular contours. *Sensors*, 18(2):649.

Lions, P.-L. (1982). *Generalized solutions of Hamilton–Jacobi equations*. Pitman.

Lubbe, R. and Worthington, M. (2006). A field investigation of fracture compliance. *Geophysical Prospecting*, 54(3):319–331.

Lucio, P., Lambaré, G., and Hanyga, A. (1996). 3D multivalued travel time and amplitude maps. *Pure and Applied Geophysics*, 148:113–136.

Luo, S. and Qian, J. (2011). Factored singularities and high-order Lax-Friedrichs sweeping schemes for point-source traveltimes and amplitudes. *Journal of Computational Physics*, 230:4742–4755.

Luo, S. and Qian, J. (2012). Fast sweeping method for factored anisotropic eikonal equations: multipicative and additive factors. *Journal of Scientific Computing*, 52:360–382.

Luo, Y. and Schuster, G. T. (1991). Wave-equation traveltime inversion. *Geophysics*, 56(5):645–653.

Mangel, A. R., Moysey, S. M., and Bradford, J. (2020). Reflection tomography of time-lapse gpr data for studying dynamic unsaturated flow phenomena. *Hydrology and Earth System Sciences*, 24(1):159–167.

Martinez, A. and Byrnes, A. P. (2001). Modeling dielectric-constant values of geologic materials: An aid to ground-penetrating radar data collection and interpretation. *Midcontinent Geoscience*, pages 1–16.

Martínez, J. M. and Schmitt, D. R. (2013). Anisotropic elastic moduli of carbonates and evaporites from the weyburn-midale reservoir and seal rocks. *Geophysical Prospecting*, 61(Rock Physics for Reservoir Exploration, Characterisation and Monitoring):363–379.

Matonti, C., Guglielmi, Y., Viseur, S., Bruna, P., Borgomano, J., Dahl, C., and Marié, L. (2015). Heterogeneities and diagenetic control on the spatial distribution of carbonate rocks acoustic properties at the outcrop scale. *Tectonophysics*, 638:94–111.

Matonti, C., Guglielmi, Y., Viseur, S., Garambois, S., and Marié, L. (2017). P-wave velocity anisotropy related to sealed fractures reactivation tracing the structural diagenesis in carbonates. *Tectonophysics*, 705:80–92.

McCann, D. and Forde, M. (2001). Review of ndt methods in the assessment of concrete and masonry structures. *Ndt & E International*, 34(2):71–84.

McCollum, B. and Snell, F. (1932). Asymmetry of sound velocity in stratified formations. *Physics*, 2(3):174–185.

McMechan, G. A. (1983). Seismic tomography in boreholes. *Geophysical Journal International*, 74(2):601–612.

Meléndez, A., Jiménez, C. E., Sallarès, V., and Ranero, C. R. (2019). Anisotropic p-wave travel-time tomography implementing thomsen's weak approximation in tomo3d. *Solid Earth*, 10(6):1857–1876.

Menningen, J., Siegesmund, S., Tweeton, D., and Träupmann, M. (2018). Ultrasonic tomography: non-destructive evaluation of the weathering state on a marble obelisk, considering the effects of structural properties. *Environmental Earth Sciences*, 77(17):601.

Métivier, L. and Brossier, R. (2016). The seiscope optimization toolbox: A large-scale nonlinear optimization library based on reverse communication. *Geophysics*, 81(2):F11–F25.

Metje, N., Atkins, P., Brennan, M., Chapman, D., Lim, H., Machell, J., Muggleton, J., Pennock, S., Ratcliffe, J., Redfern, M., et al. (2007). Mapping the underworld–state-of-the-art review. *Tunnelling and underground space technology*, 22(5-6):568–586.

Michelena, R. J., Muir, F., and Harris, J. (1993). Anisotropic traveltime tomography. *Geophysical Prospecting*, 41(4):381–412.

Millard, S., Shaari, A., and Bungey, J. (2002). Field pattern characteristics of gpr antennas. *NDT & E International*, 35(7):473–482.

Mirebeau, J.-M. and Portegies, J. (2019). Hamiltonian fast marching: A numerical solver for anisotropic and non-holonomic eikonal pdes. *Image Processing On Line*, 9:47–93.

Mohorovicic, A. (1909). Das beben vom 8. x. 1909. *Jb. Met. Obs. Zagreb (Agram)*, 9:1–63.

Moos, D. and Zoback, M. D. (1983). In situ studies of velocity in fractured crystalline rocks. *Journal of Geophysical Research: Solid Earth*, 88(B3):2345–2358.

Moser, T. J. (1991). Shortest path calculation of seismic rays. *Geophysics*, 56(1):59–67.

Moser, T. J., Nolet, G., and Snieder, R. (1992). Ray bending revisited. *Bulletin of the Seismological Society of America*, 82:259–288.

Musgrave, M. (1970). *Crystal acoustics; introduction to the study of elastic waves and vibrations in crystals*. Holden-Day.

Nelson, R. (2001). *Geologic analysis of naturally fractured reservoirs*. Elsevier.

Nocedal, J. (1980). Updating Quasi-Newton Matrices With Limited Storage. *Mathematics of Computation*, 35(151):773–782.

Nocedal, J. and Wright, S. J. (2006). *Numerical Optimization*. Springer, 2nd edition.

Nolet, G. (1987). *Seismic tomography with applications in global seismology and exploration geophysics*. D. Reidel publishing Company.

Nolet, G. and Moser, T. J. (1993). Teleseismic delay times in a 3-D Earth and a new look at the S discrepancy. *Geophysical Journal International*, 114:185–195.

O'Connell, R. J. and Budiansky, B. (1974). Seismic velocities in dry and saturated cracked solids. *Journal of geophysical Research*, 79(35):5412–5426.

Oldham, R. (1906). The constitution of the earth. *Quarterly Journal of the Geological Society of London*, 62:456–475.

Operto, S., Brossier, R., Gholami, Y., Métivier, L., Prieux, V., Ribodetti, A., and Virieux, J. (2013). A guided tour of multiparameter full waveform inversion for multicomponent data: from theory to practice. *The Leading Edge*, Special section Full Waveform Inversion(September):1040–1054.

Operto, S., Virieux, J., Ribodetti, A., and Anderson, J. E. (2009). Finite-difference frequency-domain modeling of visco-acoustic wave propagation in two-dimensional TTI media. *Geophysics*, 74 (5):T75–T95.

Orlando, L. and Palladini, L. (2019). Time-lapse laboratory tests to monitor multiple phases of dnapl in a porous medium. *Near Surface Geophysics*, 17(1):55–68.

Paige, C. C. and Saunders, M. A. (1982). ALGORITHM 583 LSQR : Sparse linear equations and least squares problems. *ACM Transactions on Mathematical Software*, 8(2):195–209.

Peraldi, R. and Clement, A. (1972). Digital processing of refraction data study of first arrivals. *Geophysical Prospecting*, 20(3):529–548.

Peterson, Jr, J. E. (2001). Pre-inversion corrections and analysis of radar tomographic data. *Journal of Environmental & Engineering Geophysics*, 6(1):1–18.

Pica, A. (1997). Fast and accurate finite-difference solutions of the 3-D eikonal equation parameterized in celerity. In *Expanded Abstracts*, pages 1774–1777. Society of Exploration Geophysics.

Pinard, H., Garambois, S., Métivier, L., Dietrich, M., Sénéchal, G., and Rousset, D. (2016). Full-waveform inversion of gpr data acquired between boreholes in rustrel carbonates. In *Inter-Disciplinary Underground Science & Technology (i-DUST 2016), Avignon (France)*, volume 12. E3S Web of Conferences.

Plessix, R. E. (2006). A review of the adjoint-state method for computing the gradient of a functional with geophysical applications. *Geophysical Journal International*, 167(2):495–503.

Plessix, R. E. and Cao, Q. (2011). A parametrization study for surface seismic full waveform inversion in an acoustic vertical transversely isotropic medium. *Geophysical Journal International*, 185:539–556.

Podvin, P. and Lecomte, I. (1991). Finite difference computation of traveltimes in very contrasted velocity model : a massively parallel approach and its associated tools. *Geophysical Journal International*, 105:271–284.

Polytec (2013a). *Vibrometer Controller: OFV-5000*. Polytec.

Polytec (2013b). *Vibrometer Single Point Sensor Head: OFV-505/-503*. Polytec.

Powers, M. H. (1997). Modeling frequency-dependent gpr. *The leading edge*, 16(11):1657–1662.

Pratt, R. and Chapman, C. (1992). Traveltime tomography in anisotropic media—ii. application. *Geophysical Journal International*, 109(1):20–37.

Pšencık, I., Ruzek, B., Lokajıcek, T., and Svitek, T. (2018). Determination of rock-sample anisotropy from p-and s-wave traveltime inversion. *Geophysical Journal International*, 214(2):1088–1104.

Pyrak-Nolte, L. and Morris, J. (2000). Single fractures under normal stress: The relation between fracture specific stiffness and fluid flow. *International Journal of Rock Mechanics and Mining Sciences*, 37(1-2):245–262.

Pyrak-Nolte, L. J., Myer, L. R., and Cook, N. G. (1990a). Anisotropy in seismic velocities and amplitudes from multiple parallel fractures. *Journal of Geophysical Research: Solid Earth*, 95(B7):11345–11358.

Pyrak-Nolte, L. J., Myer, L. R., and Cook, N. G. (1990b). Transmission of seismic waves across single natural fractures. *Journal of Geophysical Research: Solid Earth*, 95(B6):8617–8638.

Qian, J., Zhang, Y.-T., and Zhao, H.-K. (2007). A fast sweeping method for static convex Hamilton–Jacobi equations. *Journal of Scientific Computing*, 31:237–271.

Qin, F. and Schuster, G. (1993). First-arrival travel-time calculation for anisotropic media. *Geophysics*, 58:1349–1358.

Rawlinson, N., Hauser, J., and Sambridge, M. (2007). Seismic ray tracing and wavefront tracking in laterally heterogeneous media. *Advances in Geophysics*, 49:203–267.

Rubin, Y. and Hubbard, S. S. (2006). *Hydrogeophysics*, volume 50. Springer Science & Business Media.

Sabbione, J. I. and Velis, D. (2010). Automatic first-breaks picking: New strategies and algorithms. *Geophysics*, 75(4):V67–V76.

Salcedo, M., Garambois, S., Brito, D., and Sanjuan, F. (2021). Multiparameter anisotropic first-arrival seismic tomography of acoustic laboratory data in carbonates. In *NSG2021 2nd Conference on Geophysics for Infrastructure Planning, Monitoring and BIM*, volume 2021, pages 1–5. European Association of Geoscientists & Engineers.

Salcedo, M., Garambois, S., Le Bouteiller, P., Li, Y., Sénéchal, G., Danquigny, C., and Virieux, J. (2020). Matrix-free crosshole elliptical-anisotropy tomography: parametrization analysis and ground-penetrating radar applications in carbonates. *Near Surface Geophysics*, 18(6):697–712.

Salcedo, M., Garambois, S., Le Bouteiller, P., and Virieux, J. (2019). Anisotropie matrix-free tomography using discontinuous galerkin of gpr data acquired between boreholes in rustrel carbonates. In *10th International Workshop on Advanced Ground Penetrating Radar*, volume 2019, pages 1–7. European Association of Geoscientists & Engineers.

Samyn, K., Mathieu, F., Bitri, A., Nachbaur, A., and Closset, L. (2014). Integrated geophysical approach in assessing karst presence and sinkhole susceptibility along flood-protection dykes of the loire river, orléans, france. *Engineering geology*, 183:170–184.

Sayers, C. (1994). The elastic anisotropy of shales. *Journal of Geophysical Research*, 99:767–774.

Scales, J. A. (1987). Tomographic inversion via the conjugate gradient method. *Geophysics*, 52(2):179–185.

Schijns, H., Schmitt, D. R., Heikkinen, P. J., and Kukkonen, I. T. (2012). Seismic anisotropy in the crystalline upper crust: observations and modelling from the outokumpu scientific borehole, Finland. *Geophysical Journal International*, 189(1):541–553.

Schuster, G. T. (2017). *Seismic inversion*. Society of Exploration Geophysicists.

Sei, A. and Symes, W. W. (1994). Gradient calculation of the traveltime cost function without ray tracing. In *SEG Technical Program Expanded Abstracts*, pages 1351–1354. SEG.

Sethian, J. and Popovici, A. (1999). 3-D traveltime computation using the fast marching method. *Geophysics*, 64:516–523.

Sethian, J. A. (1996). A fast marching level set method for monotonically advancing fronts. *Proceedings of the National Academy of Sciences of the United States of America*, 93:1591–1595.

Sethian, J. A. (1999). Fast marching methods. *SIAM Review*, 41(2):199–235.

Shearer, P. M. (2009). *Introduction to seismology*. Cambridge University Press, Cambridge, UK.

Shen, C. (2020). *Experimental and numerical studies of seismic wave propagation in carbonate rocks at the laboratory scale*. PhD thesis, Université de Pau et des Pays de l'Adour.

Shen, C., Brito, D., Diaz, J., Bordes, C., Virieux, J., and Garambois, S. (2021). Tomographic imaging of a carbonate core using different ultrasonic seismic sources at the laboratory scale: Piezoelectric versus point-like pulsed-laser. In *First International Meeting for Applied Geoscience & Energy*, pages 3390–3394. Society of Exploration Geophysicists.

Siegesmund, S., Kruhl, J. H., and Lüschen, E. (1996). The significance of rock fabrics for the geological-interpretation of geophysical anisotropies.

Stewart, R. (1988). An algebraic reconstruction technique for weakly anisotropic velocity. *Geophysics*, 53(12):1613–1615.

Taillandier, C., Noble, M., Chauris, H., and Calandra, H. (2009). First-arrival travel time tomography based on the adjoint state method. *Geophysics*, 74(6):WCB1–WCB10.

Takeuchi, H. and Saito, M. (1972). Seismic surface waves. *Methods in computational physics*, 11:217–295.

Tavakoli F., B., Operto, S., Ribodetti, A., and Virieux, J. (2019). Matrix-free anisotropic slope tomography: theory and application. *Geophysics*, 84(1):R35–R57.

Thomsen, L. A. (1986). Weak elastic anisotropy. *Geophysics*, 51:1954–1966.

Thurber, C. H. (1992). Hypocenter-velocity structure coupling in local earthquake tomography. *Physics of the Earth and Planetary Interiors*, 75(1-3):55–62.

Tikhonov, A. and Arsenin, V. (1977). *Solution of ill-posed problems*. Winston, Washington, DC.

Tong, P. (2021). Adjoint-state traveltime tomography: Eikonal equation-based methods and application to the anza area in southern california. *Journal of Geophysical Research: Solid Earth*, 126(5):e2021JB021818.

Trampert, J. and Lévêque, J.-J. (1990). Simultaneous iterative reconstruction technique: physical interpretation based on the generalized least squares solution. *Journal of Geophysical Research*, 95:12553–12559.

Trinh, P. T., Brossier, R., Métivier, L., Virieux, J., and Wellington, P. (2017). Bessel smoothing filter for spectral element mesh. *Geophysical Journal International*, 209(3):1489–1512.

Tronicke, J., Tweeton, D. R., Dietrich, P., and Appel, E. (2001). Improved crosshole radar tomography by using direct and reflected arrival times. *Journal of Applied Geophysics*, 47(2):97–105.

Tsai, Y.-H. R., Chen, L.-T., Osher, S., and Zhao, H.-K. (2003). Fast sweeping algorithms for a class of Hamilton–Jacobi equations. *SIAM Journal on Numerical Analysis*, 41(2):673–694.

Tsitsiklis, J. N. (1995). Efficient algorithms for globally optimal trajectories. *IEEE Transactions on Automatic Control*, 40(9):1528–1538.

Tsvankin, I. (2001). Seismic signature and analysis of reflection data in anisotropic media. In Helbig, K. and Treitel, S., editors, *Seismic Exploration*, volume 29 of *Handbook of Geophysical Exploration*. Pergamon.

Tsvankin, I. and Thomsen, L. (1994). Nonhyperbolic reflection moveout in anisotropic media. *Geophysics*, 59:1290–1304.

Van Avendonk, H. J., Harding, A. J., Orcutt, J. A., and McClain, J. S. (1998). A two-dimensional tomographic study of the clipperton transform fault. *Journal of Geophysical Research: Solid Earth*, 103(B8):17885–17899.

VanDecar, J. and Crosson, R. (1990). Determination of teleseismic relative phase arrival times using multi-channel cross-correlation and least squares. *Bulletin of the Seismological Society of America*, 80(1):150–169.

Vanorio, T. and Mavko, G. (2011). Laboratory measurements of the acoustic and transport properties of carbonate rocks and their link with the amount of microcrystalline matrix. *Geophysics*, 76(4):E105–E115.

Vasco, D. W., Peterson Jr, J. E., and Lee, K. H. (1997). Ground-penetrating radar velocity tomography in heterogeneous and anisotropic media. *Geophysics*, 62(6):1758–1773.

Vasco, D. W., Peterson Jr, J. E., and Majer, E. L. (1998). Resolving seismic anisotropy: Sparse matrix methods for geophysical inverse problems. *Geophysics*, 63(3):970–983.

Vereecken, H., Binley, A., Cassiani, G., Revil, A., and Titov, K. (2006). Applied hydrogeophysics. In *Applied hydrogeophysics*, pages 1–8. Springer.

Vidale, D. (1988). Finite-difference calculation of travel time. *Bulletin of the Seismological Society of America*, 78:2062–2076.

Vidale, J. (1990). Finite-difference calculation of travel times in three dimensions. *Geophysics*, 55(5):521–526.

Vigh, D., Cheng, X., Jiao, K., Sun, D., and Kapoor, J. (2014). Multiparameter tti full waveform inversion on long-offset broadband acquisition: a case study. In *Expanded Abstracts*, pages 1061–1065. Society of Exploration Geophysics.

Vinje, V., Iversen, E., Astebøl, K., and Gjøystdal, H. (1996a). Estimation of multivalued arrivals in 3D models using wavefront construction-part I. *Geophysical Prospecting*, pages 819–842.

Vinje, V., Iversen, E., Astebøl, K., and Gjøystdal, H. (1996b). Estimation of multivalued arrivals in 3D models using wavefront construction-part II: Tracing and interpolation. *Geophysical Prospecting*, pages 843–858.

Vinje, V., Iversen, E., and Gjøystdal, H. (1993). Traveltime and amplitude estimation using wavefront construction. *Geophysics*, pages 1157–1166.

Virieux, J., Bretaudeau, F., Métivier, L., and Brossier, R. (2013). Joint inversion of seismic velocities and source location without rays using the truncated Newton and the adjoint-state method. In *Abstracts*, page B4.

Virieux, J., Calandra, H., and Plessix, R. E. (2011). A review of the spectral, pseudo-spectral, finite-difference and finite-element modelling techniques for geophysical imaging. *Geophysical Prospecting*, 59:794–813.

Virieux, J., Etienne, V., Cruz-Atienza, V., Brossier, R., Chaljub, E., Coutant, O., Garambois, S., Mercerat, D., Prieux, V., Operto, S., Ribodetti, A., and Tago, J. (2012). Modelling seismic wave propagation for geophysical imaging. In Kanao, M., editor, *Seismic Waves - Research and Analysis*, pages 253–304. InTech.

Virieux, J., Farra, V., and Madariaga, R. (1988). Ray tracing for earthquake location in laterally heterogeneous media. *Journal Geophysical Research*, 93(B6):1116–1120.

Virieux, J. and Lambaré, G. (2015). Theory and observations: Body waves, ray methods, and finite-frequency effects. *Treatise on Geophysics (Second Edition)*, 1:169–200.

Waheed, U. and Alkhalifah, T. (2017). A fast sweeping algorithm for accurate solution of the tilted transversely isotropic eikonal equation using factorization. *Geophysics*, 82(6).

Waheed, U., Alkhalifah, T., and Wang, H. (2015a). Efficient traveltime solutions of the acoustic TI eikonal equation. *Journal of Computational Physics*, 282(Supplement C):62–76.

Waheed, U. B., Flagg, G., and Yarman, C. E. (2016). First-arrival traveltime tomography for anisotropic media using the adjoint-state method. *Geophysics*, 81(4):R147–R155.

Waheed, U. B., Yarman, C. E., and Flagg, G. (2015b). An iterative, fast-sweeping-based eikonal solver for 3D tilted anisotropic media. *Geophysics*, 80:C49–C58.

Watanabe, T. and Sassa, K. (1996). Seismic attenuation tomography and its application to rock mass evaluation. In *International journal of rock mechanics and mining sciences & geomechanics abstracts*, volume 33, pages 467–477. Elsevier.

Wei, J. and Di, B. (2008). A physical model study of effect of fracture aperture on seismic wave. *Science in China Series D: Earth Sciences*, 51(2):233–240.

Wellington, P., Brossier, R., Hamitou, O., Trinh, P., and Virieux, J. (2017). Efficient anisotropic dip filtering via inverse correlation functions. *Geophysics*, 82(4):A31–A35.

Williamson, P. (1991). A guide to the limits of resolution imposed by scattering in ray tomography. *Geophysics*, 56:202–207.

Williamson, P. R. and Worthington, M. H. (1993). Resolution limits in ray tomography due to wave behavior: Numerical experiments. *Geophysics*, 58:727–735.

Winterstein, D. (1990). Velocity anisotropy terminology for geophysicists. *Geophysics*, 55(8):1070–1088.

Wirgin, A. (2004). The inverse crime. *arXiv preprint math-ph/0401050*.

Woodward, M. J. (1992). Wave-equation tomography. *Geophysics*, 57:15–26.

Worthington, M. and Lubbe, R. (2007). The scaling of fracture compliance. *Geological Society, London, Special Publications*, 270(1):73–82.

Zelt, C. and Barton, P. J. (1998). Three-dimensional seismic refraction tomography: a comparison of two methods applied to data from the Faeroe basin. *Journal of Geophysical Research*, 103(B4):7187–7210.

Zelt, C. and Smith, R. B. (1992). Seismic traveltime inversion for 2-D crustal velocity structure. *Geophysical Journal International*, 108:16–34.

Zhang, L., Rector III, J. W., and Hoversten, G. M. (2005). Eikonal solver in the celerity domain. *Geophysical Journal International*, 162:1–8.

Zhao, H. (2005). A fast sweeping method for eikonal equations. *Mathematics of computation*, 74:603–627.

Zhou, B. and Greenhalgh, S. (2005). Analytic expressions for the velocity sensitivity to the elastic moduli for the most general anisotropic media. *Geophysical Prospecting*, 53(4):619–641.

Zhou, B. and Greenhalgh, S. (2008a). Non-linear traveltime inversion for 3-d seismic tomography in strongly anisotropic media. *Geophysical Journal International*, 172(1):383–394.

Zhou, B. and Greenhalgh, S. (2008b). Non-linear traveltime inversion for 3-d seismic tomography in strongly anisotropic media. *Geophysics*, 172:383–394.

Zhou, H.-W. (2014). *Practical seismic data analysis*. Cambridge University Press.

Zhu, T. and Chun, K.-Y. (1994). Understanding finite-frequency wave phenomena: phase-ray formulation and inhomogeneity scattering. *Geophysical Journal International*, 119:78–90.